THE MINISTRY OF EDUCATION AND SCIENCE OF THE RUSSIAN FEDERATION

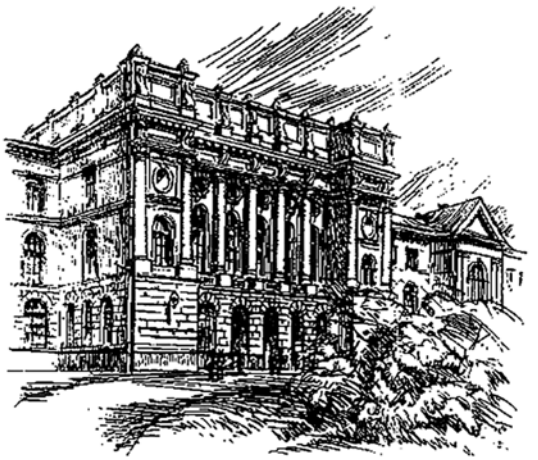

ST. PETERSBURG STATE POLYTECHNICAL UNIVERSITY JOURNAL

Physics and Mathematics

4-2(182) 2013

Polytechnical University Publishing House
Saint Petersburg
2013

ST. PETERSBURG STATE POLYTECHNICAL UNIVERSITY JOURNAL

The journal is published under the scientific and methodical guidance of RAS since 1995.

The journal is included in the List of leading peer-reviewed scientific journals and other editions to publish major findings of theses for the research degrees of Doctor of Sciences and Candidate of Sciences.

The publications are presented in the VINITI RAS Abstract Journal and Ulrich's Periodical Directory International Database.

The journal is published since 2008 as part of the periodical edition 'Nauchno-tekhnicheskie vedomosti SPbGPU' (ISSN 1994-2354).

The journal is registered with the Federal Service for Supervision in the Sphere of Telecom, Information Technologies and Mass Communications (ROSKOMNADZOR). Certificate ПИ № ФС77-52144 issued December 11, 2012.

Subscription index **71823** in the «Journals and Magazines» catalogue, Rospechat agency.

The journal is in the Russian Science Citation Index (RSCI) database.

Address: 195251 Politekhnicheskaya St. 29, St. Petersburg, Russia.
Phone: (812) 294-22-85.

МИНИСТЕРСТВО ОБРАЗОВАНИЯ И НАУКИ РОССИЙСКОЙ ФЕДЕРАЦИИ

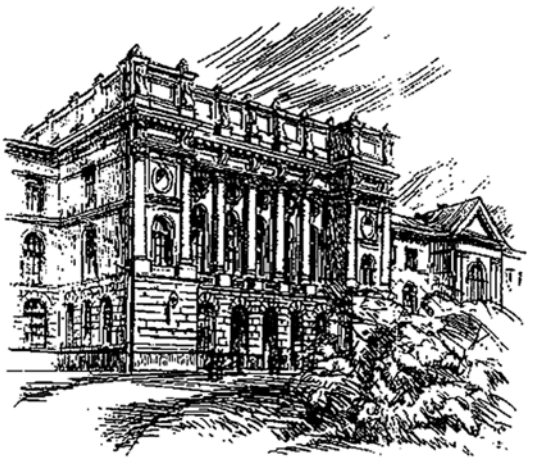

НАУЧНО-ТЕХНИЧЕСКИЕ ВЕДОМОСТИ

САНКТ-ПЕТЕРБУРГСКОГО ГОСУДАРСТВЕННОГО ПОЛИТЕХНИЧЕСКОГО УНИВЕРСИТЕТА

Физико-математические науки

4-2(182) 2013

Издательство Политехнического университета
Санкт-Петербург
2013

Журнал с 1995 года издается под научно-методическим руководством Российской академии наук.

Журнал с 2002 г. входит в Перечень ведущих рецензируемых научных журналов и изданий, в которых должны быть опубликованы основные результаты диссертаций на соискание ученых степеней доктора и кандидата наук.

Сведения о публикациях представлены в Реферативном журнале ВИНИТИ РАН, в международной справочной системе «Ulrich's Periodical Directory».

С 2008 года выпускается в составе сериального периодического издания «Научно-технические ведомости СПбГПУ» ISSN 1994-2354.

Журнал зарегистрирован Федеральной службой по надзору в сфере информационных технологий и массовых коммуникаций (Роскомнадзор). Свидетельство о регистрации ПИ № ФС77-52144 от 11 декабря 2012 г.

Подписной индекс **71823** в каталоге «Газеты. Журналы» Агентства «Роспечать».

Журнал включен в базу данных «Российский индекс научного цитирования» (РИНЦ), размещенную на платформе Научной электронной библиотеки на сайте http://www.elibrary.ru

При перепечатке материалов ссылка на журнал обязательна.

Точка зрения редакции может не совпадать с мнением авторов статей.

Адрес редакции и издательства: Россия, 195251, Санкт-Петербург, ул. Политехническая, д. 29.
Тел. редакции (812) 294-22-85.

Contents

Physical Optics

Theoretical Physics

Содержание

Отчеты о международном сотрудничестве

Физика конденсированного состояния

Физическая электроника

Физическая оптика

Теоретическая физика

UDC 538.913: 620.22 - 022.53

A.V. Filimonov [1], A.I. Rudskoy [1], A.A. Naberezhnov [1,2], S.B. Vakhrushev [1,2], A.E. Fotiadi [1], E.Yu. Koroleva [1,2], I.V. Golosovsky [3], Yu.A. Kumzerov [1,2], B. Nacke [4]

[1]St. Petersburg State Polytechnical University
29 Politechnicheskaya St., St. Petersburg, 195251, Russia
[2] Ioffe Physical Technical Institute
26 Politechnicheskaya St., St. Petersburg, 194021, Russia
[3] Petersburg Nuclear Physics Institute,
Gatchina, Leningrad District, 188300, Russia
[4] Leibniz University of Hannover, ETP
4 Wilhelm-Busch-Str., 30167 Hannover, Germany

NANOCOMPOSITE MATERIALS ON THE BASE OF DIELECTRIC POROUS MATRICES

А.В. Филимонов, А.И. Рудской, А.А. Набережнов, С.Б. Вахрушев, А.Э. Фотиади, Е.Ю. Королева, И.В. Голосовский, Ю.А. Кумзеров, Б. Наке

НАНОКОМПОЗИТНЫЕ МАТЕРИАЛЫ НА БАЗЕ ДИЭЛЕКТРИЧЕСКИХ ПОРИСТЫХ МАТРИЦ

The correlations between physical properties and structure of various types of nanocomposite magnetic and ferroelectric materials on the basis of natural and artificial porous have been studied by different experimental methods. The temperature evolution of the structure, order parameter and dielectric response are studied as functions of characteristic size of nanoparticles. It is shown the existence of crossover of phase transition (PT) from the first order to the second one for ultra-small ferroelectric and magnetic particles.

NANOCOMPOSITES, POROUS MATRICES, NEUTRON DIFFRACTION, DIELECTRIC RESPONSE.

Рассматривается влияние условий искусственно ограниченной геометрии на макроскопические свойства, кристаллическую структуру и фазовые переходы в нанокомпозитных материалах на основе пористых матриц с нанометровыми каналами, содержащих внедренные сегнетоэлектрические и магнитные материалы. Показано, что для ряда материалов наблюдается изменение рода фазового перехода, температуры перехода в зависимости от размера наночастицы и характера атомных колебаний. Показано, что для ряда нанокомпозитных материалов, содержащих сегнетоэлектрики, наблюдается резкий рост эффективной диэлектрической проницаемости ε в высокотемпературной фазе.

НАНОПОРИСТЫЕ СТРУКТУРЫ, НЕЙТРОННАЯ СПЕКТРОСКОПИЯ, НАНОКОМПОЗИТЫ, ДИЭЛЕКТРИЧЕСКАЯ СПЕКТРОСКОПИЯ.

I. Introduction

The physical properties of nanostructured materials are one of the «hot» points of modern solid state physics, and they are not only of fundamental interest but also of practical importance. Indeed, it is shown that finite-size effects result in drastic changes of physical properties of ultra-dispersed materials. The observed phenomena become especially significant if the characteristic size of the dispersed particles becomes comparable with the correlation length of the order parameter critical fluctuations, and the development of new nanotechnologies stimulates strongly the studies of various nanostructured and ultra-dispersed substances.

The experimental implementation of new effects in the physics of nanostructures relies upon our ability to create new types of structures and devices. Our understanding of material processing in the pursuit of ultra-small structures is steadily advancing. Epitaxial growth and lateral microstructuring techniques have made it possible to create low-dimensional electronic systems with quantum-confined structures, i. e., quantum wells, quantum wires, and quantum dots.

There are other methods of preparation of such dispersed substances, and one of them is intruding materials into artificial or natural porous matrices. Embedding substances into various porous matrices has some advantages in comparison with other methods:

(a) This method gives a possibility to produce nanostructures with a large range of controlled characteristic sizes from ~ 1 to ~300 nm.

(b) It is possible to prepare nanostructures with various geometry and topology: three-dimensional (3D) dendrite and regular structures, 2D film-like structures, 1D nanowires or 0D small nanoparticles.

One can produce nanoparticles of various substances and compounds: metals, ferroelectrics, dielectrics, insulators, semiconductors, superconductors, magnetic materials and so on.

It is possible to prepare a very large amount (up to several cubic centimeters) of nanocomposite materials (NCM) (or materials in a restricted geometry). This permits us to use some experimental methods that require a large amount of nanostructures (for example, neutron scattering, heat capacity measurements etc.).

Such NCM have been extensively studied during the last years, and it is shown that the reduction of physical size from the microscopic scale down to the meso- and nanoscopic scales results in a change of the majority of physical properties of NCM, such as temperature and type of phase transitions (PT) [1–6], dielectric permittivity [7–9], atomic mobility of constituent ions [10–12], liquids flowing in a confined geometry [12, 13] and so on. One of the important aspects of NCM is phase stability as a function of spatial dimension, geometry, topology and the size of nanoparticles. The properties of NCM and, in particular, various types of PT (superconducting [14–16], superfluid [17, 18], melting-freezing [6, 19–24], and other PTs [4, 7, 25–33] in different NCMs) have been extensively studied by calorimetry [19, 21, 32], NMR [23, 33–34], ultrasonic [35] and dielectric [7–9, 25] measurements, Raman [36, 37], X-ray [26, 28, 30, 38] and neutron scattering [4, 6, 11, 39, 40–48], differential thermal analysis [49], etc. It has been shown that NCMs can form either a system of isolated particles [6] or a net of interconnected dendrite clusters [44, 45], and their physical properties differ drastically from those in corresponding bulk samples and strongly depend on different characteristics of porous matrices and embedded substances such as pore size and geometry, wetting ability, surface tension, interaction between NCM and the surface of the host matrix, and so on.

This contribution is a review of properties and structure peculiarities of magnetic and ferroelectric nanocomposite materials created on the basis of various artificial and natural porous matrices such as porous glasses (3D dendrite interconnected net of nanochannels), artificial opals (3D regular net of nanocaverns), chrysotile asbestos (quasi-1D nanowires), MCM-41 and SBA-15.

II. Nanocomposites with Magnetic Ordering

The magnetic nanoparticles are of great interest because of their unique physical properties in terms of practical applications. It is shown that these properties drastically change in the conditions of restricted or confined geometry. These conditions assume:

the number of atoms at the surface of nanoparticles becomes comparable with the total number of atoms;

particle size is comparable with the length of the magnetic and atomic interaction.

Although the integral methods (e. g., Мцss-bauer spectroscopy, SQUID measurements and others) have the higher luminosity and sensibility in contrast with diffraction, the physical interpretation of any experiment is impossible without knowledge of detailed magnetic and atomic structure of nanoparticles. Obviously, similar information can be obtained by the diffraction methods only, because the electronic (or other) microscopy does not provide the proper accuracy and resolution.

As host matrices we have used porous glasses with average pore diameter of 70 ± 3 Å, SBA-15 matrices with channel diameters of 47 − 87 Å and MCM-41 matrices with channel diameters of 24 − 35 Å. MnO, CoO and Fe_2O_3 were synthesized into the matrices by a chemical bath deposition method. Manganese oxide was selected since the magnetic behavior of the bulk had been well studied. This oxide has an antiferromagnetic structure, for which the magnetic and nuclear Bragg reflections are well separated [50, 51]. The magnetic order in bulk MnO occurs by the first order transition at 117 ± 1 K [52], accompanied by a distortion of the cubic structure [51, 53].

A. The Magnetic Order inside and on the Surface of Nanoparticles

1. Reduction of Magnetic Moment

First neutron diffraction experiments with nanoparticles in the condition of «a restricted geometry» had been performed with the classic antiferromagnet MnO embedded into porous glass [4]. Manganese oxide is very suitable for the studies of magnetism in «the restricted geometry». First, the oxide has a simple antiferromagnetic structure, for which the magnetic and nuclear Bragg reflections are well separated. Secondly, MnO is easily synthesized inside the cavities. Thus, it is possible to introduce a large quantity of oxide sufficient to perform neutron research. And thirdly, manganese has a negative nuclear scattering length, while the oxygen has a positive scattering length. This provides a good contrast in the neutron diffraction that allows controlling stoichiometry with high accuracy.

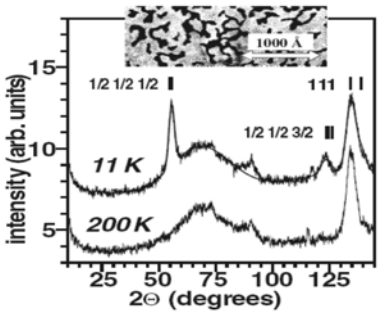

Fig. 1. Neutron diffraction patterns of MnO embedded into a porous glass. The stripes mark the positions of Bragg reflections corresponding to the trigonal distorted lattice. The solid line corresponds to the calculated profile. In the inset the fragment of a typical micrograph of pore network in porous glasses is shown

At last, ion Mn^{2+} has a large magnetic moment of 5 μ_B/ion. The magnetic order in the bulk MnO occurs by the first order transition at ~ 117 K, accompanied by a distortion of the cubic structure [53]. Indeed, new Bragg reflections appearing below 122 K (Néel temperature) show the onset of the correlated magnetic order in the embedded nanoparticles (Fig. 1). The diffraction lines are broadened with respect to the instrumental resolution, indicating that the correlation length is finite. The observed diffuse background is due to the porous silica glass. The indexing of the observed magnetic reflections corresponds to antiferromagnetic ordering similar to that for the bulk MnO. The shape of the reflections below the Néel temperature indicates structural distortions and matches to the trigonal distortion of a cubic lattice.

From the intensity of the magnetic Bragg reflections, the ordered magnetic moment at 10 K was found to be 3.84(4) μ_B/ion. This value, averaged over the magnetic region, turns out

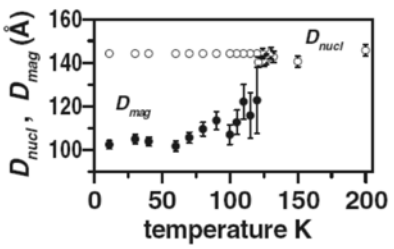

Fig. 2. Temperature dependencies of the volume-averaged diameters of magnetic (D_{mag}) and nuclear (D_{nucl}) regions, solid and open circles respectively

to be noticeably smaller than the experimental value of 4.892 μ_B/ion reported for MnO.

Moreover, the average size of a magnetic cluster turns out to be significantly smaller than the average size of a nanoparticle (Fig. 2). In the diffraction experiment, the surface spins, disordered on atomic scale, do not contribute to the coherent magnetic Bragg reflections. Therefore, the reduction of the net moment can be easily explained by random moment canting. The difference between D_{mag} and D_{nucl} could be due to several factors. It could result from a breakdown of large magnetic aggregates into smaller ones because of the necks or other irregularities in porous media. Another explanation could come from the random canting of spins at the surface of the nanoparticle near the pore walls and the formation of a «layer» with spin disorder. As a result, the orientation of the surface magnetic moments could be altered from that in the core. Such disordering is a well-established phenomenon for nanoparticles.

2. The Electron Spin Resonance (ESR) in MnO

ESR in MnO inside porous media clear shows the existence of the local spin ordering [54]. The analysis of the ESR signal from confined MnO shows two signal components, one of which corresponding to crystallized MnO, while another component is due to MnO in an amorphous state. Such analysis allows us to investigate the magnetic behavior of the crystallized and amorphous parts of the embedded MnO separately.

The ESR signal associated with the crystalline MnO within porous glass shows a behavior having many similarities to the bulk. However, in contrast to the bulk (compare (*a*) and (*c*) panels in Fig. 3), the strong ESR signal due to disordered surface spins is observed below the transition.

3. Magnetic Moments in Different Crystallographic Positions in Maghemite γ-Fe_2O_3

Classical ferrimagnetics, iron oxides, in particular maghemite (γ-Fe_2O_3), are widespread in nature. They have been known since ancient times and are widely applied at present [55]. Neutron diffraction experiments with maghemite show that the oxide, incorporated within porous glass, has the spinel structure with unoccupied positions, which corresponds to the known structure of maghemite [56].

The spinel structure contains two types of voids: tetrahedral (eightfold A position) and octahedral (16-fold B position). Magnetic ions can occupy both positions (Fig. 4). Maghemite has the structural formula

$$(Fe^{3+})[Fe^{3+}_{5/6}\square_{1/6}]_2\{O^{2-}\}_4.$$

In this formula, the parentheses and square brackets refer to the tetrahedral and octahedral voids, respectively, and the symbol □ corresponds to vacancies.

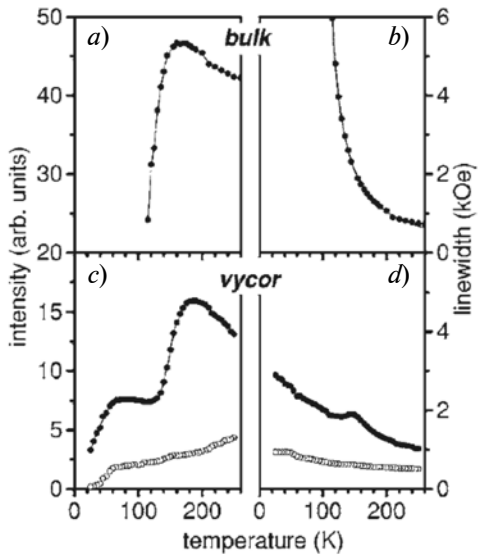

Fig. 3. Intensity (*a*) and lineshape (*b*) of the ESR signal from the bulk MnO. Intensity (*c*) and linewidth (*d*) of the ESR signal from MnO confined to a porous glass.
Open circles correspond to the signal from crystalline MnO and solid circles correspond to the signal from amorphous MnO

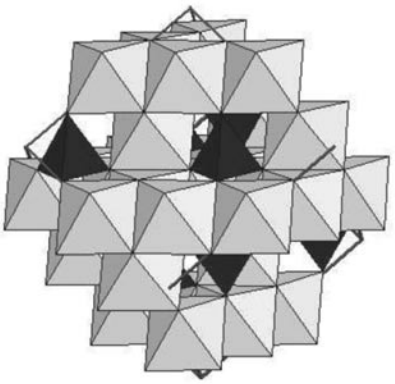

Fig. 4. Crystal structure of spinel with tetrahedral (A) position (in black) and octahedral (B) position (in grey)

It appears that the magnetic moments in confinement are noticeably different in the A and B positions, although Fe^{3+} does not carry any spin moment and crystal field effect should be negligible. Such effect is not observed in the bulk and results from the size-effect.

Let us consider the nearest environment of the magnetic ions at two positions. The magnetic ion in the A position has 4 neighbors in the same positions with the same moment direction and 12 neighbors in the B position with the opposite spin direction. The ion in the octahedral B position has 6 neighbors with the same spin direction in B positions and 6 neighbors with the opposite spin direction in A positions. Assuming the same spin values in the A and B positions, and taking into account the spin directions, the exchange integrals in the A and B positions are proportional to $J_A = -12J_{AB} + 4J_{AA}$ and $J_B = -6J_{BA} + 6J_{BB}$, respectively. Substituting the exchange integral values known for the bulk (we suppose that they are close to those in confinement) maghemite, we obtain $J_A/J_B = 2.19$. Thus, the moment in the B position is bound two times more weakly by the exchange interaction in respect with the A position. The more weakly bound spin in the B position must evidently be more disordered due to the breakings of local symmetry, and, consequently, its mean value is lower.

4. The Coexistence of two Magnetic Phases

This coexistence takes place because of the different constants anisotropy on the surface and in the cores of hematite nanoparticles confined to porous glass [57]. The bulk hematite has the corundum crystal structure and presents two-sublattice antiferromagnet with the Néel temperature of 950 K. At 260 K hematite undergoes a spin-reorientation transition known as the «Morin transition». Below the transition the moments in two magnetic sub-lattices are exactly antiparallel and aligned along the rhombohedral [111] axis (*c*-axis in the hexagonal setting) (AF phase). Above the transition, the moments lie in the basal plane (111) with a slight canting resulting in a weak net moment originating from Dzyaloshinskii – Moriya anisotropic super-exchange interaction (WF phase). The spin flip is related to a competition of two terms with different temperature dependences: the magnetic dipolar interaction and the single-ion anisotropy arising from higher order spin-orbital effects that leads to the different sign of the anisotropy constant.

It turns out that the magnetic contributions into the neutron diffraction patterns from the hematite nanoparticles measured at 300 K and at 10 K are similar. It means that at least down to 10 K there is no any phase transition in confined nanoparticles. In other words, «Morin transition» is suppressed in the «restricted geometry».

Analysis of the observed intensities of the magnetic reflections shows that they substantially differ from the intensities which correspond to the single WF or to the single AF phases. The observed patterns can be equally well described by two models which are indistinguishable in the frame of the neutron powder diffraction.

The first model assumes that the resulting moment tilts from the rhombohedral axis. The alternative model assumes two magnetic phases: in one phase the magnetic moments are aligned along the rhombohedral axis, as in the bulk hematite below the Morin transition (AF phase), and in the other phase the magnetic moments are confined to the perpendicular plane, as in the bulk hematite above the Morin transition (WF phase).

The data analysis of the neutron diffraction taking into account the results of Mössbauer spectroscopy supports the last model of the two co-existing magnetic phases, corresponding to the phases which in the bulk hematite exist

separately above and below the Morin transition. In the case of a nanoparticle, one phase exists at the surface, while another one exists in the core, because of the difference in the anisotropy constants.

B. Magnetic Phase Transitions in the «Restricted Geometry»

1. Continuous Transition in the Nanostructured Nanoparticles

The temperature dependencies of the magnetic moment of the embedded nanoparticles MnO and that in bulk are shown in Fig. 5 [4]. Fitting the observed magnetic moment dependence with the power law

$$m(T) \sim (1 - T/T_N)^{\beta}$$

yields the Néel temperature T_N =122.0(2) in contrast with T_N of 117 K in the bulk.

In Fig. 5 it is clearly seen that the discontinuous, first order transition in the bulk becomes continuous in the «restricted geometry». Rigorously, singularities at phase transitions occur in the thermodynamical limit only, when the system is infinite along some directions in space [58]. If the system is finite along all dimensions, it cannot exhibit a singular behavior. Computer simulation of phase transition in finite-size systems confirms this general idea.

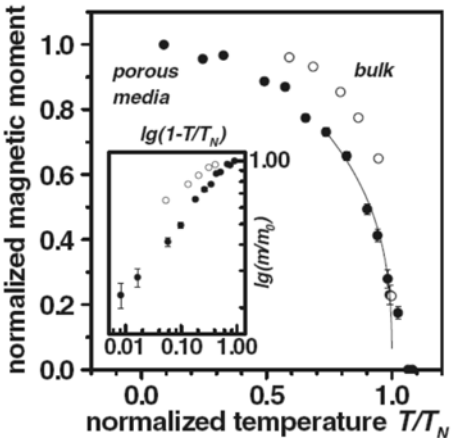

Fig. 5. Temperature dependence of the scaled magnetic moment of MnO embedded in porous glass (solid circles) and of the bulk MnO (open circles). The solid line corresponds to a fit with the power law. The moment dependencies on a logarithmic scale are shown in the inset

There is extensive literature which shows that continuity and «smoothing» («rounding») of the phase transition in the «restricted geometry» is a general phenomenon that comes from the restrictions on the length of the magnetic fluctuations by the size of nanoparticles [59, 60].

Indeed, the correlation length ξ when approaching the transition from the above can be described by a power law:

$$\xi(T) = \xi(0)\left|1 - \frac{T}{T_C(bulk)}\right|^{\nu}.$$

Here ν is so-called critical exponent. In the case of a finite system, the $\xi(T)$ at transition temperature T_C is restricted by the characteristic size of the nanoparticle L:

$$\xi(T_C) = L = \xi(0)\left|1 - \frac{T}{T_C(bulk)}\right|^{\nu}.$$

It immediately follows that T_C in confinement should be lower than the T_C in the bulk:

$$T_C = T_C(bulk)\left[1 - \frac{\xi(0)}{L}\right]^{1/\nu}.$$

Really, this law is observed in all known cases (see, for example, confined CoO [61]). However, the nanostructured compounds with Mn^{2+} ions do not obey this law. Probably, it is connected with the specific electronic structure of Mn^{2+}. Up to now, there has been no clear explanation of this phenomenon.

2. Evolution of the Magnetic Phase Transition in MnO, Nanostructured within the Channels of MCM Matrices

Unusual behavior was observed for nanoparticles of MnO nanostructured within the channels of the MCM-41 matrices in the form of thin nanoribbons. In Fig. 6, the temperature dependencies of the normalized magnetic moment for MnO confined within the channels of different diameter are shown. The solid line corresponds to a fit with the power law

$$m(T) \sim (1 - T/T_N)^{\beta}.$$

Critical exponent β corresponds to the definite theoretical model of the magnetic system. For example, $\beta = 0.5$ corresponds to so-called mean-field theory, when in a three-dimensional system all possible magnetic bonds are working.

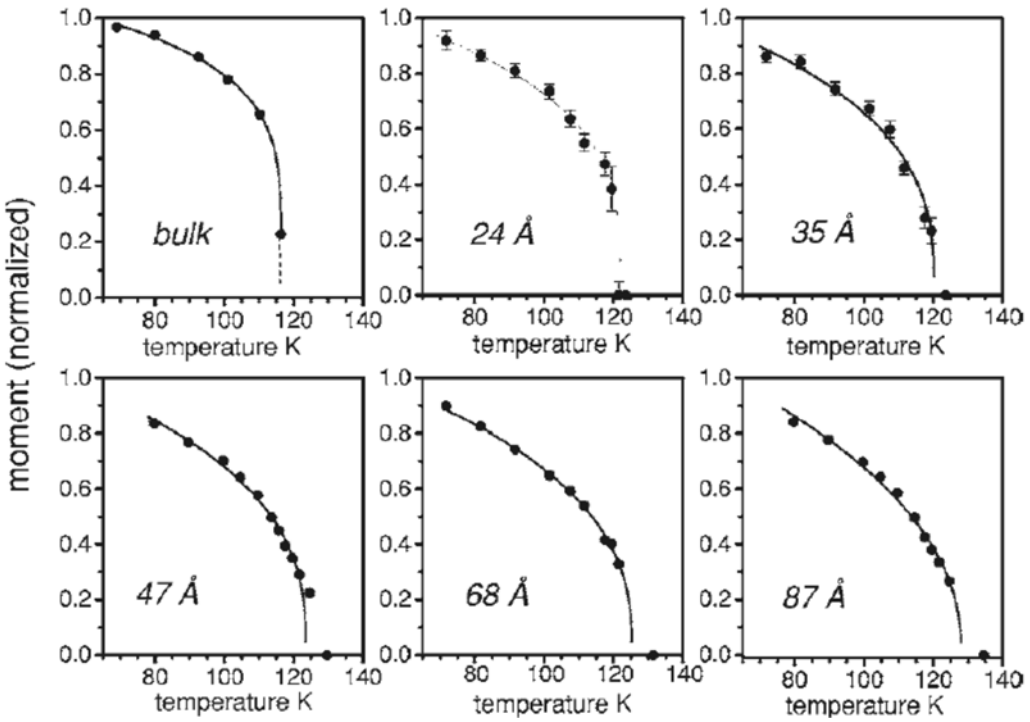

Fig. 6. Temperature dependences of the magnetic moment for MnO confined within the channels of different diameters. The solid lines correspond to a fit with the power law

From neutron and X-ray powder diffraction, it follows that the lengths and thinnesses of the nanoribbons are similar for all matrices. Therefore, the channel diameter is the only characteristic parameter which defines the dimension of the system. In Fig. 7, the channel dependence of the critical exponent β and T_N are shown. It is seen, that with the channel diameter decrease the critical exponent β decreases, and this corresponds to a decrease of the dimensionality of the magnetic system. In other words, with the channel decrease the system anisotropy increases and magnetic system of a nanoparticle becomes more and more close to the one-dimensional model.

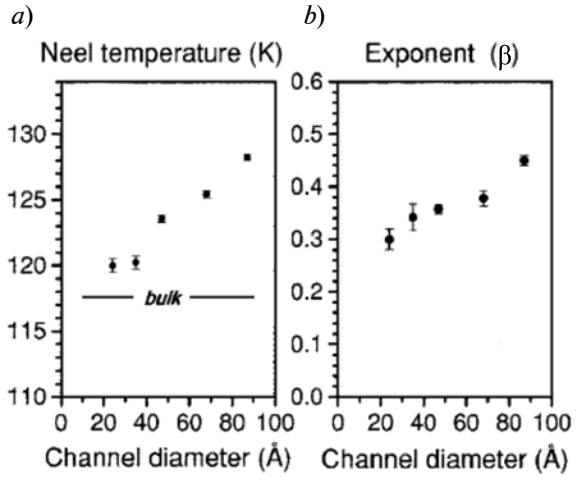

Fig. 7. Dependencies of the Néel temperature T_N (*a*) and exponent β (*b*) on channel diameters from the fitting with the power law

Nanoparticles confined within large channels are expected to behave as constrained three-dimensional systems. However, with a decreasing channel diameter, one expects a crossover with one-dimensional behavior. In this case, the magnetic fluctuations should destroy the long-range magnetic order, and T_N should go to zero. However, in our case we see that T_N does not extrapolate to zero with the decreasing channel diameter (Fig. 6).

C. «Exchange Biased» Magnetic Moment in the «Core-Shell» Systems

Such systems present the antiferromagnetic core of MnO with a thin layer of ferrimagnetic γ-Mn_2O_3 [62, 63]. Remarkably, while the MnO

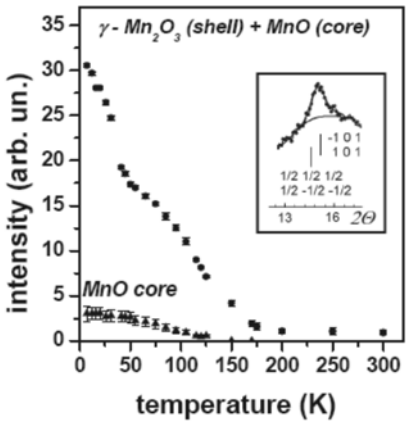

Fig. 8. Temperature dependence of the intensity of the magnetic peak (shown in the insert) with the next contributions from the MnO core: reflections (1/2, 1/2, 1/2), (1/2, −1/2, −1/2) and from the γ-Mn_2O_3 shell: reflections (1, 0, 1) and (−1, 0, 1). The contribution from the MnO core calculated from the profile analysis is shown by triangles

core is found to have a T_N not far from its bulk value (117 K), the magnetic order of the ferrimagnetic shell persists far above T_C (43 K) of the bulk. In Fig. 8, the temperature evolution of the characteristic magnetic reflection is displayed.

It is clearly seen that the magnetic signal, which is proportional to the square of the ferrimagnetic moment observed above T_N and T_C, grows up to the room temperature.

We attribute the observed stable magnetic moment in the ferrimagnetic γ-Mn_2O_3 shell to the exchange coupling between the antiferromagnetic MnO core and the ferrimagnetic shell, as it has been observed in the film layered systems. This phenomenon should be considered as a proximity effect, when the net ferromagnetic moment due to the local violation at the surface (interface) of antiferromagnetic core biases the ferrimagnetic constituent.

III. Ferroelectrics in a Restricted Geometry

For NCM with embedded ferroelectrics, very interesting and sometimes surprising results have been obtained during the last years. In particular, the dielectric measurements of $NaNO_2$, KH_2PO_4 (KDP), KD_2PO_4 (DKDP), Roshelle salt, KNO_3 within porous glasses and artificial opals have shown the unexpected growth of the real and imaginary parts of the dielectric susceptibility ε above the temperature T_C of the ferroelectric PT [7–9, 27, 44, 64]. In such a situation, the increase of the imaginary part of ε could be attributed to the appearance of conductivity, but in this case the microscopic origin of such conductivity was absolutely unclear. The most remarkable result was the giant growth of ε (up to 10^8 at 100 Hz) upon approaching the bulk melting temperature that was observed for $NaNO_2$ embedded in artificial opals.

These experimental results were the starting point for a detailed study of the temperature evolution of structure of confined $NaNO_2$. To understand the microscopic nature of observed giant growth of dielectric permittivity in paraelectric phase, we have performed the complex study of the structure and properties of these NCM including neutron scattering, measurements of heat capacity, NMR, small angle neutron scattering (SANS), dielectric measurements, etc.

A. Samples

Sodium nitrite belongs to order-disorder ferroelectrics and undergoes the first order phase transition at $T_C \approx 437$ K. At room temperature (RT), $NaNO_2$ has a body centered orthorhombic lattice ($a = 3.57$ Å, $b = 5.578$ Å, $c = 5.39$ Å) with two molecules per unit cell, and its space group is *Im*2*m*. In the low-temperature ferroelectric phase, the spontaneous polarization points along the *b*-axis and appears due to a partial alignment of NO_2 groups along this axis, accompanied by the displacement of sodium ions. At high temperature (above T_C), a mirror plane perpendicular to the *b*-axis appears, and the space group changes into *Immm*. Bulk sodium nitrite melts at 554.1 K.

KDP and medium deuterated DKDP have tetragonal structure at the ambient temperature and undergoes a phase transition at about 123 K to ferroelectric phase with the space group (SG) *Fdd*2. The high-deuterated DKDP undergoes ferroelectric phase transition at 223 K. In the bulk KNO_3 crystals, ferroelectric phase is observed only when cooling at atmospheric pressure in the temperature range from 383 K to 398 K.

As porous matrices, we have used porous glasses with average pore diameters of 320 ± 20, 46 ± 5, 20 ± 3, 7 ± 1 and 3.0 ± 0.5 nm, ar-

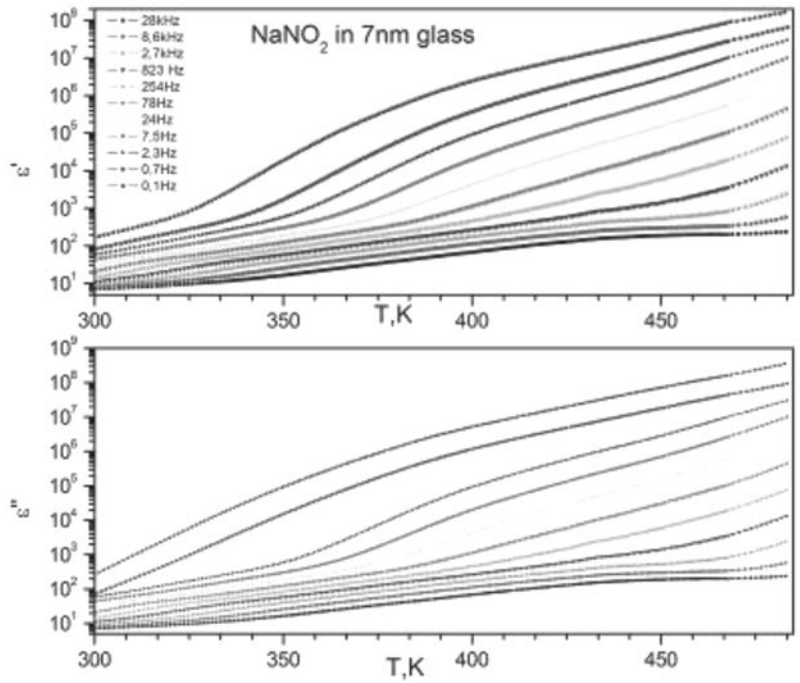

Fig. 9. Temperature dependences of real ε' and imaginary ε'' parts of dielectric response for $NaNO_2$ within 7 nm porous glasses at different frequencies

tificial opals and chrysotile asbestos with the average diameter of channels of 6 ± 1 nm. The samples with nanostructured $NaNO_2$ and KNO_3 were produced by immersion of empty vacuum dried porous glasses in the melted $NaNO_2$ (or KNO_3) for several hours. Due to high wetting ability these salts penetrate into the pores and fill about $22 - 25$ % of total sample volume. KDP, DKDP and Rochelle salt were prepared from water solutions of the salts. The filling in this case was about 10 % of the total sample volume.

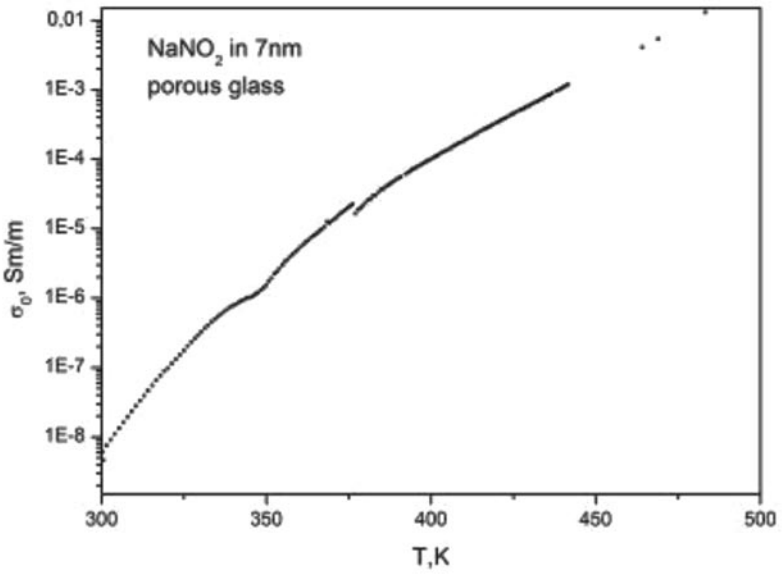

Fig. 10. Temperature dependences of NCM conductivity; $E_a \approx 0.96$ eV

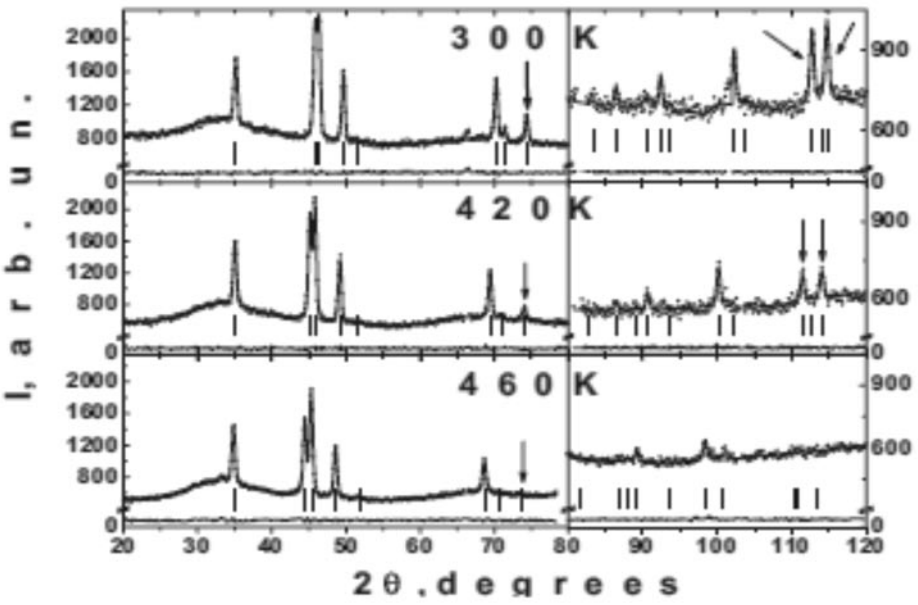

Fig. 11. Neutron diffraction patterns at 300 K, 420 K and 460 K. The arrows indicate the positions of (022), (132) and (123) Bragg peaks in the ferroelectric phase

B. Dielectric Data

In Fig. 9, the temperature dependences of real ε' and imaginary part ε'' of dielectric permittivity of NCM with $NaNO_2$ embedded into 7 nm porous glasses are presented. At low frequencies, the exponential growth of ε is observed. At 0.1 Hz the value of ε' achieves 10^8 at 490 K, but we have not observed the peak corresponding to the ferroelectric PT in the ε(T) dependences. It links with great growth of conductivity in the vicinity of PT due to high mobility of sodium ions approaching (and above) T_C. The anomalies at T_C are observed on dependency $d\varepsilon'/dT$ only. From the analysis of dispersion curves, we have determined the parameters of relaxation phenomena and the value of DC (direct current) conductivity σ(T) of NCM. This dependency is presented in Fig. 10 and follows Arrhenius law with activation energy ~ 1 eV.

C. Structure Evolution and Phase Transitions

The diffraction patterns at 300 K, 420 K (below T_C) and 460 K (above T_C) for sodium nitrite within 7 nm glasses are presented in Fig. 11. At all temperatures the structure of embedded sodium nitrite corresponds to the orthorhombic structure of the bulk $NaNO_2$, but in addition to normal diffraction peaks, a diffuse background due to scattering on porous silica glass is also observed. The widths of the observed diffraction peaks are larger than the instrumental resolution, but clearly smaller than the value expected for scattering on isolated 7 nm particles. The average size (≈ 45 nm) of clusters was determined from the structure refinement and was found to be practically temperature independent up to 460 K. Heating through T_C results in the decrease of intensity of most peaks at large scattering angles 2θ, i. e. at large $h\ k\ l$, and this effect is much stronger than in the bulk material. Above 523 K, we did not observe any diffraction peaks corresponding to the sodium nitrite structure, i. e. nanocomposite $NaNO_2$ melted entirely below the bulk T_{melt}. In the case of $NaNO_2$, there are two principal distinguishing groups of Bragg peaks: the intensity of diffraction peaks is proportional to

$$|F|^2 = F^2_{real} + \eta^2(T) \times F^2_{im},$$

where F_{real} and F_{im} are the real and imaginary parts of the structure factor F, and η is the order parameter for the ferroelectric phase.

For sodium nitrite, there are two families of reflections with different dependences on η: the first ones where $F_{im} \sim 0$ or $F^2_{im} << F^2_{real}$ (for example (110), (011), (101) and (200)) are

Table

Real and imaginary parts of the structure factor for sodium nitrite in the ferroelectric phase for different reflections

h	k	l	F^2_{real}	F^2_{im}
0	1	1	2.83	0.02
1	1	0	6.74	0.07
1	0	1	8.17	0
2	0	0	8.18	0
0	2	0	10.82	0.009
1	1	2	0.006	0.687
0	2	2	0.254	3.864
0	1	3	0.01	1.065
1	3	0	0.36	0.266
2	2	0	3.81	0.054
1	3	2	0.054	2.762
1	2	3	0.3	2.718
0	4	2	0.028	5.128

independent from the order parameter, and the second ones (the part of them marked by arrows in Fig. 11) where $F^2_{im} >> F^2_{real}$ ((022), (123), (132)). The values of F^2_{im} and F^2_{real} for different reflections in the ferroelectric phase are presented in the Table. It is easy to see that the intensities of these peaks are practically proportional to η^2. The curves $\eta(T)$ for NCM (Fig. 12) can be well fitted by the power law $(1 - T/T_C)^\beta$ with $T_C = 418.5 \pm 3.5$ and 423.6 ± 2.1 K for the 3 and 7 nm porous glasses correspondingly. The critical exponent β is equal to 0.33 ± 0.04 for both NCMs. This value of β is in a good agreement with the value (0.362 ± 0.004) obtained for the 3D Ising model [66] by computer simulation of finite-size scaling for a second order PT. The $\eta(T)$ curve for NCM for the 20 nm porous glass differs principally from those for nanocomposites with 3 and 7 nm pores and looks similar to the dependence obtained for the bulk [65]. The crossover of PT for small nanoparticles from the first order to the second order was confirmed by measuring heat capacity [67]. In Fig. 13, the temperature dependences of the unit cell volume for all types of NCM and for the bulk are presented. These curves for NCM are visibly different from that for the bulk. The appearance of the fast increase of the volume for

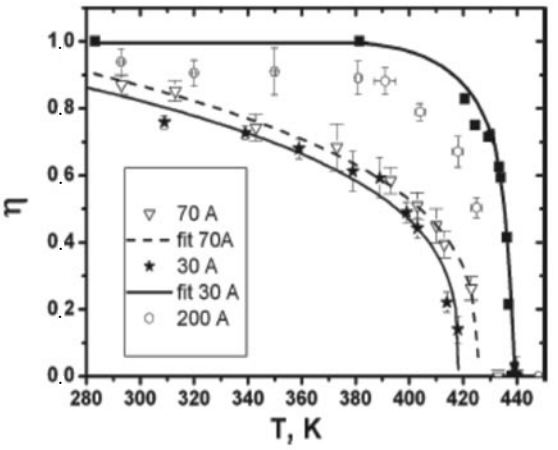

Fig. 12. Temperature dependences of the order parameter for the bulk (black squares) [65] and $NaNO_2$ embedded into porous glasses with average pore diameters 30 Å (stars), 70 Å (open triangles) and 200 Å (open circles)

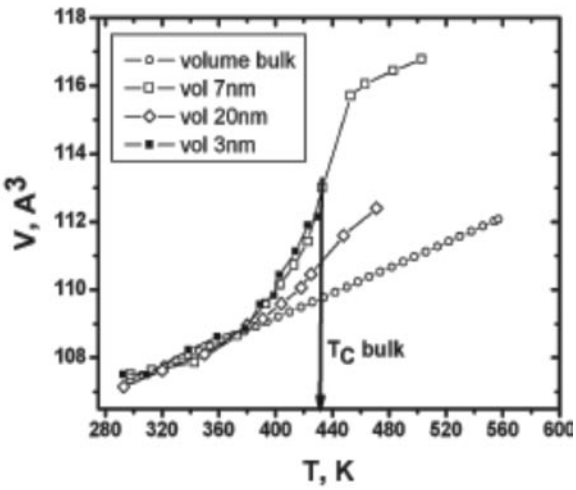

Fig. 13. Temperature dependences of the unit cell volume for 3 nm (black squares), 7 nm (open squares) and 20 nm (open rhombuses) porous glasses and the massive sodium nitrite

all NCMs is observed at ~380 K, i. e. below T_C, and at high temperature these values exceed the unit cell volume of bulk sodium nitrite in the vicinity of the melting point. Such a behavior can be considered as an evidence of lattice «softening» in NCM with 3 and 20 nm pores as it was proved earlier for sodium nitrite within 7 nm glasses. This essential increase of unit cell volume by ~8 % (and decrease of density) must lead to visible change of contrast at SANS. Indeed, it is easy to see in Fig. 14 that upon heat-

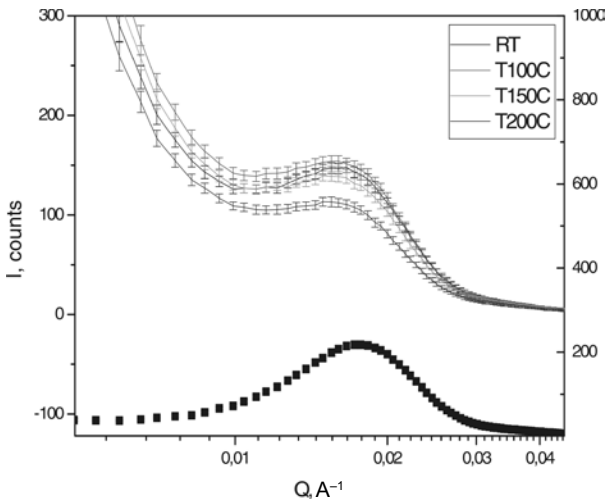

Fig. 14. Temperature dependences of intensity of SANS for $NaNO_2$ within 7 nm porous (glasses). Black line corresponds to scattering on empty porous glasses

ing through T_C (~164 °C), the contrast changes half as much at $Q \approx 0.018$ Å^{-1}.

D. Thermal Vibrations and Pre-Melted State

Analysis of neutron diffraction patterns permits us to obtain information concerning thermal motions of constituent ions of sodium nitrite within porous matrices.

The results at 420 K (below T_C) and 460 K (above T_C) are presented as ellipsoids of 50 % probability in Fig. 15 and as ellipsoids of 5 % probability in Fig. 16 (inasmuch as oxygen thermal displacements are very large for a porous sample). For the bulk material, these ellipsoids are close to a sphere at all temperatures, and the amplitudes of thermal motion do not change practically on heating throughout T_C. For confined sodium nitrit below T_C, these ellipsoids are clearly anisotro pic and slightly larger than for the bulk, bu upon heating through T_C, the picture change drastically. In the paraelectric phase (abov T_C), the vibrations of Na and N form practi cally flat disks perpendicular to the **b** direc tion for Na and the **a** direction for N as result of mixed rotation around the *a* and axes, while oxygen ions form very stretched ellipsoids predominantly along the *a* and *c* directions, as should be expected at increasing rotation around the *b* axis. The values of oxygen thermal displacements along the *c* and *a* directions at 460 K (above T_C) are equal to 1.21 and 0.93 E, respectively (i. e., more than 25 % of O—O (3.34 E) distance for neighboring NO_2 groups). These values essentially exceed the Lindemann criterion for melting. This experimental fact (and the sharp growth of unit cell volume upon heating through T_C) permits to conclude that above T_C and up to melting (~525 K), a specific volume pre-melted state with high mobility of constituent ions is formed in confined sodium nitrite at the temperature more than 100 K below the bulk T_{melt}. It is necessary to underline that this pre-melted state is not connected with very spreading surface (we have observed the diffraction peaks essentially above T_C), but it has a volume character and probably originates from some size effect of yet unclear nature. Measurements of NMR on ^{23}Na isotope confirm the growth (by ~20 times) of sodium mobility in this NCM upon heating [68].

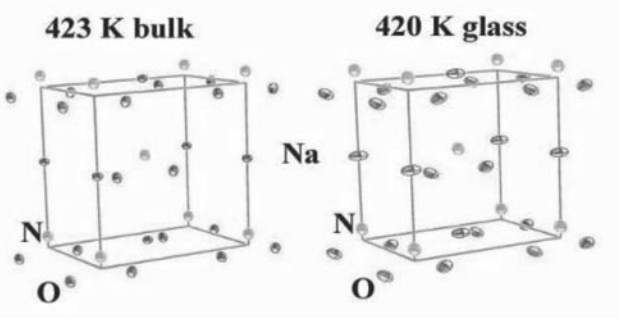

Fig. 15. Ellipsoids of thermal motions for the bulk (left) and confined within 7 nm porous glasses (right) $NaNO_2$ below T_C

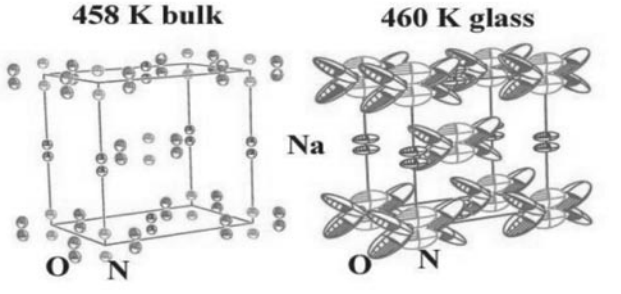

Fig. 16. Ellipsoids of thermal motions for the bulk (left) and confined within 7 nm porous glasses (right) $NaNO_2$ above T_C

E. Size Effect and Metastable Phases

The neutron diffraction patterns for high-deuterated DKDP show strong broadening of Bragg reflections due to a size-effect leading to large peak overlapping. Surprisingly, the measured patterns at all the temperatures appear to be inconsistent with the profiles simulated in the frame of the orthorhombic $Fdd2$ and tetragonal $I\bar{4}2d$ space groups (SG). From the comparison of the obtained diffraction patterns with the simulated ones, calculated for different crystal structures reported for DKDP (KDP) (see Table), it follows that the observed patterns can be best fitted by the monoclinic crystal structure with SG $P2_1$ and the unit-cell parameters close to the ones reported in [69] for high-deuterated DKDP. Unfortunately, the hydrogen positions for this monoclinic structure are unknown. Moreover, due to low symmetry and strong peak overlapping, it is impossible to refine these positions from our data. Therefore, we have refined the averaged diameter (size) of the embedded nanoparticles and the unit-cell parameters only in the so-called «matching mode» by the FULLPROF program. The temperature dependences of these parameters are shown in Fig. 17 and there are no anomalies in the temperature

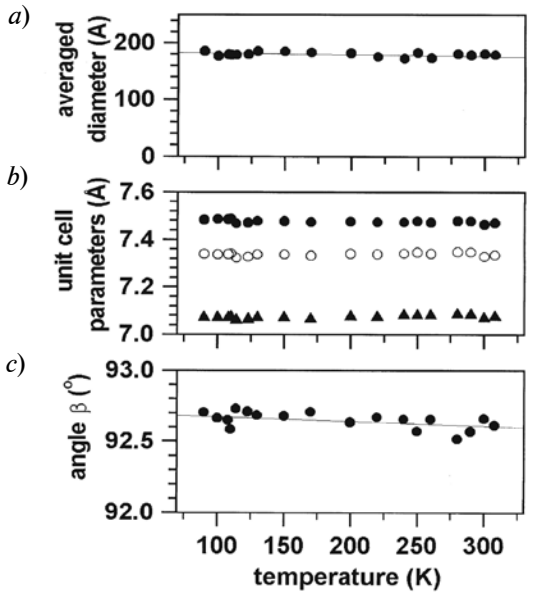

Fig. 17. Temperature dependences of refined averaged diameter of nanoparticles (*a*); unit cell parameters for monoclinic cells (*b*): *a* (solid circles), *b*/2 (open circles) and *c* (triangles); monoclinic angle β (*c*) for high-deuterated DKDP embedded into 7 nm porous glasses

interval of 90 – 308 K, i. e. the ferroelectric phase transition is absent in this temperature span for confined DKDP. It is shown that the

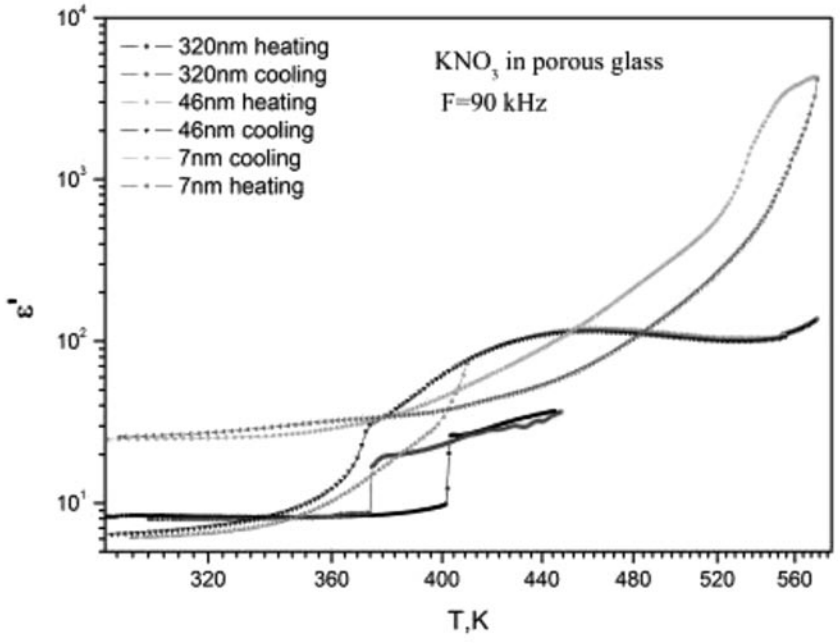

Fig. 18. Temperature dependences of the real part of dielectric permittivity for KNO_3 within various porous glasses on cooling and heating

monoclinic modification of the high-deuterated $K(D_{1-x}H_x)_2PO_4$ can exist at room temperature [70, 71] and crystallize from the high-deuterated (≈ 98%) aqueous solution only [70], but at ambient conditions this modification transforms into the tetragonal form in a few days [71]. Our samples with DKDP were crystallized from the aqueous solution too and were prepared some months before the beginning of the experiment and stored at ambient conditions. Therefore, the stability of the observed monoclinic phase is surprising. It is possible that such stability is associated with the size-effect and/or with peculiarities of the interaction of DKDP with porous matrix [72 − 74].

Some years ago, it was shown that thin films of KNO_3 exhibit ferroelectric properties at room temperature [75]. One of the simple ways to produce nano-sized ferroelectrics is introducing them into the porous glass matrices. As it is shown in the paper [64] for KNO_3 embedded into porous glasses, decreasing the pore diameter from 320 nm down to 46 nm leads to broadening the temperature range in which the metastable ferroelectric phase exists. In Fig. 18 the temperature dependencies of ε' on heating and cooling for KNO_3 embedded into 320, 46 and 7 nm porous glasses are presented. It is easy to see that the increase of nanoparticle sizes leads to smearing PT and to increasing thermal hysteresis. For NCM with 7 nm pores, a sharp growth of ε' due to potassium nitrate melting within pores is observed and T_{melt} in this case is essentially smaller than it is in the bulk (600 K).

IV. Summary

We have studied the physical properties and crystal structure of various ferroelectric and magnetic NCMs on the basis of porous matrices with different average pore diameters, and we can define some common features for these materials.

1. Embedding from wetting melt and chemical embedding produce nonspherical clusters with the average diameter which is larger than the pore diameter.

2. For some NCMs, there is a critical size of nanoparticles when the crossover of PT type is observed.

3. Examined ferroelectric NCMs with small particles demonstrate the giant dielectric permittivity in the paraelectric phase.

4. A new volume pre-melted state with extremely large thermal motions of constituent ions has been recovered for sodium nitrite.

5. The confinement can stabilize the phases that are usually metastable.

REFERENCES

1. **Zhong W.L., Wang Y.G., Zhang P.L.** Phase transitions in finite-size ferroelectrics. *Ferroelectr. Rev.*, 1998, 1, pp. 131−193.

2. **Neubeck W., Ranno L., Hunt M.B., Vettier C., Givord D.** Epitaxial MnO thin films grown by pulsed laser deposition. *Applied Surface Science*, 1999, 138, pp. 195−198.

3. **Li S., Eastman J.A., Li Z., Foster C.M., Newnham R.E., Cross L.E.** Size effects in nanostructured ferroelectrics. *Physics Letters A*, 1996, 212(6), pp. 341−346.

4. **Golosovsky I.V., Mirebeau I., André G., Kurdyukov D.A., Kumzerov Y.A., Vakhrushev S.B.** Magnetic ordering and phase transition in MnO embedded in a porous glass. *Physical Review Letters*, 2001, 86(25), 5783.

5. **Sheng P., Cohen R.W., Schrieffer J.R.** Melting transition of small molecular clusters. *Journal of Physics C: Solid State Physics*, 1981, 14(20), L565.

6. **Kumzerov Y.A., Nabereznov A.A., Vakhrushev S.B., Savenko B.N.** Freezing and melting of mercury in porous glass. *Physical Review B*, 1995, 52, pp. 4772−4774.

7. **Pan'kova S.V., Poborchii V.V., Solov'ev V.G.** The giant dielectric constant of opal containing sodium nitrate nanoparticles. *Journal of Physics: Condensed Matter*, 1996, 8(12), L203.

8. **Colla E.V., Fokin A.V., Kumzerov Y.A.** Ferroelectrics properties of nanosize KDP particles. *Solid State Communications*, 1997, 103(2), pp. 127−130.

9. **Colla E.V., Koroleva E.Y., Kumzerov Y.A., Savenko B.N., Vakhrushev S.B.** Ferroelectric phase transitions in materials embedded in porous media. *Ferroelectrics Letters Section*, 1996, 20(5−6), pp. 143−147.

10. **Beskrovny A., Golosovsky I., Fokin A., Kumzerov Y., Kurbakov A., Naberezhnov A., Vakhrushev S.** Structure evolution and formation of a pre-melted state in $NaNO_2$ confined within porous glass. *Applied Physics A*, 2002, 74(1), s1001−s1003.

11. **Fokin A.V., Kumzerov Y.A., Okuneva N.M., Naberezhnov A.A., Vakhrushev S.B., Golosovsky I.V., Kurbakov A.I.** Temperature evolution of sodium nitrite structure in a restricted geometry. *Physical Review Letters*, 2002, 89(17), 175503.

12. **Charnaya E.V., Loeser T., Michel D., Tien C., Yaskov D., Kumzerov Y.A.** Spin-lattice relaxation enhancement in liquid gallium confined within nanoporous matrices. *Physical Review Letters*, 2002, 88(9), 097602.

13. **Drake J.M., Grest G.S., Klafter J., Kopelman R.** Dynamics in Small Confining Systems. Pittsburgh, PA, Materials Research Society, 1999.

14. **Graf M.J., Huber T.E., Huber C.A.** Superconducting properties of indium in the restricted geometry of porous Vycor glass. *Physical Review B*, Eds., 1992. 45(6), 3133.

15. **Charnaya E.V., Tien C., Lin K.J., Wur C.S., Kumzerov Y.A.** Superconductivity of gallium in various confined geometries. *Physical Review B*, 1998, 58(1), 467.

16. **Panova G.K., Naberezhnov A.A., Fokin A.V.** Surface and volume superconductivity of Pb embedded in nanopores. *Physics of the Solid State*, 2008, 50(7), pp. 1370–1373.

17. **Chan M.H.W., Blum K.I., Murphy S.Q., Wong G.K.S., Reppy J.D.** Disorder and the superfluid transition in liquid^{4} He. *Physical Review Letters*, 1988, 61(17), 1950.

18. **Larson M., Mulders N., Ahlers G.** Thermal expansion coefficient near the superfluid transition of^{4} He in an aerogel. *Physical Review Letters*, 1992, 68(26), 3896.

19. **Mu R., Malhotra V.M.** Effects of surface and physical confinement on the phase transitions of cyclohexane in porous silica. *Physical Review B*, 1991, 44(9), 4296.

20. **Duffy J.A., Wilkinson N.J., Fretwell H.M., Alam M.A., Evans R.** Phase transitions of CO_2 confined in nanometer pores as revealed by positronium annihilation. *Journal of Physics: Condensed Matter*, 1995, 7(50), L713.

21. **Jackson C.L., & McKenna G.B.** The melting behavior of organic materials confined in porous solids. *The Journal of Chemical Physics*, 1990, 93, 9002.

22. **Beamish J.R., Hikata A., Tell L., Elbaum C.** Solidification and superfluidity of/sup 4/He in porous Vycor glass. *Physical Review Letters*, 1983, 50(6).

23. **Borisov B.F., Charnaya E.V., Plotnikov P.G., Hoffmann W.D., Michel D., Kumzerov Y.A. [et al.].** Solidification and melting of mercury in a porous glass as studied by NMR and acoustic techniques. *Physical Review B*, 1998, 58(9), 5329.

24. **Bellissent-Funel M.C., Lal J., Bosio L.** Structural study of water confined in porous glass by neutron scattering. *The Journal of Chemical Physics*, 1993, 98, 4246.

25. **Kanata T., Yoshikawa T., Kubota K.** Grain-size effects on dielectric phase transition of $BaTiO_3$ ceramics. *Solid State Communications*, 1987, 62(11), pp. 765–767.

26. **Ishikawa K., Yoshikawa K., Okada N.** Size effect on the ferroelectric phase transition in PbTiO_{3} ultrafine particles. *Physical Review B*, 1988, 37(10), 5852.

27. **Colla E.V., Fokin A.V., Koroleva E.Y., Kumzerov Y.A., Vakhrushev S.B., Savenko B.N.** Ferroelectric phase transitions in materials embedded in porous media. *Nanostructured Materials*, 1999, 12(5), pp. 963–966.

28. **Anliker K., Brugger H.R., and Кдnzig W.** *Helv. Phys.Acta*, 1954, Vol. 27, p. 99 .

29. **Saegusa K., Rhine W.E., Bowen H.K.** Effect of composition and size of crystallite on crystal phase in lead barium titanate. *Journal of the American Ceramic Society*, 1993, 76(6), pp. 1505–1512.

30. **Uchino K., Sadanaga E., Hirose T.** Dependence of the crystal structure on particle size in barium titanate. *Journal of the American Ceramic Society*, 1989, 72(8), pp. 1555–1558.

31. **Marquardt P., Gleiter H.** Ferroelectric phase transition in microcrystals. *Physical Review Letters*, 1982, 48, pp. 1423–1424.

32. **Zhong W.L., Wang Y.G., Zhang P.L.** Size effects on phase transitions in ferroelectric films. *Physics letters A*, 1994, 189(1), pp. 121–126.

33. **Buchheit W., Kreibig U., Мыller D., Voigt A.** NMR of ^{23}Na in small particles of ferroelectric $NaNO_2$. *Zeitschrift für Physik B. Condensed Matter*, 1978, 2(1), pp. 83–91.

34. **Vakhrushev S.B., Kumzerov Y.A., Fokin A., Naberezhnov A.A., Zalar B., Lebar A., Blinc R.** ^{23} Na spin-lattice relaxation of sodium nitrite in confined geometry. *Physical Review B*, 2004, 70(13), 132102.

35. **Steytler D.C., Dore J.C., Wright C.J.** Neutron diffraction study of cubic ice nucleation in a porous silica network. *The Journal of Physical Chemistry*, 1983, 87(14), pp. 2458–2459.

36. **Wiltzius P., Bates F.S., Dierker S.B., Wignall G.D.** Structure of porous Vycor glass. *Physical Review A*, 1987, 36(6), 2991.

37. **Koroleva E.Y., Nuzhnyy D., Pokorny J., Kamba S., Kumzerov Y.A., Vakhrushev S.B., Petzelt J.** The negative phonon confinement effect in nanoscopic sodium nitrite. *Nanotechnology*, 2009, 20(39), 395706.

38. **Saegusa K., Rhine W.E., Bowen H.K.** Effect of composition and size of crystallite on crystal phase in lead barium titanate. *Journal of the American*

Ceramic Society, 1993, 76(6), pp. 1505–1512.

39. **Colla E.V., Fokin A.V., Koroleva E.Y., Kumzerov Y.A., Vakhrushev S.B., Savenko B.N.** Ferroelectric phase transitions in materials embedded in porous media. *Nanostructured Materials*, 1999, 12(5), pp. 963–966.

40. **Steytler D.C., Dore J.C., Wright C.J.** Neutron diffraction study of cubic ice nucleation in a porous silica network. *The Journal of Physical Chemistry*, 1983, 87(14), pp. 2458–2459.

41. **Dore J.C., Dunn M., Chieux P.** Neutron diffraction studies of ice nucleation in porous silica. *Le Journal de Physique Colloques*, 1987, 48(C1), pp. C1–457.

42. **Benham M.J., Cook J.C., Li J.C., Ross D.K., Hall P.L., & Sarkissian B.** Small-angle neutron scattering study of adsorbed water in porous Vycor glass: Supercooling phase transition and interfacial structure. *Physical Review B*, 1989, 39(1), 633.

43. **Wiltzius P., Bates F.S., Dierker S.B., Wignall G.D.** Structure of porous Vycor glass. *Physical Review A*, 1987, 36(6), 2991.

44. **Naberezhnov A., Fokin A., Kumzerov Y., Sotnikov A., Vakhrushev S., Dorner B.** Structure and properties of confined sodium nitrite. *The European Physical Journal E*, 2003, 12(1), pp. 21–24.

45. **Golosovsky I.V., Delaplane R.G., Naberezhnov A.A., Kumzerov Y.A.** Thermal motion in lead confined within a porous glass. *Physical Review B*, 2004, 69(13), 132301.

46. **Golosovsky I.V., Mirebeau I., Elkaim E., Kurdyukov D.A., Kumzerov Y.A.** Structure of MnO nanoparticles embedded into channel-type matrices. *The European Physical Journal B. Condensed Matter and Complex Systems*, 2005, 47(1), pp. 55–62.

47. **Golosovsky I.V., Salazar-Alvarez G., Lypez-Ortega A., González M.A., Sort J., Estrader M., Nogués J.** Magnetic proximity effect features in antiferromagnetic/ferrimagnetic core-shell nanoparticles. *Physical Review Letters*, 2009, 102(24), 247201.

48. **Marquardt P., Gleiter H.** Ferroelectric phase transition in microcrystals. *Physical Review Letters*, 1982, 48, pp. 1423–1424.

49. **Shull C.G., Strauser W.A., Wollan E.O.** Neutron diffraction by paramagnetic and antiferromagnetic substances. *Physical Review*, 1951, 83(2), 333.

50. **Roth W.L.** Magnetic structures of MnO, FeO, CoO, and NiO. *Physical Review*, 1958, 110(6), 1333.

51. **Lines M.E., Jones E.D.** Antiferromagnetism in the face-centered cubic lattice. II. Magnetic properties of MnO. *Physical Review*, 1965, 139(4A), A1313.

52. **Rodbell D.S., Owen J.** Sublattice magnetization and lattice distortions in MnO and NiO. *Journal of Applied Physics*, 1964, 35, 1002.

53. **Golosovsky I.V., Arčon D., Jagličič Z., Cevc P., Sakhnenko V.P., Kurdyukov D.A., Kumzerov Y.A.** ESR studies of MnO embedded into silica nanoporous matrices with different topology. *Physical Review B*. 2005, 2(14), 144410.

54. **Dronskowski R.** The little maghemite story: A classic functional material. *Advanced Functional Materials*, 2001, 11(1), pp. 27–29.

55. **Golosovsky I.V., Tovar M., Hoffman U., Mirebeau I., Fauth F., Kurdyukov D.A., Kumzerov Y.A.** Diffraction studies of the crystalline and magnetic structures of γ-Fe_2O_3 iron oxide nanostructured in porous glass. *Journal of Experimental and Theoretical Physics Letters*, 2006, 83(7), pp. 298–301.

56. **Golosovsky I.V., Mirebeau I., Fauth F., Kurdyukov D.A., Kumzerov Y.A.** Magnetic structure of hematite nanostructured in a porous glass. *Solid State Communications*, 2007, 141(4), pp. 178–182.

57. **Cabrera G.G.** First order phase transitions in a solid with finite size. *International Journal of Modern Physics B*, 1990, 4(10), pp. 1671–1692.

58. **Binder K., Landau D.P.** Finite-size scaling at first-order phase transitions. *Physical Review B*, 1984, 30(3), 1477.

59. **Barber M.N.** Phase transitions and critical phenomena, Vol. 8, ed. C. Domb and L. Lebowitz. New York: Academic, 1983. 145 p.

60. **Golosovsky I.V., Mirebeau I., André G., Tovar M., Tobbens D.M., Kurdyukov D.A., Kumzerov Y.A.** Magnetic phase transition in a nanostructured antiferromagnet CoO embedded in porous glass. *Physics of the Solid State*, 2006, 48(11), pp. 2130–2133.

61. **Salazar-Alvarez G., Sort J., Surinach S., Baró M.D., Nogués J.** Synthesis and size-dependent exchange bias in inverted core-shell MnO/Mn_3O_4 nanoparticles. *Journal of the American Chemical Society*, 2007, 129(29), pp. 9102–9108.

61a. **Berkowitz A.E., Rodriguez G.F., Hong J.I., An K., Hyeon T., Agarwal N. [et al.].** Antiferromagnetic MnO nanoparticles with ferrimagnetic Mn_3O_4 shells: Doubly inverted core-shell system. *Physical Review B*, 2008, 77(2), 024403.

62. **Poprawski R., Rysiakiewicz-Pasek E., Sieradzki A., Ciżman A., Polańska J.** Ferroelectric phase transitions in KNO_3 embedded into porous glasses. *Journal of Non-Crystalline Solids*, 2007, 353(47), pp. 4457–4461.

62a. **da Costa Lamas A., Chang S.L., Caticha-Ellis S.** On the use of powder diffractometry in the study of phase transitions case of $NaNO_2$. *Physica Status Solidi (A)*, 1981, 68(1), pp. 173–178.

63. **Landau D.P.** Computer simulation studies of magnetic phase transitions. *Journal of Magnetism and Magnetic Materials*, 1999, 200(1), pp. 231–247.

64. **Kutnjak Z., Vodopivec B., Blinc R., Fokin A.V., Kumzerov Y.A., Vakhrushev S.B.** Calorimetric and dielectric studies of ferroelectric sodium nitrite confined in a nanoscale porous glass matrix. *The Journal of Chemical Physics*, 2005, 123, 084708.

65. **Vakhrushev S.B., Kumzerov Y.A., Fokin A., Naberezhnov A.A., Zalar B., Lebar A., Blinc R.** ^{23}Na spin-lattice relaxation of sodium nitrite in confined geometry. *Physical Review B*, 2004, 70(13), 132102.

66. **Nelmes R.J.** The crystal structure of monoclinic KD_2PO_4. *Physica Status Solidi (B)*, 1972, 52(2), pp. K89–K93.

67. **Itoh K., Matsubayashi T., Nakamura E., Motegi H.** *X*-ray study of high-temperature phase transitions in KH_2PO_4. *Journal of the Physical Society of Japan*, 1975, 39, 843.

68. **Mathew M., Wong-Ng** W. Crystal structure of a new monoclinic form of potassium dihydrogen phosphate containing orthophosphacidium ion, $[H_4PO_4]^{+1}$. *Journal of Solid State Chemistry*, 1995, 114(1), pp. 219–223.

69. **Burkovsky R.G., Filimonov A.V., Rudskoy A.I., Hirota K., Matsuura M., Vakhrushev S.B.** Diffuse scattering anisotropy and inhomogeneous lattice deformations in the lead magnoniobate relaxor PMN above the Burns temperature. *Physical Review B*, 2012, 85(9), 094108.

70. **Burkovsky R.G., Bronwald Y.A., Filimonov A.V., Rudskoy A.I., Chernyshov D., Bosak A. [et al.].** Structural heterogeneity and diffuse scattering in morphotropic lead zirconate-titanate single crystals. *Physical Review Letters*, 2012, 109(9), 097603.

71. **Tagantsev A.K., Vaideeswaran K., Vakhrushev S.B., Filimonov A.V., Burkovsky R.G., Shaganov A. [et al.].** The origin of antiferroelectricity in $PbZrO_3$. *Nature communications*, 2013, 4.

72. **Scott J.F., Duiker H.M., Beale P.D., Pouligny B., Dimmler K., Parris M. [et al.].** Properties of ceramic KNO_3 thin-film memories. *Physica B+C*, 1988, 150(1), pp. 160–167.

СПИСОК ЛИТЕРАТУРЫ

1. **Zhong W.L., Wang Y.G., Zhang P.L.** Phase transitions in finite-size ferroelectrics. *Ferroelectr. Rev.*, 1998, 1, pp. 131–193.

2. **Neubeck W., Ranno L., Hunt M.B., Vettier C., Givord D.** Epitaxial MnO thin films grown by pulsed laser deposition. *Applied Surface Science*, 1999, 138, pp. 195–198.

3. **Li S., Eastman J.A., Li Z., Foster C.M., Newnham R.E., Cross L.E.** Size effects in nanostructured ferroelectrics. *Physics Letters A*, 1996, 212(6), pp. 341–346.

4. **Golosovsky I.V., Mirebeau I., Andrй G., Kurdyukov D.A., Kumzerov Y.A., Vakhrushev S.B.** Magnetic ordering and phase transition in MnO embedded in a porous glass. *Physical Review Letters*, 2001, 86(25), 5783.

5. **Sheng P., Cohen R.W., Schrieffer J.R.** Melting transition of small molecular clusters. *Journal of Physics C: Solid State Physics*, 1981, 14(20), L565.

6. **Kumzerov Y.A., Nabereznov A.A., Vakhrushev S.B., Savenko B.N.** Freezing and melting of mercury in porous glass. *Physical Review B*, 1995, 52, pp. 4772–4774.

7. **Pan'kova S.V., Poborchii V.V., Solov'ev V.G.** The giant dielectric constant of opal containing sodium nitrate nanoparticles. *Journal of Physics: Condensed Matter*, 1996, 8(12), L203.

8. **Colla E.V., Fokin A.V., Kumzerov Y.A.** Ferroelectrics properties of nanosize KDP particles. *Solid State Communications*, 1997, 103(2), pp. 127–130.

9. **Colla E.V., Koroleva E.Y., Kumzerov Y.A., Savenko B.N., Vakhrushev S.B.** Ferroelectric phase transitions in materials embedded in porous media. *Ferroelectrics Letters Section*, 1996, 20(5–6), pp. 143–147.

10. **Beskrovny A., Golosovsky I., Fokin A., Kumzerov Y., Kurbakov A., Naberezhnov A., Vakhrushev S.** Structure evolution and formation of a pre–melted state in $NaNO_2$ confined within porous glass. *Applied Physics A*, 2002, 74(1), s1001–s1003.

11. **Fokin A.V., Kumzerov Y.A., Okuneva N.M., Naberezhnov A.A., Vakhrushev S.B., Golosovsky I.V., Kurbakov A.I.** Temperature evolution of sodium nitrite structure in a restricted geometry. *Physical Review Letters*, 2002, 89(17), 175503.

12. **Charnaya E.V., Loeser T., Michel D., Tien C., Yaskov D., Kumzerov Y.A.** Spin-lattice relaxation enhancement in liquid gallium confined within nanoporous matrices. *Physical Review Letters*, 2002, 88(9), 097602.

13. **Drake J.M., Grest G.S., Klafter J., Kopelman R.** Dynamics in Small Confining Systems. Pittsburgh, PA, Materials Research Society, 1999.

14. **Graf M.J., Huber T.E., Huber C.A.** Superconducting properties of indium in the restricted geometry of porous Vycor glass. *Physical Review B*, Eds., 1992. 45(6), 3133.

15. **Charnaya E.V., Tien C., Lin K.J., Wur C.S., Kumzerov Y.A.** Superconductivity of gallium in various confined geometries. *Physical Review B*, 1998, 58(1), 467.

16. **Panova G.K., Naberezhnov A.A., Fokin**

A.V. Surface and volume superconductivity of Pb embedded in nanopores. *Physics of the Solid State*, 2008, 50(7), pp. 1370–1373.

17. **Chan M.H.W., Blum K.I., Murphy S.Q., Wong G.K.S., Reppy J.D.** Disorder and the superfluid transition in liquid^{4} He. *Physical Review Letters*, 1988, 61(17), 1950.

18. **Larson M., Mulders N., Ahlers G.** Thermal expansion coefficient near the superfluid transition of^{4} He in an aerogel. *Physical Review Letters*, 1992, 68(26), 3896.

19. **Mu R., Malhotra V.M.** Effects of surface and physical confinement on the phase transitions of cyclohexane in porous silica. *Physical Review B*, 1991, 44(9), 4296.

20. **Duffy J.A., Wilkinson N.J., Fretwell H.M., Alam M.A., Evans R.** Phase transitions of CO_2 confined in nanometer pores as revealed by positronium annihilation. *Journal of Physics: Condensed Matter*, 1995, 7(50), L713.

21. **Jackson C.L., & McKenna G.B.** The melting behavior of organic materials confined in porous solids. *The Journal of Chemical Physics*, 1990, 93, 9002.

22. **Beamish J.R., Hikata A., Tell L., Elbaum C.** Solidification and superfluidity of/sup 4/He in porous Vycor glass. *Physical Review Letters*, 1983, 50(6).

23. **Borisov B.F., Charnaya E.V., Plotnikov P.G., Hoffmann W.D., Michel D., Kumzerov Y.A. [et al.].** Solidification and melting of mercury in a porous glass as studied by NMR and acoustic techniques. *Physical Review B*, 1998, 58(9), 5329.

24. **Bellissent-Funel M.C., Lal J., Bosio L.** Structural study of water confined in porous glass by neutron scattering. *The Journal of Chemical Physics*, 1993, 98, 4246.

25. **Kanata T., Yoshikawa T., Kubota K.** Grain-size effects on dielectric phase transition of $BaTiO_3$ ceramics. *Solid State Communications*, 1987, 62(11), pp. 765–767.

26. **Ishikawa K., Yoshikawa K., Okada N.** Size effect on the ferroelectric phase transition in PbTiO_{3} ultrafine particles. *Physical Review B*, 1988, 37(10), 5852.

27. **Colla E.V., Fokin A.V., Koroleva E.Y., Kumzerov Y.A., Vakhrushev S.B., Savenko B.N.** Ferroelectric phase transitions in materials embedded in porous media. *Nanostructured Materials*, 1999, 12(5), pp. 963–966.

28. **Anliker K., Brugger H.R., and Кдnzig W.** *Helv. Phys.Acta*, 1954, Vol. 27, p. 99 .

29. **Saegusa K., Rhine W.E., Bowen H.K.** Effect of composition and size of crystallite on crystal phase in lead barium titanate. *Journal of the American Ceramic Society*, 1993, 76(6), pp. 1505–1512.

30. **Uchino K., Sadanaga E., Hirose T.** Dependence of the crystal structure on particle size in barium titanate. *Journal of the American Ceramic Society*, 1989, 72(8), pp. 1555–1558.

31. **Marquardt P., Gleiter H.** Ferroelectric phase transition in microcrystals. *Physical Review Letters*, 1982, 48, pp. 1423–1424.

32. **Zhong W.L., Wang Y.G., Zhang P.L.** Size effects on phase transitions in ferroelectric films. *Physics letters A*, 1994, 189(1), pp. 121–126.

33. **Buchheit W., Kreibig U., Mьller D., Voigt A.** NMR of ^{23}Na in small particles of ferroelectric $NaNO_2$. *Zeitschrift für Physik B. Condensed Matter*, 1978, 2(1), pp. 83–91.

34. **Vakhrushev S.B., Kumzerov Y.A., Fokin A., Naberezhnov A.A., Zalar B., Lebar A., Blinc R.** ^{23} Na spin-lattice relaxation of sodium nitrite in confined geometry. *Physical Review B*, 2004, 70(13), 132102.

35. **Steytler D.C., Dore J.C., Wright C.J.** Neutron diffraction study of cubic ice nucleation in a porous silica network. *The Journal of Physical Chemistry*, 1983, 87(14), pp. 2458–2459.

36. **Wiltzius P., Bates F.S., Dierker S.B., Wignall G.D.** Structure of porous Vycor glass. *Physical Review A*, 1987, 36(6), 2991.

37. **Koroleva E.Y., Nuzhnyy D., Pokorny J., Kamba S., Kumzerov Y.A., Vakhrushev S.B., Petzelt J.** The negative phonon confinement effect in nanoscopic sodium nitrite. *Nanotechnology*, 2009, 20(39), 395706.

38. **Saegusa K., Rhine W.E., Bowen H.K.** Effect of composition and size of crystallite on crystal phase in lead barium titanate. *Journal of the American Ceramic Society*, 1993, 76(6), pp. 1505–1512.

39. **Colla E.V., Fokin A.V., Koroleva E.Y., Kumzerov Y.A., Vakhrushev S.B., Savenko B.N.** Ferroelectric phase transitions in materials embedded in porous media. *Nanostructured Materials*, 1999, 12(5), pp. 963–966.

40. **Steytler D.C., Dore J.C., Wright C.J.** Neutron diffraction study of cubic ice nucleation in a porous silica network. *The Journal of Physical Chemistry*, 1983, 87(14), pp. 2458–2459.

41. **Dore J.C., Dunn M., Chieux P.** Neutron diffraction studies of ice nucleation in porous silica. *Le Journal de Physique Colloques*, 1987, 48(C1), pp. C1–457.

42. **Benham M.J., Cook J.C., Li J.C., Ross D.K., Hall P.L., & Sarkissian B.** Small-angle neutron scattering study of adsorbed water in porous Vycor glass: Supercooling phase transition and interfacial structure. *Physical Review B*, 1989, 39(1), 633.

43. **Wiltzius P., Bates F.S., Dierker S.B., Wignall G.D.** Structure of porous Vycor glass. *Physical Review A*, 1987, 36(6), 2991.

44. **Naberezhnov A., Fokin A., Kumzerov Y., Sotnikov A., Vakhrushev S., Dorner B.** Structure and properties of confined sodium nitrite. *The European Physical Journal E*, 2003, 12(1), pp. 21–24.

45. **Golosovsky I.V., Delaplane R.G., Naberezhnov A.A., Kumzerov Y.A.** Thermal motion in lead confined within a porous glass. *Physical Review B*, 2004, 69(13), 132301.

46. **Golosovsky I.V., Mirebeau I., Elkaim E., Kurdyukov D.A., Kumzerov Y.A.** Structure of MnO nanoparticles embedded into channel-type matrices. *The European Physical Journal B. Condensed Matter and Complex Systems*, 2005, 47(1), pp. 55–62.

47. **Golosovsky I.V., Salazar-Alvarez G., Lypez-Ortega A., González M.A., Sort J., Estrader M., Nogués J.** Magnetic proximity effect features in antiferromagnetic/ferrimagnetic core-shell nanoparticles. *Physical Review Letters*, 2009, 102(24), 247201.

48. **Marquardt P., Gleiter H.** Ferroelectric phase transition in microcrystals. *Physical Review Letters*, 1982, 48, pp. 1423–1424.

49. **Shull C.G., Strauser W.A., Wollan E.O.** Neutron diffraction by paramagnetic and antiferromagnetic substances. *Physical Review*, 1951, 83(2), 333.

50. **Roth W.L.** Magnetic structures of MnO, FeO, CoO, and NiO. *Physical Review*, 1958, 110(6), 1333.

51. **Lines M.E., Jones E.D.** Antiferromagnetism in the face-centered cubic lattice. II. Magnetic properties of MnO. *Physical Review*, 1965, 139(4A), A1313.

52. **Rodbell D.S., Owen** J. Sublattice magnetization and lattice distortions in MnO and NiO. *Journal of Applied Physics*, 1964, 35, 1002.

53. **Golosovsky I.V., Arčon D., Jagličič Z., Cevc P., Sakhnenko V.P., Kurdyukov D.A., Kumzerov Y.A.** ESR studies of MnO embedded into silica nanoporous matrices with different topology. *Physical Review B.* 2005, 2(14), 144410.

54. **Dronskowski R.** The little maghemite story: A classic functional material. *Advanced Functional Materials*, 2001, 11(1), pp. 27–29.

55. **Golosovsky I.V., Tovar M., Hoffman U., Mirebeau I., Fauth F., Kurdyukov D.A., Kumzerov Y.A.** Diffraction studies of the crystalline and magnetic structures of γ-Fe_2O_3 iron oxide nanostructured in porous glass. *Journal of Experimental and Theoretical Physics Letters*, 2006, 83(7), pp. 298–301.

56. **Golosovsky I.V., Mirebeau I., Fauth F., Kurdyukov D.A., Kumzerov Y.A.** Magnetic structure of hematite nanostructured in a porous glass. *Solid State Communications*, 2007, 141(4), pp. 178–182.

57. **Cabrera G.G.** First order phase transitions in a solid with finite size. *International Journal of Modern Physics B*, 1990, 4(10), pp. 1671–1692.

58. **Binder K., Landau D.P.** Finite-size scaling at first-order phase transitions. *Physical Review B*, 1984, 30(3), 1477.

59. **Barber M.N.** Phase transitions and critical phenomena, Vol. 8, ed. C. Domb and L. Lebowitz. New York: Academic, 1983. 145 p.

60. **Golosovsky I.V., Mirebeau I., André G., Tovar M., Tobbens D.M., Kurdyukov D.A., Kumzerov Y.A.** Magnetic phase transition in a nanostructured antiferromagnet CoO embedded in porous glass. *Physics of the Solid State*, 2006, 48(11), pp. 2130–2133.

61. **Salazar-Alvarez G., Sort J., Surinach S., Baró M.D., Nogués J.** Synthesis and size-dependent exchange bias in inverted core-shell MnO/Mn_3O_4 nanoparticles. *Journal of the American Chemical Society*, 2007, 129(29), pp. 9102–9108.

61a. **Berkowitz A.E., Rodriguez G.F., Hong J.I., An K., Hyeon T., Agarwal N. [et al.].** Antiferromagnetic MnO nanoparticles with ferrimagnetic Mn_3O_4 shells: Doubly inverted core-shell system. *Physical Review B*, 2008, 77(2), 024403.

62. **Poprawski R., Rysiakiewicz-Pasek E., Sieradzki A., Ciżman A., Polańska J.** Ferroelectric phase transitions in KNO_3 embedded into porous glasses. *Journal of Non-Crystalline Solids*, 2007, 353(47), pp. 4457–4461.

62a. **da Costa Lamas A., Chang S.L., Caticha-Ellis S.** On the use of powder diffractometry in the study of phase transitions case of $NaNO_2$. *Physica Status Solidi (A)*, 1981, 68(1), pp. 173–178.

63. **Landau D.P.** Computer simulation studies of magnetic phase transitions. *Journal of Magnetism and Magnetic Materials*, 1999, 200(1), pp. 231–247.

64. **Kutnjak Z., Vodopivec B., Blinc R., Fokin A.V., Kumzerov Y.A., Vakhrushev S.B.** Calorimetric and dielectric studies of ferroelectric sodium nitrite confined in a nanoscale porous glass matrix. *The Journal of Chemical Physics*, 2005, 123, 084708.

65. **Vakhrushev S.B., Kumzerov Y.A., Fokin A., Naberezhnov A.A., Zalar B., Lebar A., Blinc R.** ^{23}Na spin-lattice relaxation of sodium nitrite in confined geometry. *Physical Review B*, 2004, 70(13), 132102.

66. **Nelmes R.J.** The crystal structure of monoclinic KD_2PO_4. *Physica Status Solidi (B)*, 1972, 52(2), pp. K89–K93.

67. **Itoh K., Matsubayashi T., Nakamura E., Motegi H.** *X*-ray study of high-temperature phase transitions in KH_2PO_4. *Journal of the Physical Society of Japan*, 1975, 39, 843.

68. **Mathew M., Wong-Ng** W. Crystal structure of a new monoclinic form of potassium dihydrogen phosphate containing orthophosphacidium ion,

$[H_4PO_4]^{+1}$. *Journal of Solid State Chemistry*, 1995, 114(1), pp. 219–223.

69. **Burkovsky R.G., Filimonov A.V., Rudskoy A.I., Hirota K., Matsuura M., Vakhrushev S.B.** Diffuse scattering anisotropy and inhomogeneous lattice deformations in the lead magnoniobate relaxor PMN above the Burns temperature. *Physical Review B*, 2012, 85(9), 094108.

70. **Burkovsky R.G., Bronwald Y.A., Filimonov A.V., Rudskoy A.I., Chernyshov D., Bosak A. [et al.].** Structural heterogeneity and diffuse scattering in morphotropic lead zirconate-titanate single crystals. *Physical Review Letters*, 2012, 109(9), 097603.

71. **Tagantsev A.K., Vaideeswaran K., Vakhrushev S.B., Filimonov A.V., Burkovsky R.G., Shaganov A. [et al.].** The origin of antiferroelectricity in $PbZrO_3$. *Nature communications*, 2013, 4.

72. **Scott J.F., Duiker H.M., Beale P.D., Pouligny B., Dimmler K., Parris M. [et al.].** Properties of ceramic KNO_3 thin-film memories. *Physica B+C*, 1988, 150(1), pp. 160–167.

ФИЛИМОНОВ Алексей Владимирович – *доктор физико-математических наук, доцент кафедры физической электроники Санкт-Петербургского государственного политехнического университета.*
195251, Россия, Санкт-Петербург, Политехническая ул., 29
filimonov@rphf.spbstu.ru

РУДСКОЙ Андрей Иванович – *доктор технических наук, член-корреспондент РАН, заведующий кафедрой пластической обработки металлов Санкт-Петербургского государственного политехнического университета.*
195251, Россия, Санкт-Петербург, Политехническая ул., 29
rector@spbstu.ru

НАБЕРЕЖНОВ Александр Алексеевич – *кандидат физико-математических наук, старший научный сотрудник лаборатории нейтронных исследований Физико-технического института им. А.Ф. Иоффе РАН.*
194021, Россия, Санкт-Петербург, Политехническая ул., 26
alex.nabereznov@mail.ioffe.ru

ВАХРУШЕВ Сергей Борисович – *доктор физико-математических наук, старший научный сотрудник, заведующий лабораторией нейтронных исследований Физико-технического института им. А.Ф. Иоффе РАН, профессор кафедры физической электроники Санкт-Петербургского государственного политехнического университета.*
194021, Россия, Санкт-Петербург, Политехническая ул., 26
s.vakhrushev@mail.ioffe.ru

ФОТИАДИ Александр Эпаминондович – *доктор физико-математических наук, профессор, заведующий кафедрой физической электроники Санкт-Петербургского государственного политехнического университета.*
195251, Россия, Санкт-Петербург, Политехническая ул., 29
fotiadi@rphf.spbstu.ru

КОРОЛЕВА Екатерина Юрьевна – *кандидат физико-математических наук, старший научный сотрудник Физико-технического института им. А.Ф. Иоффе РАН, доцент кафедры физической электроники Санкт-Петербургского государственного политехнического университета.*
194021, Россия, Санкт-Петербург, Политехническая ул., 26
e.yu.koroleva@mail.ioffe.ru

ГОЛОСОВСКИЙ Игорь Викторович – *доктор физико-математических наук, ведущий научный сотрудник отделения нейтронных исследований Петербургского института ядерной физики им. Б.П. Константинова РАН.*
188300, Россия, Ленинградская область, Гатчина, Орлова Роща
golosov@mail.pnpi.spb.ru

КУМЗЕРОВ Юрий Александрович – *доктор физико-математических наук, главный научный сотрудник, заместитель директора отделения физики диэлектриков и полупроводников Физико-технического института им. А.Ф. Иоффе РАН, профессор кафедры физической электроники Санкт-Петербургского государственного политехнического университета.*

194021, Россия, Санкт-Петербург, Политехническая ул., 26

yu.kumzerov@mail.ioffe.ru

НАКЕ Бернард – *доктор инженерии, профессор, директор Института электротехники Университета Вильгельма Лейбница.*

30167, Германия, Ганновер, Вельфенгартен, 1

nacke@etp.uni-hannover.de

UDC 533.9

F. Wagner, V.Yu. Sergeev, P.R. Goncharov

[1] St. Petersburg State Polytechnical University,
29 Politekhnicheskaya St., St. Petersburg, 195251, Russia

THE RESEARCH LABORATORY OF THE PHYSICS OF ADVANCED TOKAMAKS OF THE ST. PETERSBURG STATE POLYTECHNICAL UNIVERSITY

Ф. Вагнер, В.Ю. Сергеев, П.Р. Гончаров

ЛАБОРАТОРИЯ ФИЗИКИ УЛУЧШЕННОГО УДЕРЖАНИЯ ПЛАЗМЫ ТОКАМАКОВ САНКТ-ПЕТЕРБУРГСКОГО ГОСУДАРСТВЕННОГО ПОЛИТЕХНИЧЕСКОГО УНИВЕРСИТЕТА

Within the Research Laboratory of the Physics of Advanced Tokamaks, which has been founded in 2011 on the basis of a MEGA-Grant, the two groups from the University and the Ioffe Institute cooperate on the three tokamaks, Globus-M, TUMAN-3M and FT-2. The research of both partners benefitted from the means of the MEGA-Grant. The laboratory has given itself a transparent governing structure and its annual outcome is assessed by an international advisory committee. A graduate school has been founded to ensure proper education. The Laboratory could serve as a model for integrated research and education centre in Russian thermonuclear program. The urgent need to modernize the Russian fusion devices has become obvious.

RESEARCH LABORATORY, THERMO-NUCLEAR FUSION, TOKAMAK DEVICES, PLASMA CONFINEMENT, PLASMA DIAGNOSTICS, PLASMA HEATING, THEORY AND EXPERIMENT, EDUCATION WITHIN RLPAT.

В рамках Лаборатории физики улучшенного удержания плазмы токамаков, организованной в 2011 на основе МЕГА-гранта, две группы из Университета и из ФТИ имени А.Ф. Иоффе РАН объединили свои усилия в работах по трем токамакам: Глобус-М, ТУМАН-3М и ФТ-2. Исследования обоих партнеров обеспечиваются из средств МЕГА-гранта. Лаборатория сформировала прозрачную структуру управления. Результаты ее работы ежегодно оцениваются Международным консультативным комитетом. Была создана школа для обеспечения выпускников Университета специальным образованием. Лаборатория может служить моделью интеграции исследований и образования, необходимых в Российской термоядерной программе. Кажется очевидной настоятельная необходимость модернизации российских установок термоядерного синтеза.

ИССЛЕДОВАТЕЛЬСКАЯ ЛАБОРАТОРИЯ, ТЕРМОЯДЕРНЫЙ СИНТЕЗ, ТОКАМАКИ, УДЕРЖАНИЕ ПЛАЗМЫ, ДИАГНОСТИКА ПЛАЗМЫ, НАГРЕВ ПЛАЗМЫ, ТЕОРИЯ И ЭКСПЕРИМЕНТ, ОБУЧЕНИЕ В РАМКАХ RLPAT.

I. Introduction

The Research Laboratory of the Physics of Advanced Tokamaks (RLPAT, www.rlpat.ru) has been founded in 2011 at the St. Petersburg State Polytechnical University on the basis of a MEGA-Grant from the Russian government (Agreement No. 11.G34.31.0041). The grant has been awarded for 2 years and terminates 31.12.2013. The mission of the RLPAT is: «to organize a scientific laboratory in the University for investigating experimentally and theoretically regimes with improved plasma confinement; to provide it with equipment for such investigations; to actively involve gradu-

ate and post-graduate students in the scientific work». The speciality of the organization of the laboratory is that it strengthens the traditional cooperation between SPbSPU and the Ioffe Physical-Technical Institute of the Russian Academy of Sciences in the field of fusion research. Russian science enjoys an extremely fruitful history in fusion research; the development of the tokamak confinement concept is one of the science legacies of Russia. The culmination of this effort is the realization of the experimental fusion reactor ITER based on the tokamak concept. Russia is one of the seven ITER partners and contributes within 10 % of the costs. The great history of fusion research of Russia is the background of our efforts and represents strong responsibility and commitment.

II. Organization of the RLPAT

The laboratory comprises about 100 members with nearly equal parts from SPbSPU and the Ioffe Institute. It is structured into 7 scientific groups, 4 from SPbSPU and 3 from the Ioffe Institute:

1. Group of «Plasma fuelling and exhaust and related diagnostics», headed by Prof. V. Sergeev of SPbSPU;
2. Group of «Theory and modeling of edge plasma of tokamaks», headed by Prof. V. Rozhansky of SPbSPU;
3. Group of «Tokamak plasma turbulence», headed by Prof. V. Bulanin of SPbSPU;
4. Group of «RF plasma heating», headed by Prof. G. Sominski of SPbSPU;
5. «Globus-M» – group headed by Dr. V. Gusev from the Ioffe Institute;
6. «FT-2» – group headed by Prof. E. Gusakov from the Ioffe Institute;
7. «TUMAN-3M» – group headed by Prof. S. Lebedev from the Ioffe Institute.

Groups 1, 2 and 5 are the only ones in Russia with experience in divertor tokamak physics. Groups 3 and 5 are the only ones working in Russia in the field of turbulence and flow interaction with spontaneous H-mode – the operational regime of ITER; Groups 6 and 7 also contribute to the understanding this important topic. Group 4 specializes in the technology of gyrotrons – an important way to heat a future fusion reactor by electron-cyclotron-resonance heating. Russian industry is also very strong (GYCOM company) in gyrotron development. Groups 5 and 6 study non-inductive current initiation and current drive – again in a field of relevance for ITER and a fusion neutron source, FNS. Groups 5 and 7 are involved in fast ion confinement issues.

The RLPAT has given itself a governance structure based on the postulate that all executive and scientific decisions should be carried out in a transparent form after thorough discussion within the Executive Committee or the Scientific Committee, respectively. The Executive Committee has four members from SPbSPU and Ioffe Institute and is chaired by the «Leading Scientist», F. Wagner, or his deputy, V. Sergeev. The Scientific Committee is formed by the group leaders of the RLPAT. The governance structure of the RLPAT is such that its leadership can easily be transferred to someone from the University or the Ioffe Institute. It does not require the presence of the Leading Scientist forever.

To ensure regular progress control along international standards, an International Advisory Committee (IAC) has been formed. Its members are W. Morris (chair, UK), H. Wilson (UK), S. Kaye (USA), B. Kuteev (Russia), A. Litvak (Russia). The foreign members come from the field of spherical tokamaks which Globus-M also belongs to. The IAC has had two meetings up to now, one in 2012, and one in 2013. It operates along specific «Terms of References» defined by the Executive Committee and it summarizes its findings and recommendations in a report which is sent to the heads of university, the Ioffe Institute and to the RF ministry of education and science.

If properly financed, e. g. in an institutional form as it is necessary for fusion with its long-term objectives, the RLPAT represents a structure which formalizes the cooperation between SPbSPU and an Academy institute. This cooperation is supposed to ensure filling two gaps in the Russian fusion program – participating in new devices like the upcoming Globus-M2 tokamak and educating young people in fusion physics. There is a tremendous need in performing the both tasks.

II. Research of the RLPAT

With the MEGA-Grant, the tokamak devices of the Ioffe Institute could not be modernized, but the diagnostics and heating periphery with which the SPbSPU staff cooperates with could be improved. According to the Russian fusion program which aims at a fusion energy source in the cooperation with ITER and at a fusion neutron source as a national goal, the research of RLPAT centers around the needs of ITER and the FNS. The programmatic guideline for the work within the RLPAT is the scenario to use the potential of spherical tokamaks in terms of creating a neutron source. This development would be carried out with strong partners in Europe and the USA. The strategy of the Ioffe Institute is to replace, in near future, the present spherical tokamak, Globus-M, by the upgrade into Globus-M2 and finally to aim at Globus-M3, a non-nuclear device which could accompany a nuclear one to be built elsewhere, where the corresponding nuclear licensing is possible. Globus-M2 and more so Globus-M3 could explore the physics of anisotropic, strongly beam-driven plasmas.

The major topics where the RLPAT can contribute at present to such a strategy are:

the study of plasma confinement, specifically the conditions for this and the transition physics of the H-mode. The most successful paradigm to explain the H-mode transition is the non-linear interaction of turbulent eddies which adopt sufficient anisotropy between radial and poloidal flow components so that the Reynolds stress develops at the plasma edge whose induced zonal flow adds to the L-mode background mean flow. As a consequence of sheared flow, the turbulence is ultimately quenched, the local confinement improved and a large ion pressure gradient appears at the plasma edge. Its related electric field stabilizes the new boundary conditions of low turbulence. In all the three tokamaks of the Ioffe Institute, the oscillatory form of the zonal flow (local ExB plasma poloidal flow), so called GAMs, due to the background turbulent field, are observed [1, 2]. The recent discovery of GAMs in Globus-M [1] has been achieved by the new microwave Doppler reflectometry system from the MEGA-Grant.

As the GAM frequency depends on the ion mass, the study of GAMs has been linked to that of the isotopic effect on confinement. This is an important field because this effect forces ITER to operate during the non-nuclear phase with helium, as the H-mode is not expected in hydrogen. RLPAT has an excellent potential for further exploring the inherent physics of the H-mode: Globus-M operates with a spontaneously developed H-mode but does not show an isotopic effect on confinement [4]; TUMAN-3M can operate with an induced H-mode [5] and displays an isotopic effect [unpublished]. Both devices show GAMs which disappear – as expected – when the H-mode sets in. FT-2 can develop an alternative good confinement regime to compare with and has specific diagnostic means to explore the non-linear relation of turbulence and GAMs, and has interesting observations regarding the isotopic effect [6]. This is an ongoing research field.

Other important areas of confinement research are the strong density dependence of an energy confinement time τ_E in case of Globus-M compared to the saturation effects observed in the other two devices, and the trade-off between strong plasma current I_p scaling of τ_E in case of larger aspect ratio and strong toroidal magnetic field B_t scaling in case of spherical tokamaks [7, 4, 9]. In this context, the density profile shape may play a significant role (e. g. for the stabilization of so-called η_i-turbulence). The new pellet injector purchased from the MEGA-Grant and mounted onto TUMAN-3M will help clarifying these issues.

Another important issue for both ITER and the FNS is fast ion confinement. This can be studied in Globus-M and TUMAN-3M. In TUMAN-3M, the classical aspects of ion confinement and slowing down can be explored in the future with a new NPA from the MEGA-Grant. Critical for ion confinement is the radial plasma location [8]. The aspects of the toroidal field ripple have to be investigated in more details. In Globus-M, the heating ions are not well confined owing to the low current and magnetic field [9]. This is clearly shown by neutron and by spectrally resolved charge exchange measurements. Though, this is a strongly negative aspect for plasma heating; it seems, on

the other hand, that this condition renders the beam confinement to respond sensitively to the MHD properties of the discharge. Both, sawteeth and Alfven Eigenmodes, lead to fast ion redistribution and losses. This sensitivity can be used to understand better how the mode-fast particle interaction happens on a microscopic scale and causes ion losses. These studies are of utmost importance both for ITER and an FNS because beam current drive is essential and necessitates perfect beam ion confinement also during MHD active periods.

Steady-state operation is even more mandatory for an FNS aiming more at large fluences than at pure fusion. Therefore, all current drive issues are of highest relevance. The theory group of the Ioffe Institute and the groups of both Globus-M and FT-2 tokamaks are well prepared to study lower hybrid current drive. An exciting period is ahead of Globus-M because a novel antenna arrangement which allows poloidal wave launch will be operated soon [10]. New klystrons, provided by the MEGA-Grant, will improve the conditions of Lower Hybrid heating and current drive in this device.

In FT-2, the onset of ion heating by LH waves which stops the bulk electron interaction and diminishes the current drive efficiency has been shown to be shifted to larger density values by replacing hydrogen with deuterium. This is a highly relevant experimental verification of the theoretical expectation. It will be interesting to see to what extent this aspect also affects non-inductive current build-up. This technique is mandatory for spherical tokamaks operated without explicit ohmically heating system. Advancement in this area requires a close cooperation between the three teams: Globus-M, FT-2 and the theory group.

A highlight in the fusion related research of SPbSPU is edge and divertor modeling. The working horse for this purpose is the B2SOLPS code series [11]. This code is the world-wide standard for edge modeling thanks to its advanced physics e. g. its including the effects of drifts. Because the Russian fusion program does not possess a powerful divertor device, most of the modeling and advancements of the code are driven by external interests. The latest step in this development is the cooperation with ITER and the development of a custom-made code version B2SOLPS-IO. Thanks to the increasing diagnostic possibilities of Globus-M to study the edge and divertor plasmas, also some of the modeling activities are concentrating on this device now and, starting from it, on modeling the next step, Globus-M2.

In order to improve modeling, the diagnostic capabilities for the plasma edge were improved thanks to the MEGA-Grant support and will be further improved. The most crucial edge parameter is the scrape-off layer width in the plasma mid-plane. The existing data predict a width in the mm-range for ITER. This is a tremendous threat for the safe and steady-state operation of a fusion device and more research is urgently needed in this field. In the frame of the RLPAT, the first power deposition profiles at the Globus-M divertor target have been measured [12]. These studies will be complemented by a new diagnostics, a supersonic He beam which allows the simultaneous measurement of the density and electron temperature in the divertor chamber of Globus-M.

The group «RF plasma heating» of the RLPAT deals with the improvement of gyrotron technology. Gyrotrons are used for ECRH. This is a sophisticated technology used both in tokamaks and stellarators and also foreseen for ITER. ECRH allows heating without complex plasma-antenna matching as well as current drive and MHD control. The RLPAT group is engaged in improving the electron beam quality and enhancing gyrotron efficiency [13], developing electron beam diagnostics [14] cold field emitters [15]. It works in close cooperation with the developers and manufacturers of high-power gyrotrons from IAP RAS and Gycom (Russia), and Karlsruhe Institute of Technology (KIT, Germany). Of specific interest is the diagnostics of the helical electron beam, which allows to understand better the physical processes possibly leading to higher efficiency gyrotrons [13, 14]. Without a suppressed collector and without space-charge oscillations, a record efficiency of 46 % has recently been obtained with multi-sectional control electrodes and high uniformity and emission efficiency of the thermionic cathodes. Another area of applied research is the development of cold field emitters for mm-wave and THz gyrotrons [14].

IV. Education within RLPAT

A Graduate School has been founded with full recognition by the university. It embraces about 25 graduates. In regular meetings, they present the progress of their work to their supervisors as well as to other professors of the school who are available. Presentations and discussions are held in English. The advantage of training via a Graduate School is that the graduates benefit from the knowledge, experience and contributions of all the professors of the school. In addition, the students train themselves in soft skills like presentation techniques and language capability. Deficiencies in supervision are more easily detected in such a cooperative structure. The student members of a graduate school are more ready to form a scientific community, which allows the better integration of newcomers. The graduate school invites external speakers who cover special topics. This year, five lecturers were invited covering topics like ITER physics, diagnostic techniques, stellarator and mirror machine physics. The lectures are available via the RLPAT Web page. Successful students of the graduate school have been singled out to present their material at international conferences. A separate budget has been set aside for this purpose.

V. The Russian Fusion Program and the Need for RLPAT

For a long time, Russia was leading in tokamak fusion research. In the last decades, Russia has lost its leading role at least in experimental work. The devices of the Russian tokamak program are old and do not contribute to the solutions of present and urgent problems as they are internationally defined and tackled, e. g. in the frame of the ITPA activity. As an outsider, one can recognize the existence of a fusion program in Russia – the participation in ITER and the development of a fusion neutron source. However, it is difficult to recognize, however, a clear national strategy: how to implement an experimental program, which would allow tackling the open scientific issues in broad front or an administrative structure, which would allow implementing such a strategy.

From the seven ITER partners, Russia has the lowest ratio of expenses for the national program to those of ITER. The Russian figure is 0.35; the average value of the other six partners is 0.93. The threat is that Russia will not provide sufficient number of people trained in the most relevant fusion issues and being able to nationalize sufficiently the know-how gained with ITER. The consequence of the present scientific infrastructure situation is that the scientific presence and visibility of Russian fusion scientists – at least in experimental research – is strongly limited. In the last IAEA Fusion-Energy-Conference in 2012 in the USA, Russia was on position #6 among 7 ITER partners, in terms of their contributions and oral papers, and it was only followed by India. Two out of 4 oral papers were given by RLPAT members.

Summarizing, there is a tremendous need of the Russian fusion program to expand the scientific activities in the fusion research and to educate a new generation of scientists capable of working within the national fusion program and with ITER. It is also necessary to broaden the capability to transfer the know-how gained by the operation of ITER into the national program as it is the original intension connected with a commitment to ITER. For these goals, the RLPAT is the proper organizational form to strengthen the cooperative fusion research in St. Petersburg area. The first period of the MEGA-Grant has improved strongly the research possibilities of the SPbSPU to do research in the field of high-temperature fusion plasma physics in cooperation with the experimental teams of the three tokamaks of the Ioffe Institute. RLPAT meets all criteria of a modern institution for research and education. It is structured in such a way that it can contribute to the advancement of fusion research along the major development branches: (1) basic fusion research, (2) preparation of the Ioffe Institute device Globus-M2, (3) contributions to the physics basis of the Russian project of the fusion neutron source and (4) to contribute to the identical physics needs of ITER.

VI. Outlook

The IAC of the RLPAT wrote in its first report: «In summary: the RLPAT presents a very special opportunity for fusion research in Russia, and it has made an excellent start». This was sufficient encouragement to apply for the

prolongation of the RLPAT functioning beyond the present two funding years. Fusion is a long-term effort and therefore, the institutions working in this field need long-term support institutionalized by national research priorities. Since Chernobyl and Fukushima, the attractiveness of fission as an energy source has reduced. At a power capacity based on the renewable wind and photovoltaic energies which add up to 25 % of the electric load at the end of 2012, Germany presently experiences the limitations of intermittent electricity supply. Then, there only remains fusion.

Acknowledgement

We are grateful to the Scientific Council members for their valuable contributions to this report.

REFERENCES

1. **Askinazi L.G., Vildjunas M.I., Zhubr N.A., Komarov A.D., Kornev V.A., Krikunov S.V., Krupnik L.I., Lebedev S.V., Rozhdestvensky V.V., Tendler M., Tukachinsky A.S., Khrebtov S.M.** Evolution of geodesic acoustic mode in ohmic H-mode in TUMAN-3M tokamak. *Tech. Phys. Letters*, 2012, Vol. 38, No. 3, pp. 268–271.

2. **Yashin A.Yu., Askinazi L.G., Belokurov A.A., Bulanin V.V., Lebedev S.V., Kornev V.A., Petrov A.V., Tukachinsky A.S., Vildjunas M.I.** GAM observation in the TUMAN-3M tokamak using Doppler reflectometry. Proc. of the 40th EPS Conf. on Plasma Physics, 2013, ECA, Vol. 37D, art. no. P2.179.

3. **Bulanin V.V., Gusev V.K., Khromov N.A., Kurskiev G.S., Minaev V.B., Patrov M.I., Petrov A.V., Petrov Yu.V., Prisiazhniuk D.V., Sakharov N.V., Shchegolev P.B., Tolstyakov S.Yu., Varfolomeev V.I., Wagner F., Yashin A.Yu.** Observation of geodesic acoustic modes in Globus-M spherical torus. Submitted to *Tech. Phys. Letters*, 2013.

4. **Sakharov N.V., Berezutskiy A.A., Chernyshev F.V., Gusev V.K., Iblyaminova A.D., Khromov N.A., Kurskiev G.S., Melnik A.D., Minaev V.B., Novokhatsky A.N., Patrov M.I., Petrov Yu.V., Tolstyakov S.Yu., Wagner F., Zhilin E.G.** Study of the isotopic effect on ohmic L- and H-mode confinement on Globus-M. Proc. of 39th EPS Conference on Plasma Phys. & 16th Int. Congress on Plasma Phys., Stockholm, 2012, ECA, Vol. 36C, art. no. P2.004.

5. **Lebedev S.V., Andrejko M.V., Askinazi L.G., Golant V.E., Kornev V.A., Levin L.S., Rozhansky V.A., Tendler N., Tukachinsky A.S.** Ohmic H-mode studies in TUMAN-3. *Plasma Phys. Control. Fusion*, 1994, Vol. 36, pp. B289–B299.

6. **Gurchenko A.D., Gusakov E.Z., Altukhov A.B., Selyunin E.P., Esipov L.A., Kantor M.Y., Kouprienko D.V., Lashkul S.I., Stepanov A.Y., Wagner F.** Spatial structure of the geodesic acoustic mode in the FT-2 tokamak by upper hybrid resonance Doppler backscattering. *Plasma Phys. Control. Fusion*, 2013, Vol. 55, No. 8, art. no. 085017.

7. **Gusev V.K., Chernyshev F.V., Golant V.E., Leonov V.M., Levin R.G., Minaev V.B., Mineev A.B., Patrov M.I., Petrov Yu.V., Sakharov N.V., Tolstyakov S.Yu., Varfolomeev V.I., Voronin A.V., Zhilin E.G.** Density limits and control in the Globus-M spherical tokamak. *Nucl. Fusion*, 2006, Vol. 46, No. 8, pp. S584–S591.

8. **Kornev V.A., Chernyshev F.V., Melnik A.D., Askinazi L.G., Wagner F., Vildjunas M.I., Zhubr N.A., Krikunov S.V., Lebedev S.V., Razumenko D.V., Tukachinsky A.S.** The influence of plasma horizontal position on the neutron rate and flux of neutral atoms in injection heating experiment on the TUMAN-3M Tokamak. *Tech. Phys. Letters*, 2013, Vol. 39, No. 22, pp. 64–72. (rus)

9. **Gusev V.K., Chernyshev F.V., Golant V.E., Leonov V.M., Levin R.G., Minaev V.B., Mineev A.B., Patrov M.I., Petrov Yu.V., Sakharov N.V., Tolstyakov S.Yu., Varfolomeev V.I., Voronin A.V., Zhilin E.G.** Globus-M results as the basis for a compact spherical tokamak with enhanced parameters Globus-M2. *Nucl. Fusion*, 2013, Vol. 53, art. no. 093013.

10. **Dyachenko V.V., Irzak M.A., Cherotchenko E.D., Shcherbinin O.N.** Simulation of the conditions of wave excitation for the optimization of the lower hybrid current drive in the Globus-M spherical tokamak. *Plasma Phys. Rep.*, 2013, Vol. 39, pp. 120–129.

11. **Rozhansky V., Kaveeva E., Molchanov P., Veselova I., Voskoboynikov S., Coster D., Counsell G., Kirk A., Lisgo S.** New B2SOLPS5.2 transport code for H-mode regimes in tokamaks. *Nucl. Fusion*, 2009, Vol. 49, art. no. 025007.

12. **Bykov A.S., Sergeev V.Yu., Khromov N.A., Gusev V.K., Petrov Yu.V., Sakharov N.V., Tolstyakov S.Yu., Wagner F.** Measurements of the SOL heat flux width on Globus-M. Proc. of the 40th EPS Conf. on Plasma Physics, 2013, ECA, Vol. 37D, art. no. P1.132.

13. **Louksha O.I., Samsonov D.B., Sominskii G.G., Semin S.V.** Dynamic processes in helical electron beams in gyrotrons. *Tech. Phys.*, 2013, Vol. 58, No. 5, pp. 751–759.

14. **Arkhipov A., Dvoretskaya N., Gantenbein G., Kern S., Louksha O., Rzesnicki T., Samartsev A., Sominskii G.** Reconstruction of energy distributions in electron beams on the dasis of dremsstrahlung X-ray spectra. *IEEE Trans. Plasma Science*, 2013, Vol. 41, No. 10, p. 2786–2789.

15. **Tumareva T.A., Sominskii G.G.** Operation of activated-fullerene-coated field emitters in technical vacuum. *Tech. Phys.*, 2013, Vol. 58, No. 7, p. 1048–1051.

СПИСОК ЛИТЕРАТУРЫ

1. **Askinazi L.G., Vildjunas M.I., Zhubr N.A., Komarov A.D., Kornev V.A., Krikunov S.V., Krupnik L.I., Lebedev S.V., Rozhdestvensky V.V., Tendler M., Tukachinsky A.S., Khrebtov S.M.** Evolution of geodesic acoustic mode in ohmic H-mode in TUMAN-3M tokamak. *Tech. Phys. Letters*, 2012, Vol. 38, No. 3, pp. 268–271.

2. **Yashin A.Yu., Askinazi L.G., Belokurov A.A., Bulanin V.V., Lebedev S.V., Kornev V.A., Petrov A.V., Tukachinsky A.S., Vildjunas M.I.** GAM observation in the TUMAN-3M tokamak using Doppler reflectometry. Proc. of the 40th EPS Conf. on Plasma Physics, 2013, ECA, Vol. 37D, art. no. P2.179.

3. **Bulanin V.V., Gusev V.K., Khromov N.A., Kurskiev G.S., Minaev V.B., Patrov M.I., Petrov A.V., Petrov Yu.V., Prisiazhniuk D.V., Sakharov N.V., Shchegolev P.B., Tolstyakov S.Yu., Varfolomeev V.I., Wagner F., Yashin A.Yu.** Observation of geodesic acoustic modes in Globus-M spherical torus. Submitted to *Tech. Phys. Letters*, 2013.

4. **Sakharov N.V., Berezutskiy A.A., Chernyshev F.V., Gusev V.K., Iblyaminova A.D., Khromov N.A., Kurskiev G.S., Melnik A.D., Minaev V.B., Novokhatsky A.N., Patrov M.I., Petrov Yu.V., Tolstyakov S.Yu., Wagner F., Zhilin E.G.** Study of the isotopic effect on ohmic L- and H-mode confinement on Globus-M. Proc. of 39th EPS Conference on Plasma Phys. & 16th Int. Congress on Plasma Phys., Stockholm, 2012, ECA, Vol. 36C, art. no. P2.004.

5. **Lebedev S.V., Andrejko M.V., Askinazi L.G., Golant V.E., Kornev V.A., Levin L.S., Rozhansky V.A., Tendler N., Tukachinsky A.S.** Ohmic H-mode studies in TUMAN-3. *Plasma Phys. Control. Fusion*, 1994, Vol. 36, pp. B289–B299.

6. **Gurchenko A.D., Gusakov E.Z., Altukhov A.B., Selyunin E.P., Esipov L.A., Kantor M.Y., Kouprienko D.V., Lashkul S.I., Stepanov A.Y., Wagner F.** Spatial structure of the geodesic acoustic mode in the FT-2 tokamak by upper hybrid resonance Doppler backscattering. *Plasma Phys. Control. Fusion*, 2013, Vol. 55, No. 8, art. no. 085017.

7. **Gusev V.K., Chernyshev F.V., Golant V.E., Leonov V.M., Levin R.G., Minaev V.B., Mineev A.B., Patrov M.I., Petrov Yu.V., Sakharov N.V., Tolstyakov S.Yu., Varfolomeev V.I., Voronin A.V., Zhilin E.G.** Density limits and control in the Globus-M spherical tokamak. *Nucl. Fusion*, 2006, Vol. 46, No. 8, pp. S584–S591.

8. **Kornev V.A., Chernyshev F.V., Melnik A.D., Askinazi L.G., Wagner F., Vildjunas M.I., Zhubr N.A., Krikunov S.V., Lebedev S.V., Razumenko D.V., Tukachinsky A.S.** The influence of plasma horizontal position on the neutron rate and flux of neutral atoms in injection heating experiment on the TUMAN-3M Tokamak. *Tech. Phys. Letters*, 2013, Vol. 39, No. 22, pp. 64–72. (rus)

9. **Gusev V.K., Chernyshev F.V., Golant V.E., Leonov V.M., Levin R.G., Minaev V.B., Mineev A.B., Patrov M.I., Petrov Yu.V., Sakharov N.V., Tolstyakov S.Yu., Varfolomeev V.I., Voronin A.V., Zhilin E.G.** Globus-M results as the basis for a compact spherical tokamak with enhanced parameters Globus-M2. *Nucl. Fusion*, 2013, Vol. 53, art. no. 093013.

10. **Dyachenko V.V., Irzak M.A., Cherotchenko E.D., Shcherbinin O.N.** Simulation of the conditions of wave excitation for the optimization of the lower hybrid current drive in the Globus-M spherical tokamak. *Plasma Phys. Rep.*, 2013, Vol. 39, pp. 120–129.

11. **Rozhansky V., Kaveeva E., Molchanov P., Veselova I., Voskoboynikov S., Coster D., Counsell G., Kirk A., Lisgo S.** New B2SOLPS5.2 transport code for H-mode regimes in tokamaks. *Nucl. Fusion*, 2009, Vol. 49, art. no. 025007.

12. **Bykov A.S., Sergeev V.Yu., Khromov N.A., Gusev V.K., Petrov Yu.V., Sakharov N.V., Tolstyakov S.Yu., Wagner F.** Measurements of the SOL heat flux width on Globus-M. Proc. of the 40th EPS Conf. on Plasma Physics, 2013, ECA, Vol. 37D, art. no. P1.132.

13. **Louksha O.I., Samsonov D.B., Sominskii G.G., Semin S.V.** Dynamic processes in helical electron beams in gyrotrons. *Tech. Phys.*, 2013, Vol. 58, No. 5, pp. 751–759.

14. **Arkhipov A., Dvoretskaya N., Gantenbein G., Kern S., Louksha O., Rzesnicki T., Samartsev A., Sominskii G.** Reconstruction of energy distributions in electron beams on the dasis of dremsstrahlung x-ray spectra. *IEEE Trans. Plasma Science*, 2013, Vol. 41, No. 10, p. 2786–2789.

15. **Tumareva T.A., Sominskii G.G.** Operation of activated-fullerene-coated field emitters in technical vacuum. *Tech. Phys.*, 2013, Vol. 58, No. 7, pp. 1048–1051.

ВАГНЕР Фридрих – *заведующий исследовательской лабораторией физики улучшенного удержания плазмы токамаков Санкт-Петербургского государственного политехнического университета, почетный директор Института физики плазмы им. Макса Планка, Германия (Director Emeritus of the Max-Planck-Institut für Plasmaphysik).*
195251, Россия, Санкт-Петербург, Политехническая ул., 29
fritz.wagner@ipp.mpg.de

СЕРГЕЕВ Владимир Юрьевич – *доктор физико-математических наук, профессор кафедры физики плазмы и заместитель заведующего Научно-исследовательской лабораторией физики улучшенного удержания плазмы токамаков Санкт-Петербургского государственного политехнического университета.*
195251, Россия, Санкт-Петербург, Политехническая ул., 29
v.sergeev@spbstu.ru

ГОНЧАРОВ Павел Романович – *Ph.D., старший научный сотрудник Научно-исследовательской лаборатории управляемого термоядерного синтеза Санкт-Петербургского государственного политехнического университета.*
195251, Россия, Санкт-Петербург, Политехническая ул., 29
p.goncharov@spbstu.ru

UDC 621.38

O.I. Louksha, G.G. Sominski, A.V. Arkhipov,
N.V. Dvoretskaya, D.B. Samsonov, S.V. Syomin, F. Wagner

St. Petersburg State Polytechnical University,
29 Politekhnicheskaya St., St. Petersburg, 195251, Russia

GYROTRON RESEARCH AT THE ST. PETERSBURG STATE POLYTECHNICAL UNIVERSITY

О.И. Лукша, Г.Г. Соминский, А.В. Архипов,
Н.В. Дворецкая, Д.Б. Самсонов, С.В. Сёмин, Ф. Вагнер

ГИРОТРОННЫЕ ИССЛЕДОВАНИЯ В САНКТ-ПЕТЕРБУРГСКОМ ГОСУДАРСТВЕННОМ ПОЛИТЕХНИЧЕСКОМ УНИВЕРСИТЕТЕ

This paper presents the results of investigations performed by the researchers of the Department of Physical Electronics in the laboratory headed by Prof. F. Wagner and supported by the Ministry of Education and Science of the Russian Federation on the basis of MEGA-Grant. Methods for the improvement of helical electron beam quality and for enhancement of gyrotron efficiency, new gyrotron electron beam diagnostics are discussed.

GYROTRON, EFFICIENCY, HELICAL ELECTRON BEAM, DIAGNOSTICS, SAINT-PETERSBURG STATE POLYTECHNICAL UNIVERSITY, DEPARTAMENT OF PHYSICAL ELECTRONICS.

В статье представлены результаты исследований, выполненных сотрудниками кафедры физической электроники в рамках межфакультетской лаборатории, возглавляемой проф. Ф. Вагнером и поддерживаемой мегагрантом Министерства образования и науки Российской Федерации. Обсуждаются разработанные авторами методы повышения качества винтового электронного потока и эффективности работы гиротронов, а также новые методы диагностики электронных потоков в гиротронах.

ГИРОТРОН, ЭФФЕКТИВНОСТЬ, ВИНТОВОЙ ЭЛЕКТРОННЫЙ ПОТОК, ДИАГНОСТИКА, САНКТ-ПЕТЕРБУРГСКИЙ ГОСУДАРСТВЕННЫЙ ПОЛИТЕХНИЧЕСКИЙ УНИВЕРСИТЕТ, КАФЕДРА ФИЗИЧЕСКОЙ ЭЛЕКТРОНИКИ.

I. Introduction

The principal step in the practical application of millimeter and submillimeter waves is connected with the discovery of the mechanism of coherent radiation of electron oscillators rotating in a constant magnetic field [1]. This mechanism underlies operation of devices named cyclotron-resonance masers (CRMs) or gyrodevices. Unique possibilities of gyrodevices allowed to achieve megawatt-level power in millimeter wavelength range and to obtain high power in submillimeter and terahertz ranges, which is much more than the power of conventional vacuum microwave devices, such as magnetrons, klystrons, travelling wave tubes and others. Gyrotrons became essential tools in controlled fusion experiments for the purposes of plasma heating and electron current drive. A high-power electron cyclotron system operating at 170 GHz planned for the ITER tokamak should be mentioned as an example of such application. This system consists of up to 26 gyrotrons. The specification for each gyrotron is to generate 1 MW or more during thousands of seconds. Gyrotrons are also used in material processing, particle acceleration, spectroscopy,

radar systems, etc (see, e. g., [2, 3]).

In a gyrotron, the megawatt power level can be achieved on condition that its subsystems operate in a regime of extreme heat load. Therefore, the efficiency and limiting capabilities of the electron-optical system, the microwave cavity, the radiation output unit and the collector determine total efficiency and maximum achievable parameters of a gyrotron. Typically, the efficiency of high-power gyrotrons does not exceed 30 – 35 % without depressed collectors [4]. One of the basic problems of high-power gyrotrons is to form a high-quality helical electron beam (HEB). The «classical» electron-optical system of gyrodevices consists of the magnetron-injection gun (MIG) and the region of growing magnetic field where the transverse energy of electrons increases. This system is used for the formation of a hollow beam with small electron orbits in a wide range of gyrotron operation. In a well designed and aligned system, the main factor of beam quality deterioration is connected with the action of the self-field of electron space charge resulting partially from non-uniformities of electron emission and from the development of various types of parasitic space-charge instabilities [5]. One of them is the low-frequency instability developing in the cloud of electrons reflected from the magnetic mirror and accumulated in the trap between the cathode and the cavity. This instability should be avoided because the reflection of electrons from the mirror and the development of parasitic low-frequency oscillations (LFOs) in the trapped space charge are the main obstacles for gyrotron operation in high pitch factor regimes and for the achievement of high gyrotron efficiency.

An integrated theoretical and experimental study of low-frequency collective processes in gyrotron electron beams and of the effect of these processes on the operation of gyrodevices was performed at SPbSPU [5–12]. New understanding was obtained of the nature of LFOs, of the mechanisms of their excitation and their influence on the HEB characteristics. Methods for suppressing parasitic LFOs by optimizing the distributions of electric and magnetic fields were developed and studied experimentally in a 74.2 GHz, 100 kW gyrotron. The data on influence of cathode emission non-uniformities on the HEB characteristics allowed formulating the requirements for gyrotron cathodes needed for effective operation of high-power gyrotrons. Currently, the mentioned investigations continue in the frames of the laboratory headed by Prof. F. Wagner [13]. Our activity in the laboratory also concerns developing effective methods aimed at determination of the HEB characteristics in gyrotrons and at the development of cold field emitters for high-frequency gyrotrons. In this paper, we present the current status of gyrotron research in this laboratory.

II. Improvement of the Electron Beam Quality and Enhancement of Gyrotron Efficiency

One of the developed methods for suppressing LFOs is based on the optimization of the electric field distribution in the MIG region [14]. This method was advanced by using a special control electrode insulated from the cathode unit. With this electrode it is possible to regulate the electric field distribution directly in an operating gyrotron.

A. Trajectory Analysis of the MIG with a Control Electrode

In the simulations we have tested the electron-optical system of the SPbSPU gyrotron with the following operating-regime parameters: the accelerating voltage U_0 = 30 kV, the beam current I_b = 10 A, the cavity magnetic field B_0 = 2.75 T, and the magnetic compression ratio B_0/B_c = 18 (B_c is the cathode magnetic field). A part of the cathode unit in the region above the emissive strip was replaced by a control electrode. The distribution of electric field in the gun was varied by regulating the voltage U_{cont} between the control electrode and the cathode. The EGUN code was used in the 2D simulation procedure.

The key parameter determining intensity of parasitic LFOs is the coefficient of electron reflection from the magnetic mirror that can be changed by varying the pitch factor α, the transverse velocity spread $\delta v_\perp$, and the shape of the velocity distribution function $F(v_\perp)$ [10]. For fixed values of U_0, I_b, B_0, B_0/B_c, the increase of voltage U_{cont} in the range from −12 to +5 kV, as resulted from the simulations, causes an increase of both α and $\delta v_\perp$. Fig. 1 shows the

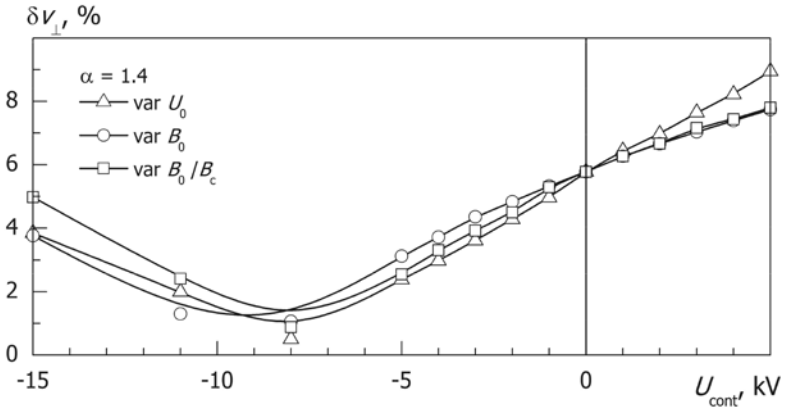

Fig. 1. Transverse velocity spread $\delta v_\perp$ (rms-value) as a function of control electrode voltage U_{cont} for the pitch factor maintaining at $\alpha = 1.4$ by the adjustment of voltage U_0, magnetic field B_0, and compression ratio B_0/B_c

dependencies $\delta v_\perp (U_{cont})$ calculated for the pitch-factor $\alpha = 1.4$. This value of α was maintained by varying one of the parameters U_0, B_0 or B_0/B_c. As follows from Fig. 1, the optimization of the electric field distribution by regulating the control electrode voltage allows to improve electron beam quality due to the reduction of the velocity spread component induced by dc space charge in the MIG region. Applying the optimal negative voltage to the control electrode can provide regimes of gyrotron operation with high pitch factors and without parasitic LFOs, which are promising for the achievement of high gyrotron efficiency.

B. Experiments on Suppression of LFOs in the Gyrotron with a Multi-Sectional Control Electrode

The measurements were made in the SPbSPU gyrotron equipped with a set of diagnostic tools for determining the HEB characteristics, specifically the distributions of emission current density on the cathode surface, electron energy spectra in the collector region, and characteristics of low-frequency dynamic processes in the electron space charge [10]. The MIG design discussed above was implemented in this tube. In the experimental version, the control electrode consists of four sections shifted one from another in azimuthal direction (Fig. 2). These sections are electrically isolated. Therefore, it is possible to regulate the electric field distribution in the gun region by varying the potentials of these sections.

The intensity of parasitic LFOs was measured at the operating values of the working parameters U_0, I_b, B_0, B_0/B_c and at different values of the potentials of the control electrode

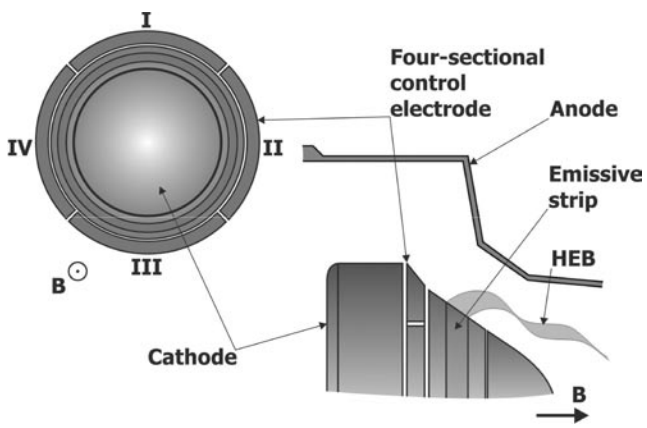

Fig. 2. Schematic drawing of the SPbSPU gyrotron gun region

sections. In the case of connected sections, the electric field distribution is azimuthally quasi-uniform. For this scheme we observed the growth of the oscillation intensity with increasing control voltage, which can be generally explained by increasing both the pitch factor and the velocity spread (see the data of the simulations). Additional suppression of LFOs (in comparison with the scheme of connected sections) was achieved when the azimuthal distribution of electric field correlated with the azimuthal distribution of the cathode emission current density $j_e(\theta)$. The distribution $j_e(\theta)$ for the studied emitter was similar to the distributions described in [10] and was characterized by reduced emission from the cathode area equal to approximately a quarter of the circumference of the emissive strip. This reduced emission was caused by an inhomogeneity in the heating of the emitter due to a gap in the cathode heater winding. The reduction of the emission current density results in a decrease of potential depression owing to the electron space charge and in an increase of the pitch factor and reflection from the mirror for the electrons emitted from this area. Section I of the control electrode (see Fig. 2) was located near the cathode area with reduced emission. As an example, we can indicate the following regime providing the high quality HEB: the cathode potential $\varphi_c = -30$ kV, the potential of Section I $\varphi_I = -29$ kV, the potential of the other sections $\varphi_{II\text{-}IV} = -26$ kV. For this regime the LFOs amplitude was the same as for the initial regime without control voltage ($\varphi_{I\text{-}IV} = \varphi_c$). However, the calculated pitch factor was higher ($\alpha = 1.5$ and 1.4, respectively). Improvement of the HEB quality is thought to be the result of the decrease of the velocity spread caused by the cathode emission non-uniformity. Additionally, the mechanism of LFOs suppression due to the losses of the trapped electrons by their interception with the control electrode can also play a role [14].

C. Experiments on the Enhancement of Gyrotron Efficiency

In the next experiments the influence of potentials of the control sections on gyrotron output power and efficiency was studied. The measurements were made with a LaB_6 cathode being characterized byrelatively high emission uniformity (emission spread $\delta j_e < 25$ %). For this cathode the maximum value of gyrotron efficiency at the main $TE_{12,3}$ mode was about 42 % in the absence of any control voltage. Such a high efficiency was caused by suppression of the parasitic LFOs due to the optimization of the electric and magnetic field distributions [11]. Controlling the electric field distribution with the control electrode allowed to obtain further enhancement of the gyrotron efficiency. Fig. 3 shows the dependencies of the efficiency η on the cavity magnetic field B_0 in the zone of the $TE_{12,3}$ mode for the control voltages $U_{cont} = 0$ and -5 kV (the scheme of connected control sections). The regime with $U_{cont} = -5$ kV was characterized by reduced LFOs amplitude, which allowed to increase the average pitch factor in HEB by increasing the compression ratio. This resulted in an enhancement of the efficiency. The maximum achievable value of η is equal to

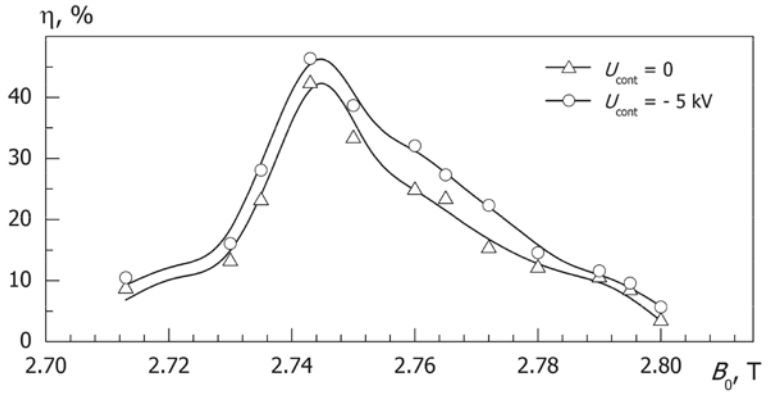

Fig. 3. Efficiency η at the main $TE_{12,3}$ mode as a function of magnetic field B_0 for different control electrode voltage U_{cont} ($U_0 = 30$ kV, $I_b = 9$ A, $B_0/B_c = 18.35$)

~ 46 % (see Fig. 3). At present, the experiments on the enhancement of the gyrotron efficiency by the optimization of the electric field distribution are in progress.

III. Diagnostics of Helical Electron Beam in Gyrotrons

A. X-Ray Diagnostics

Bremsstrahlung X-rays produce at the collector can be used for the definition of electron energy distributions in gyrotrons and other microwave devices with high-energy electron beams. Knowledge of the energy distributions in electron beams can be helpful in the solution of various practical problems, e. g. for benchmarking computer codes, for the control of beam adjustment accuracy (if spatially resolved data on electron spectra are available), for the development of depressed collector systems, and so on. The diagnostic technique is based on processing X-ray spectra measured with a spectrometer placed outside the gyrotron [15, 16]. This method is relatively inexpensive in realization and non-disturbing.

Successful proof-of-principle experiments were performed at the Karlsruhe Institute of Technology (Germany) with the 2 MW, 170 GHz coaxial cavity short-pulse (< 10 ms) pre-prototype ITER gyrotron and with the 1 MW multi-frequency (100–140 GHz) tunable gyrotron for the ASDEX Upgrade ECH system. In the multi-frequency gyrotron, the X-ray spectrometer was placed beyond the 2-mm-thick aluminum window and collected photons elastically scattered in the aluminum layer. This layout allowed us to obtain spectra of bremsstrahlung X-rays averaged over the complete collector surface.

Then the gyrotron was operated in a low-current regime without any significant rf fields, and all electrons reached the collector with the same energy corresponding to the accelerating voltage, the measured X-ray spectra were in very good agreement with basic theory, i. e. with Kramers' law and exponential attenuation of low-energy photons in aluminum (Fig. 4). This confirmed the correct performance of the technique and the equipment in use.

In the regimes of normal gyrotron operation electron energy was partially spent for mm-wave pumping and the measured bremsstrahlung spectra were different. Fig. 5, *a* shows a typical X-ray spectrum measured in the presence of MW-level output power at the voltage of 85 kV, the beam current of 45 A, and the output power of 750 kW. The dashed lines given for comparison represent analytical approximations of the X-ray spectra measured in low-current regimes at $U = 62$ kV and 87 kV. The electron energy distribution reconstructed from the X-ray spectrum is shown in Fig. 5, *b*. We collected the electron energy spectra for different regimes of the multi-frequency gyrotron, which yielded helpful information about its performance.

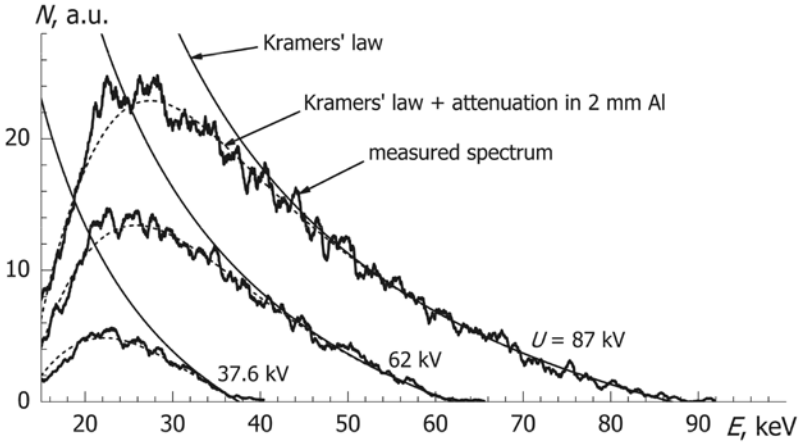

Fig. 4. Bremsstrahlung spectra $N(E)$ measured in low-current regimes without rf oscillations at different accelerating voltages U.
Good agreement of the measured spectra with basic theory (dash lines) confirms the consistency of the data

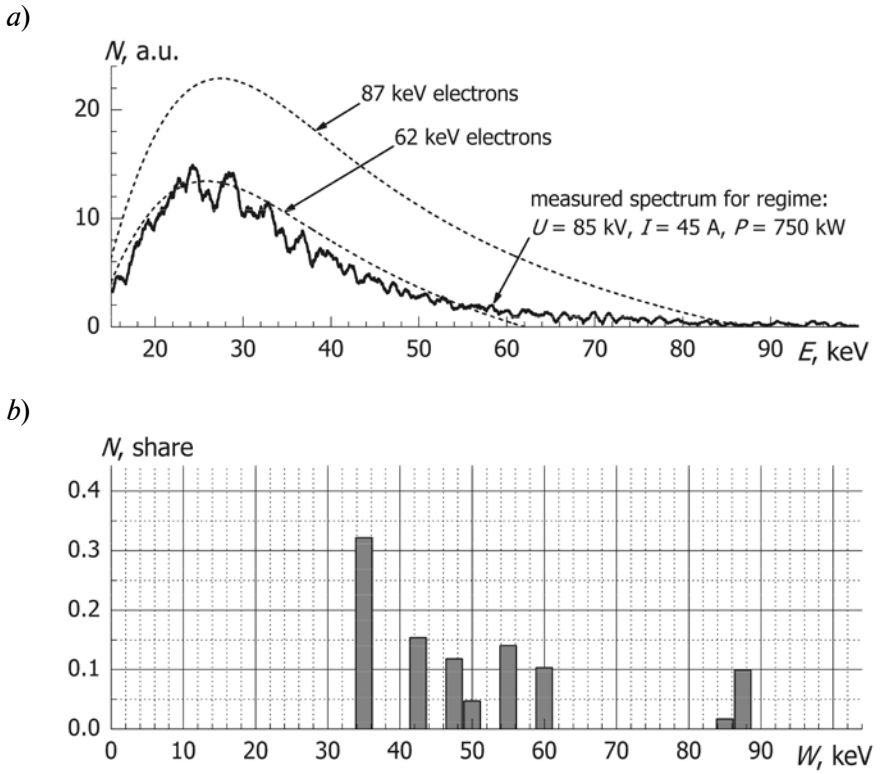

Fig. 5. X-ray spectrum $N(E)$ measured in the presence of mm-wave oscillations and basic functions (analytical approximation of measured spectrum) for 62 keV and 87 keV electrons (*a*). Electron energy distribution $N(W)$ calculated from the given measured X-ray spectrum (*b*)

The performed testing experiments confirmed that the bremsstrahlung-based diagnostics of energy distributions in electron beams can be successfully applied to high-power gyrotrons. Experience from these experiments can be used for adaptation of this diagnostics to the geometry and operating regimes of a particular gyrotron.

B. Microwave Diagnostics

Another diagnostic method is aimed at the determination of electron velocities in the region before HEB entering the microwave cavity. Data on average pitch factor and velocity spread in this region are very important for the determination of the efficiency of the energy transformation from electrons to the rf field in the cavity. Analytical and numerical calculations show the possibility to obtain information about the axial velocity distribution of electrons on the base of frequency dependencies of the gain of a GHz signal propagating in a special slow-wave structure located in the beam formation region. The slow-wave structure in the form of a diaphragmatic waveguide (Fig. 6) was designed to implement this diagnostics for the determination of electron velocities in the SPbSPU gyrotron. The set of calculated de-

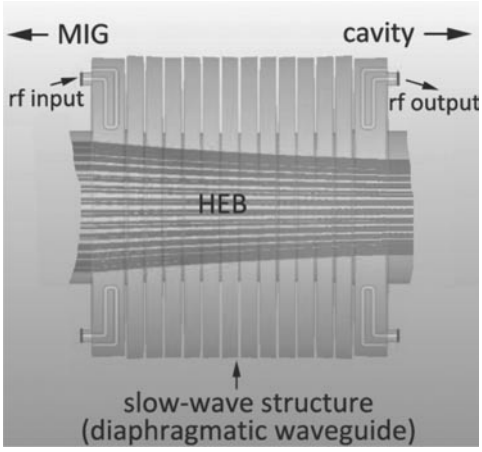

Fig. 6. Schematic drawing of the beam formation region between the gun and the cavity with the slow-wave structure

pendencies of gain on frequency varying in the range 5 – 6 GHz were obtained for different HEB parameters of this gyrotron. The data of the numerical simulations will be used as basis for processing corresponding dependencies in future experiments.

IV. Conclusion

The gyrotron research performed at SPbSPU is aimed at the enhancement of gyrotron efficiency and the development of new methods for helical electron beam diagnostics. The acquired knowledge and developed technical solutions can be used for the next generation of effective high-power gyrotrons, used in controlled fusion experiments. The following investigations are planned in the continuation of the performed gyrotron research as reported in this paper:

1. Development of methods for effective recuperation of electron energy in gyrotrons with depressed collector. Study of the possibility to achieve enhanced gyrotron efficiency resulting from both improvement of HEB quality and energy recovery in the collector region.

2. Application of new diagnostic methods for the investigation of electron energy spectra in the working regimes of high-power gyrotrons using X-ray diagnostics, and for the determination of velocity characteristics of electrons in the SPbSPU gyrotron using microwave diagnostics.

This work was supported by the Ministry of Education and Science of the Russian Federation (contract 11.G34.31.0041) and by the Russian Foundation for Basic Research (grant 11-02-01442).

REFERENCES

1. **Gaponov A.V.** Interaction between electron fluxes and electromagnetic waves in waveguides. *Izv. Vuzov. Radiofizica*, 1959, vol. 2, No. 3, pp. 450–462. (rus)

2. Applications of high-power microwaves. Ed. by A.V. Gaponov-Grekhov, V.L. Granatstein. Norwood, MA, Artech House, 1994. 364 p.

3. **Nusinovich G.S.** Introduction to the physics of gyrotrons. Baltimore, MD, Johns Hopkins University Press, 2004. 352 p.

4. **Thumm M.** State-of-the-art of high power gyro-devices and free electron masers, update 2010. KIT Scientific Report 7575. Karlsruhe Institute of Technology, 2011. 124 p.

5. **Louksha O.I., Samsonov D.B., Sominskii G.G., Semin S.V.** Dynamic Processes in Helical Electron Beams in Gyrotrons. *Technical Physics*, 2013, vol. 58, No. 5, pp. 751–759.

6. **Louksha O.I., Sominski G.G.** Space-temporal characteristics of collective processes in helical electron beams of gyrotron-type systems. *Zhurnal Tekhnicheskoi Fiziki*, 1995, vol. 65, No. 2, pp. 198–202. (rus)

7. **Borzenkov D.V., Luksha O.I.** Numerical simulation of space-charge dynamics in a gyrotron trap. *Technical Physics*, 1997, vol. 42, No. 9, pp. 1071–1074.

8. **Kas'yanenko D.V., Louksha O.I., Piosczyk B., Sominskij G.G., Thumm M.** Low-frequency parasitic space-charge oscillations in the helical electron beam of a gyrotron. *Radiophysics and Quantum Electronics*, 2004, vol. 47, No. 5-6, pp. 463–470.

9. **Louksha O.I., Piosczyk B., Sominski G.G., Thumm M., Samsonov D.B.** Suppression of parasitic space-charge oscillations in a gyrotron. *Radiophysics and Quantum Electronics*, 2006, vol. 49, No. 10, pp. 793–798

10. **Louksha O.I., Piosczyk B., Sominski G.G., Thumm M., Samsonov D.B.** High-power gyrotrons for controlled fusion systems and technology: search for ways to enhancement of efficiency. *Izv. RAN. Energetika*, 2006, No. 5, pp. 131–146. (rus)

11. **Louksha O.I., Samsonov D.B., Sominski G.G., Piosczyk B., Thumm M.K.** Experimental study of gyrotron efficiency enhancement by improvement of electron beam quality. *Conference Digest Joint 32nd Int. Conf. Infrared and Millimeter Waves, and 15th Int. Conf. Terahertz Electronics*, Cardiff, UK, Sept. 3–7, 2007. pp. 880–881.

12. **Luksha O.I.** Simulation of low-frequency collective processes in gyrotron electron beams. *Radiophysics and Quantum Electronics*, 2009, vol. 52, No. 5-6, pp. 386–397.

13. **Wagner F., Sergeev V.Yu., Goncharov P.R.** The Research Laboratory of the Physics of Advanced Tokamaks of the St. Petersburg State Polytechnical University. *St. Petersburg State Polytechnical University Journal: Physics and Mathematics*, 2013, No. 4-2(182), pp. 30–37.

14. **Louksha O.I., Samsonov D.B., Sominskii G.G., Tsapov, A.A.** Improvement of the helical electron beam quality and the gyrotron efficiency by controlling the electric field distribution near a magnetron injection gun. *Technical Physics*, 2012, vol. 57, No. 6, pp. 835–839.

15. **Arkhipov A.V., Dvoretskaya N.V., Kern St., Louksha O.I., Sominski G.G.** Reconstruction

of energy spectra of electrons bombarding a solid target. *St. Petersburg State Polytechnical University Journal: Physics and Mathematics*, 2012, No. 1(141), pp. 68–73. (rus)

16. **Arkhipov A., Dvoretskaya N., Gantenbein G., Kern S., Louksha O., Rzesnicki T., Samartsev A., Sominski G.** Reconstruction of energy distributions in electron beams on the basis of bremsstrahlung X-ray spectra. *IEEE Trans. Plasma Science*, 2013, vol. 41, No. 10, pp. 2786–2789.

СПИСОК ЛИТЕРАТУРЫ

1. **Гапонов А.В.** Взаимодействие непрямолинейных электронных пучков с электромагнитными волнами в линиях передачи // Известия вузов. Радиофизика. 1959. Т. 2. № 3. С. 450–462.

2. Applications of high-power microwaves. Ed. by A.V. Gaponov-Grekhov, V.L. Granatstein. Norwood, MA, Artech House, 1994. 364 p.

3. **Nusinovich G.S.** Introduction to the physics of gyrotrons. Baltimore, MD, Johns Hopkins University Press, 2004. 352 p.

4. **Thumm M.** State-of-the-art of high power gyro-devices and free electron masers, update 2010. KIT Scientific Report 7575. Karlsruhe Institute of Technology, 2011. 124 p.

5. **Лукша О.И., Самсонов Д.Б., Соминский Г.Г. Сёмин С.В.** Динамические процессы в винтовых электронных потоках гиротронов// Журнал технической физики. 2013. Т. 83. Вып. 5. С. 132–140.

6. **Лукша О.И., Соминский Г.Г.** Пространственно-временные характеристики коллективных процессов в винтовых электронных пучках систем гиротронного типа // Журнал технической физики. 1995. Т. 65. Вып. 2. С. 198–202.

7. **Борзенков Д.В., Лукша О.И.** Численное моделирование динамики пространственного заряда в ловушке гиротрона// Журнал технической физики. 1997. Т. 67. Вып. 9. С. 98–102.

8. **Касьяненко Д.В., Лукша О.И., Пиосчик Б., Соминский Г.Г., Тамм М.** Низкочастотные паразитные колебания пространственного заряда в винтовом электронном пучке гиротрона// Известия вузов. Радиофизика 2004. Т. 47. № 5-6. С. 463–470.

9. **Louksha O.I., Piosczyk B., Sominski G.G., Thumm M., Samsonov D.B.** Suppression of parasitic space-charge oscillations in a gyrotron. *Radiophysics and Quantum Electronics*, 2006, vol. 49, No. 10, pp. 793–798.

10. **Лукша О.И., Пиосчик Б., Соминский Г.Г., Тамм М., Самсонов Д.Б.** Мощные гиротроны для систем управляемого термоядерного синтеза и технологии: поиск путей повышения эффективности // Известия РАН. Энергетика. 2006. № 5. С. 131–146.

11. **Louksha O.I., Samsonov D.B., Sominski G.G., Piosczyk B., Thumm M.K.** Experimental study of gyrotron efficiency enhancement by improvement of electron beam quality. *Conference Digest Joint 32nd Int. Conf. Infrared and Millimeter Waves, and 15th Int. Conf. Terahertz Electronics*, Cardiff, UK, Sept. 3–7, 2007. pp. 880–881.

12. **Luksha O.I.** Simulation of low-frequency collective processes in gyrotron electron beams. *Radiophysics and Quantum Electronics*, 2009, vol. 52, No. 5-6, pp. 386–397.

13. **Wagner F., Sergeev V.Yu., Goncharov P.R.** The Research Laboratory of the Physics of Advanced Tokamaks of the St. Petersburg State Polytechnical University. *St. Petersburg State Polytechnical University Journal: Physics and Mathematics*, 2013, No. 4-2(182), pp. 30-37.

14. **Louksha O.I., Samsonov D.B., Sominskii G.G., Tsapov, A.A.** Improvement of the helical electron beam quality and the gyrotron efficiency by controlling the electric field distribution near a magnetron injection gun. *Technical Physics*, 2012, vol. 57, No. 6, pp. 835–839.

15. **Архипов А.В., Дворецкая Н.В., Керн Ш., Лукша О.И., Соминский Г.Г.** Определение энергетического спектра электронов, бомбардирующих твердотельную мишень // Научно-технические ведомости СПбГПУ. Физико-математические науки. 2012. № 1 (141). С. 68–73.

16. **Arkhipov A., Dvoretskaya N., Gantenbein G., Kern S., Louksha O., Rzesnicki T., Samartsev A., Sominski G.** Reconstruction of energy distributions in electron beams on the basis of bremsstrahlung X-ray spectra. *IEEE Trans. Plasma Science*, 2013, vol. 41, No. 10, pp. 2786–2789.

ЛУКША Олег Игоревич – *доктор физико-математических наук, доцент кафедры физической электроники Санкт-Петербургского государственного политехнического университета.*

195251, Россия, Санкт-Петербург, Политехническая ул., 29

louksha@rphf.spbstu.ru

СОМИНСКИЙ Геннадий Гиршевич – *доктор физико-математических наук, профессор кафедры физической электроники Санкт-Петербургского государственного политехнического университета.*
195251, Россия, Санкт-Петербург, Политехническая ул., 29
sominski@rphf.spbstu.ru

АРХИПОВ Александр Викторович – *кандидат физико-математических наук, доцент кафедры физической электроники Санкт-Петербургского государственного политехнического университета.*
195251, Россия, Санкт-Петербург, Политехническая ул., 29
arkhipov@rphf.spbstu.ru

ДВОРЕЦКАЯ Наталья Владиславовна – *ведущий инженер кафедры физической электроники Санкт-Петербургского государственного политехнического университета.*
195251, Россия, Санкт-Петербург, Политехническая ул., 29
nat@rphf.spbstu.ru

САМСОНОВ Дмитрий Борисович – *кандидат физико-математических наук, инженер кафедры физической электроники Санкт-Петербургского государственного политехнического университета.*
195251, Россия, Санкт-Петербург, Политехническая ул., 29
dima_samsonov@bk.ru

СЁМИН Сергей Владимирович – *студент кафедры физической электроники Санкт-Петербургского государственного политехнического университета.*
195251, Россия, Санкт-Петербург, Политехническая ул., 29
starosta2094@mail.ru

ВАГНЕР Фридрих – *заведующий исследовательской лабораторией физики улучшенного удержания плазмы токамаков Санкт-Петербургского государственного политехнического университета, почетный директор Института физики плазмы им. Макса Планка, Германия (Director Emeritus of the Max-Planck-Institut für Plasmaphysik)*
195251, Россия, Санкт-Петербург, Политехническая ул., 29
fritz.wagner@ipp.mpg.de

UDC 53.047

D.N. Artamonov, V.V. Korzhova, O.L. Vlasova, I.B. Bezprozvanny

St. Petersburg State Polytechnical University,
29 Politekhnicheskaya St., St. Petersburg, 195251, Russia

OPTOGENETIC APPROACH ALLOWS CONTROLLING MORPHOLOGICAL PARAMETERS OF DENDRITIC SPINES IN CORTICO-STRIATAL CO-CULTURE

Д.Н. Артамонов, В.В. Коржова, О.Л. Власова, И.Б. Безпрозванный

ОПТОГЕНЕТИЧЕСКИЙ ПОДХОД ДЛЯ КОНТРОЛЯ МОРФОЛОГИЧЕСКИХ ПАРАМЕТРОВ ДЕНДРИТНЫХ ШИПИКОВ В КОРТИКО-СТРИАТНОЙ КУЛЬТУРЕ

Optogenetics is a unique technique that allows controlling the physiological condition within single cell or specific cell population, including controlling individual neuron activity. In the present work optogenetics has been applied to control the morphology and density of synaptic connections between striatal and cortical neurons in mixed cortico-striatal co-culture system. Different methods for visualization of medium spiny neurons dendritic spines have been compared. Studying synaptic dysfunction is necessary for understanding both normal physiology of brain and pathological mechanisms in different neurodegenerative diseases. The described approach could be utilized in a numerous biomedical applications.

OPTOGENETICS, DENDRITIC SPINES, SYNAPTIC TRANSMISSION, NEURONAL CULTURE.

Оптогенетика – современный подход, позволяющий манипулировать физиологическим состоянием отдельных нейронов. В данной работе оптогенетический подход был применен для контроля морфологических параметров дендритных шипиков, образуемых между нейронами коры и стриатума в смешанной кортико-стриатной культуре. Также было проведено сравнение различных методов визуализации дендритных шипиков средних шипиковых нейронов стриатума в культуре. Изучение синаптических взаимодействий нейронов является важным для понимания как нормального функционирования нервной системы, так и понимания механизмов патологии. Данный подход может найти широкое применение в биомедицинских исследованиях.

ОПТОГЕНЕТИКА, ДЕНДРИТНЫЕ ШИПИКИ, СИНАПТИЧСКАЯ ПЕРЕДАЧА, КУЛЬТУРА НЕЙРОНОВ.

I. Introduction

All neurons communicate to each other through contacts called synapses. Synapses are sites of neuronal contacts that transmit chemical and electrical signals in the brain [1]. Total number of spines could be estimated as high as 10^{14}. Most synapses could be divided into two types. Inhibitory GABAergic (*gamma*-aminobutyric acid) synapses are the first. The second are excitatory glutamatergic synapses. Dendritic spines are small protrusions on dendritic shaft where excitatory synapses are located. Dendritic spines exhibit morphological changes after various physiological or pathological impacts. Spines shape demonstrates a high level of heterogeneity. Modification of this shape could be the morphological basis for synaptic plasticity. Synapses and dendritic spines are dynamic structures whose plasticity is considered to be the basis of learning and memory [2–4].

Several studies show that different spine shapes could have significantly different influ-

ence on brain function. Changing in the number of spines and morphology of individual spines recently has been connected to several neurological disorders. Different authors are discussing this connection at Alzheimer Disease [5, 6]. Recent paper [7] shows that multiple autism-linked genes lead to synapse elimination in autism mouse-model. Synaptic density is also connected to the progress of Parkinson disease [8] and different neuropsychiatric disorders e. g. schizophrenia and depression [9, 10]. Dendritic spine changes are also associated with normal aging [11]. However, in spite of numerous studies of structural changes of neurons and dendritic spines morphology during normal aging and pathological processes, the functional properties of these changes remain poorly understood. Synapse strength is closely correlated with dendritic spine morphology, and synaptic activity regulates spine shape and density during brain development, learning and aging.

Postsynaptic spines are usually classified into three groups according to their morphological properties. Mushroom spines have a large head and a fine neck; thin spines have a smaller head and a narrow neck; stubby spines have no obvious distinction between the head size and the attachment to the dendritic shaft.

Narrow necks observed in thin and mushroom spines serve for calcium compartmentalization and other second messenger molecules. Therefore, these types of spine could play a significant role in synaptic plasticity. The spine head of mushroom spines is much larger than in other spines, indicating that membrane dynamics and receptor turnover occur. Mushroom spines usually are suggested as memory storage sites. Taken together, these observations suggest that each spine shape is playing a particular role in neuronal function [12].

The study of synaptic connections is the key to understanding the functioning of neural circuits. At present, information on contacts between neurons is obtained mainly from electrical stimulation studies, which don't allow precise control of neuronal activity and also disturb nearby cells. However, recently developed optogenetics technique [13–15] allows modulating the electrical activity of neurons, modifying the strength of synaptic connections and functional analysis of the interaction between neurons.

Optogenetics is the method of studying cells by genetically introducing photosensitive components which could modify the properties of the cell in response to illumination with a certain wavelength light beam. This requires expression of specific proteins – opsins, which are light activated ion channels or pumps. Two of the most usually employed opsins are channelrhodopsin ChR2 [13] and halorodopsin NpHR [16]. ChR2 is a member of light-activated cation channels which allow photodepolarizing the membrane and activating the cells. Halorhodopsin, on the other hand, is a light-driven anionic pump selective for chloride ions, and it is used for photohyperpolarization and thus inactivation of cells. Upon delivery of the opsin gene using genetic engineering in a neuron, the light-sensitive channels appear on the plasma membrane, and the cell itself becomes photosensitive. The interesting fact is that these two opsins have maximum absorption spectrum at different wavelengths thereby allowing using them at the same time. During the exposure of blue light channelrodopsin opens (maximum absorption – 470 nm), which in turn causes the movement of positive ions into the cell, allowing the neuron membrane depolarization and generation of action potentials. When the orange light activates halorodopsin (absorption maximum – 580 nm), the neuronal membrane is hyperpolarizing, causing inhibition of the neuron. High temporal resolution of the optogenetics method allows precise regulation of synaptic events and is, therefore, an important tool to study interneuron connections. The most convenient model for such studies is an *in vitro* culture of neurons forming synaptic contacts *in vivo*, e. g. a mixed culture of neurons from the cortex and striatum.

The aim of this study was to adapt optogenetic approach to modify the strength of synaptic connections between cortical cells and medium spiny neurons (MSN) in the cortico-striatal mixed neuronal culture.

II. Methods

A. Neuronal Culture

In the present work mixed cortico-striatal cultures were prepared. Dissociated cultures

were established as previously described [17]. Briefly, striata and cortices of P0-P1 WT pups were dissected, digested with papain, dissociated and plated on poly-D-lysine (Sigma) coated 12 mm coverslips in Neurobasal-A medium (Invitrogen) supplemented with 2 % B27 (Gibco), 5 % FBS (Gibco), 1mM glutamine (Invitrogen) and kept at 37 °C in a 5 % CO_2 incubator. Cortices from a single brain were used to plate 9 wells, and striata from a single brain were used to plate 3 wells (1 : 3 cortical to MSN ratio; density $4 \cdot 10^5$ cells/well). Cultures were incubated for 14–21 days. For the optogenetics studies we used modified protocol allowing gene delivery in the specific neuronal population. On the first day dissociated culture of cortical neurons from neonatal mouse brain were prepared. Cultures were kept at 37 °C in 5 % CO_2 for one day. To achieve opsin expression in neurons, we used viral delivery system. On the second day of culturing, the cells were transfected using the lentiviral construct containing the channelrodopsin or halorodopsin gene fused with GFP. On the third day striatal intact neurons were plated on top of the cortical culture Thus, striatal and cortical neurons in the culture were differed by opsin gene expression that can be identified by expression of GFP in cortical neurons. The virus has previously been produced in HEK293T cell line according to the protocol. Viral delivery system allows achieving high levels of opsin expression in the cell culture several days later.

B. Immunochemistry

For immunocytochemical staining two primary antibodies were used: rabbit antibodies against neuronal marker MAP2 (Cell Signalling Technology), and mouse antibodies against the MSN marker DARPP32 (Cell Signalling Technology); secondary antibodies: anti- rabbit and mouse with fluorophores Alexa Fluor 488 and 593 (Invitrogen). Cells were fixed with 4 % paraformaldehyde and stained at 15 day *in vitro*. After staining cells were analyzed with the confocal microscope Zeiss LSM 700. For further morphology analysis, the sequence of micrographs of dentritic shafts and spines with an interval of 0.15 m in depth forming a three-dimensional image of neurons were obtained. Immersion lens with a 100-fold magnification was utilized, resolution of the image was 1024×1024 pixels. 3-dimensional images were obtained with Zeiss software ZEN 2011 Black edition.

C. Lucifer Yellow Dye Injection

Coverslips with mixed live neuronal cultures were placed in a Warner chamber of patch-clamp setup (Olympus IX71 microscope). During the experiment cells were placed in artificial cerebrospinal fluid containing the following (in mM): 85 NaCl, 24 $NaHCO_3$, 25 glucose, 2.5 KCl. The glass electrodes for dye injection were pulled from borosilicate glass capillary tubes (Sutter) using the Sutter Instruments P97. The electrode resistance ranged between 150 – 300 MΩ when filled with PBS. MSNs were selected visually under the microscope and patched with the electrodes filled with Lucifer yellow (L-12926, Invitrogen). Dye injection was performed by application of a constant negative current in the range of 500 – 800 pA for 10 min (Multiclamp 700B, Molecular Devices). Five neurons were injected in each coverslip. Neuron culture was then immediately fixed in 4 % PFA – sucrose. Injected neurons were analyzed by confocal imaging (Zeiss) with 100× lens magnification.

D. Transfection of Neurons

For morphology analysis of spines expression of dsTomato in neurons was achieved through calcium-phosphate transfection of plasmid encoding this protein. Transfection was performed as previously described at DIV 9 – 12 [18]. Neuron culture was incubated with Ca-containing solution of the plasmid (1 mg) until clearly visible precipitate was formed. Then the precipitate was being dissolved in acidified medium Neurobasal-A (Invitrogen) for 30 min and washed with culture medium without FBS. Transfected neurons were incubated for 14 – 19 days at 37 °C and 5 % CO_2, and used for morphology analysis 2 – 5 days after transfection.

E. Optical Stimulation

For optogenetic activation of opsins, pulses of light were generated. Coverslips with neuronal culture were placed under the microscope. Halogen arc lamp directly coupled to

the microscope light path was used as a source of light. Pulses of blue light (470 nm optical filter) and orange light (590 nm optical filter) were generated using Uniblitz shutter.

F. Morphological Analysis of Spines

Each image has a maximum resolution of 1024 × 1024 pixels. Approximately 10 neurons were analyzed for each coverslip. At least 10 coverslips from 4 – 5 cultures were utilized for each experiment. The secondary apical dendrites of medium spiny neurons were selected for taking images.

Morphological analysis was performed with Neuron Studio software [19], which automatically reconstructs a three-dimensional image of spines and distributes them into three groups (mushroom, thin, stubby) by several parameters. We used the following parameters: min stubby size – 50, non-stubby – 20, neck ratio – 1.1, thin ratio – 1.5, mushroom size – 0.35. The distribution density of spines was defined as the average number of spines per 10 um.

III. Results

Cortico-striatal co-culture model system was used as a simple and relevant *in vitro* model of synaptic connections between two populations of neurons. Study of changes in corticostriatal synaptic connections and dendritic spine morphology could be considered as signs of dysfunction.

Cultured neurons are the primary model system for studying the basic mechanisms regulating neuronal morphological structure and function.

A. MSN Spine Visualization Methods Comparison

First objective of present work was establishing the most convenient method of spine analysis and quantification in medium spiny neurons in culture. The most common method of spine analysis is Goldgi staining. However, this technique does not allow seeing the differences between spine types. The main focus of this part was establishing a relevant method of spine shape analysis. For our study, we tested three other methods. These include immunocytochemistry, dsTomato transfection and dye injection into live neurons.

All these methods allow visualization of three types of dendritic spines and perform confocal 3-D analysis of images. During the immunochemistry procedure, cells were fixed at DIV 14–15 and then stained against DARPP-32. Tomato transfection was performed at DIV 9–12 with live cultured neurons. After transfection, cells were kept in the incubator until DIV 14–15 and then fixed. For dye injections live neurons were also utilized at DIV 14–15. During this experiment, cells were kept out of incubator in CSF for about 30 min and then immediately fixed.

Spines of MSNs are very sensitive to any external impact. So, two methods performed with live neurons – transfection and dye injection – seriously affected both spine density and spine distribution between different spine types. Images were obtained 24 hours after tomato transfection. Spines were eliminated after transfection. Mean spine density in dsTomato transfected neurons was almost twice less than in immunostained culture. Despite the fact that this method is a standard for hippocampal neurons in culture, tomato transfection causes serious damage for MSNs spines and seems to be an absolutely inappropriate method for morphological analysis.

At the same time, the spine morphology in MSNs in culture was studied using Lucifer yellow injection technique. In Fig. 1 we compare the spine morphology data obtained by different methods in the same batch of cultures – immunocytochemistry and Lucifer yellow dye injections – using patch pipettes. MSNs suffer from dramatic decrease of mushroom spines after dye injection (10 min of injection). Analysis of spines after dye injections showed little decrease in the number of spines in culture compared to the culture immunostained against DARPP-32 protein. Also Lucifer yellow injection method shows altered ratio of spine types with mushroom spine decrease and thin and stubby spines increase. During the dye injection, neuron membrane becomes damaged. Additional stress for a cell during this procedure is a small negative current required for dying to spread out within the cell. However, this method affects spine density to a lesser degree than transfection. These results indicate that mushroom spines are transforming into other

a) anti-DARPP32 immunostaining

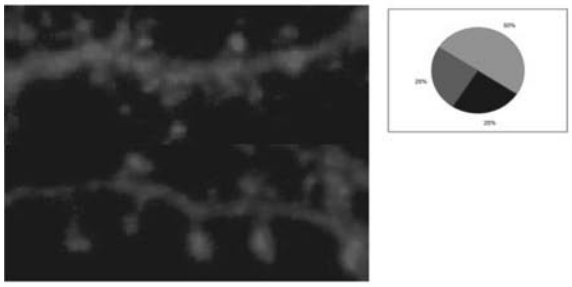

b) Lucifer-yellow dye injection

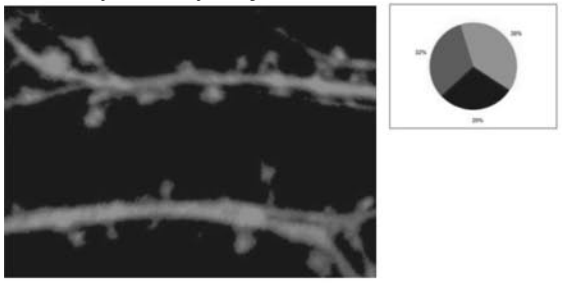

c) Tomato transfection

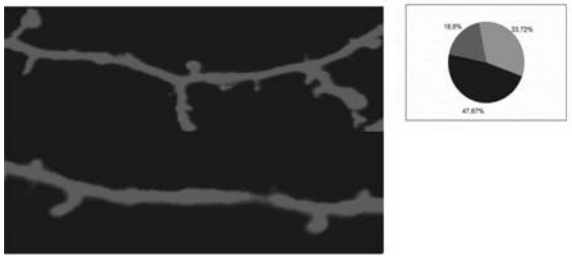

d) Spine density

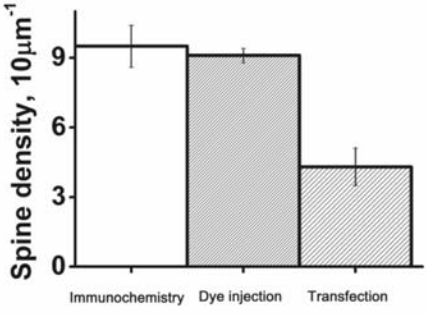

Fig. 1. Spine morphology of MSNs determined by immunocytochemistry (*a*), Lucifer yellow dye injection (*b*) and Tomato transfection (*c*). In the diagram: mushroom – light grey, thin – dark grey, stubby – black. Spine density analyzed after all methods (*d*). Error bars indicate standard deviation

types during these stressful conditions.

Overall, only the most nonperturbative method – immonocytochemistry – allows performing spine shape analysis with minimum impact on neuron health and dendritic spines.

B. Optogenetics Manipulation with Spine Morphology

Previously, we pointed out that cortical neurons in the culture immediately respond hyper- and depolarization after rhodopsins activation in orange and blue light, respectively [17]. MSN of the striatum has not expressed channelrodopsin. However, during activation of cortical neurons with blue light, hyperactivity was registered in MSNs.

Recorded activity of MSNs was completely blocked by addition of an inhibitor of AMPA receptor inhibitor DNQX. This indicates that nerve impulse transmission between MSNs and cortical neurons occurs through synaptic contacts.

One of the most important indicators of the strength and activity of synapses is their morphology, mainly – the head size of dendritic spines (this parameter is positively correlated with the amount of AMPA-receptors on postsynaptic terminal). It is known that the activation of synaptic connections between neurons increases the sizes of spines [20].

In a series of experiments we demonstrated the ability to change the strength of synaptic connections between neurons – dendritic spines – in response to exposition to the light of a certain wavelength. In this case, culture protocol was established as follows. On the first day dissociated culture of cortical neurons from neonatal mouse brain was prepared. On the second day the cells in the culture were transfected using the lentiviral construct containing halorodopsin gene fused with GFP. On the third day striatal intact neurons were plated on the top of the cortical culture. Thus halorodopsin expression was only confirmed in cortical neurons. GFP-labeling allows easy identification of cortical cells with fluorescent microscope.

For selective targeting the cells of interest we used whole-field illumination. Importantly, applying our updated protocol for gene delivery via lenti-viral systems, we were able to transfect only cortical neurons and the remains of striatal neurons unaffected and therefore insensitive either to blue or orange light.

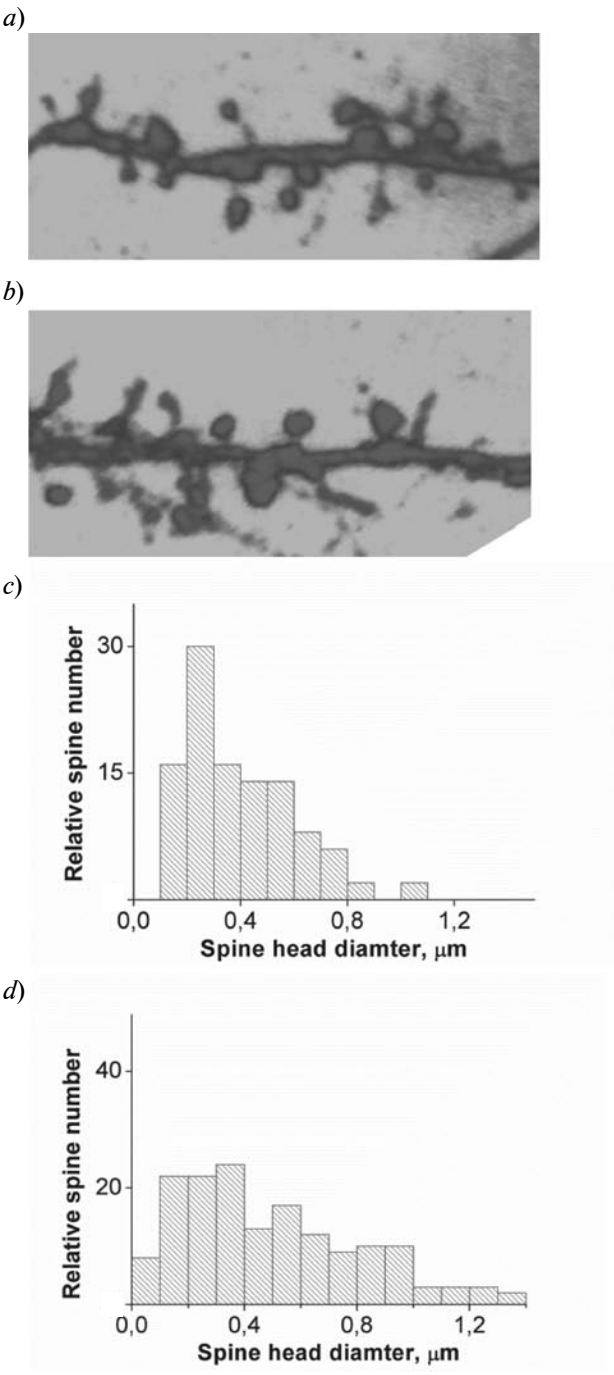

Fig. 2. Dendritic spine morphology of MSNs before (*a*) and after (*b*) optical activation of cortical neurons for 20 min at DIV 14; spine head distribution before (*c*) and after (*d*) blue light exposure

To analyze the functional significance of optogenetically induced activity of cortical neurons, quantitative evaluation of spine morphology changes at the postsynaptic side was performed. In a series of experiments we demonstrated the ability to change the synaptic connections between neurons and synapses when they were exposed to light of a certain wavelength. Dendritic spines of MSNs where most of the synapses are localized has been studied in a confocal microscope after immunocytochemical staining of neurons against striatum specific protein DARPP-32, so only medium spiny neurons were considered for spine quantification. Images were analyzed using the Neuron Studio.

It was found that the excitation of ChR2-expressing cortical neurons with a blue light for 20 minutes caused MSN spines increase in size (Fig. 2) indicating the benefit of physiologically significant impact on synaptic contacts with this method. Head diameter of mushroom spines was quantified, distribution of this parameter is presented in Fig. 2, *c*, *d*.

Thus, in this part of work we showed that in a mixed cortico-striatal coculture functional synaptic connections between cortical neurons and MSNs could be modulated by optogenetics.

In the next series of experiments mixed culture of neurons was exposed to orange light for over 45 min, then cells were immediately fixed in 4 % formaldehyde solution. Previously we demonstrated that during orange light irradiation electrical activity disappeared in both cortical neurons and MSN on the post-synaptic side [17].

We inhibited the activity of cortical neurons with optogenetics, using halorhodopsin. Transfection procedure was similar as described above. Only cortical neurons were infected with virus containing Halo-GFP plasmid. Orange light exposure silences cortical cells. As a result, MSNs demonstrate inhibiting activity. After 20 and 45 min of continuous orange light irradiation, cells were fixed and stained against DARPP-32 for spine analysis. Data is presented in Fig. 3. As it is shown here, MSN spines are sensitive to the long exposure. We observed a decrease of spine density in MSN only after 45 min. However, after 20 min MSN all spines survived and demonstrated no change by types. Activation of halorhodopsin did not inhibit all the activity of the cells. Several spikes could be observed under orange light. So we suppose

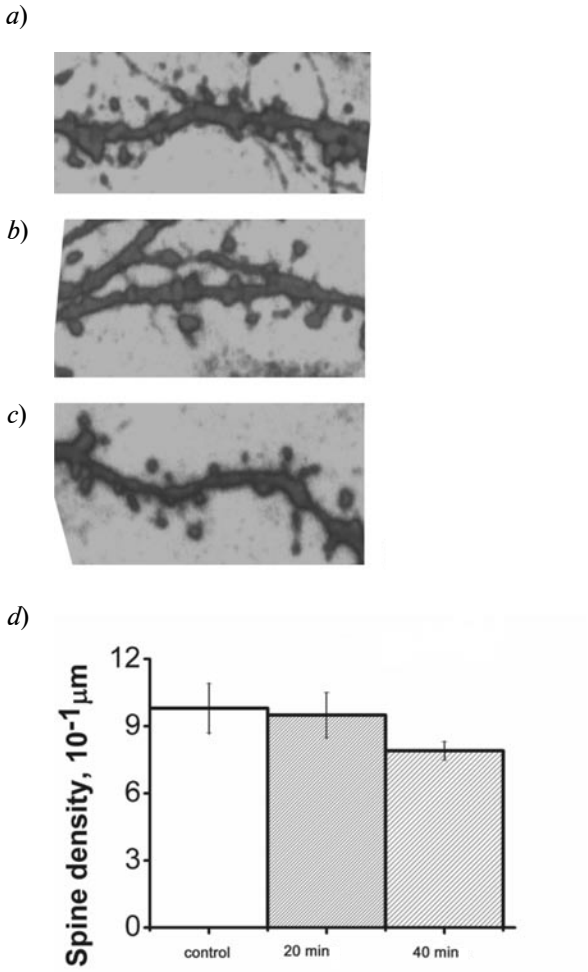

Fig. 3. MSN spines morphology (*a* – *c*) and spine density (*d*) before (*a*) and after (*b*, *c*)orange light exposure – 20 and 45 min. DIV 15. Error bars indicate standard deviation

that this residual activity from cortical cells is enough to maintain spines during short period of inhibition.

IV. Conclusion

Overall, we demonstrated an optical approach to controlling dendritic spine morphology using neurons expressing different opsins. This versatile method can be applied to studying the role of dendritic spines in live cultured neurons using widefield fluorescence or confocal microscopy. Cultures prepared from transgenic mouse models are primary model systems to study almost every neurodevelopmental and neurodegenerative disease. Future directions include optogenetic manipulation with dendritic spines in living animals modeling different diseases. This will require production of high-efficient LEDs and lasers in a clean room for material fabrication. While using these powerful light sources, it will be possible to activate or inhibit neurons directly in living brain. Thus, the precise speed and accuracy of optogenetics spine control, as compared to spine modification with different drugs, is absolutely necessary for studying the complicated mechanisms underlying normal and aberrant dendritic spine role in progress of neurological disorder as well as in normal aging.

This work was supported by grants FCKP Kadri («Научные и научно-педагогические кадры инновационной России» на 2009–2013 годы) –

№ 2012-1.1-12-000-1002-1101, соглашение №14. B37.21.0121 и 2012-1.2.2-12-000-1014-5674, соглашение № 14.B37.21.0219, and Russian Federation government grant (Грант государственной поддержки научных исследований, проводимых под руководством ведущих ученых в российских образовательных учреждениях высшего профессионального образования), № 11.G34.31.0056.

REFERENCES

1. **Edwards F.A.** Anatomy and electrophysiology of fast central synapses lead to a structural model for long-term potentiation. *Physiol. Rev.,* 1995, Vol. 75, pp. 759–787.

2. **Holtmaat A., Svoboda K.** Experience-dependent structural synaptic plasticity in the mammalian brain. *Nat. Rev. Neurosci.,* 2009, Vol. 10, pp. 647–658.

3. **Kasai H., Fukuda M., Watanabe S., Hayashi-Takagi A., Noguchi J.** Structural dynamics of dendritic spines in memory and cognition. *Trends Neurosci.,* 2010, Vol. 33, pp. 121–129.

4. **Alvarez V.A., Sabatini B.L.** Anatomical and physiological plasticity of dendritic spines. *Annu. Rev. Neurosci,* 2007, Vol. 30, pp. 79–97.

5. **Yu W., Lu B.** Synapses and dendritic spines as pathogenic targets in alzheimer's disease. *Neural Plasticity,* 2012, Vol. 2012, Article ID 247150, doi:10.1155/2012/247150.

6. **Popugaeva E., Supnet C., Bezprozvanny I.** Presenilins, deranged calcium homeostasis, synaptic loss and dysfunction in alzheimer's disease. *Messenger,* 2012, Vol. 1, pp. 53–62.

7. **Tsai N.P., Wilkerson J.R., Guo W., Maksimova M.A., DeMartino G.N., Cowan C.W., Huber K.M.** Multiple autism-linked genes mediate synapse elimination via proteasomal degradation of a synaptic scaffold PSD-95. *Cell,* 2012, Dec 21, Vol. 151(7), pp. 1581–1594. doi: 10.1016/j.cell.2012.11.040.

8. **Pienaar I.S., Burn D., Morris C., Dexter D.** Synaptic protein alterations in Parkinson's disease. *Mol. Neurobiol.*, 2012, Vol. 45(1), pp. 126–143. doi: 10.1007/s12035-011-8226-9. Epub 2011 Dec 29.

9. **Glantz L.A., Lewis D.A.** Decreased dendritic spine density on prefrontal cortical pyramidal neurons in schizophrenia. *Arch. Gen. Psychiatry*, 2000, Vol. 57(1), pp. 65–73.

10. **Penzes P., Cahill M.E., Jones K.A., VanLeeuwen J.E., Woolfrey K.M.** Dendritic spine pathology in neuropsychiatric disorders. *Nat. Neurosci,* 2011, Vol. 14(3), pp. 285–293.

11. **Dickstein D.L., Weaver C.M., Luebke J.I., Hof P.R.** Dendritic spine changes associated with normal aging. *Neuroscience,* 2012, Oct. 13. pii: S0306-4522(12)01009-3. doi: 10.1016/j.neuroscience.2012.09.077.

12. **Bourne J., Harris K.M.** Do thin spines learn to be mushroom spines that remember? *Curr. Opin. Neurobiol.*, 2007, 17(3):381–386.

13. **Boyden E.S., Zhang F., Bamberg E., Nagel G., Deisseroth K.** Millisecond-timescale, genetically targeted optical control of neural activity. *Nat. Neurosci.*, 2005, Vol. 8(9), pp. 1263–1268.

14. **Fenno L., Yizhar O., Deisseroth K.** The development and application of optogenetics. *Annu. Rev. Neurosci.,* 2011, Vol. 34, pp. 389–412. doi: 10.1146/annurev-neuro-061010-113817.

15. **Aston-Jones G., Deisseroth K.** Recent advances in optogenetics and pharmacogenetics. *Brain Res.* 2013, Feb 17. pii: S0006-8993(13)00100-5. doi: 10.1016/j.brainres.2013.01.026. [Epub ahead of print].

16. **Han X., Boyden E.S.** Multiple-color optical activation, silencing, and desynchronization of neural activity, with single-spike temporal resolution. *PLoS One.* 2007. Vol. Mar. 21;2(3):e299.

17. **Artamonov D., Korzhova V., Wu J., Rybalchenko P., Im C., Krasnoborova V., Vlasova O., Bezprozvanny I.** Characterization of synaptic dysfunction in an *in vitro* corticostriatal model system of Huntington's disease. *Bio Membranes*, 2013, Vol. 30(4), pp. 1–13.

18. **Jiang M., Chen G.** High Ca^{2+} phosphate transfection efficiency in low-density neuronal cultures. *Nature Protocols.* 2006. Vol. 1(2), pp. 695–700.

19. **Rodriguez A., Ehlenberger D.B., Dickstein D.L., Hof P.R., Wearne S.L.** Automated three-dimensional detection and shape classification of dendritic spines from fluorescence microscopy images. *PLoS One.* 2008, Vol. 3(4): e1997 doi:10.1371/ journal.pone. 0001997.

20. **Sheng M., Kim M.J.** Postsynaptic signaling and plasticity mechanisms. *Science.*, 2002, Vol. 298(5594), pp. 776–80.

СПИСОК ЛИТЕРАТУРЫ

1. **Edwards F.A.** Anatomy and electrophysiology of fast central synapses lead to a structural model for long-term potentiation. *Physiol. Rev.,* 1995, Vol. 75, pp. 759–787.

2. **Holtmaat A., Svoboda K.** Experience-dependent structural synaptic plasticity in the mammalian brain. *Nat. Rev. Neurosci.,* 2009, Vol. 10, pp. 647–658.

3. **Kasai H., Fukuda M., Watanabe S., Hayashi-Takagi A., Noguchi J.** Structural dynamics of dendritic spines in memory and cognition. *Trends Neurosci.,* 2010, Vol. 33, pp. 121–129.

4. **Alvarez V.A., Sabatini B.L.** Anatomical and physiological plasticity of dendritic spines. *Annu. Rev. Neurosci,* 2007, Vol. 30, pp. 79–97.

5. **Yu W., Lu B.** Synapses and dendritic spines as pathogenic targets in alzheimer's disease. *Neural Plasticity,* 2012, Vol. 2012, Article ID 247150, doi:10.1155/2012/247150.

6. **Popugaeva E., Supnet C., Bezprozvanny I.** Presenilins, deranged calcium homeostasis, synaptic loss and dysfunction in alzheimer's disease. *Messenger,* 2012, Vol. 1, pp. 53–62.

7. **Tsai N.P., Wilkerson J.R., Guo W., Maksimova M.A., DeMartino G.N., Cowan C.W., Huber K.M.** Multiple autism-linked genes mediate synapse elimination via proteasomal degradation of a synaptic scaffold PSD-95. *Cell,* 2012, Dec 21, Vol. 151(7), pp. 1581–1594. doi: 10.1016/j.cell.2012.11.040.

8. **Pienaar I.S., Burn D., Morris C., Dexter D.** Synaptic protein alterations in Parkinson's disease. *Mol. Neurobiol.*, 2012, Vol. 45(1), pp. 126–143. doi: 10.1007/s12035-011-8226-9. Epub 2011 Dec 29.

9. **Glantz L.A., Lewis D.A.** Decreased dendritic spine density on prefrontal cortical pyramidal neurons in schizophrenia. *Arch. Gen. Psychiatry*, 2000, Vol. 57(1), pp. 65–73.

10. **Penzes P., Cahill M.E., Jones K.A., VanLeeuwen J.E., Woolfrey K.M.** Dendritic spine pathology in neuropsychiatric disorders. *Nat. Neurosci,* 2011, Vol. 14(3), pp. 285–293.

11. **Dickstein D.L., Weaver C.M., Luebke J.I., Hof P.R.** Dendritic spine changes associated with normal aging. *Neuroscience,* 2012, Oct. 13. pii: S0306-4522(12)01009-3. doi: 10.1016/j.neuroscience.2012.09.077.

12. **Bourne J., Harris K.M.** Do thin spines learn to be mushroom spines that remember? *Curr. Opin. Neurobiol.*, 2007, 17(3):381–386.

13. **Boyden E.S., Zhang F., Bamberg E., Nagel G., Deisseroth K.** Millisecond-timescale, genetically targeted optical control of neural activity. *Nat. Neurosci.*, 2005, Vol. 8(9), pp. 1263–1268.

14. **Fenno L., Yizhar O., Deisseroth K.** The development and application of optogenetics. *Annu. Rev. Neurosci.,* 2011, Vol. 34, pp. 389–412. doi: 10.1146/annurev-neuro-061010-113817.

15. **Aston-Jones G., Deisseroth K.** Recent advances in optogenetics and pharmacogenetics. *Brain Res.* 2013, Feb 17. pii: S0006-8993(13)00100-5. doi: 10.1016/j.brainres.2013.01.026. [Epub ahead of print].

16. **Han X., Boyden E.S.** Multiple-color optical activation, silencing, and desynchronization of neural activity, with single-spike temporal resolution. *PLoS One.* 2007. Vol. Mar. 21;2(3):e299.

17. **Artamonov D., Korzhova V., Wu J., Rybalchenko P., Im C., Krasnoborova V., Vlasova O., Bezprozvanny I.** Characterization of synaptic dysfunction in an *in vitro* corticostriatal model system of Huntington's disease. *Bio Membranes*, 2013, Vol. 30(4), pp. 1–13.

18. **Jiang M., Chen G.** High Ca^{2+} phosphate transfection efficiency in low-density neuronal cultures. *Nature Protocols.* 2006. Vol. 1(2), pp. 695–700.

19. **Rodriguez A., Ehlenberger D.B., Dickstein D.L., Hof P.R., Wearne S.L.** Automated three-dimensional detection and shape classification of dendritic spines from fluorescence microscopy images. *PLoS One.* 2008, Vol. 3(4): e1997 doi:10.1371/ journal.pone. 0001997.

20. **Sheng M., Kim M.J.** Postsynaptic signaling and plasticity mechanisms. *Science.*, 2002, Vol. 298(5594), pp. 776–80.

АРТАМОНОВ Дмитрий Николаевич – *кандидат биологических наук, научный сотрудник Лаборатории молекулярной нейродегенерации Санкт-Петербургского государственного политехнического университета.*

195251, Россия, Санкт-Петербург, Политехническая ул., 29
artdmitrii@gmail.com

КОРЖОВА Виктория Валерьевна – *лаборант Лаборатории молекулярной нейродегенерации Санкт-Петербургского государственного политехнического университета.*

195251, Россия, Санкт-Петербург, Политехническая ул., 29
viktoria.korzhova@gmail.com

ВЛАСОВА Ольга Леонардовна – *доктор физико-математических наук, доцент, директор Научно-образовательного центра «Фундаментальные основы медицинских и биомедицинских технологий» Санкт-Петербургского государственного политехнического университета.*

195251, Россия, Санкт-Петербург, Политехническая ул., 29
olvlasova@yandex.ru

БЕЗПРОЗВАННЫЙ Илья Борисович – *доктор биологических наук, заведующий лабораторией молекулярной нейродегенерации Санкт-Петербургского государственного политехнического университета.*

195251, Россия, Санкт-Петербург, Политехническая ул., 29
mnlabspb@gmail.com

UDC 538.915

L.G. Gerchikov

St. Petersburg State Polytechnical University,
29 Politekhnicheskaya St., St. Petersburg, 195251, Russia

ELECTRON-ION SCATTERING AND PLASMON DAMPING IN METALLIC CLUSTERS

Л.Г. Герчиков

ЭЛЕКТРОН-ИОННОЕ РАССЕЯНИЕ И ПЛАЗМОННОЕ ЗАТУХАНИЕ В МЕТАЛЛИЧЕСКИХ КЛАСТЕРАХ

Processes of electron scattering on fine ionic structure leading to the decay of dipole plasmon oscillations in alkali metal clusters are investigated. The study is based on separation of the collective plasmon oscillations and single particle excitations. Coupling between these two types of electronic motions caused by electron-ion scattering leads to the plasmon damping. The relative contributions of elastic and inelastic electron-ion scattering to plasmon linewidth are considered. The results are compared with experimental data on cluster photoabsorption for sodium clusters of different size.

CLUSTER, PLASMON, SCATTERING, OSCILLATION, EXCITATION, DAMPING.

Исследована роль электрон-ионного рассеяния в затухании коллективных плазмонных возбуждений в кластерах щелочных металлов. Теоретическая модель основана на разделении коллективных плазмонных возбуждений электронов кластера, соответствующих осцилляциям центра масс электронов, и одночастичных электронных возбуждений в системе их центра масс. Перемешивание этих типов движения электронов вследствие электрон-ионного рассеяния ведет к затуханию плазмонных колебаний. Оценены сравнительные вклады упругого и неупругого электрон-ионного рассеяния в уширение плазмонного резонанса. Результаты сравниваются с экспериментальными данными по ширинам плазмонных резонансов в спектрах фотопоглощения кластеров натрия.

КЛАСТЕР, ПЛАЗМОН, РАССЕЯНИЕ, КОЛЕБАНИЕ, ВОЗБУЖДЕНИЕ, ЗАТУХАНИЕ.

I. Introduction

The optical response of alkali-metal clusters is dominated by the surface dipole plasmon resonance [1, 2]. This collective electronic excitation corresponds to a coherent oscillation of the electronic cloud against the positively charged ionic background, i. e. to the vibration of electronic center of mass (CM). The position and the width of giant plasmon resonance has been experimentally determined for various sodium clusters in numerous experimental works on cluster spectroscopy [3–8]. An adequate theoretical prediction for the resonance position has been given within the Linear Response theory using either the Time Dependent Local Density Approximation (TDLDA) [9–11] or the Random Phase Approximation with Exchange (RPAE) [12–14]. However, in spite of intensive study, the fundamental questions concerning the origin of plasmon decay width is still not well understood.

In the first attempts to evaluate the plasmon resonance width, the nonhomogeneous broad-

ening of electron energy levels due to the thermal fluctuation of the cluster background has been considered [15–24]. This mechanism of the line broadening is connected with adiabatic dependence of electron energy upon the position of the ions. Therefore, the corresponding linewidth is not connected with the life time of electron excitations. The obtained plasmon width decreases with the cluster radius growth. This fact is easy to understand since the role of such adiabatic electron-ion coupling diminishes with the increase of cluster size vanishing in the bulk limit. On the other hand, the experimentally observed resonance width does not monotonically decrease as a function of cluster size. On the contrary, it periodically varies due to the shell effects in the range of $0.2 - 0.3$ eV [8]. Therefore, this contribution to the resonance width can be essential only for the very small clusters with less than tens of atoms.

Another approach considers the decay of collective plasmon mode via excitations of the single-particle electronic transitions [25]. This mechanism is well known in the theory of collective fermionic excitations in nuclear and plasma physics as Landau damping. The main question for Landau damping mechanism is the origin of the coupling interaction that is responsible for the relaxation of plasmon mode excitation energy among numerous electronic degrees of freedom. Indeed, for example, in the case of the homogenous infinite positive cluster background there is not such coupling interaction at all, and electron cloud can oscillate with plasmon frequency against positive background without any perturbation of its intrinsic motion and therefore without any damping. Therefore, possible relaxation of the collective plasmon excitation can be expected from the deviation of ionic background potential in real cluster from a pure homogenous positive infinite jellium, namely from the fine ionic structure and the cluster boarder.

The boarder of the cluster background has been traditionally considered in the past as the main source of the coupling interaction [25]. Electron scattering on the spherical cluster border leads to well-known inverse radius dependence of Landau damping width [26–28], $\Gamma = Cv_F/R$, where R is the cluster radius, v_F is the Fermi velocity of cluster valence electrons and C is a constant about one unit. However, this result is valid only for the relatively large clusters with more than thousand atoms, and this has been proved by a direct numerical calculations [29]. This simple formula is based on the assumption that the spectrum of dipole electron excitations is continuous and therefore it cannot be applied to the small metallic clusters with less than hundred atoms [28]. Indeed, for such small clusters, which will be considered in the present paper, the use of this formula strongly overestimates experimentally observed plasmon width [8].

Therefore, one can associate the plasmon width with electron scattering on the fine ionic structure. In the resent paper we propose a simple transparent analytical model in order to clarify the physical nature of the plasmon damping caused by electron-ion scattering. Our model is developed with the use of a new description of the collective plasmon excitation based on the separation of the center of mass (CM) and the intrinsic motion of delocalized valence electrons [30]. The method relies on the smallness of the CM oscillation amplitude compared to the cluster radius.

Considering the electron-ionic collisions, one can distinguish elastic electron-ion scattering and inelastic scattering on the ionic vibrations, phonons when the plasmon decay is accompanied by simultaneous emission or absorption of phonons. The last case has been studied in our previous paper [31]. Electron-phonon coupling yields the temperature dependent plasmon width that for the 100 K clusters amounts approximately to one fourth of the total plasmon width.

The present paper is focused on the elastic electron-ion scattering. We use the pseudopotential to describe the electron scattering on an isolated sodium atom and the simple Fermi gas model to describe the intrinsic single-particle excitations. For simplicity we consider only the spherical sodium clusters.

II. Collective Plasmon Mode

To distinguish the dipole plasmon mode from all other electron excitations it is convenient to separate the intrinsic and the CM electron coordinates. We will start with the total electron Hamiltonian of the cluster which

includes the electron kinetic energy, the energy of interelectronic Coulomb interaction and interaction with ionic background:

$$\widehat{H} = \sum_a \frac{\widehat{p}_a^2}{2} + \frac{1}{2}\sum_{a\neq b}\frac{1}{|\mathbf{r}_a - \mathbf{r}_b|} + \sum_a V_{ion}(\mathbf{r}_a), \quad (1)$$

where $V_{ion}(\mathbf{r})$ is the potential of ionic background, the summation is performed over all the cluster valence electrons.

Let us designate the CM vector by $\mathbf{R}$ and the intrinsic electron coordinates, i. e. the electron coordinates in CM reference frame, by $\mathbf{r}'_a$:

$$\mathbf{R} = \frac{1}{N}\sum_a \mathbf{r}_a, \quad \mathbf{r}'_a = \mathbf{r}_a - \mathbf{R}, \quad (2)$$

where N is the number of valence electrons.

Similarly, the momentum of the center of mass motion is equal to $\widehat{\mathbf{P}} = \sum_a \hat{\mathbf{p}}_a$ and electronic momenta in the CM reference frame are $\widehat{\mathbf{p}}'_a = \hat{\mathbf{p}}_a - \widehat{\mathbf{P}}/N$ respectively. We separate the intrinsic and CM coordinates in Eq. (1) assuming that the amplitude of CM displacement $\mathbf{R}$ is much smaller than the cluster radius R_0 (we will demonstrate below that this condition is usually fulfilled). Radius of the cluster background we determine by standard expression $R_0 = r_s N_{at}^{1/3}$ [9, 11] using the Wigner – Seitz radius r_s of the bulk material ($r_s = 4$ a.u. for sodium) and the number of atoms in a cluster. So we can expand the potential of the ionic background $V_{ion}(\mathbf{r}'_a + \mathbf{R})$ in Eq.(1) in power series with respect to $\mathbf{R}$, and the total electron Hamiltonian (1) can be written as:

$$\widehat{H} = \widehat{H}' + \frac{\widehat{P}^2}{2N} + U(\mathbf{r}'_a, \mathbf{R}), \quad (3)$$

where $U(\mathbf{r}'_a, \mathbf{R})$ is alteration of V_{ion} under the displacement of the CM:

$$U(\mathbf{r}'_a, \mathbf{R}) = \sum_a (V_{ion}(\mathbf{r}_a) - V_{ion}(\mathbf{r}'_a)) = \\ = \sum_{n=1,a} \frac{1}{n!}(\mathbf{R}\nabla)^n V_{ion}(\mathbf{r}'_a). \quad (4)$$

Operator $\widehat{H}'$ is the Hamiltonian of intrinsic motion. It has the form of the total Hamiltonian (1) with natural replacement of all electronic coordinates and momenta by corresponding values in CM system.

Let us start with zero approximation which implies that CM and intrinsic electron motions are completely independent. This approximation is based on the following simple fact. Within the standard jellium model [9, 11] which treats the ionic background as the positive charge density $\rho_i = 3/4\pi r_s^3$ homogeneously distributed throughout the entire cluster volume, for sufficiently large cluster the coordinates of CM and intrinsic motion separate. Indeed, neglecting the electrons outside the cluster volume, i. e. the spill out electrons, and using the condition $\sum_a \mathbf{r}'_a = 0$, one immediately finds that

$$U(\mathbf{r}'_a, \mathbf{R}) = (4\pi\rho_i / 3)R^2 / 2$$

and does not depend upon the intrinsic electron coordinates. Therefore, the CM oscillates in a pure parabolic potential with Mie frequency $\omega_{Mie} = r_s^{-3/2}$. As a result, one can write the total electron wave function as a product of wave functions of CM and intrinsic motions:

$$\Psi(\mathbf{r}_a) = \Psi(\mathbf{R})\Phi(\mathbf{r}'_a), \quad (5)$$

which assumes that the CM motion does not perturb the intrinsic wave function $\Phi(\mathbf{r}'_a)$, , i. e. the CM oscillates adiabatically with respect to all other electronic degrees of freedom.

According to the standard adiabatic theory [32], the wave function (5) turns out to be the eigen wave function of the total electron Hamiltonian (3). Here the wave function of intrinsic motion $\Phi(\mathbf{r}'_a)$ is the eigen wave function of the intrinsic Hamiltonian $\widehat{H}'$ with corresponding eigen energy ε_ν. The CM wave function $\Psi(\mathbf{R})$ is the eigen wave function of the effective plasmon Hamiltonian obtained as average of the total electron Hamiltonian (3) over intrinsic motion:

$$\widehat{H}_P = \frac{\widehat{P}^2}{2N} + U_{eff}(\mathbf{R}), \quad (6)$$

where the role of effective potential for CM motion $U_{eff}(\mathbf{R})$ is played by the diagonal matrix element of $U(\mathbf{r}'_a, \mathbf{R})$:

$$U_{eff}(\mathbf{R}) = \left\langle \Phi_\nu(\mathbf{r}'_a) \middle| U(\mathbf{r}'_a, \mathbf{R}) \middle| \Phi_\nu(\mathbf{r}'_a) \right\rangle. \quad (7)$$

Let us use the expansion (4) for $U(\mathbf{r}'_a, \mathbf{R})$. All odd terms vanish after the averaging over intrinsic wave function $\Phi_\nu(\mathbf{r}'_a)$. The first nonvanishing term corresponds to the pure oscillator potential

$$U_{eff}(\mathbf{R}) = N\frac{\omega_p^2 R}{2}, \ \omega_p^2 = \frac{4\pi}{3N}\int \rho_e \rho_i dV, \quad (8)$$

where ρ_e and ρ_i are the electronic and ionic densities, respectively. Here we consider spherical clusters with isotropic density distributions ρ_e and ρ_i. For homogeneous jellium distribution of ionic background with sharp edge

$$\rho_i = \frac{3}{4\pi r_s^3}\theta(R_0 - r). \quad (9)$$

Eq. (8) gives us

$$\omega_p = \omega_{Mie}\sqrt{1 - \frac{\delta N}{N}}, \quad (10)$$

where δN is the number of spill out electrons.

Thus, within this approximation the electron energy spectrum is given as the sum of intrinsic energies ε_ν and the energies of harmonic oscillations of CM

$$E_{n,\nu} = \varepsilon_\nu + \omega_p\left(n + \frac{1}{2}\right), \quad (11)$$

where n is the quantum number of oscillator state $\Psi_n(\mathbf{R})$, i. e. the number of excited plasmons.

Within the dipole approximation, external electromagnetic laser field acts only on the CM wave function and does not excite the intrinsic motion, i. e. $\nu = 0$. A time dependent electric field simply induces a transition from the 1s ground state to the 1p state of CM motion, ω_p above the ground state. Consequently, the many-body wave function (5) for the single plasmon excitation $|i\rangle$ is the product of this collective harmonic oscillation function $\Psi_{1p}(\mathbf{R})$ and the ground state many-body wave function $\Phi_0(\mathbf{r}'_a)$ depending only on the intrinsic coordinates, thus

$$\langle \mathbf{R}, \mathbf{r}'_a | i\rangle = \Psi_{1p}(\mathbf{R})\Phi_0(\mathbf{r}'_a).$$

The average displacement of the electronic CM for 1p state is equal to $\sqrt{\langle R^2\rangle} = \sqrt{3/2\omega_p N}$. For Na_{92} cluster the ratio $\sqrt{\langle R^2\rangle}/R_0 = 0.02$ and it decreases for the lager clusters as $N^{-5/6}$. This fact confirms the applicability of the performed power expansion (4). Besides the dipole surface plasmon mode, there are a lot of non-optically active excitations $|f\rangle$ of the intrinsic electron motion. In our notations, the corresponding many-electron wave function is written as

$$\langle \mathbf{R}, \mathbf{r}'_a | f\rangle = \Psi_{1s}(R)\Phi_\nu(\mathbf{r}'_a)$$

with the collective wave function being the 1s state of the CM harmonic oscillator and with wave function of intrinsic excitation ν.

III. Plasmon Damping

Within the zero approximation, we neglect the coupling terms in the total electron Hamiltonian Eqs. (3), (4) which cause the transitions between plasmon $|i\rangle$ and intrinsic $|f\rangle$ excitations. Formally, this coupling originates from the non-diagonal matrix elements of $U(\mathbf{r}'_a, \mathbf{R})$. The first term of the expansion $U(\mathbf{r}'_a, \mathbf{R})$ (4) provides the leading contribution to the coupling. Therefore, below we will keep only this coupling term in the expansion (4):

$$W(\mathbf{r}'_a, \mathbf{R}) = \sum_a (\mathbf{R}\nabla)V_{ion}(\mathbf{r}'_a). \quad (12)$$

This term corresponds to the additional time-dependent electromagnetic field arising in the CM system due to the plasmon oscillations. Note that within the jellium model potential $W(\mathbf{r}'_a, \mathbf{R})$ actually coincides with the well-known separable approximation for electron-electron interaction between dipole plasmon excitation and single particle electronic excitations in cluster [25]. The total Hamiltonian of the cluster $\hat{H}$ (3) now can be written as

$$\hat{H} = \hat{H}'(\mathbf{r}'_a) + \hat{H}_P(\mathbf{R}) + W(\mathbf{r}'_a, \mathbf{R}), \quad (13)$$

where $W(\mathbf{r}'_a, \mathbf{R})$ couples plasmon $|i\rangle$ and intrinsic $|f\rangle$ excitations.

The relaxation of plasmon excitation originates from the electronic transitions from optically excited state $|i\rangle$ to all possible final states $|f\rangle$ caused by the coupling term $W(\mathbf{r}'_a, \mathbf{R})$ in Hamiltonian Eq. (13). The rate of such transitions, i. e. the corresponding plasmon width Γ, we will calculate using the first-order time-dependent perturbation theory:

$$\Gamma = 2\pi\sum_f \left|\langle f | W(\mathbf{r}'_a, \mathbf{R}) | i\rangle\right|^2 \delta(\varepsilon_f - \varepsilon_i). \quad (14)$$

The transition matrix element $\langle f | W(\mathbf{r}'_a, \mathbf{R}) | i\rangle$ in Eq.(14) is given by the product of an oscillator matrix element $\langle 1p | \mathbf{R} | 1s\rangle = 1/\sqrt{2N\omega_p}$ [32] and a matrix element of intrinsic motion:

$$\langle f | W(\mathbf{r}'_a, \mathbf{R}) | i\rangle = \frac{\left\langle \Phi_\nu(\mathbf{r}'_a)\left|\frac{d}{dz'}V_{ion}(\mathbf{r}'_a)\right|\Phi_0(\mathbf{r}'_a)\right\rangle}{\sqrt{2N\omega_p}}. \quad (15)$$

Here the axe z is chosen along the direction of plasmon oscillations.

For homogenous infinite positive jellium background, $V_{ion}(\mathbf{r}') = \omega_p^2 r'^2 / 2$, matrix element (15) apparently vanishes. Indeed, in this case $\langle f | W(\mathbf{r}'_a, \mathbf{R}) | i \rangle$ is proportional to the dipole matrix element of the intrinsic motion which equals to zero by the definition of the CM frame. In the real cluster, background potential V_{ion} differs from the pure harmonic pattern due to the fine ionic structure and the cluster border.

To estimate the matrix element $\langle f | W(\mathbf{r}'_a, \mathbf{R}) | i \rangle$ let us assume that the excitation in the intrinsic electronic system is a pure particle-hole transition and that particles and holes inside the cluster are plane waves in the Fermi gas model. We represent the ionic potential V_{ion} as a sum of pseudopotentials v_p of each ion

$$V_{ion}(\mathbf{r}) = \sum_a v_p(\mathbf{r} - \mathbf{R}_a). \qquad (16)$$

Here $\mathbf{R}_a$ denotes the position of the a-th ion.

However, the simple homogeneous Fermi gas model should be improved in order to reproduce the main features of intrinsic excitation in real cluster. Indeed, when we represent the intrinsic excitation in the cluster by a particle-hole transition of the Fermi gas using the plane waves for electronic wave functions, we do not take into account the electron confinement as well as many-body effects. In order to introduce the electron confinement, we will restrict the integration in the matrix element (15) by the cluster sphere. Electron correlation leads to the screening pseudo-potentials by cluster delocalized electrons. We will take into account this many-body effect by using the permittivity of homogeneous Fermi gas. Also the employed model should be corrected in order to correspond to intrinsic excitations. Namely, the dipole matrix element for particle-hole transitions should be zero in the CM frame. Otherwise matrix element $\langle f | W | i \rangle$ is not zero even for the pure harmonic background potential $V_{ion}(\mathbf{r}') = \omega_{Mie}^2 r'^2 / 2$. We will correct this effect by the subtraction the linear term

$$d(\omega_{Mie}^2 r'^2 / 2) / dz' = \omega_{Mie}^2 z'$$

from the operator in the matrix element (15). Within these assumptions, matrix element (15) is written as

$$\langle f | W(\mathbf{r}'_a, \mathbf{R}) | i \rangle = \\ = \frac{1}{\sqrt{2N\omega_p}\,\varepsilon(q)} \int_{r<R_0} e^{iq\mathbf{r}} \left(\frac{dV_{ion}(\mathbf{r})}{dz} - \omega_{Mie}^2 z \right) d\mathbf{r}^3, \qquad (17)$$

where $q = p_e - p_h$ is the moment of electron-hole pair, $\varepsilon(q)$ is the permittivity of homogeneous Fermi gas:

$$\varepsilon(q) = 1 + \frac{4p_F}{\pi q^2}. \qquad (18)$$

It will be convenient to extend the integration in the right hand side of Eq.(17) over the infinite volume. It can be done by the addition and subtraction of the integral of

$$\exp(iq\mathbf{r}) dV_{ion}(\mathbf{r})/dz$$

outside the cluster border, $r > R_0$. For simplicity, outside the cluster where the fine ionic structure is not so important, we will replace the real background potential $V_{ion}(\mathbf{r})$ by the spherical jellium model potential:

$$V_{jell}(\mathbf{r}) = \begin{cases} \frac{\omega_{Mie}^2}{2}(r^2 - 3R_0^2), & r < R_0; \\ -\frac{N}{r}, & r > R_0. \end{cases} \qquad (19)$$

Then the matrix element (17) becomes equal to

$$\langle f | W(\mathbf{r}'_a, \mathbf{R}) | i \rangle = \\ = \frac{q_z}{\sqrt{2N\omega_p}\,\varepsilon(q)} (V_{ion}(\mathbf{q}) - V_{jell}(\mathbf{q})), \qquad (20)$$

where

$$V_{jell}(\mathbf{q}) = \frac{12\pi N}{q^3 R_0} j_1(qR_0) \qquad (21)$$

is the Fourier transform of the jellium potential (j_1 is the spherical Bessel function);

$$V_{ion}(\mathbf{q}) = v_p(\mathbf{q}) F(\mathbf{q}) \qquad (22)$$

is the Fourier transform of the ionic background potential, $v_p(\mathbf{q})$ is the Fourier transform of the pseudo-potential,

$$F(\mathbf{q}) = \sum_{a=1}^{N} e^{i\mathbf{q}\mathbf{R}_a} \qquad (23)$$

is the structure formfactor of the ionic background.

Using Eq.(20) one obtains from Eq.(14):

$$\Gamma = \frac{2\pi}{N\omega_p}\int \frac{d^3p_e d^3p_h}{(2\pi)^6}(p_{e_z} - p_{h_z})^2 \times \\ \times \left|V_{ion}(\mathbf{p}_e - \mathbf{p}_h) - V_{jell}(\mathbf{p}_e - \mathbf{p}_h)\right|^2 \times \\ \times\delta\left(\frac{p_e^2}{2} - \frac{p_h^2}{2} - \omega_p\right). \quad (24)$$

Here we integrate over hole momentum below the Fermi level $p_h < p_F = 1.92/r_s$ and over the electronic momentum above the Fermi sphere $p_e > p_F$.

Note that Eq.(24) does not account for the Landau damping connected with electron scattering on the cluster surface. Indeed, in the case of homogenous jellium background, $V_{ion}(\mathbf{q}) = V_{jell}(\mathbf{q})$, Eq.(24) gives zero width identically. The non-zero result requests more detailed description of electronic wave function near the cluster surface. According to Eq. (15), the coupling matrix element arises in the case of $V_{ion}(\mathbf{q}) = V_{jell}(\mathbf{q})$ from the region of spill-out electrons where in our simple model electron wave function is put equal to zero.

We perform numerical calculations of plasmon linewidth according to Eq.(24) for series of sodium clusters Na_N of different size $8 \le N \le 93$ with forms close to spherical. The results are presented in Fig. 1 by triangles (see curve *2*).

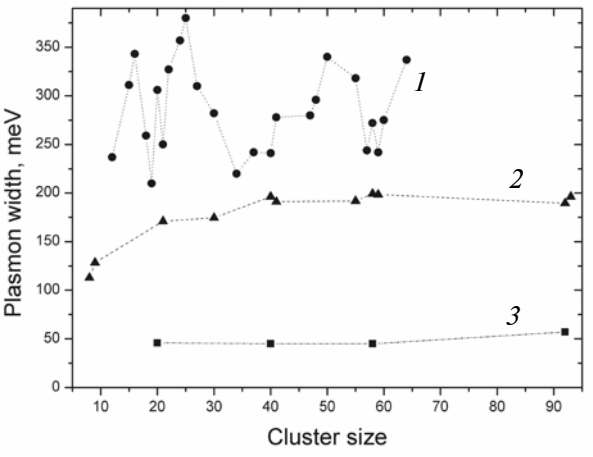

Fig. 1. Plasmon resonance widths in sodium clusters as a function of cluster size: *1* – experimental data on photoabsorption spectra (FWHM); *2*, *3* – the calculated contributions of elastic (*2*) and inelastic (*3*) electron-ion scattering to plasmon width

The following pseudo-potential $v_p(r)$ for sodium has been used:

$$v_p(r) = -\frac{1}{r} + B\frac{\exp(-\beta r^2)}{r} + C\exp(-\gamma r^2), \quad (25)$$

where $B = 1.0$, $C = 0.5$, $\beta = 0.35$, $\gamma = 0.8$, the numbers are given in atomic units.

Our calculations demonstrate that this contribution to plasmon width increases with cluster size for small clusters ($N \le 40$). For larger cluster, the increase saturates as linewidth approaches the bulk value limit. In the limit of bulk sodium, the electron interaction with regular ionic crystal structure results in the band energy spectrum. Plasmon damping associates in this case with interband photoexcitation at plasmon resonance energy ω_p and amounts to 173 meV [8]. This value is in a good agreement with results of our calculations for large clusters.

Note that in the model of electron-ion coupling developed here, the ionic structure considered as frozen. It means that only the elastic electron-ion scattering is taken into account. Indeed, according to Eqs. (14), (24) the energy of collective excitation ω_p is transfered entirely to the single particle excitations. Besides the elastic electron-ion scattering, one can also consider the inelastic scattering on the ionic vibrations, phonons, when the plasmon decay is accompanied by simultaneous emission or absorption of phonons. The plasmon width associated with electron-phonon interaction have been studied in our paper [31]. This contribution to the plasmon width is temperature dependent. For comparison with experimental data on plasmon linewidth [8], we calculated electron-phonon contribution at the same cluster temperature $T = 100$ K as at the photoabsorption measurements. Electron interactions with volume and surface phonon modes both give size dependent contributions to plasmon width. However, their sum shown in Fig. 1 by squares (see curve *3*) does not almost depend on cluster size. Our calculations demonstrate that inelastic electron-ion scattering provides a few times smaller contribution to the plasmon width than

the elastic scattering does.

The experimentally observed plasmon width obtained from the analysis of Na_N photoabsorption spectra [8] are shown in Fig. 1 by circles (see curve *1*). The size dependence of experimental width is non-monotone. For comparison with our theoretical calculations, we should concentrate on spherical clusters with $N = 8, 20, 40, 58, 92$. These clusters have the lowest plasmon width. The joint contribution of elastic and inelastic electron-ion scattering to plasmon width correlates with experimental linewidth for spherical clusters. For non-spherical clusters, experimental linewidth exceeds the calculated values by 100–150 meV. This discrepancy should be attributed to the electron scattering on cluster surface which is not taken into account in our calculations. The good agreement between our calculations and experimental data achieved for closed shell clusters testify that this contribution is not essential for spherical clusters. The well-known formula $\Gamma = C v_F / R_0$ [25] for plasmon width associated with electron scattering on cluster boarder strongly overestimates the effect because it does not take into account that only spill-out electrons contribute to this type of plasmon damping. For non-spherical clusters the effect of electron scattering on cluster surface is much larger due to the mixture of electronic states with different angular momenta. In this case, the dipole collective plasmon excitation decays into numerous single particle excitations with various angular momenta. It leads to much more effective plasmon damping than in the case of spherical clusters where the number of single particle excitations involved in plasmon damping is restricted by the dipole ones.

IV. Conclusion

The plasmon damping associated with electron scattering on the fine ionic structure is described within a simple analytical model. The developed model is based on the separation of the collective plasmon and single particle electron excitations. The coupling between these excitations caused by electron scattering on fine ionic structure leads to plasmon damping. We demonstrate that elastic electron-ion scattering is much more essential than the inelastic electron scattering on ionic vibrations. In the case of spherical clusters it provides the leading contribution to the total plasmon width. In the case of non-spherical clusters the electron scattering on cluster surface is also essential.

REFERENCES

1. **Herberland, H.** Clusters of atoms and molecules: Solvation and chemistry of free clusters, and embedded, supported and compresses clusters. Berlin, Springer-Verlag, 1994. Springer Series in Chemical Physics. Vol. 52, 56.

2. **Kreibig, U., Vollmer M.** Optical properties of metal clusters. Berlin, Springer-Verlag, 1994. Print. Springer Series in Physics.

3. **Knight W.D.** Metallic free clusters. *Z. Phys. D: Atoms, Molecules and Clusters*, 1989, Vol. 12, Iss. 1–4, pp. 315–318.

4. **Brechignac C., Cahuzac Ph., Carlier F., Leygnier J.** Collective excitation in closed-shell potassium cluster ions. *Chem. Phys. Lett.,* 1989, Vol. 164, Iss. 4, pp. 433–437.

5. **de Heer W.A.** The physics of simple metal clusters: experimental aspects and simple models. *Rev. Mod. Phys.*, 1993, Vol. 265, pp. 611–676.

6. **Selby K., Kresin V., Masui J., Vollmer M., de Heer, W.A., Scheidemann A., Knight W.D.** Photoabsorption spectra of sodium clusters. *Phys. Rev. B*, 1991, Vol. 43, pp. 4565–4572.

7. **Wang C.R.C., Pollack S., Cameron D., Kappes M.M.** Optical absorption spectroscopy of sodium clusters as measured by collinear molecular beam photodepletion. *J. Chem. Phys,* 1990, Vol. 93, pp. 3787–3801.

8. **Schmidt M., Haberland H.** Optical spectra and their moments for sodium clusters, Na_n^+, with $3 \le n \le 64$. *Eur. J. Phys. J. D*, 1999, Vol. 6, pp. 109–118.

9. **Ekardt W.** Collective multipole excitations in small metal particles: Critical angular momentum l^{cr} for the existence of collective surface modes. *Phys. Rev. B*, 1985, Vol. 32, pp. 1961–1970.

10. **Yannouleas C., Broglia R.A.** Collective and single-particle aspects in the optical response of metal microclusters. *Phys. Rev. A*, 1991, Vol. 44, pp. 5793–5802.

11. **Brack M.** The physics of simple metal clusters: self-consistent jellium model and semiclassical approaches. *Rev. Mod. Phys*, 1993, Vol. 265, pp. 677–732.

12. **Guet C., Johnson W.R.** Dipole excitations of closed-shell alkali-metal clusters. *Phys. Rev. B*, 1992, Vol. 45, pp. 11283–11287.

13. **Madjet M., Guet C., Johnson W.R.** Comparative study of exchange-correlation effects on the electronic and optical properties of alkali-metal clusters. *Phys. Rev. A*, 1995, Vol. 51, pp. 1327–1339.

14. **Ivanov V.K., Ipatov A.N.** Correlations in clusters and related systems. New perspectives of the many-body problem. Ed by J.P. Connerade. Singapore, World Scientific Publishing, 1996, pp. 141–168.

15. **Pacheco J.M., Broglia R.A.** Effect of surface fluctuations in the line shape of plasma resonances in small metal clusters. *Phys. Rev. Lett.*, 1989, Vol. 62, pp. 1400–1402.

16. **Bertsch, G.F., Tománek D.** Thermal line broadening in small metal clusters. *Phys. Rev. B,* 1989, Vol. 40, Iss. 5, pp. 2749–751.

17. **Penzar Z., Ekardt W., Rubio A.** Temperature effects on the optical absorption of jellium clusters. *Phys. Rev. B*, 1990, Vol. 42, pp. 5040–5045.

18. **Pacheco J.M., Broglia R.A., Mottelson B.R.** The intrinsic line width of the plasmon resonances in metal microclusters at very low temperatures: quantal surface fluctuations. *Z. Phys. D*, 1991, Vol. 21, pp. 289–292.

19. **Wang Y., Lewenkopf C., Tománek D., Bertsch G.** Collective electronic excitations and their damping in small alkali clusters. *Chem. Phys. Lett. D*, 1993, Vol. 205, pp. 521–528.

20. **Montag B., Hirschmann T., Meyer J., Reinhard P.-J.** *Z. Phys. D*, 1994, Vol. 32, pp. 125–136.

21. **Montag B., Reinhard P.-J.** Width of the plasmon resonance in metal clusters. *Phys. Rev. B*, 1995, Vol. 51, 14686.

22. **Reinhard P.-G., Babst J., Fischer B., Kohl C., Calvayrac F., Suraud E., Hirschmann T., Brack M.** Ionic and electronic-structure of metal clusters. *Z. Phys. D*, 1997, Vol. 40, pp. 314–316.

23. **Pacheco J.M., Schone W.-D.** Shape phase transitions in the absorption spectra of atomic clusters. *Phys. Rev. Lett*, 1997, Vol. 79(25), p. 4986–4989.

24. **Calvayrac F., Reinhard P-J., Suraud E.J.** Ionic structure and plasmon response in sodium clusters. *J. Phys. B*, 1998, Vol. 31, No. 6, pp. 1367–1378.

25. **Bertsch G.F., Broglia R.A**. Oscillations in Finite Quantum Systems. Cambridge University Press, 1994. 212 p.

26. **Kawabata A., Kubo R.** Electronic properties of fine metallic particles. II. Plasma resonance absorption. *J. Phys. Soc. Jpn*, 1966, Vol. 21, pp. 1765–1772.

27. **Lushnikov A.A., Simonov A.J.** Surface plasmons in small metal particles. *Z. Phys*, 1974, Vol. 270, pp. 17–24.

28. **Yannouleas C., Broglia R.A.** Landau damping and wall dissipation in large metal clusters. *Annals of Physics*, 1992, Vol. 217, pp. 105–141.

29. **Yannouleas C.** Microscopic description of the surface dipole plasmon in large Na_N clusters ($950 \le N \le 12050$). *Phys. Rev. B*, 1998, Vol. 58, pp. 6748–6751.

30. **Gerchikov L.G., Guet C., Ipatov A.N.** Multiple plasmons and anharmonic effects in small metallic clusters. *Phys. Rev. A*, 2002, Vol. 66, p. 053202 (8 p.).

31. **Gerchikov L.G., Guet C., Ipatov A.N.** Relaxation of optical excitations in metal clusters due to the electron-phonon interaction. *Phys. Rev. A*, 2001, Vol. 65, p. 013201 (6 p.).

32. **Landau L.D., Lifshitz E.M.** Quantum mechanics: (3rd ed.) Pergamon Press, Oxford, 1977, 672 p.

СПИСОК ЛИТЕРАТУРЫ

1. **Herberland, H.** Clusters of atoms and molecules: Solvation and chemistry of free clusters, and embedded, supported and compresses clusters. Berlin, Springer-Verlag, 1994. Springer Series in Chemical Physics. Vol. 52, 56.

2. **Kreibig, U., Vollmer M.** Optical properties of metal clusters. Berlin, Springer-Verlag, 1994. Print. Springer Series in Physics.

3. **Knight W.D.** Metallic free clusters. *Z. Phys. D: Atoms, Molecules and Clusters*, 1989, Vol. 12, Iss. 1–4, pp. 315–318.

4. **Brechignac C., Cahuzac Ph., Carlier F., Leygnier J.** Collective excitation in closed-shell potassium cluster ions. *Chem. Phys. Lett.,* 1989, Vol. 164, Iss. 4, pp. 433–437.

5. **de Heer W.A.** The physics of simple metal clusters: experimental aspects and simple models. *Rev. Mod. Phys.*, 1993, Vol. 265, pp. 611–676.

6. **Selby K., Kresin V., Masui J., Vollmer M., de Heer, W.A., Scheidemann A., Knight W.D.** Photoabsorption spectra of sodium clusters. *Phys. Rev. B*, 1991, Vol. 43, pp. 4565–4572.

7. **Wang C.R.C., Pollack S., Cameron D., Kappes M.M.** Optical absorption spectroscopy of sodium clusters as measured by collinear molecular beam photodepletion. *J. Chem. Phys,* 1990, Vol. 93, pp. 3787–3801.

8. **Schmidt M., Haberland H.** Optical spectra and their moments for sodium clusters, Na_n^+, with $3 \le n \le 64$. *Eur. J. Phys. J. D*, 1999, Vol. 6, pp. 109–118.

9. **Ekardt W.** Collective multipole excitations in small metal particles: Critical angular momentum l^{cr} for the existence of collective surface modes. *Phys. Rev. B*, 1985, Vol. 32, pp. 1961–1970.

10. **Yannouleas C., Broglia R.A.** Collective and

single-particle aspects in the optical response of metal microclusters. *Phys. Rev. A*, 1991, Vol. 44, pp. 5793–5802.

11. **Brack M.** The physics of simple metal clusters: self-consistent jellium model and semiclassical approaches. *Rev. Mod. Phys*, 1993, Vol. 265, pp. 677–732.

12. **Guet C., Johnson W.R.** Dipole excitations of closed-shell alkali-metal clusters. *Phys. Rev. B*, 1992, Vol. 45, pp. 11283–11287.

13. **Madjet M., Guet C., Johnson W.R.** Comparative study of exchange-correlation effects on the electronic and optical properties of alkali-metal clusters. *Phys. Rev. A*, 1995, Vol. 51, pp. 1327–1339.

14. **Ivanov V.K., Ipatov A.N.** Correlations in clusters and related systems. New perspectives of the many-body problem. Ed by J.P. Connerade. Singapore, World Scientific Publishing, 1996, pp. 141–168.

15. **Pacheco J.M., Broglia R.A.** Effect of surface fluctuations in the line shape of plasma resonances in small metal clusters. *Phys. Rev. Lett.*, 1989, Vol. 62, pp. 1400–1402.

16. **Bertsch, G.F., Tománek D.** Thermal line broadening in small metal clusters. *Phys. Rev. B,* 1989, Vol. 40, Iss. 5, pp. 2749–751.

17. **Penzar Z., Ekardt W., Rubio A.** Temperature effects on the optical absorption of jellium clusters. *Phys. Rev. B*, 1990, Vol. 42, pp. 5040–5045.

18. **Pacheco J.M., Broglia R.A., Mottelson B.R.** The intrinsic line width of the plasmon resonances in metal microclusters at very low temperatures: quantal surface fluctuations. *Z. Phys. D*, 1991, Vol. 21, pp. 289–292.

19. **Wang Y., Lewenkopf C., Tománek D., Bertsch G.** Collective electronic excitations and their damping in small alkali clusters. *Chem. Phys. Lett. D*, 1993, Vol. 205, pp. 521–528.

20. **Montag B., Hirschmann T., Meyer J., Reinhard P.-J.** *Z. Phys. D*, 1994, Vol. 32, pp. 125–136.

21. **Montag B., Reinhard P.-J.** Width of the plasmon resonance in metal clusters. *Phys. Rev. B*, 1995, Vol. 51, 14686.

22. **Reinhard P.-G., Babst J., Fischer B., Kohl C., Calvayrac F., Suraud E., Hirschmann T., Brack M.** Ionic and electronic-structure of metal clusters. *Z. Phys. D*, 1997, Vol. 40, pp. 314–316.

23. **Pacheco J.M., Schone W.-D.** Shape phase transitions in the absorption spectra of atomic clusters. *Phys. Rev. Lett*, 1997, Vol. 79(25), p. 4986–4989.

24. **Calvayrac F., Reinhard P-J., Suraud E.J.** Ionic structure and plasmon response in sodium clusters. *J. Phys. B*, 1998, Vol. 31, No. 6, pp. 1367–1378.

25. **Bertsch G.F., Broglia R.A**. Oscillations in Finite Quantum Systems. Cambridge University Press, 1994. 212 p.

26. **Kawabata A., Kubo R.** Electronic properties of fine metallic particles. II. Plasma resonance absorption. *J. Phys. Soc. Jpn*, 1966, Vol. 21, pp. 1765–1772.

27. **Lushnikov A.A., Simonov A.J.** Surface plasmons in small metal particles. *Z. Phys*, 1974, Vol. 270, pp. 17–24.

28. **Yannouleas C., Broglia R.A.** Landau damping and wall dissipation in large metal clusters. *Annals of Physics*, 1992, Vol. 217, pp. 105–141.

29. **Yannouleas C.** Microscopic description of the surface dipole plasmon in large Na_N clusters ($950 \le N \le 12050$). *Phys. Rev. B*, 1998, Vol. 58, pp. 6748–6751.

30. **Gerchikov L.G., Guet C., Ipatov A.N.** Multiple plasmons and anharmonic effects in small metallic clusters. *Phys. Rev. A*, 2002, Vol. 66, p. 053202 (8 p.).

31. **Gerchikov L.G., Guet C., Ipatov A.N.** Relaxation of optical excitations in metal clusters due to the electron-phonon interaction. *Phys. Rev. A*, 2001, Vol. 65, p. 013201 (6 p.).

32. **Landau L.D., Lifshitz E.M.** Quantum mechanics: (3rd ed.) Pergamon Press, Oxford, 1977, 672 p.

ГЕРЧИКОВ Леонид Григорьевич – *кандидат физико-математических наук, доцент кафедры экспериментальной физики Санкт-Петербургского государственного политехнического университета.*

195251, Россия, Санкт-Петербург, Политехническая ул., 29

lgerchikov@rambler.ru

UDC 538.915

L.G. Gerchikov[1], Yu.A. Mamaev[1], Yu.P. Yashin[1], V.V. Kuz'michev[1], K. Aulenbacher[2], E. Riehn[2]

[1] St. Petersburg State Polytechnical University
29 Politekhnicheskaya St., St. Petersburg, 195251, Russia
[2] Institute of Nuclear Physics, Johannes Gutenberg University
Saarstraße 21, 55122 Mainz, Germany.

ELECTRONIC TRANSPORT IN STRAINED AlInGaAs/AlGaAs SUPERLATTICES

Л.Г. Герчиков, Ю.А. Мамаев, Ю.П. Яшин, В.В. Кузьмичев, К. Ауленбахер, Э. Райх

ЭЛЕКТРОННЫЙ ТРАНСПОРТ В НАПРЯЖЕННЫХ СВЕРХРЕШЕТКАХ AlInGaAs/AlGaAs

Transport of spin polarized electrons in semiconductor AlInGaAs/AlGaAs superlattices (SL) with strained quantum wells used for photoemitter application is studied. The experimental study is based on the time resolved measurements of electron emission from the cathode after its photoexcitation by fs laser pulse. We report the variation of the SL response time with the number of superlattice periods. We have also performed theoretical calculations of photocathode pulse response and compared the obtained results with experimental data. Our analysis testifies the presence of partial electron localization in SL. We demonstrate that electron localization suppresses electronic transport and strongly limits the cathode quantum efficiency.

SUPERLATTICE, DFIFFUSION, PHOTOEMISSION, ELECTRONIC TRANSPORT.

Экспериментально и теоретически исследован транспорт поляризованных электронов в фотокатодах на основе полупроводниковой, сильно напряженной сверхрешетки. Экспериментальное исследование основано на измерении с разрешением по времени электронной эмиссии из фотокатода после его фотовозбуждения фемтосекундным лазерным импульсом. Экспериментально определены времена фотоотклика сверхрешеток с различным числом периодов. Проведены расчеты фотооклика катодов и результаты сопоставлены с экспериментальными данными. Сделан вывод о наличии в свехрешетке частичной локализации фотоэлектронов. Показано, что электронная локализация подавляет электронный транспорт и сильно ограничивает квантовую эффективность фотокатодов.

СВЕРХРЕШЕТКА, ДИФФУЗИЯ, ФОТОЭМИССИЯ, ЭЛЕКТРОННЫЙ ТРАНСПОРТ.

I. Introduction

At the present time strained semiconductor superlattices (SL) are known as most effective basis of highly polarized electron sources [1]. Such photoemitters combine the advantages of conventional polarized electron sources based on a strained semiconductor layer with additional possibilities for band structure engineering of photocathode working layers based on strained SL. The major goal of SL development for photoemitter applications in the past decade was the achievement of electron polarization more than 90 %. For this purpose several types of SLs with highest possible valence band splitting have been developed, namely the SLs with strained quantum wells (QW) [2, 3] and with strained barriers [4]. Valence band splitting in SL, i. e. the energy splitting between the upper heavy and light hole minibands, is formed due to the combination of two effects: the strain deformation of SL layers and the quantum confinement. The aim of the optimal SL design is to provide a valence band splitting of more

than 70–80 meV together with good transport properties and high structural quality.

However, the significant progress in electron polarization was achieved at the expense of the quantum efficiency (QE) which does not exceed 1 % at the polarization maximum. Indeed, the maximum spin polarization of photoelectrons takes place at the photoabsorption threshold where the photoabsorption coefficient is rather small. Strained SL cannot be made too thick due to the possible strain relaxation resulting in structural defects, smaller residual strain and lower polarization. The best combination of polarization P = 92 % and QE = 0.85 % has been achieved for AlInGaAs/AlGaAs SL with strained QWs [3]. Thus, the further progress of polarized electron sources based on semiconductor SLs is shifted towards the developing highly effective photoemitters in order to meet the modern requirements of high energy physics [5].

Our study demonstrates that simple increase of the SL thickness does not lead to increase of QE like it is observed in the case of conventional photoemitters with GaAs working layer [6, 7]. In order to understand this surprising phenomenon, we perform the time resolved measurements of electron emission from the cathodes after their excitation by fs laser pulse. This method has been developed by K. Aulenbacher et al. [6] while studying the spin polarized electron transport in conventional photocathodes. The series of AlInGaAs/AlGaAs SLs containing from 6 to 15 periods have been fabricated and studied. In all samples we observe two exponential decays of electron emission, which indicates the presence of partial electron localization in a SL. The fast decay is caused by electron emission from the first electronic miniband while slow response decay is connected with electrons trapped by the localized states.

We also developed a theoretical description of electron transport in a SL based on the time dependent kinetic equation and calculated the photocathode pulse response [8]. The obtained results are in a good agreement with the experimental observations. The employed model determines the time of electron transport in SL, electron capture and detachment times, portion of photoelectrons that have been localized by the traps in SL and corresponding losses of QE.

II. Experiment

We have studied the pulse response of six photocathodes based on AlInGaAs/AlGaAs SL with strained QWs. All samples were grown on a p-type (100) GaAs substrate by molecular beam epitaxy (MBE). The cathode structure contains a thick $Al_xGa_{1-x}As$ (x = 0.35 – 0.40) buffer layer that is p-doped by beryllium to the level $6 \cdot 10^{18}$ cm^{-3}. On the top of the buffer, the cathode working layer was grown containing 6 to 15 periods of $Al_xIn_yGa_{1-x-y}As(a)$/$Al_zGa_{1-z}As(b)$ SL p-doped to a lower level of $3 \cdot 10^{17}$ cm^{-3}. Layer composition, x, y, z, values of the QW– (a) and barrier- (b) layer thickness as well as the number of SL periods (N) are shown in Table 1. Above the SL, a 6 nm GaAs

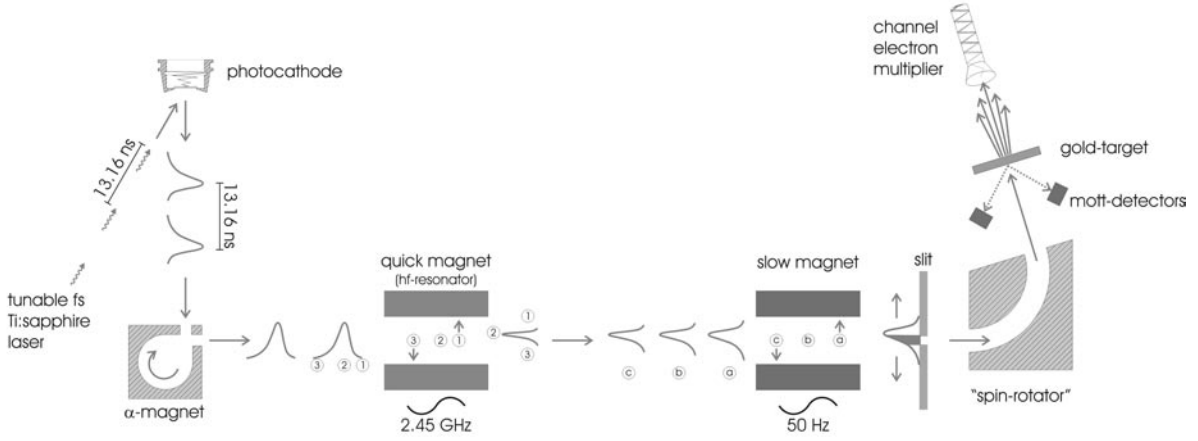

Fig. 1. Experimental setup

Table 1

Composition of photocathode working layers

Sample	QW		Barrier	Thickness		Period
	x, %	y, %	z, %	a, nm	b, nm	N
SL 5-998	20	16	28	3.5	4.0	15
SL 5-337	20	16	28	5.0	4.0	15
SL 7-395	20	19	40	5.4	2.1	12
SL 7-396	20	19	40	5.4	2.1	12
SL 6-905	20	15.5	36	5.1	2.3	10
SL 6-908	20	15.5	36	5.1	2.3	6

Values given: Number of SL periods (N), concentration of Al (x) and In (y) in $Al_xIn_yGa_{1-x-y}As$ QW layer; Al concentration (z) in $Al_zGa_{1-z}As$ barrier layers and their thicknesses (a – QWs, b – barriers).

heavily Be-doped to the level of $7\cdot10^{18}$ cm^{-3} ($1\cdot10^{19}$ cm^{-3} for SL 5-998) surface layer was grown to produce thin band bending region (BBR). Finally, the GaAs surface was activated by repeated deposition of cesium and oxygen to achieve the negative electron affinity. All the experiments were performed at room temperature.

The experimental setup is shown in Fig. 1. The electron pulses are generated by an approximately 150 fs long laser pulse from a titanium-sapphire laser. An increase of pulse length to 300 fs takes place during optical beam transport to the cathode. These light pulses are synchronized to the output of a klystron which drives a 2.45 GHz-deflection cavity. By passing the first deflection cavity (quick magnet in Fig. 1), the longitudinal profile of the electron bunches is transferred into a corresponding transverse profile. The pulse profile can then be measured by moving the electron pulse in the second deflection cavity (slow magnet in Fig. 1) over a narrow slit and detecting the transmitted current. By analyzing the spin polarization of the transmitted electrons with a Mott polarimeter, a time resolved polarization measurement is obtained. The details of the apparatus are described in [6].

III. Theory

We describe the electron transport in a SL by means of the time dependent kinetic equation:

$$\frac{\partial\hat{\rho}}{\partial t} = -\frac{i}{\hbar}\left[\hat{H}\hat{\rho}\right] + I\{\hat{\rho}\}. \qquad (1)$$

Here ρ is the electron density matrix, $\hat{H}$ is the effective electron Hamiltonian for the first electronic miniband $e1$ which describes the quantum electron motion along SL axis. The collision term $I\{\rho\}$ on the right-hand side of Eq.(1) takes into account all the processes of electron scattering on impurities and phonons, the processes of photoexcitation, recombination and electron extraction into BBR.

We calculate the miniband energy spectrum using the multiband Kane model, including the conduction band Γ_6, the states of light and heavy holes of the valence band Γ_8 and also the states of the spin-orbit splitted Γ_7 band [9]. The width ΔE of the $e1$ miniband along the SL axis in the considered samples is in the range 20–40 meV. These values are much smaller than the conduction band offsets which appear to be larger than 200 meV for all considered samples. Consequently, the vertical electron motion along SL axes can be well described within the tight binding approximation. For effective Hamiltonian $\hat{H}$ it means that we have to take into account the coupling matrix element $V \equiv H_{n,n+1} = \Delta E/4$ between the neighboring QWs only. This matrix element determines the tunneling time between neighboring QWs $\tau_{QW} = \pi\hbar/2V = 2\pi\hbar/\Delta E$ which is about 100 fs for our samples. The total time of ballistic motion through the SL containing N QW amounts to $\tau_{SL} = 2\pi\hbar N/\Delta E$.

Taking into account the transition matrix elements for the neighboring QW only, the kinetic equation (1) for electron population of each QWs, i. e. for the diagonal elements ρ_{nn} of density matrix, is written as

$$\frac{\partial \rho_{nn}}{\partial t} = -\frac{2V}{\hbar}\,\mathrm{Im}\{\rho_{n,n+1}\} + \frac{2V}{\hbar}\,\mathrm{Im}\{\rho_{n-1,n}\} + I\{\hat{\rho}\}_{nn}. \quad (2)$$

The first two terms in the right-hand side of Eq.(2) corresponds to the electron currents from n-th QW to two neighboring QWs with the numbers $n + 1$ and $n - 1$, respectively.

The diagonal elements of the collision term $I\{\rho\}$ on the right-hand side of Eqs. (1), (2) are connected with photoexcitation and recombination processes. Calculation of the photogeneration rate is described in details in Ref. [9]. The recombination contribution to the collision term is given by the diagonal matrix element ρ_{nn}/τ_r, where τ_r is the electron recombination time. For the final N-th QW close to the BBR, there is an additional contribution connected with electron tunneling to the BBR. Corresponding electron extraction current I can be written via the number of electrons in the last QW, ρ_{NN}, and tunneling time through the last barrier τ_f:

$$I = \frac{\rho_{NN}}{\tau_f}. \quad (3)$$

The non-diagonal density matrix elements $\rho_{nn'}$ and corresponding electron currents between the neighboring QWs in Eq. (2) are determined by transition matrix element V and non-diagonal elements of the collision term $I\{\hat{\rho}\}_{nn'}$. The last ones we will right within the constant relaxation time approximation:

$$I\{\hat{\rho}\}_{nn'} = -\hat{\rho}_{nn'} / \tau_p. \quad (4)$$

Due to the weak coupling between the neighboring QWs, the momentum relaxation time τ_p is mostly determined by the processes of electron scattering within each QW layer. In the stationary case, in approximation accounting for the neighboring QWs only, it follows from Eqs. (1), (4) that

$$\rho_{n,n+1} = -i\frac{V\tau_p}{\hbar}(\rho_{n+1,n+1} - \rho_{nn}). \quad (5)$$

Consequently, the electron current from n-th to $(n + 1)$-th QW is equal to

$$I_{n,n+1} = \frac{2V}{\hbar}\,\mathrm{Im}\{\rho_{n,n+1}\} = -\frac{2V^2\tau_p}{\hbar^2}(\rho_{n+1,n+1} - \rho_{nn}). \quad (6)$$

For numerical calculations, we take the momentum relaxation time equal to $\tau_p = 75$ fs. Note that τ_p is comparable to the time of free electron tunneling between neighboring QWs τ_{QW}. Therefore, electron transport along SL axis is diffusion, not the ballistic motion.

To calculate the tunneling time from SL to BBR τ_f, we solve the separate quantum mechanical problem of free electron motion through the single QW to BBR [8]. It is worth noting that the obtained τ_f is larger than the tunneling time between neighboring QWs τ_{QW}, e. g. for SL 5-998 $\tau_f = 0.25$ ps while $\tau_{QW} = 0.1$ ps. It is quite natural because the tunneling between the neighboring QWs is a resonant process and its probability is proportional to the first order of the tunneling exponent $\exp(-\kappa b)$, where κ is the electronic wave vector under the barrier and b is the barrier width. The tunneling through the last barrier is a non-resonant process and its probability is much smaller since it is proportional to the second order of the tunneling exponent $\exp(-2\kappa b)$. Hence, the total time of electron motion from SL to BBR is mainly determined by the slowest process, i. e. by the tunneling through the last barrier.

Eq. (3) can be considered as the boundary condition at the SL/BBR interface. At the opposite side of SL, i. e. at the buffer interface, the electron current is equal to zero, $I = 0$. In the case of electron diffusion in the bulk sample, the boundary conditions are usually written via the surface recombination velocity $S = j/n$, where j is the diffusion current density and n is the electron concentration. Since electron current in buffer layer is zero, we assume zero surface recombination velocity $S = 0$ at the buffer interface. At the opposite side of working layer, at the BBR interface, the surface recombination velocity, according to Eq.(3), is equal to

$$S = \frac{d}{\tau_f}, \quad (7)$$

where $d = a + b$ is the SL period.

Surface recombination velocities for our SL based cathodes calculated according to Eq. (7) are smaller than in the case of con-

ventional photoemitters. For example, in case of SL 5-998, $S = 3 \cdot 10^6$ cm/s, for SL 6-905 $S = 5 \cdot 10^6$ cm/s while in the bulk GaAs $S = 10^7$ cm/s [6, 7].

For numerical simulation of the cathode response, we solve the time-dependent kinetic Eq. (1) with time dependence of the laser pulse intensity described by the Gaussian profile. The obtained electron current $I(t)$ (3) is compared to the experimental pulse response (see next section). The calculated pulse response exponentially decays with time, and we define the corresponding decay time as electron transport time τ_t. It is possible, however, to derive the approximate analytical expression for τ_t. In the steady state under the stationary pumping, kinetic Eq. (1) has an analytical solution (Eqs.(5, 6)), which is correct if the miniband width ΔE is smaller than the photoelectron energy distribution. The transport time defined in the stationary case as the ratio of number of electrons inside the SL to the generation rate, $\tau_t = \sum_{n=1}^{N} \rho_{nn} / I$, $I = I_{n,n+1}$, is equal to

$$\tau_t = \frac{\hbar^2 (N - 1/2)(N-1)}{6|V|^2 \tau_p} + N\tau_f. \qquad (8)$$

According to Eq. (8), the transport time is a sum of the diffusion time within the SL given by the first term on the right-hand side, and the time $N\tau_f$, taken to penetrate through the last barrier to the BBR. For the twelve-period SL 5-998, Eq.(8) gives the transport time $\tau_t = 5$ ps. The main contribution, 3 ps, comes from the tunneling through the last barrier to BBR.

Note that in the limit of thick SL, $N >> 1$, Eq. (8) transfers into a corresponding expression of the standard diffusion model in the bulk sample:

$$\tau_t = \frac{L^2}{3D} + \frac{L}{S}, \qquad (9)$$

where $L = Nd$ is the SL length.

The surface recombination velocity S is given by Eq. (7), and diffusion coefficient D of SL is equal to

$$D = \frac{2|V|^2 d^2 \tau_p}{\hbar^2}. \qquad (10)$$

The typical value of D is about 15 cm^2/s, e. g. for SL 5-998 $D = 12$ cm^2/s and for SL 6-905 $D = 17$ cm^2/s. It is a few times smaller than the diffusion coefficient $D = 40$ cm^2/s in the bulk GaAs [6, 7].

Our calculations of the cathode QE and pulse response according to the kinetic scheme described above revealed the significant discrepancy between experiment and theory. Namely, theory predicts the gradual increase of QE with the growth of SL thickness up to the hundreds nanometers while such increase actually saturates at few tens nanometers thicknesses (see the next section). Then, the theory predicts the simple exponential decay of pulse response with time described by Eq. (8), while the experimental signal reveals a non-exponential decay (see the next section). These facts indicate the presence of partial electron localization in a SL. That is why we include in the density matrix ρ the localized electron states besides the delocalized miniband states and introduce in the collision term $I\{\hat{\rho}\}$ processes of electron capture and detachment with characteristic times τ_c and τ_d respectively. We do not consider transitions between electron states localized within the different QWs, because such transitions are non-resonant and hence they are very slow compared to the interwell transitions via miniband states described by Eq.(6). Coupling between the localized and delocalized (miniband) states occurs via capture and detachment processes within each QW. In the extended kinetic scheme accounting for the partial electron localization, these processes are described by the diagonal matrix elements in the collision term $\rho_{nm,nm}/\tau_c$ and $\rho_{nl,nl}/\tau_d$, for capture and detachment, respectively. Here indexes m and l after the QW number n in the density matrix subscripts indicate whether the electron state is miniband or localized, respectively.

IV. Results and Discussion

We have measured QE for series of cathodes based on SL with composition close to SL 6-905 and containing from 2 to 20 periods. The results are presented in Fig. 2. The significant scattering of experimental data is connected with large variation of electron emission probability from BBR to the vacuum via cathode surface activated with Cs–O. This feature of

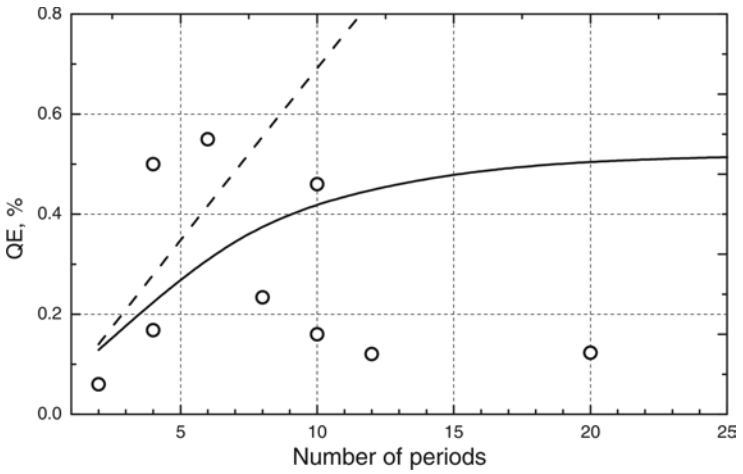

Fig. 2. Quantum efficiency dependence on SL thickness.
Open dots show the experimental results. Solid and dashed lines show the theoretical results calculated with and without electron localization, respectively

experimental data impedes the detailed comparison between the experiment and theory. Nevertheless, one can conclude that the experimental measurements do not support the linear increase of QE calculated without accounting for electron localization (dashed line). The influence of electron localization is shown by solid line which has been calculated assuming partial electron localization. It demonstrates that electron localization strongly suppresses the QE increase. The parameters of electron localization used for these calculations are shown in Table 2 for SL 6-905 sample. Their choice will be discussed below. The electron recombination time in SL was taken τ_r = 50 ps [10].

The more detailed study of electron transport in the considered nanostructures was done by means of time resolved pulse response measurements. For all considered samples presented in Table 1, we calculated the pulse response by the numerical solution of Eq. (1). The obtained results, together with the experimental data, are shown in Fig. 3 and presented in Table 2. The dashed lines in Fig. 3 show the pulse response calculated without electron localization. It exponentially decays with the decay time equal to the time of miniband electron transport τ_t quite close to the approximate Eq. (8). The calculated miniband electron times τ_t are presented in the third column of the Table 2. Fig. 3 demonstrates that in all samples experimental signal decays faster than τ_t. We interpret this fact

Table 2

Parameters of vertical electron transport

Sample	Number of periods	Miniband transport time, ps	Capture time, ps	Detachment time, ps	Response time, ps	Diffusion length, periods	Electron losses, %
SL 5-998	15	5.8	4.5	6.0	2.3	36	12
SL 5-337	15	15.8	5.5	160	4.0	8	64
SL 7-395	12	4.5	3.7	200	2.1	11	45
SL 7-396	12	4.5	9.0	110	3.0	18	23
SL 6-905	10	2.5	2.1	130	1.1	10	41
SL 6-908	6	1.2	4.5	50	0.95	19	9

Values given: Transport time of *e*1 miniband (τ_t), capture time (τ_c), detachment time (τ_d), response time (τ), diffusion length and losses of photoelectrons SL.

as an evidence of partial electron localization. Indeed, in the presence of electronic traps, the electron current will decay faster due to combination of two processes: electron transport from SL to BBR with subsequent emission into the vacuum and electron capture by the traps. Roughly, the decay (or response) time can be approximated as $\tau = 1/(1/\tau_{t.} + 1/\tau_{c.})$. The resulting response times are presented in the sixth column of the Table 2. The solid lines in Fig. 3 show the pulse response calculated taking into account electron capture and reverse detachment processes. Fig. 3 demonstrates quite good agreement of the experiment and theory. The capture and detachment times are used as fitting parameters, and their values are shown in Table 2. These times depend on the trap density and strongly vary from one sample to another. This fact masks the response time dependence on the number of SL periods. Thus six (SL 6-908) and ten (SL 6-905) period samples have close response times though the miniband transport time of the longer SL is more than two times larger than for the shorter one.

Samples with shorter capture and larger detachment times have the larger level of electron localization. In these samples electron transport is suppressed because considerable part of photoelectrons is localized by the traps and have low chance to escape to BBR prior to recombination. To demonstrate the effect of localization on QE, we show in the last two columns of Table 2 the diffusion length $L_D = (D\tau_r)^{1/2}$ and electronic losses in SL. In the samples with high localization level, the diffusion length is comparable with SL thickness, which in turn leads to considerable electronic losses. This fact explains why QE does not increase with the growth of SL thickness. The increase of the SL thickness beyond the diffusion length just leads to needless electronic losses. It is demonstrated by the solid curve in Fig. 2 calculated with the following parameter of SL 6-905 sample: $L_D/d = 10$.

The sample with the best transport properties is SL 6-908. It has the largest ratio of diffusion length to SL thickness $L_D/L = 3$ and consequently the lowest electronic losses. If all the

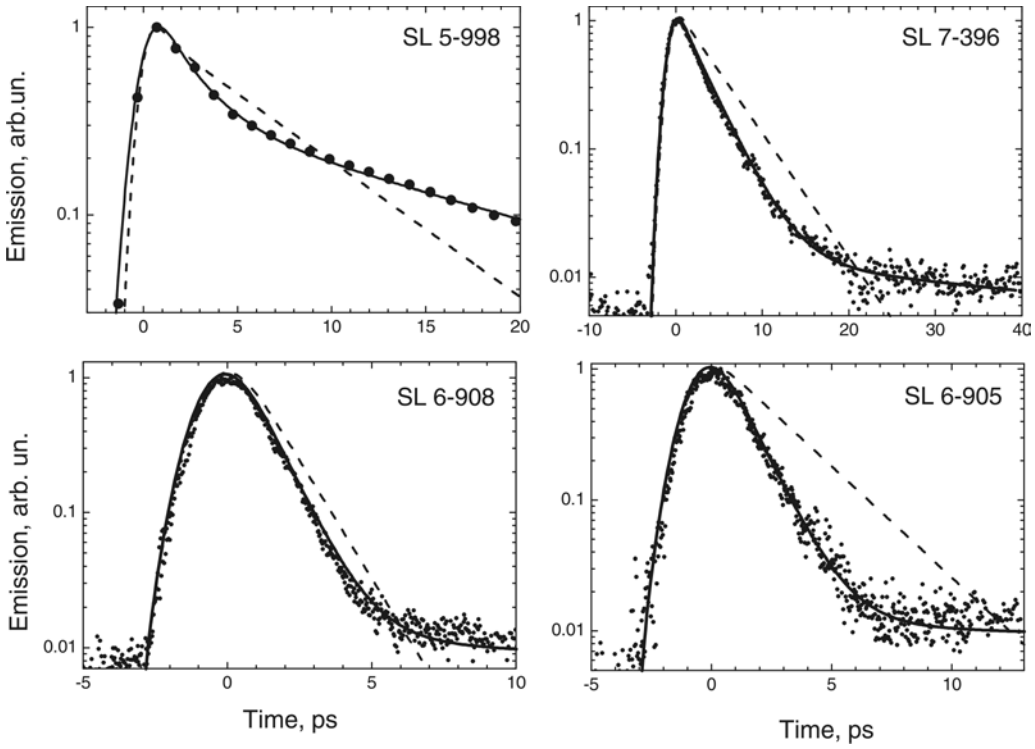

Fig. 3. Pulse response of SL 5-998, SL 7-396, SL 6-905 and SL 6-908 samples. Experimental signal is shown by dots, solid and dashed lines show the pulse response calculated with and without partial electron localization respectively

electrons in SL 6-908 are delocalized, the ratio L_D/L should be equal to 6.5. Roughly, this ratio indicates how QE can be enhanced if one is able to fabricate the cathode with SL thickness beyond L_D keeping the constant SL transport properties. However, our study shows that longer SLs have worse transport properties, e. g. SL 6-905 compared to SL 6-908.

Within the present work, we do not determine the nature of the localized electronic states as well as possible dependence of their density on SL thickness. The photocathode structure is heavily *p*-doped in order to achieve thin BBR. The highest doping level about 10^{19} cm^{-3} is applied in BBR, but the working layer is also heavily doped up to $3{\cdot}10^{17}$ cm^{-3}. Fluctuations of impurity potential might be responsible for the formation of localized electron states. Such phenomena have been observed earlier in GaAs/AlAs SLs at a comparable doping level of $1{\cdot}10^{17}$ – $7{\cdot}10^{17}$ cm^{-3} [11]. The 60 % of localized states in the lowest electron miniband e1 at the doping level of $4{\cdot}10^{17}$ cm^{-3} have been reported. The drop of vertical electron conductivity caused by partial electron localization was observed.

Unavoidable fluctuations of the layer composition and thicknesses can also contribute to partial electron localization. However, one can assume that the density of electronic traps formed due to these mechanisms should not depend on the SL length. On the contrary, the density of structural defects such as dislocations formed in SLs due to the strain relaxation, increases with the thickness of SLs. Lattice mismatch deformation of the QW layers shifts the conduction band edge upwards by approximately 0.1 eV. Thus, the deformation potential of dislocation plays a role of deep well for miniband electrons and can form the localized electron states. Note that the strong deformation of the SL is needed to produce sufficient energy splitting between light- and heavy-hole minibands to achieve high electron polarization. Further work will be focused on the nature of electron localization. Its main goal will be to determine the maximal number of SL periods that can be grown keeping good transport properties in combination with high electron polarization.

V. Conclusions

The pulse response of series of photocathodes with AlInGaAs/AlGaAs SLs with different numbers of periods has been studied. The analysis performed argues the presence of partial electron localization in SLs. The proposed kinetic model taking into account transport of miniband electrons from a SL to BBR, their capture by electronic traps and the reverse detachment process provides a good agreement between experimental findings and theoretical results. We demonstrate that electron localization slows down electron transport and leads to detrimental losses of photoelectrons. Partial electron localization limits maximal QE and useful thickness of SL based cathode working layer.

This work was supported by DFG through SFB 443.

REFERENCES

1. **Subashiev A.V., Mamaev Yu.A., Yashin Yu.P., Clendenin J.E.** Spin-polarized electrons: generation and applications. *Phys. Low-Dimentional Structures.* 1999, Vol. 1/2, pp. 1–36.

2. **Nishitani T., Nakanishi T., Yamamoto M., Okumi S., Furuta F., Miyamoto M., Kuwahara M., Yamamoto N., Naniwa K., Watanabe O., Takeda Y., Kobayakawa H., Takashima Y., Horinaka H., Matsuyama T., Togawa K., Saka T., Tawada M., Omori T., Kurihara Y., Yoshioka M., Kato K., Baba T.** Highly polarized electrons from GaAs-GaAsP and InGaAs-AlGaAs strained-layer superlattice photocathodes. *J. Appl. Phys.,* 2005, Vol. 97, p. 94907.

3. **Mamaev Yu.A., Gerchikov L.G., Yashin Yu.P., Vasiliev D.A., Kuzmichev V.V., Ustinov V.M., Zhukov A.E., Mikhrin V.S.** Optimized photocathode for spin-polarized electron sources. *Appl. Phys. Lett.,* 2008, Vol. 93, pp. 81114–81116.

4. **Gerchikov L.G., Mamaev Yu.A., Subashiev A.V., Yashin Yu.P., Vasil'ev D.A., Kuz'michev V.V., Zhukov A.E., Semenova E.S., Vasil'ev A.P., Ustinov V.M.** Photoemission of polarized electrons from InAlGaAs/GaAs superlattices with minimum conduction band offsets. *Semiconductors*, 2006, Vol. 40, pp.1326–1332.

5. **Brachmann A., Clendenin J.E., Garwin E.L., Ioakeimidi K., Kirby R.E., Maruyama T., Prescott C.Y., Sheppard J., Turner J., Zhou F.** The polarized electron source for the International Collider

(ILC) Project. *AIP Conference Proceedings of 17th International Spin Physics Symposium* (Kyoto, Japan, 2–7 October 2006), 2007, Vol. 915, pp. 1091–1094.

6. **Aulenbacher K., Schuler J., v. Harrach D., Reichert E., Roethgen J., Subashev A., Tioukine V., Yashin Y.** Pulse response of thin III/V semiconductor photocathodes. *J. Appl. Phys.,* 2002, Vol. 92, pp. 7536–7543.

7. **Oskotskij B.D., Subashiev A.V., Mamaev Yu.A.** Polarized photoemission spectra of the strained semiconductors layers. *Phys. Low-Dim. Struct.,* 1997, Vol. 1/2, pp. 77–89.

8. **Gerchikov L.G., Aulenbacher K., Mamaev Yu.A., Riehn E.J., Yashin Yu.P.** Transport and partial localization of electrons in strained short-period semiconductor superlattices. *Semiconductors,* 2012, Vol. 46, pp. 67–74.

9. **Subashiev A.V., Gerchikov L.G., Ipatov A.I.** Optical spin orientation in strained superlattices. *J. Appl. Phys.*, 2004, Vol. 96, pp. 1511–1520.

10. **Matsuyama T., Takikita H., Horinaka H., Wada K, Nakanishi T., Okumi S., Nishitani T., Saka T., Kato T.** High spin polarization of conduction band electrons in GaAs-GaAsP strained layer superlattice fabricated as a spin-polarized electron source. *Jap. J. Appl. Phys.*, 2004, Vol. 43, pp. 3371–3375.

11. **Pusep Yu.A., Chiquito A.J., Mergulhao S., Galzerani J.C.** One-dimensional character of miniband transport in doped GaAs/AlAs superlattices. *Phys. Rev. B,* 1997, Vol. 56, pp. 3892–3895.

СПИСОК ЛИТЕРАТУРЫ

1. **Subashiev A.V., Mamaev Yu.A., Yashin Yu.P., Clendenin J.E.** Spin-polarized electrons: generation and applications. *Phys. Low-Dimentional Structures.*, 1999. Vol. 1/2, pp. 1–36.

2. **Nishitani T., Nakanishi T., Yamamoto M., Okumi S., Furuta F., Miyamoto M., Kuwahara M., Yamamoto N., Naniwa K., Watanabe O., Takeda Y., Kobayakawa H., Takashima Y., Horinaka H., Matsuyama T., Togawa K., Saka T., Tawada M., Omori T., Kurihara Y., Yoshioka M., Kato K., Baba T.** Highly polarized electrons from GaAs-GaAsP and InGaAs-AlGaAs strained-layer superlattice photocathodes. *J. Appl. Phys.,* 2005, Vol. 97, p. 94907.

3. **Mamaev Yu.A., Gerchikov L.G., Yashin Yu.P., Vasiliev D.A., Kuzmichev V.V., Ustinov V.M., Zhukov A.E., Mikhrin V.S.** Optimized photocathode for spin-polarized electron sources. *Appl. Phys. Lett.,* 2008, Vol. 93, pp. 81114–81116.

4. **Герчиков Л.Г., Мамаев Ю.А., Субашиев А.В., Яшин Ю.П., Васильев Д.А., Кузьмичев В.В., Жуков А.Е., Семенова Е.С., Васильев А.П., Устинов В.М.** Фотоэмиссия поляризованных электронов из InAlGaAs/GaAsS-сверхрешеток с минимальным разрывом зоны проводимости // Физика и техника полупроводников. 2006. Вып. 11. С. 1361 – 1367.

5. **Brachmann A., Clendenin J.E.; Garwin E.L., Ioakeimidi K., Kirby R.E., Maruyama T., Prescott C.Y., Sheppard J., Turner J., Zhou F.** The polarized electron source for the International Collider (ILC) Project. *AIP Conference Proceedings of 17th International Spin Physics Symposium* (Kyoto, Japan, 2–7 October 2006), 2007, Vol. 915, pp. 1091–1094.

6. **Aulenbacher K., Schuler J., v. Harrach D., Reichert E., Roethgen J., Subashev A., Tioukine V., Yashin Y.** Pulse response of thin III/V semiconductor photocathodes. *J. Appl. Phys.,* 2002, Vol. 92, pp. 7536–7543.

7. **Oskotskij B.D., Subashiev A.V., Mamaev Yu.A.** Polarized photoemission spectra of the strained semiconductors layers. *Phys. Low-Dim. Struct.,* 1997, Vol. 1/2, pp. 77–89.

8. **Герчиков Л.Г., Ауленбахер К., Мамаев Ю.А., Рин Э., Яшин Ю.П.** Транспорт и частичная локализация электронов в короткопериодических напряженных полупроводниковых структурах // Физика и техника полупроводников. 2012. Вып. 1. С. 70 – 89.

9. **Subashiev A.V., Gerchikov L.G., Ipatov A.I.** Optical spin orientation in strained superlattices. *J. Appl. Phys.*, 2004, Vol. 96, pp. 1511–1520.

10. **Matsuyama T., Takikita H., Horinaka H., Wada K, Nakanishi T., Okumi S., Nishitani T., Saka T., Kato T.** High spin polarization of conduction band electrons in GaAs-GaAsP strained layer superlattice fabricated as a spin-polarized electron source. *Jap. J. Appl. Phys.*, 2004, Vol. 43, pp. 3371–3375.

11. **Pusep Yu.A., Chiquito A.J., Mergulhao S., Galzerani J.C.** One-dimensional character of miniband transport in doped GaAs/AlAs superlattices. *Phys. Rev. B,* 1997, Vol. 56, pp. 3892–3895.

ГЕРЧИКОВ Леонид Григорьевич – *кандидат физико-математических наук, доцент кафедры экспериментальной физики Санкт-Петербургского государственного политехнического университета.*

195251, Россия, Санкт-Петербург, Политехническая ул., 29

lgerchikov@rambler.ru

МАМАЕВ Юрий Алексеевич – *доктор физико-математических наук, профессор кафедры экспериментальной физики Санкт-Петербургского государственного политехнического университета.*
195251, Россия, Санкт-Петербург, Политехническая ул., 29
mamaev@spes.stu.neva.ru

ЯШИН Юрий Петрович – *кандидат физико-математических наук, доцент кафедры экспериментальной физики Санкт-Петербургского государственного политехнического университета.*
195251, Россия, Санкт-Петербург, Политехническая ул., 29

КУЗЬМИЧЕВ Виталий Валерьевич – *ассистент кафедры экспериментальной физики Санкт-Петербургского государственного политехнического университета.*
195251, Россия, Санкт-Петербург, Политехническая ул., 29

АУЛЕНБАХЕР Курт – *профессор Института ядерной физики Университета Иоганна Гутенберга.*
55122, Германия, Майнц, Саарштрассе, 21
aulenbac@kph.uni-mainz.de

РАЙХ Эрик – *сотрудник Института ядерной физики Университета Иоганна Гутенберга.*
55122, Германия, Майнц, Саарштрассе, 21

UDC

T.Yu. Vergentev[1], A.G. Banshchikov [2], E.Yu. Koroleva [1,2], N.S. Sokolov [2], M.V. Zakharkin [1], N.M. Okuneva [2]

[1] St. Petersburg State Polytechnical University,
29 Politekhnicheskaya St., St. Petersburg, 195251, Russia.
[2] Ioffe Physical-Technical Institute,
26 Politekhnicheskaya St., St. Petersburg, 194021, Russia.

IN-PLANE CONDUCTIVITY OF THIN FILMS AND HETEROSTUCTURES BASED ON LaF_3-SrF_2

Т.Ю. Вергентьев, А.Г. Банщиков, Е.Ю. Королева, Н.С. Соколов, М.В. Захаркин, Н.М. Окунева

ПРОДОЛЬНАЯ ПРОВОДИМОСТЬ ТОНКИХ ПЛЕНОК И ГЕТЕРОСТРУКТУР, ОСНОВАННЫХ НА LaF_3-SrF_2

The in-plane conductivity of solid solution $La_{1-x}Sr_xF_{3-x}$ ($x = 0 \div 0.24$) films with thicknesses from 40 to 260 nm grown on glass-ceramics based on SiO_2, Al_2O_3, CaF_2 (111) and MgO (100) substrates, and LaF_3-SrF_2 heterostructures grown on MgO (100) substrates were studied by impedance spectroscopy at temperature range from room temperature to 300 °C and at frequencies from 10^{-1} to 10^6 Hz.

It was found that there was a maximum of ionic conductivity for $La_{1-x}Sr_xF_{3-x}$ ($x = 0 \div 0.24$) solid solution films at $x \approx 0.05$. The conductivity of $La_{0.95}Sr_{0.05}F_{2.95}$ films is by 2 – 4 orders of magnitude higher than that of pure lanthanum fluoride films on the substrates of magnesium oxide, sapphire and glass-ceramics. It was also shown that there was a maximum of in-plane conductivity of LaF_3-SrF_2 heterostructures for the thickness of each layer ~ 20 nm. The activation energy was evaluated from the temperature dependencies of the DC-conductivity of the films according to Arrhenius – Frenkel law. It was 400 – 800 meV for all measured samples.

SOLID SOLUTION, TYSONITE, LANTHANUM FLUORIDE, STRONTIUM FLUORIDE, IMPEDANCE, IN-PLANE CONDUCTIVITY.

Методом импедансной спектроскопии в температурном диапазоне от 300 до 570 K и частотном диапазоне от 0.1 Гц до 1 МГц, была измерена продольная проводимость тонких пленок $La_{1-x}Sr_xF_{3-x}$ ($x = 0 \div 0{,}24$) на подложках ситалла, Al_2O_3, CaF_2 (111) и MgO (100), а также продольная проводимость гетероструктур LaF_3-SrF_2 на подложках MgO (100).

ТВЕРДЫЙ РАСТВОР, ТИСОНИТ, ФТОРИД ЛАНТАНА, ФТОРИД СТРОНЦИЯ, ИМПЕДАНС, ПРОДОЛЬНАЯ ПРОВОДИМОСТЬ.

I. Introduction

During the last decades, heterostructures based on MF_2 where M = Ca, Sr, Ba, Cd, and RF_3 where R – rare-earth elements as well as solid solutions $R_{1-x}M_xF_{3-x}$ have been actively studied [1, 2]. Based on these, the prototypes of fluoride sensors [1, 2], oxygen sensors [3, 4], batteries [3] and transistors [4] have been proposed. However, there are no reports on experiments devoted to the optimization of active components of these devices.

A new approach to modification of fluoride materials was offered by Joachim Maier and co-workers [1, 2]. Creation of BaF_2-CaF_2 heterostructures with total thickness of 450 nm and different layer thicknesses (from 200 to 10 nm) resulted in increase of ionic conductivity of the samples by two orders of magnitude compared with the conductivity of pure BaF_2

and CaF_2 bulk crystals. Modeling experimental data with Guy – Chapman and Mott – Schottky's models gave good results [1, 2] which enabled the authors to suggest a mechanism of F^- ion transport to the interfaces increasing the in-plane conductivity.

The purpose of this experimental work is growing and investigating in-plane conductivity of $La_{1-x}Sr_xF_{3-x}$ solid solutions on the different types of the substrates such as glass-ceramics, Al_2O_3 and CaF_2 (111), and LaF_3-SrF_2 heterostructures on MgO (100) substrates.

II. Sample Preparation and Experimental Technique

Films of pure LaF_3, SrF_2 and solid solution $La_{1-x}Sr_xF_{3-x}$ were grown by molecular beam epitaxy (MBE) in an ultrahigh vacuum chamber, the base pressure inside being maintained below 10^{-8} Pa. Epi-ready MgO (100) substrates with the size of $10 \times 10 \times 0.5$ mm, and rectangular CaF_2(111) substrates with the sides parallel to the [1–10] and [11–2] directions were used. Single crystal CaF_2(111) substrates (8×10 mm) were prepared for growth by polishing their front side in a NH_4F water solution. Glass-ceramic based on SiO_2 and α-Al_2O_3 substrates were produced under industrial conditions. After pre-treatment with isopropyl alcohol and degreasing in the peroxide-ammonia solution, substrates were placed in the growth chamber on the front of Knudsen sells where they were heated for 20 min at 200 °C. In addition, MgO and α-Al_2O_3 substrates were then annealed to 1200 °C for 15 min. After vacuum annealing CaF_2 and glass-ceramic substrates during 10 min at 500 °C, a 200 nm buffer layer of CaF_2 was deposited at 400–800 °C on the polished side of CaF_2 substrates to smooth the surface. Ca, La and Sr fluorides were grown by evaporation of the materials in amorphous carbon crucibles. The growth chamber was equipped with a Reflection High Energy Electron Diffraction (RHEED) diffractometer for *in situ* characterization of the substrate surface prior to the growth and for monitoring the growing films. The deposition rates for evaporated fluorites were 2–3 nm/min as measured with a quartz microbalance.

There were grown solid solution $La_{1-x}Sr_xF_{3-x}$ ($x = 0 \div 0.24$) films with thicknesses from 40 to 260 nm placed on glass-ceramics, α-Al_2O_3, CaF_2 (111), MgO (100) substrates and heterostructures with different quantities of alternating LaF_3-SrF_2 layers. LaF_3 layer was the first to be grown on the substrates of MgO (100) with 200 nm total thickness for all samples. According to this thickness, the total number of LaF_3 and SrF_2 layers varied from $N = 2$ to 40. Each grown heterostructure had 200 nm of thickness. For example, if the number of layers were $N = 4$, it meant that the thickness of each (LaF_3 or SrF_2) layer was 50 nm. To apply the same quantity of ionic material, the thickness of LaF_3 was the same of SrF_2 one, and the total number of layers was even.

Later on, after short exposure to air, the gold electrodes were deposited on the grown heterostructures for electrical conductivity measurements. Interdigital Electrodes (IDE) were used for measuring in-plane conductivity of the films and heterostructures. The electrophysical parameters of the layers were measured with dielectric spectrometer Novocontrol BDS'80 in the wide temperature (300 – 570 K) and frequency (10^{-1} – 10^6 Hz) ranges. The magnitude of field strength was $V_{rms} = 50$ V/cm. The relative errors of the impedance and capacity did not exceed ~ $3 \cdot 10^{-5}$. The stability of temperature was better than 0.1 K.

III. Results and Discussion

A. The Conductivity of Substrates

Figure 1 shows the electrical conductivity

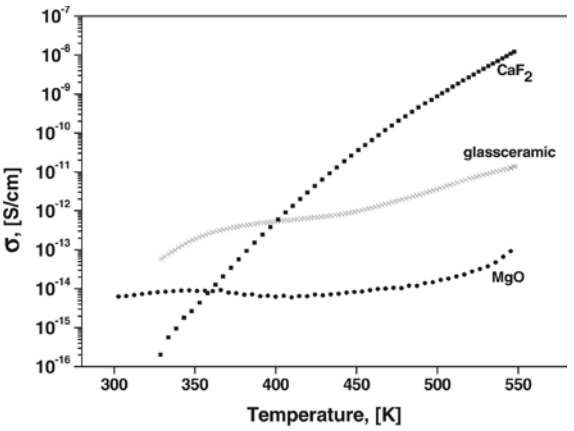

Fig. 1. Temperature dependence of the conductivity of the substrates: glass-ceramic, calcium fluoride (CaF_2) and magnesium oxide (MgO) at 0.1 Hz

behavior of CaF_2, MgO and glass-ceramic substrates, which were used in the work. Evidently, all the substrates are good dielectrics with conductivity $10^{-15} \div 10^{-11}$ S/cm in the measured temperature interval. However, the electrical conductivity of the CaF_2 substrate is strongly temperature dependent. With temperature increased by approximately 250 °C, the conductivity of CaF_2 substrate increases by 7 orders of magnitude due to calcium fluoride as an ionic conductor. Temperature behavior is well described by Arrhenius – Frenkel's law. Temperature dependences of the own conductivities of magnesium oxide and glass ceramic substrates are much smaller.

B. Comparison of the Conductivity of Thin Films Grown on the Glass-ceramic Substrates and Bulk Single Crystal

The frequency dependencies of $La_{1-x}Sr_xF_{3-x}$ thin film conductivity are shown in Fig. 2, *a*; they are typical for all examined samples. They can be divided into three regions: *1* (low frequency) – the region of conductivity increasing due to lower accumulation of charge in the electrode regions with the frequency increase, *2* (medium frequency) – frequency-independent regions and *3* (high frequency) is the universal dynamic response [1]. Analysing frequency-independent region, $\sigma(\omega)$ one can estimate the value of solid electrolyte DC-conductivity. However, such an assessment would be quite rough, more specifically DC-conductivity can be determined from the impedance hodograph (Nyquist diagram for the impedance, Fig. 2, *b*) $Z'' = f(Z')$ as

$$\sigma_{DC} = \frac{1}{R_v}\frac{d}{S},$$

where d is the distance between electrodes; S – square of the end part of heterostructure under the electrode; R_v – resistance of solid electrolytes (intersection semicircle and real part of impedance Z''). The Nyquist's plots of investigated samples consist of a semicircle and a sloped line, and this is typical for solid electrolyte systems [1].This type of the hodograph corresponds to the equivalent circuit, which consists of *RC*-chain with Warburg impedance (inset in Fig. 2, *b*) [14]. However, it characterizes the conductivity of the electro-chemical cell, which exists due to the conductivity of the film and conductivity of the substrate. The conductivity of the film can be calculated by subtracting the substrate conductivity. In our case, Kidner and co-worker's mathematical approach [15, 16] is used.

Figure 3 shows the dependence of the conductivity of $La_{1-x}Sr_xF_{3-x}$ and bulk single crystals [2]. One can see that only pure LaF_3 is a good dielectric, and even at relatively low concentrations of impurities SrF_2 ~ 1 ÷ 2 %, the conductivity of LaF_3 increases by several orders of magnitude. Both curves exhibit a

a) *b*)

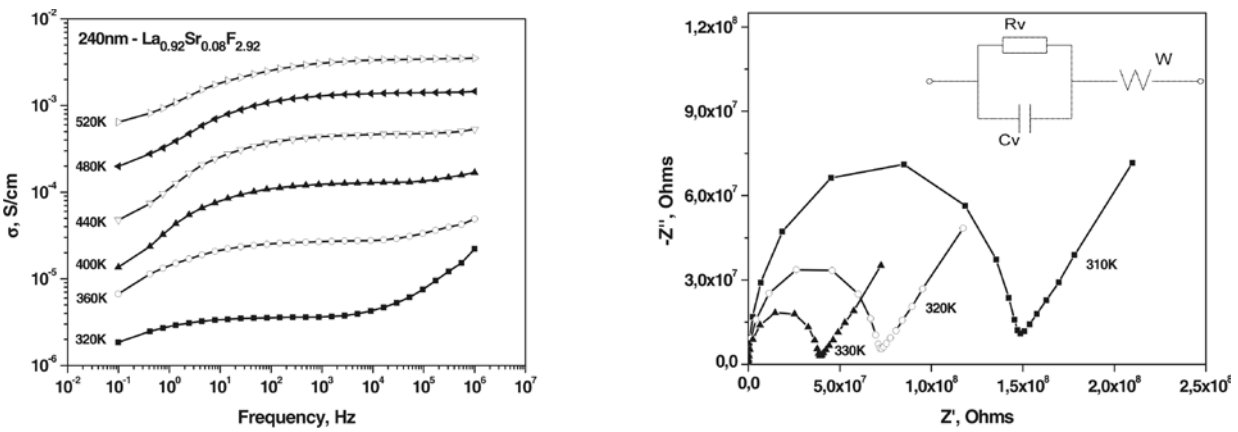

Fig. 2. *a* – Frequency dependence of the conductivity of 240 nm thick $La_{0.92}Sr_{0.08}F_{2.92}$ film at different temperatures; *b* – impedance diagrams of the same film at different temperatures.
Inset in (*b*): equivalent circuit consisting of double electric layer capacity at the interface with the electrode *Cv*, the volume resistance of the film R_v, and the Warburg element *W*

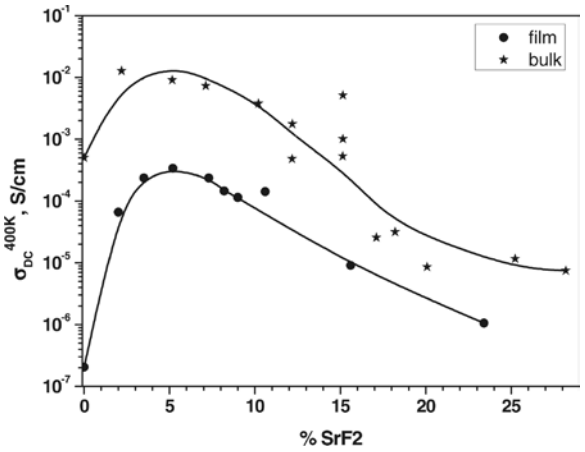

Fig. 3. Concentration dependence of the conductivity at 400 K of the $La_{1-x}Sr_xF_{3-x}$ thin films on the glass-ceramic substrates and the conductivity of bulk single crystals according to [2]

maximum of conductivity at ~ 5 % of the SrF_2 content. Conductivity of the films depending on the composition varies by four orders of magnitude, but the absolute value of the conductivity of the films is lower than the corresponding single crystal value [1, 2]. Such features can be explained by the imperfection of the crystal structure of obtained films grown at lower temperature glass-grained glass-ceramic substrates. It is not unexpected that such films show lower conductivity due to their amorphous or polycrystalline structure.

Activation energies found from the dependence of Arrhenius – Frenkel and varying from 680 meV for pure LaF_3 to 495 – 560meV for $La_{1-x}Sr_xF_{3-x}$ solid solutions, quantitatively agree with the values of activation energy of the conductivity found in [1, 2]. It should be noted that within the error bars, these values correspond to the values of the activation energy of the diffusion process obtained from the analysis of Warburg impedance at the temperatures up to 400 K. This means that the conductivity at low temperatures may be related to the diffusion mechanism [1, 2]. It is observed that the activation energy in these solid solutions strongly depends on SrF_2 content.

C. LaF_3 Thin Films on the CaF_2 and Glass-Ceramic Substrates

Epitaxial growth of $La_{1-x}Sr_xF_{3-x}$ films on CaF_2 (111) substrates is possible. However, their electric properties are different from those of the films on glass-ceramic substrates (Fig. 4). The DC-conductivity of pure LaF_3 on CaF_2 (111) substrates is higher, and it is not possible to distinguish the individual properties of the film from the substrate ones within impedance spectroscopy method. It is possible that interdiffusion of the materials leads to the formation of a solid solution in the interface of substrate and film. In this case it can be assumed that the conduction occurs along the interface and solid solution at the interface is formed. This assumption is also confirmed by the fact that the conductivity and the activation energy of conductivity for $La_{0.95}Sr_{0.05}F_{2.95}$ films on the two substrates differ a little. The highest conductivity among solid solutions based on LaF_3 has 5 % SrF_2 solid solution [2].

D. LaF_3-SrF_2 Heterostructures on MgO Substrates

The in-plane conductivity of grown heterostructures with different layer thicknesses from 100 to 5 nm are measured by impedance spectroscopy. The temperature dependencies of DC-conductivity of several grown heterostructures are shown in Fig. 5; they obey Arrhenius – Frenkel's law. The inset in this figure shows the energy activation behavior in studied samples. It is seen that the lowest activation

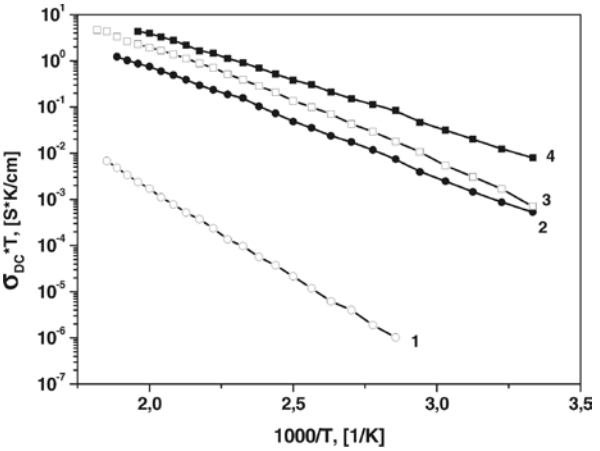

Fig. 4. *1*, *3* – DC-conductivity of thin films of pure LaF_3 and 5 % solid solution on the glass-ceramic substrates, respectively; *2*, *4* – DC-conductivity of thin films of pure LaF_3 and 5 % solid solution on the CaF_2 (111) substrates, respectively

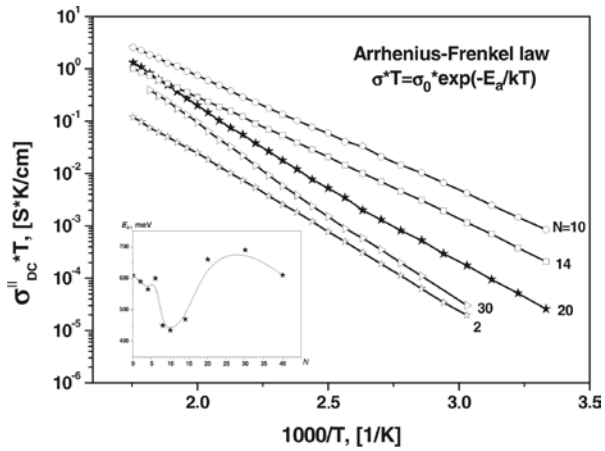

Fig. 5. Temperature behavior of the planar conductivity for several heterostructures, where N is the number of the layers.
The inset is the activation energy of the samples taken from Arrhenius – Frenkel's law

energy is demonstrated by the heterostructures with N from 6 to 10 and it equals ~430 meV. The general shape of in-plane conductivity has a peak near $N = 10$ (20 nm per layer) for all measured temperatures (Fig. 6).

For the samples with $N \geq 20$ (in which the thickness of each layer is less than 20 nm), gradual modification of the hodograph shapes is observed. Namely, the semicircle moves below the x-axis Re(Z) and the circuit can be described by equivalent circuit with CPE-element (constant phase element) and it has impedance

$$Z^*_{\mathrm{CPE}} = Z_0(j\omega)^n = \left(\frac{Z_0}{\omega^n}\right)\left[\cos\left(\frac{\pi n}{2}\right) - j\sin\left(\frac{\pi n}{2}\right)\right],$$

where $0 \leq n \leq 1$.

At $n = 0$ limit, Z^*_{CPE} does not depend on frequency and $Z_0 = R$; when $n = 1$ value Z_0 is inverse capacitance:

$$Z_0 = 1/C,$$

$$Z^*_{\mathrm{CPE}} = -\frac{1}{\omega C} \text{ [14].}$$

Thus, semicircle displacement below x-axis by an angle φ satisfies

$$\varphi = (1 - n)\ 90\ ^\circ.$$

In other words, the similar equivalent circuit broadens out of the Debay spectra and it is described by Cole – Cole spectra [3, 4]:

$$\sigma(\omega) = \sigma_\infty + \frac{\sigma_0 - \sigma_\infty}{1 + (j\omega\tau)^n}.$$

Deviation in Debay spectra for the samples $N \geq 20$ is not pronounced and $n \approx 0.85$ in the whole measured temperature range.

For comparison, Fig. 7 shows temperature behavior of planar thin film conductivity of pure LaF_3, SrF_2 and based on them $La_{1-x}Sr_xF_{3-x}$ solid solution with $x = 0.05$ and $x = 0.5$. The DC-conductivity of pure SrF_2 is estimated above 500 K only; its activation energy is 770 meV. The $La_{0.95}Sr_{0.05}F_{2.95}$ solid solution has the highest conductivity among all the possible combinations of solid solutions $LaF_3 + SrF_2$ [2], and in our case it has high conductivity with low activation energy ~420 meV. According

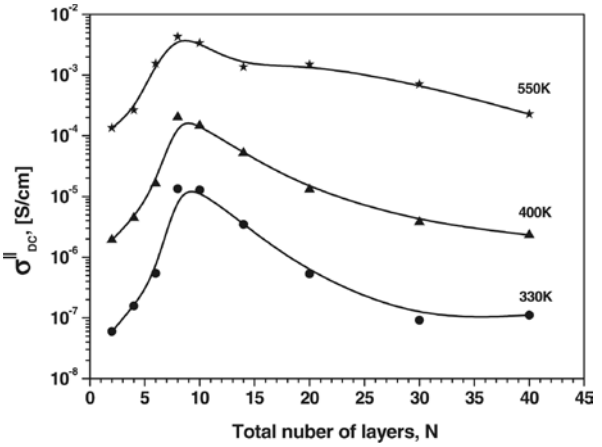

Fig. 6. Dependencies of conductivity of the heterostructures from the number of layers for different temperatures (total thickness is 200 nm)

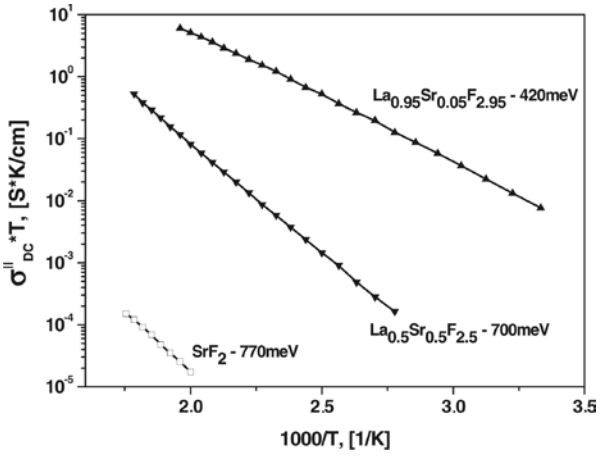

Fig. 7. The temperature behavior of the in-plane conductivity of SrF_2 films and the $La_{1-x}Sr_xF_{3-x}$ solid solutions ($x = 0.05$ and 0.5) grown on MgO (100) substrates.
The thickness of all the films is 200 nm

to [3], the 50 % solid solution of $La_{0.5}Sr_{0.5}F_{2.5}$ must have two different mixed phases: LaF_3 and defect cluster with SrF_2, separately. However, it was expected that it would be seen on the hodograph of impedance as a combination of two semicircles (two different processes of conductivity), but it is not observed in our case. RHEED does not show the characteristics associated with this fact, the diffraction patterns of the 50 % solid solution are not qualitatively different from the diffraction pattern of the 5 % solid solution.

Thus, the values of all the investigated planar DC-conductivities of the heterostructures are in the range of the conductivities of pure LaF_3 and $La_{0.95}Sr_{0.05}F_{2.95}$ solid solution. Therefore, one can assume the existence of thin interface layers enriched by F^- ions.

IV. Conclusion

The planar conductivity of $La_{1-x}Sr_xF_{3-x}$ ($x = 0 \div 0.24$) solid solution films with thicknesses from 40 to 260 nm grown on glass-ceramics, Al_2O_3, CaF_2 (111) and MgO (100), as well as heterostructures with alternating LaF_3-SrF_2 layers and total thickness of 200 nm grown on MgO (100) substrates were studied by the method of impedance spectroscopy at the temperatures ranging from room temperature to 300 °C and at frequencies from 10^{-1} to 10^6 Hz.

The highest conductivity is observed for $La_{0.95}Sr_{0.05}F_{2.95}$ films and it is hardly depends on the type of used substrates. However, the properties of pure LaF_3 on CaF_2 (111) and other substrates studied in this work are different. It may be due to the fact that the CaF_2/LaF_3 interface consists of a layer of solid solution which has been created by diffusing both components into each other.

The highest conductivity among grown on MgO (100) heterostructures is observed for the structures with $N = 10$, which corresponds to the thickness of 20 nm per each layer. This sample with 10 ordered layers of LaF_3-SrF_2 demonstrates conductivity by one order of magnitude higher than that of 50 % solid solution. Also, deviation from Debay spectra is observed in the samples with $N > 20$, it can be the result of strong mechanical stresses in the heterostructures.

The activation energies were evaluated from the temperature dependencies of the DC-conductivities of the films according to Arrhenius – Frenkel's law. The activation energies for solid solutions are ~495 – 560 meV and ~700 meV for pure LaF_3 film. The activation energies of heterostructures have the lowest values at N from 6 to 10, and they are ~430 meV, which is comparable to the activation energy for 5 % solid solution.

Acknowledgments

The work at SPbSPU was supported by Federal Program «Research and Development on High-Priority Directions of Improvement of Russia's Scientific and Technological Complex» for the years 2007–2013, Federal Program «Scientific and scientific and pedagogical shots of innovative Russia for 2009–2013»; at the Ioffe Institute it was supported by Russian Foundation for Basic Researches (grant 13-02-12429).

REFERENCES

1. **Sorokin N.I., Fominykh M.V., Krivandina E.A., Zhmurova Z.I., Sobolev B.P.** Ion transport in $R_{1-x}Sr_xF_{3-x}$ (R = La-Yb, Y) solid solutions with a LaF_3 (tysonite) structure. *Crystallography Reports*, 1996, Vol. 41, No. 4, pp. 292–310.

2. **Sorokin N.I., Sobolev B.P.** Frequency response of the low-temperature ionic conductivity of single crystals $R_{1-y}M_yF_{3-y}$ (R = La-Er; M = Ca, Sr, Ba, Cd). *Physics of the Solid State*, 2008, Vol. 50, No.3, pp. 416–421.

3. **Moritz W., Krause S., Vasiliev A.A., Godovskiy D.Yu., Malyshev V.V.** Monitoring of HF and F_2 using a field-effect sensor. *Sensors Actuators B. Chemical*, 1995, Vol. 24–25, pp. 194–196.

4. **Fergus Jeffrey W.** The application of solid fluoride electrolytes in chemical sensors. *Sensors Actuators B Chemical*, 1997, Vol. 42, pp. 119–130.

5. **Tan G.L., Wu X.J., Wang L.R., Chen Y.Q.** Investigation for oxygen sensor of LaF_3 thin film. *Sensors Actuators B. Chemical*, 1996, Vol. 34, pp. 417–421.

6. **Katsube T., Hara M., Serizawa I., Ishibashi N., Adachi N., Miura N., Yamazoe N.** MOS-type micro-oxygen sensor using LaF_3 workable at room temperature. *Japanese Journal of Applied Physics*, 1990, Vol. 29, No. 8, pp. 1392–1395.

7. **Reddy M.A., Fichtner M.** Batteries based on fluoride shuttle. *Journal of Material Chemistry*, 2011, Vol. 21, No. 43, pp. 17009–17548.

8. **Na X., Niu W., Li H., Xie J.** A novel dissolved

oxygen sensor based on MISFET structure with Pt-LaF_3 mixture film. *Sensors Actuators B. Chemical*, 2002, Vol. 87, pp. 222–225.

9. **Sata N.**, **Eberman K., Eberl K., Maier J.** Mesoscopic fast ion conduction in nanometre-scale planar heterostructures. *Nature*, 2000, Vol. 408, pp. 946–949.

10. **Guo X.X.**, **Matei I., Lee J.-S., Maier J.** Ion conduction across nanosized CaF/BaF multilayer heterostructures. *Applied Physics Letters*, 2007, Vol. 91. p. 103102.

11. **Guo X.X., Matei I., Jamnik J., Lee J.S., Maier J.** Defect chemical modeling of mesoscopic ion conduction in nanosized CaF_2/BaF_2 multilayer heterostructures. *Physical Review B*, 2007, Vol. 76, p. 125429.

12. **Guo X.X.**, **Maier J.** Comprehensive modeling of ion conduction of nanosized CaF2/BaF2 multilayer heterostructures. *Advanced Functional Materials*, 2009, Vol. 19, pp. 96–101.

13. **Ahmad M.M.**, **Yamada K., Okuda T.** Fluoride ion diffusion of superionic PbSnF4 studied by nuclear magnetic resonance and impedance spectroscopy. *J. Phys.: Condens. Matter*, 2002, Vol. 14, p. 7233.

14. **Ivanov-Schitz A.K.**, **Murin I.V.** *Solid State Ionics*: Vol. 1. St. Petersburg, SPbSU, 2000. 617 p. (rus)

15. **Kidner N.J., Homrighaus Z.J., Mason T.O., Garboczi E.J.** Modeling interdigital electrode structures for the dielectric characterization of electroceramic thin films. *Thin Solid Films*, 2006, No. 496, pp. 539–545.

16. **Kidner N.J., Meier A., Homrighaus Z.J., Wessels B.W., Mason, T.O., Garboczi E.J.** Complex electrical (impedance/dielectric) properties of electroceramic thin films by impedance spectroscopy with interdigital electrodes. *Thin Solid Films*, 2007, No. 515, pp. 4588–4595.

17. **Sher A.**, **Solomon R., Lee K., Muller M.W.** Transport Properties of LaF_3. *Physical Review*, 1966, Vol. 144, No. 2, pp. 593–604.

18. **Wei Y.Z., Sridhar S.** A new graphical representation for dielectric data. *J. Chem. Phys*, 1993, 99(4), p. 3119.

19. **Vergent'ev T.Yu.**, **Koroleva E.Yu., Kurdyukov D.A., Naberezhnov A.A., Filimonov A.V.** Behavior of the low-frequency conductivity of silver iodide nanocomposites in the superionic phase transition region. *Physics of the Solid State*, 2013, Vol. 55, No. 1, pp. 175–180.

20. **Ivanov-Schitz A.K.**, **Sorokin N.I., Sobolev B.P., Fedorov P.P.** Ionic transport in systems MF2-RF3 (M = Ca, Sr, Ba; R = La-Ln). *Proc. Int. symp. on systems with the fast ionic transport.* Bratislava, Smolenia, 1985, p. 99–103.

СПИСОК ЛИТЕРАТУРЫ

1. **Сорокин Н.И., Фоминых М.В., Кривандина Е.А., Жмурова З.И., Соболев Б.П.** // Кристаллография. 1996. Т. 41. № 2. С. 310 – 315.

2. **Сорокин Н.И., Соболев Б.П.** Частотные зависимости ионной проводимости монокристаллов $R_{1-y}M_yF_{3-y}$ (R = La·Er, M = Ca, Sr, Ba, Cd) при низких температурах // ФТТ. 2008. Т. 50. Вып. 3. С. 402 – 407.

3. **Moritz W., Krause S., Vasiliev A.A., Godovskiy D.Yu., Malyshev V.V.** Monitoring of HF and F_2 using a field-effect sensor. *Sensors Actuators B. Chemical*, 1995, Vol. 24–25, pp. 194–196.

4. **Fergus Jeffrey W.** The application of solid fluoride electrolytes in chemical sensors. *Sensors Actuators B Chemical*, 1997, Vol. 42, pp. 119–130.

5. **Tan G.L., Wu X.J., Wang L.R., Chen Y.Q.** Investigation for oxygen sensor of LaF_3 thin film. *Sensors Actuators B. Chemical*, 1996, Vol. 34, pp. 417–421.

6. **Katsube T., Hara M., Serizawa I., Ishibashi N., Adachi N., Miura N., Yamazoe N.** MOS-type micro-oxygen sensor using LaF_3 workable at room temperature. *Japanese Journal of Applied Physics*, 1990, Vol. 29, No. 8, pp. 1392–1395.

7. **Reddy M.A., Fichtner M.** Batteries based on fluoride shuttle. *Journal of Material Chemistry*, 2011, Vol. 21, No. 43, pp. 17009–17548.

8. **Na X., Niu W., Li H., Xie J.** A novel dissolved oxygen sensor based on MISFET structure with Pt-LaF_3 mixture film. *Sensors Actuators B Chemical*, 2002, Vol. 87, pp. 222–225.

9. **Sata N.**, **Eberman K., Eberl K. & Maier J**. Mesoscopic fast ion conduction in nanometre-scale planar heterostructures. *Nature*, 2000, Vol. 408, pp. 946–949.

10. **Guo X.X.**, **Matei I., Lee J.-S., Maier J.** Ion conduction across nanosized BaF multilayer heterostructures. *Applied Physics Letters*, 2007, Vol. 91. p. 103102.

11. **Guo X.X., Matei I., Jamnik J., Lee J.S., Maier, J.** Defect chemical modeling of mesoscopic ion conduction in nanosized CaF_2/BaF_2 multilayer heterostructures. *Physical Review B*, 2007, Vol. 76, p. 125429.

12. **Guo X.X.**, **Maier J.** Comprehensive modeling of ion conduction of nanosized CaF_2/BaF_2 multilayer heterostructures. *Advanced Functional Materials*, 2009, Vol. 19, pp. 96–101.

13. **Ahmad M.M.**, **Yamada K., Okuda T.** Fluoride ion diffusion of superionic $PbSnF_4$ studied by nuclear magnetic resonance and impedance spectroscopy. *J. Phys.: Condens. Matter*, 2002,

Vol. 14, p. 7233.

14. **Иванов-Шиц А.К., Мурин И.В.** Ионика твердого тела. Т. 1. СПб.: Изд-во СПбГУ, 2000. 616 с.

15. **Kidner N.J., Homrighaus Z.J., Mason T.O., Garboczi E.J.** Modeling interdigital electrode structures for the dielectric characterization of electroceramic thin films. *Thin Solid Films*, 2006, No. 496, pp. 539–545.

16. **Kidner N.J., Meier A., Homrighaus Z.J., Wessels B.W., Mason T.O., Garboczi E.J.** Complex electrical (impedance/dielectric) properties of electroceramic thin films by impedance spectroscopy with interdigital electrodes. *Thin Solid Films*, 2007, No. 515, pp. 4588–4595.

17. **Sher A., Solomon R., Lee K., Muller M.W.** Transport properties of LaF_3. *Physical Review*, 1966, Vol. 144, No. 2, pp. 593–604.

18. **Wei Y.Z., Sridhar S.** A new graphical representation for dielectric data. *J. Chem. Phys*, 1993, Vol. 99, No. 4, p. 3119.

19. **Вергентьев Т.Ю., Королева Е.Ю., Курдюков Д.А., Набережнов А.А., Филимонов А.В.** Поведение низкочастотной проводимости нанокомпозитного иодида серебра в области суперионного фазового перехода// ФТТ. 2013. Т. 55. Вып. 1. С. 157 – 162.

20. **Ivanov-Schitz A.K., Sorokin N.I., Sobolev B.P., Fedorov P.P.** Ionic transport in systems MF_2-RF_3 (M = Ca, Sr, Ba; R=La-Ln). *Proc. Int. symp. on systems with the fast ionic transport.* Bratislava, Smolenia, 1985, p. 99–103.

ВЕРГЕНТЬЕВ Тихон Юрьевич – *аспирант кафедры физической электроники Санкт-Петербургского государственного политехнического университета.*
195251, Россия, Санкт-Петербург, Политехническая ул., 29
tikhon.v@gmail.com

БАНЩИКОВ Александр Гаврилович – *кандидат физико-математических наук, старший научный сотрудник Физико-технического института им. А.Ф. Иоффе РАН.*
194021, Россия, Санкт-Петербург, Политехническая ул., 26
aban88@bk.ru

КОРОЛЕВА Екатерина Юрьевна – *кандидат физико-математических наук, старший научный сотрудник Физико-технического института им. А.Ф. Иоффе РАН, доцент кафедры физической электроники Санкт-Петербургского государственного политехнического университета.*
194021, Россия, Санкт-Петербург, Политехническая ул., 26
e.yu.koroleva@mail.ioffe.ru

СОКОЛОВ Николай Семенович – *доктор физико-математических наук, ведущий научный сотрудник Физико-технического института им. А.Ф. Иоффе РАН.*
194021, Россия, Санкт-Петербург, Политехническая ул., 26
nsokolov@fl.ioffe.ru

ЗАХАРКИН Максим Валерьевич – *студент Института физики, нанотехнологий и телекоммуникаций Санкт-Петербургского государственного политехнического университета.*
195251, Россия, Санкт-Петербург, Политехническая ул., 29
maxim.zakh@gmail.com

ОКУНЕВА Нина Михайловна – *кандидат физико-математических наук, старший научный сотрудник Физико-технического института им. А.Ф. Иоффе РАН.*
194021, Россия, Санкт-Петербург, Политехническая ул., 26
nina.okuneva@mail.ioffe.ru

UDC 538.975: 620.22 - 022.53

S.O. Lukianov [1], N.V. Andreeva [1], S.B. Vakhrushev [2]
A.V. Filimonov [1], M.C. Wurz [3], L. Rissing [3]

[1] St.Petersburg State Polytechnical University
29 Politekhnicheskaya St., St. Petersburg, 195251, Russia
[2] Ioffe Physical Technical Institute,
26 Politekhnicheskaya St., St. Petersburg, 194021, Russia
[3] Leibniz Universität Hannover, Center for Production Technology,
Institute for Micro Production Technology,
An der Universität 2, 30823 Garbsen, Germany.

SURFACE POLAR NANOREGIONS STRUCTURE OF POTASSIUM TANTALATE DOPED WITH LITHIUM OBTAINED AT CRYOGENIC TEMPERATURES USING PIEZORESPONSE FORCE MICROSCOPY TECHNIQUE

С.О. Лукьянов, Н.В. Андреева, С.Б. Вахрушев,
А.В. Филимонов, М.К. Вюрц, Л. Риссинг

ПОВЕРХНОСТНАЯ СТРУКТУРА ПОЛЯРНЫХ НАНООБЛАСТЕЙ ТАНТАЛАТА КАЛИЯ, ДОПИРОВАННОГО ЛИТИЕМ, ПОЛУЧЕННАЯ ПРИ КРИОГЕННЫХ ТЕМПЕРАТУРАХ С ПОМОЩЬЮ МЕТОДА СИЛОВОЙ МИКРОСКОПИИ ПЬЕЗООТКЛИКА

In the present work we have used a piezoresponse force microscopy (PFM) technique for the study of the polar surface structure of potassium tantalate single crystal doped with Li^+ ions (KLT-3 %) at low temperatures. The results of our measurements confirmed the existence of polar nanoregions in the temperature range of 10 – 80 K. We obtained a temperature evolution of the nanoregions and estimated their dimensions. Resolving polar nanoregions structure of KLT-3% crystal in zero-field heating after zero-field cooling regime could indicate the existence of ferroelectric phase transition in this material.

RELAXORS, POTASSIUM TANTALATE DOPED WITH LITHIUM, LOW TEMPERATURE PIEZORESPONSE FORCE MICROSCOPY.

В настоящей работе мы использовали методику силовой микроскопии пьезоотклика для изучения полярной структуры поверхности монокристалла танталата калия, допированного ионами лития Li^+ (KLT-3%) при низких температурах. Результаты наших измерений подтвердили существование полярных нанообластей в температурном диапазоне 10 – 80 K; мы также проследили температурную эволюцию нанообластей и оценили их размеры. Разрешение структуры полярных нанообластей кристалла KLT-3% в режиме нагрева без поля после охлаждения в присутствии поля могло бы свидетельствовать о сегнетоэлектрическом фазовом переходе в этом материале.

РЕЛАКСОРЫ; ТАНТАЛАТ КАЛИЯ, ДОПИРОВАННЫЙ ЛИТИЕМ; НИЗКОТЕМПЕРАТУРНАЯ СИЛОВАЯ МИКРОСКОПИЯ ПЬЕЗООТКЛИКА.

I. Introduction

Nowadays, new prospective functional materials are demanded as our science and technologies are being improved. One of the most interesting materials by now is potassium tantalate. Known as KTO, potassium tantalate is

a quantum paraelectric. It has no ferroelectric phase in spite of continuous growth of dielectric constant with decreasing temperature down to near 0 K [4]. As it is known, zero point fluctuations prevent completing a phase transition [4].

Doping of KTO with lithium alters its properties significantly. Lithium ions take place of potassium in a perovskite structure. KTO doped with lithium (KTL) shows dipole glass behavior at low temperatures [4]. This new material has a ferroelectric phase. It also demonstrates giant dielectric and piezoelectric constants and therefore can be useful for a great variety of applications in electronics, optoelectronics and electroholography for systems where absorption and refraction index are controlled by external electric field, and selectivity of wavelength and polarization of light is necessary.

NMR [1], pyroelectric [2], ultrasound [3] and *X*-ray diffraction [4] measurements confirm that Li ion occupies the off-center position which is shifted by 1.009 Å along one of the six equivalent [001] directions [5].

Measuring the temperature dependence of birefringence gave a critical lithium concentration around 2.2 % [4]. Above the critical concentration, KLT undergoes a ferroelectric phase transition [2, 6, 7].

X-ray diffraction performed on a high resolution diffractometer evidences two steps of tetragonal deformation. First, small deformation appears at a Burns temperature T_d (~100 K for KLT-2.6 %, and ~140 K for KLT-6.8 %). Second, significant deformation takes place at a ferroelectric transition temperature T_p (48 K for KLT-2.6 %, and 90 K for KLT-6.8 %). In a temperature region between T_p and T_d (pretransitional region) polar nanoregions appear and second harmonic generation microscopy shows no macroscopic polarization. Neutron scattering confirms these observations [4].

One of the most important characteristics of KLT – remarkable dielectric dispersion in a low frequency range – is thought to originate from the existence of polar nanoregions (PNR) which appear at a characteristic temperature (Burns temperature) higher than the peak temperature of the dielectric constant. The technique of second harmonic generation confirmed existence of PNR. But application of this method is limited by the minimal size of polar nanoregions under research.

The nature of polar state in a low temperature region is not clearly understood, and the mechanism of polar nanoregions appearance is not determined yet.

Piezoresponse force microscopy (PFM) technique can be a powerful tool for the investigation of PNR distribution along the KLT surface.

II. Materials and Method

All the measurements were carried out on the 8 × 8 × 3 mm^3 KLT single crystal grown by Czochralski technique . The concentration of doping Li^+ ions was 3 %. KLT-3 % crystal was polished with Struers Tegramin-30 (Struers A/S, Denmark), chemically cleaned with isopropanol and rinsed with distilled water. The roughness of the sample surface was measured with atomic-force microscope (AFM) Nano-DST (Pacific Nanotechnology, USA) and estimated over the topographical image of the surface 15×15 μm in size. Obtained roughness of the sample surface was 15 nm. According to our preliminary PFM low temperature (LT) measurements on KLT samples, the quality of the crystal surface polishing influences significantly the results due to the crosstalk of the topography and piezoresponse signals. So, we ensure the scratch-free deformation-free surface of the KLT crystal by polishing it with oxide polishing suspension after usual for AFM

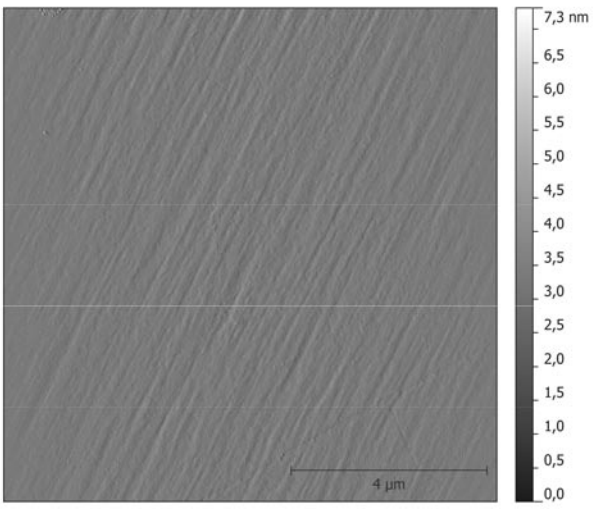

Fig. 1. Topography of KLT-3 % single crystal taken at RT with Nano DST AFM

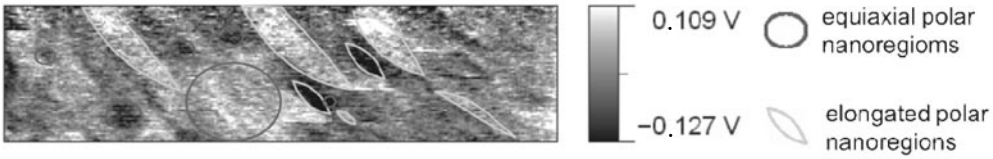

Fig. 2. Amplitude of piezoresponse signal from the surface of KLT-3 % taken at 15 K

application polishing with diamond suspension. The surface topography is depicted in Fig. 1. Presented image demonstrates complete absence of scratches remained after mechanical polishing with abrasive suspension like diamond suspension.

The surface piezoresponse of the KLT-3 % crystal was measured using a cryogenic atomic-force microscope AttoAFM I (Attocube Systems, Germany). The AttoAFM I microscope works by scanning the sample below a fixed cantilever and by measuring its deflection using a fiber based optical interferometer. A cryogenic AFM insert is combined with top-loading low vibration Helium-free cryostat. All measurements are done in He atmosphere under normal pressure condition.

To implement PFM technique with AttoAFM I microscope, we use an external lock-in amplifier SR844 (Stanford Research Systems, CA) and a function generator FC120 (Yokogawa Electric Corporation, Japan). The amplitude and frequency of external ac voltage were 3 V (peak-to-peak) and 63 kHz, respectively. Controlling ferroelectric sample state was done under conditions of the tip-surface local contact resonance. This allowed enhancing the piezoresponse from the surface by the cantilever Q-factor times [8]. All measurements were done in the temperature range of 10 – 295 K.

For measuring in PFM regime, we use soft n-type Si cantilevers (MicroMasch, Bulgaria) with the resonant frequency of 65 kHz, k constant of 0.5 N/m and tip curvature radius of 8 nm. Choice of a proper cantilever for PFM measurements was conditioned by a series of preliminary PFM LT measurements. These measurements indicated that stiff cantilevers, ensuring good tip-surface contact and thus usually preferred for PFM measurements, in our case damaged the crystal surface. Cantilevers covered with conducting layer did not provide a stable scanning in PFM regime apparently due to charge accumulation in a scanning process. The best results of LT PFM measurements were obtained with soft cantilevers without conducting coverage and with impurity conductivity.

III. Experimental Results

According to the results of PFM measurements, polar domains with weak piezoresponse were found (Fig. 2) at LT on the KLT-3 % surface.

Observed polar nanoregions (PNRs) were different in dimensions, shape and the direction of polarization. PNRs are mostly elongated, but almost equiaxial polar areas could be found as well among them. Dimensions of elongated PNRs varied in the range of 20 – 100 nm in width and of 0.1 – 1.5 μm in length. The diameter of the equiaxial regions is usually limited by the size of 50 nm.

The temperature evolution of surface piezoresponse was traced. According to the results of our measurements, we can conclude that PNRs are observed in the temperature range of 10 – 80 K. Below 40 K PNRs are uniformly distributed over the KLT surface (Fig. 3, *a*, *b*). At temperatures below 40 K a clear contrast in PFM amplitude and phase signal could be obtained, which is evident from well-determined localization of the PNRs and the absence of preferable direction of the polarization.

At 40 K a significant reduction in the PFM contrast from PNRs was obtained; in some nanoregions drastic decrease in the intensity of piezoresponse signal from the center of the nanoregions could be seen. Above 80 K (Fig. 3, *c*), the peizoresponse has vanished. The remnant PFM signal at 80 K is originated from the topographical crosstalk. Further temperature increase leads to evanescence of PNRs on the KLT-3 % single crystal surface (Fig. 3, *d*).

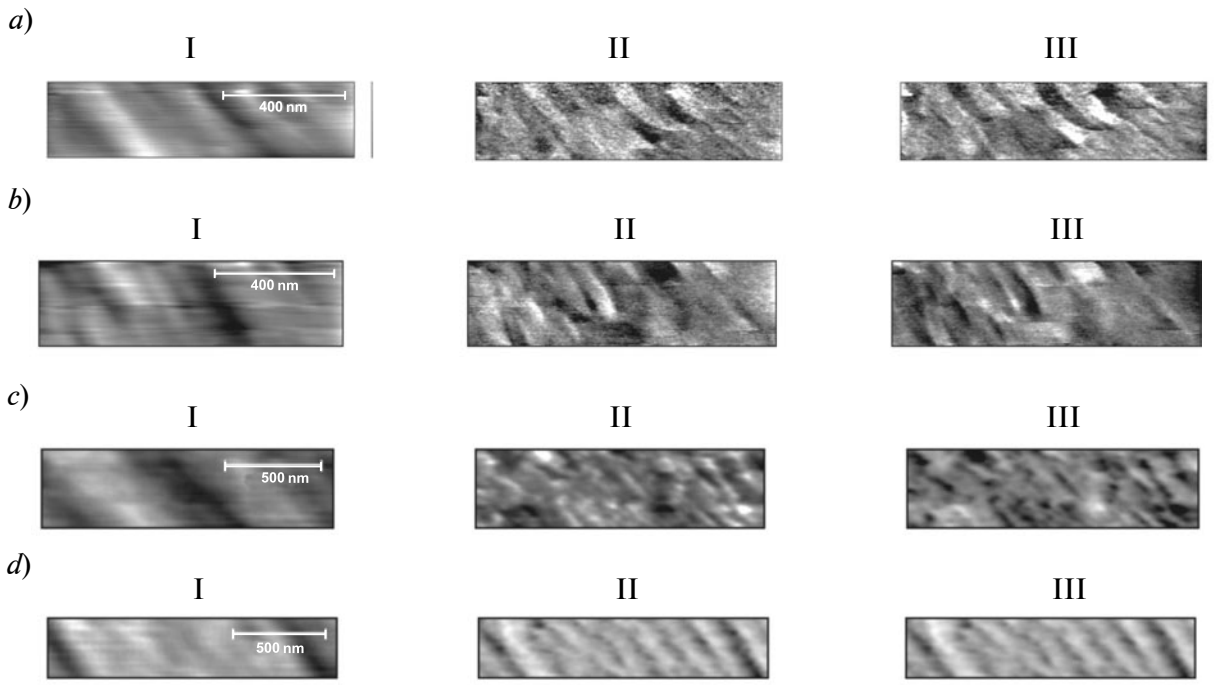

Fig. 3. Piezoresponse from the KLT-3 % single crystal in the temperature range of 10 – 295 K: 15 K (*a*), 25 K (*b*), 85 K (*c*), 295 K (*d*).
I – topography of the sample, II, III – phase and amplitude of piezoresponse signal from the surface of the sample

IV. Discussion

According to our experimental results, PNRs are visualized with PFM technique on the surface of KLT-3 % single crystal in the temperature range of 10 – 80 K. These nanoregions are distributed homogeneously over the surface, their dimensions varying from 15 nm to 1.5 μm. Comparison with the earlier results of polar structure investigation of KLT samples [4] lets us make a conclusion that the PNRs on the KLT surface are visualized without external field for the first time with PFM. In earlier works with SHG microscopy technique it was indicated that PNRs appeared on the surface of KLT-2.6 % after field cooling (FC) process at low temperatures. Thus it was supposed that the ground state of KLT is inhomogeneous, i. e. the polar phase coexists with non-polar cubic phase. Taking into account that in our measurements we resolved PNRs surface structure at LT in the absence of field, it could be concluded that KLT-3 % undergoes a ferroelectric phase transition probably around $T = 40$ K. We cannot unambiguously identify the KLT state in the temperature range of 40–80 K. Presumably, it could be considered as a cluster polar glass, but understanding the KLT-3 % phase in this temperature range further experiments is necessary. Our results are in a good agreement with those of temperature dependence of birefringence measured on KLT samples by W. Kleeman et al. and published in [9–11]. It was shown there that the critical Li^+ concentration above which KLT undergoes a ferroelectric phase transition is 2.2 % in the temperature range of 40–50 K.

Using the PFM technique we could visualize the distribution of PNRs on the surface of KLT single crystal, characterize their dimensions and shapes and trace the temperature evolution of these PNR in the temperature range of 10–80 K.

The work at SPbSPU was supported by Federal Program «Research and Development on High-Priority Directions of Improvement of Russia's Scientific and Technological Complex» for the years 2007–2013, Federal Program «Scientific and research and educational personnel of innovative Russia for 2009 – 2013» and by a grant of the St. Petersburg government.

REFERENCES

1. **Hochli T., Van der Klink J.J., Rytz D.** Condensation of random-site electric dipoles: Li in $KTaO_3$. *Phys. Rev. Lett.*, 1980, Vol. 45, pp. 1884–1887.

2. **Hochli U.T., Weibel H.E., Boatner L.A.** Stabilisation of polarised clusters in $KTaO_3$ by Li defects: formation of a polar glass. *J.Phys. C*: *Solid State Phys.*, 1979, Vol. 12, pp. L563–L567.

3. **Hochli U.T., Weibel H.E., Rehwald W.** Elastic and dielectric-dispersion in the dipole glass $K_{1-x}Li_xTaO_3$ *J.Phys. C*, 1982, Vol. 15, pp. 6129–6140.

4. **Yokota H., Uesu Y., Malibert C., Kiat J.M.** Second harmonic generation and X-ray diffraction studies of the pretransitional region and polar phase in relaxor $K_{(1-x)}$ Li_xTaO_3. *Phys. Rev. B*, 2007. Vol. 75, pp. 184113 (8 p.).

5. **Prosandeev S.A., Cockayne E., Burton B.P.** Energetics of Li atom displacements in $K_{1-x}Li_xTaO_3$: First-principles calculations. *Phys. Rev. B*, 2003, Vol. 68, pp. 014120 (13 p.).

6. **Yacoby Y., Linz A.** Vibrational properties of $KTaO_3$ at critical points in the Brillouin zone. *Phys. Rev. B*, 1974, Vol. 9, pp. 2723–2742.

7. **Yacoby Y., Just S.** Differential Raman scattering from impurity soft modes in mixed crystals of $K_{1-x}Na_xTaO_3$ and $K_{1-x}Li_xTaO_3$. *Solid State Commun.*, 15, 1974, pp. 715–718.

8. **Pliastsov S.A., Andreeva N.V., Filimonov A.V.** Low-temperature surface piezoelectricity in strontium titanate ceramics via piezoresponse force microscopy. *St. Petersburg State Polytechnical University Journal: Physics and Mathematics*, 2012, No. 1(141), pp. 7–12. (rus)

9. **Kleemann W., Kutz S., Rytz D.** Cluster glass and domain state properties of $KTaO_3$:Li. *Europhys. Lett.*, 1987, Vol. 4, pp. 239–245.

10. **Kleemann W., Kutz S., Schafer F.J., Rytz D.** Strain-induced quadrupolar ordering of dipole-glass-like $K_{1-x}Li_xTaO_3$. *Phys. Rev. B*, 1988, Vol. 37, p. 5856.

11. **Schremmer H., Kleemann W., Rytz D.** Field-induced sharp ferroelectric phase-transition in $K_{0.937}Li_{0.063}TaO_3$. *Phys. Rev. Lett.*, 1989, Vol. 62, pp. 1869–1899.

СПИСОК ЛИТЕРАТУРЫ

1. **Hochli T., Van der Klink J.J., Rytz D.** Condensation of random-site elecric dipoles: Li in $KTaO_3$. *Phys. Rev. Lett.,* 1980, Vol. 45, pp. 1884–1887.

2. **Hochli U.T., Weibel H.E., Boatner L.A.** Stabilisation of polarised clusters in $KTaO_3$ by Li defects: formation of a polar glass. *J. Phys. C. Solid State Phys.*, 1979, Vol. 12, pp. L563–L567.

3. **Hochli U.T., Weibel H.E., Rehwald W.** Elastic and dielectric-dispersion in the dipole glass $K_{1-x}Li_xTaO_3$ *J. Phys. C.*, 1982, Vol. 15, pp. 6129–6140.

4. **Yokota H., Uesu Y., Malibert C., Kiat J.M.** Second harmonic generation and X-ray diffraction studies of the pretransitional region and polar phase in relaxor $K_{(1-x)}$ Li_xTaO_3. *Phys. Rev. B.*, 2007. Vol. 75, pp. 184113.

5. **Prosandeev S.A., Cockayne E., Burton B.P.** Energetics of Li atom displacements in $K_{1-x}Li_xTaO_3$: First-principles calculations. *Phys. Rev. B.* 2003, Vol. 68, p. 014120.

6. **Yacoby Y., Linz A.** Vibrational properties of $KTaO_3$ at critical points in the Brillouin zone. *Phys. Rev. B.*, 1974, Vol. 9, pp. 2723–2742.

7. **Yacoby Y., Just S.** Differential Raman scattering from impurity soft modes in mixed crystals of $K_{1-x}Na_xTaO_3$ and $K_{1-x}Li_xTaO_3$. *Solid State Commun.*, 1974, Vol. 15, pp. 715–718.

8. **Андреева Н.В., Плясцов С.А., Филимонов А.В.** Исследование поверхностного пьезоотклика керамики титаната стронция методами силовой микроскопии пьезоотклика при низких температурах// Научно-технические ведомости СПбГПУ. Физико-математические науки. 2012. № 1 (141). С. 7–12.

9. **Kleemann W., Kutz S., Rytz D.** Cluster glass and domain state properties of $KTaO_3$:Li. *Europhys. Lett.*, 1987, Vol. 4, pp. 239–245.

10. **Kleemann W., Kutz S., Schafer F.J., Rytz D.** Strain-induced quadrupolar ordering of dipole-glass-like $K_{1-x}Li_xTaO_3$. *Phys. Rev. B.*, 1988, Vol. 37, p. 5856.

11. **Schremmer H., Kleemann W., Rytz D.** Field-induced sharp ferroelectric phase-transition in $K_{0.937}Li_{0.063}TaO_3$. *Phys. Rev. Lett.*, 1989, Vol. 62, pp. 1869–1899.

ЛУКЬЯНОВ Сергей Олегович – *сотрудник кафедры физической электроники Санкт-Петербургского государственного политехнического университета.*

195251, Россия, г. Санкт-Петербург, Политехническая ул., 29

serjluk4@gmail.com

АНДРЕЕВА Наталья Владимировна – *кандидат физико-математических наук, доцент кафедры физической электроники Санкт-Петербургского государственного политехнического университета.*
195251, Россия, г. Санкт-Петербург, Политехническая ул., 29
nvandr@gmail.com

ВАХРУШЕВ Сергей Борисович – *доктор физико-математических наук, профессор, заведующий лабораторией нейтронных исследований Физико-технического института им. А.Ф. Иоффе РАН.*
194021, Россия, г. Санкт-Петербург, Политехническая ул., 26

ФИЛИМОНОВ Алексей Владимирович – *доктор физико-математических наук, доцент, доцент кафедры физической электроники Санкт-Петербургского государственного политехнического университета.*
195251, Россия, г. Санкт-Петербург, Политехническая ул., 29
filimonov@rphf.spbstu.ru

ВЮРЦ Марк Кристофер – *доктор инженерных наук, главный инженер Института микротехнологий Университета Вильгельма Лейбница.*
30823, Германия, Гарбсен, Университет, 2

РИССИНГ Лутц – *доктор инженерных наук, профессор, директор Института микротехнологий Университета Вильгельма Лейбница.*
30823, Германия, Гарбсен, Университет, 2

UDC 536.421

E.N. Lushin, R.A. Castro

Herzen State Pedagogical University of Russia
48 Moyka Emb., St. Petersburg, 191186, Russia

DETERMINATION OF THE GLASS TRANSITION TEMPERATURE IN POLYMER COMPOSITES AND SYSTEMS

E.N. Лушин, R.A. Кастро

ОПРЕДЕЛЕНИЕ ТЕМПЕРАТУРЫ СТЕКЛОВАНИЯ ПОЛИМЕРНЫХ КОМПОЗИЦИОННЫХ МАТЕРИАЛОВ И СИСТЕМ

The results of the study of the frequency dependence of the dielectric constant in a wide range of temperature in tetrazole polymers are presented. It has been found that the temperature at which the dielectric constant changes sharply in all systems is the glass transition temperature.

TETRAZOLE POLYMERS, GLASS TRANSITION TEMPERATURE, DIELECTRIC RELAXATION.

Представлены результаты исследования частотной зависимости диэлектрической проницаемости в широком интервале температур в тетразолсодержащих полимерах. Обнаружено, что температура, при которой происходит смена характера зависимости обратной величины диэлектрической проницаемости от температуры, для всех изученных нами систем совпадает с их температурой стеклования.

ТЕТРАЗОЛСОДЕРЖАЩИЕ ПОЛИМЕРЫ, ТЕМПЕРАТУРА СТЕКЛОВАНИЯ, ДИЭЛЕКТРИЧЕСКАЯ РЕЛАКСАЦИЯ.

The physical properties of the polymer in glass state are significantly different from the same properties in rubbery state. The conventional boundary between these two states is the glass transition temperature T_g , which is the most important characteristic of amorphous polymers introduced by Uberrighter. Under the glass transition temperature we mean the temperature under which the viscosity of the polymer is no less than 10^{12} Pa·s. This temperature is also understood as the temperature below which the motion of chain segments of polymer molecules is «frozen» [1].

There are many methods of experimental determination of glass transition temperature. The measurement of mechanical and dielectric loss is among them. The use of the dielectric method can be sometimes difficult because measuring the temperature-frequency dependence of the dielectric loss in low-frequency region can cause certain problems. That is why it is important to expand the possibilities of dielectric spectroscopy method to determine T_g. This paper suggests using the temperature dependence of the inverse value of the dielectric permeability ($1/\varepsilon_1$) as a criterion to estimate the value of T_g.

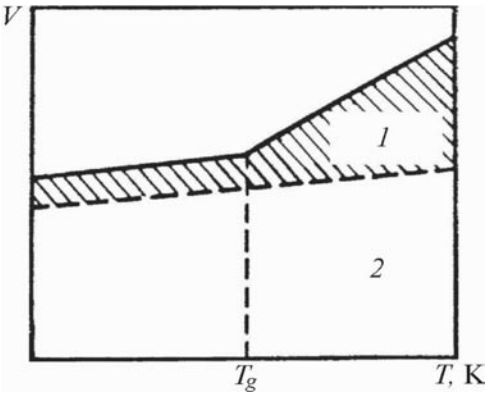

Fig. 1. The temperature dependence of the specific volume of amorphous solids

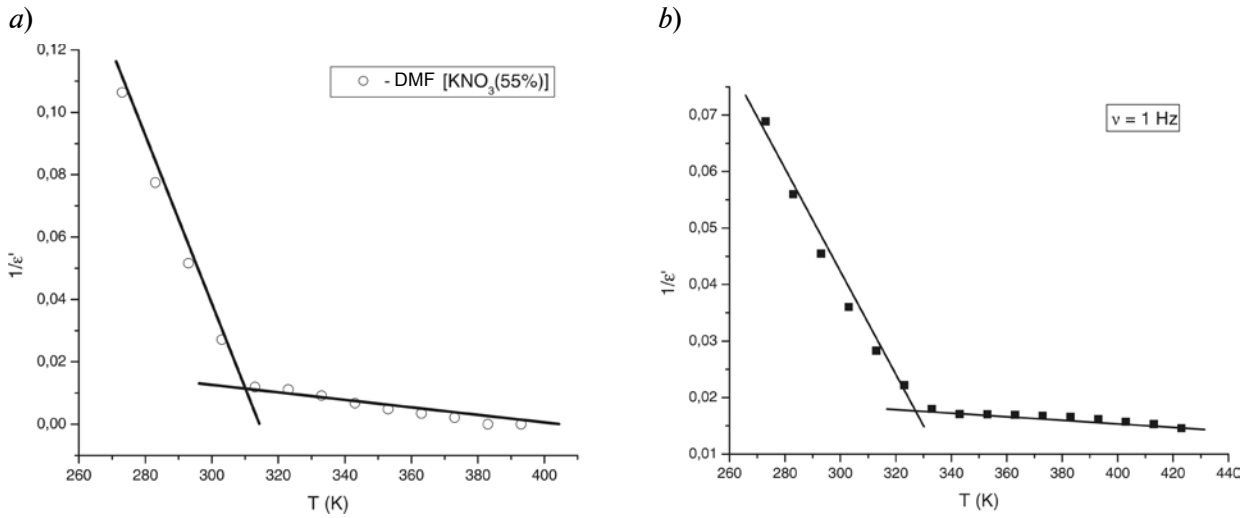

Fig. 2. Temperature dependences of the inverse of the dielectric constant of the sample #1 (*a*) and #3 (*b*)

According to the model suggested by the authors [2], the temperature dependence of the inverse value of dielectric permeability has a linear character. It is experimentally obtained that for many polymer systems in the dependence $(1/\varepsilon_1) = f(T)$ there are at least two regions which correspond to the system being in glass and rubbery state respectively. It means that on condition of certain critical temperature, there is a change in the character of the temperature dependence of $(1/\varepsilon_1)$. The same temperature dependence is also observed for polymer density ($\rho \sim 1/V$) (Fig. 1). That is why the temperature dependence $1 / \varepsilon'$ can be used to determine glass transition range.

The dielectric measurements were carried out using an impedance analyzer ALPHA-N Analyzer from Novocontrol Technologies, covering a frequency range from 0.1 Hz to 1 MHz and working at different increasing temperature steps from 173 up to 523 K. A drop of the polymer mixture with two silica spacers of 50 μm thickness was placed between two gold plated electrodes (20 mm of dia-

A comparison between experimental data of this work and from literature

Number of sample	Compound composition (Polymer-plasticizer-[modifier]- hardener)	T_g $(1/\varepsilon' = f(T))$	T_g from literature
		K	
1	(MPVT-A) (DMF) [KNO_3(55%)] (TON-2)	310	310 [3]
2	(MPVT-A) (DMF) [KCl(70%)] (TON-2)	326	326 [4]
3	(MPVT-A) (DMFA) (MeO-TON)	328	329 [5]
4	(MPVT-A) (DMFA) (TON-2)	324	325 [5]
5	(MPVT-A) (DMFA) (Dur-TON)	327	–

(TON-2) – 2,4,6-triethylbenzene-1,3-dicyanobenzene-di-N-oxide
(MeO-TON) – 3,6-methoxy-1,4-dicyanobenzene-di-N-oxide
(Dur-TON) – 2,3,5,6-methyl-1,4-dicyanobenzene-di-N-oxide
(DMFA) – dimethylformamide C_3H_7NO
(DMF) – dimethylphthalate $C_{10}H_{10}O_4$

meter) of a parallel plate capacitor. The sample cell was mounted on a cryostat and exposed to a heated gas stream being evaporated from a liquid nitrogen Dewar. The temperature control was performed within ±0.5 K, using the Novocontrol Cryosystem. Novocontrol GmbH supplied all these modules.

For polymer composite materials based on poly-N-methylalil-5-vinyltetrazol (MPVT-A) with the modifier KNO_3 (55 %), the glass transition temperature is T_g = 310 K (Fig. 2, *a*) (the critical temperature is 310 K); for MeO-TON, the glass transition temperature is T_g = 328 K (Fig. 2, *b*) (the critical temperature is 329 K). The experimental results we obtained can allow us to conclude that for a broad class of systems this critical temperature coincides with the glass transition temperature (see Table).

The first region is characterized by the abrupt decrease of $1 / \varepsilon'$. Such significant changes of the temperature dependence of the dielectric parameters are connected with the main thermal transition from glass state to rubber state (or vice versa). The second region corresponds to rubbery state. The analysis of the temperature dependence shows that this region is characterized by the smooth decrease of the value $1 / \varepsilon'$ and the curve flattens out to the steady plateau.

The temperature under which there is a change in the character of the temperature dependence of the inverse value of dielectric permeability for all the systems we studied coincides with their glass transition temperature.

Thus, the measurement of $1/\varepsilon_1$ temperature dependence can be used as a new alternative method to determine T_g for polymer systems and composites.

REFERENCES

1. **Kozlov N.A., Mitrofanov A.D.** Polymer physics: Studies. Manual. Vladimir, Vladimir State University, 2001. 345 p. (rus)

2. **Vendik I.B., Vendik O.G., Afanasjev V.P., Sokolova I.M., Chigirev D.A., Castro R.A.** The relaxation model of dynamic mechanical and dielectric properties of polymer materials. *Proceedings of XII International Conference on Dielectrics*. 2011. St. Petersburg, Russia. May 23 – 26, 2011. pp. 216–219. (rus)

3. **Bartenev G.M., Frenkel S.Ya.** Polymer physics. Leningrad, Chemistry, 1990. 433 p. (rus)

4. **Kalinin M.A., Petrekov P.V. Lushin E.N., Tereshchenko I.A., Sapozhnikova T.V.** Abstracts and Papers of IVth Russian scientific-practical conference of students and young scien tists. Altai State Technical University, BTI. Bijsk, Altai State Technical University Publishing House, 2010. P. 59. (rus)

5. **Nasonov A.D., Paznikov E.A., Kalinin M.A., Petrekov P.V., Golub P.D.** The influence of the chemical structure of modifiers on the viscoelastic properties of the tetrazole polymer. *Electronic Journal: The scientists note*, pp. 11–14. Available at: http://www.scientific-notes.ru/index.php?page=6&new=15 (rus)

6. **Petrekov P.V.** Study of the relaxation properties of the tetrazole polymer and model compounds based on it. Diss. on competition. Art. Ph.D. Bijsk., 2012. (rus)

СПИСОК ЛИТЕРАТУРЫ

1. **Козлов Н.А., Митрофанов А.Д.** Физика полимеров: Учеб. пособие. Владимир: Владимирский гос. ун-т, 2001. 345 с.

2. **Вендик И.Б., Вендик О.Г., Афанасьев В.П., Соколова И.М., Чигирев Д.А., Кастро Р.А.** Релаксационная модель динамических, механических и диэлектрических характеристик полимерных материалов // Матер. XII Междунар. конф. по физике диэлектриков. 2011. СПб., Россия, 23 – 26 мая. С. 216 – 219.

3. **Бартенев Г.М., Френкель С.Я.** Физика полимеров. Л.: Химия, 1990. 433 с.

4. **Калинин М.А., Петреков П.В., Лушин Е.Н., Терещенко И.А., Сапожникова Т.В.** // Тезисы и доклады 4-й Всерос. научно-практ. конф. студентов, аспирантов и мол. ученых с междунар. участием «Технологии и оборудование химич., биотехнол. и пищевой пр-сти», 27 – 29 апреля 2011 г., г. Бийск: Изд-во Алтайского гос. техн. ун-та, 2010. С. 59.

5. **Насонов А.Д., Пазников Е.А., Калинин М.А., Петреков П.В., Голуб П.Д.** Влияние химического строения модификаторов на вязкоупругие свойства тетразолсодержащего полимера // Электронный научный журнал Курского гос. ун-та. 2010. № 3(15). Режим доступа: http://www.scientific-notes.ru/index.php?page=6&new=15

6. **Петреков П.В.** Исследование релаксационных свойств тетразолсодержащего полимера и модельных составов на его основе. Автореф. дис. ... канд. техн. наук. Бийск, БТИ АлтГТУ, 2012. 16 с.

КАСТРО Арата Рене Алехандро – *доктор физико-математических наук, профессор кафедры физической электроники Российского государственного педагогического университета им. А.И. Герцена.*
191186, Россия, Санкт-Петербург, наб. р. Мойки, 48
recastro@mail.ru

ЛУШИН Евгений Николаевич – *аспирант кафедры физической электроники Российского государственного педагогического университета им. А.И. Герцена.*
191186, Россия, Санкт-Петербург, наб. р. Мойки, 48
lushin.ev@gmail.com

UDC 537.632.3

A.V. Ilinsky [1], R.A. Castro [2], L.A. Nabiullina [2], M.E. Pashkevich [3], E.B. Shadrin [1]

[1] Ioffe Physical Technical Institute of the Russian Academy of Sciences
26 Polytekhnicheskaya St., St. Petersburg, 194021, Russia
[2] Herzen State Pedagogical University of Russia
48 Moika Emb., St. Petersburg, 191186, Russia
[3] St. Petersburg State Polytechnical University,
29 Politekhnicheskaya St., St. Petersburg, 195251, Russia

DIELECTRIC SPECTROSCOPY AS THE MEANS OF DIAGNOSTICS OF ELECTRONIC STATES OF SILLENITS

А.В. Ильинский, Р.А. Кастро, Л.А. Набиуллина, М.Э. Пашкевич, Е.Б. Шадрин

ДИЭЛЕКТРИЧЕСКАЯ СПЕКТРОСКОПИЯ КАК СРЕДСТВО ДИАГНОСТИКИ ЭЛЕКТРОННЫХ СОСТОЯНИЙ СИЛЛЕНИТОВ

The physical parameters of impurity centers of $Bi_{12}SiO_{20}$ crystals have been determined by the dielectric spectroscopy method.

DIELECTRIC SPECTROSCOPY, SILLENITES, THERMO-STIMULATED CURRENTS.

Методом диэлектрической спектроскопии определены физические параметры примесных центров кристаллов $Bi_{12}SiO_{20}$.

ДИЭЛЕКТРИЧЕСКАЯ СПЕКТРОСКОПИЯ, СИЛЛЕНИТЫ, ТЕРМОСТИМУЛИРОВАННЫЕ ТОКИ.

I. Introduction

Sillenite crystals have been drawing the attention of scientists for a long time. It is due to the unique physical properties of sillenites: easiness of the synthesis of big crystals, high optical transparency in visible and near infrared ranges, high dark resistance and photosensitivity, high electro-optical (EO) effects, and big optical rotatory power. It is possible to use sillenites for recording, processing and storage of an optical information, including recording holograms [1].

In recent times, the attention of scientists has been concentrated on the research of magneto-optical properties of sillenites [2, 3]. Nonlinear properties of Faraday and magneto-optical Kerr effects in undoped $Bi_{12}SiO_{20}$ have been found out. The results of these researches are interpreted with the use of electro-magneto-gyration model. The electro-gyration part of common effects is caused by the formation of the internal electric field induced by optical orientation of spins. It has been shown that magnetism of not lone-electron pair of Bi-O-heptahedron in crystal lattice brings the contribution to total optical rotatory power. In connection with this creation of the algorithm of the express-analysis of optoelectronic parameters of sillenites is very topical.

The proposed paper is devoted to the express analysis of $B_{12}SiO_{20}$ (BSO) crystals by dielectric spectroscopy methods. These methods are widely applied by research of temperature and light influence on physical properties of many materials [4, 5].

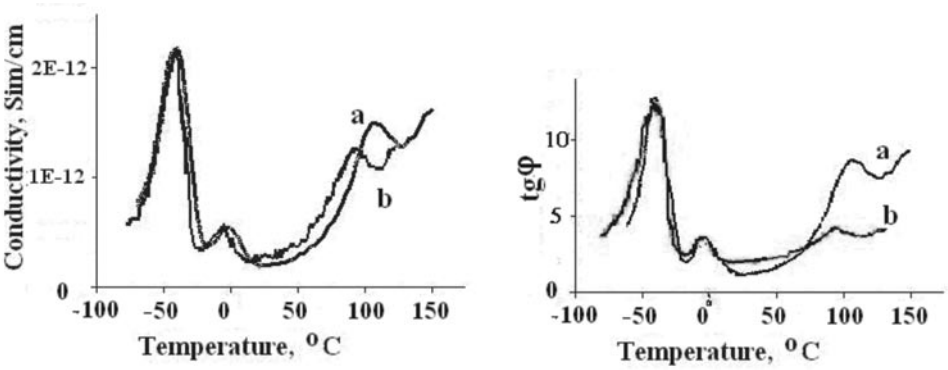

Fig. 1. Temperature dependences of conductivity σ (left) and dielectric loss tangent tg φ (right) of BSO-samples at 100 Hz (*a*) and 10 Hz (*b*) frequencies

II. Samples and the Technique of the Experiment

Investigations were provided on undoped BSO samples which had been grown by Chokhralsky method. The sizes of the samples were 10×10×1 mm. Dark specific resistance was 10^{13} Ω·m. Researches of dielectric spectra and thermo-stimulated currents (TSC) were carried out with the use of dielectric spectrometer «Alpha-Beta Impedance Analizer» produced by the Novocontrol Technologies firm. The temperature T of the sample during the TSC-measurements at frequencies of 10 Hz and 100 Hz changed from −50 °C up to +150 °C with the constant speed of 5 °C/min. Furthermore, the measurements of temperature and frequency dependences of a dielectric loss tangent, and also of the real and imaginary parts of the dielectric constant in the range from 10^{-2} to 10^{5} Hz were made. The sample was located between the facings of the condenser. The amplitude I_0 of a current through the sample was measured at the application of a sine voltage $U(t)$ to the sample. The phase difference φ between oscillations $U(t)$ and $I(t)$ was measured, too. With the use of a special converter, these data were transformed into the data on physical characteristics of the sample, using computer programs developed by the Novocontrol Technologies firm.

During the analysis of the experimental data it was assumed that the equivalent circuit of the crystal was parallel connection of the resistance R_x and electrocapacity C_x of the sample. At the initial stage the values of the real and imaginary parts of the dielectric constant were calculated using the following formula:

$$|\varepsilon'| = I_0 \mathrm{tg}\varphi / [(1 + \mathrm{tg}^2\varphi)^{1/2} \omega C_0 U_0];$$

$$|\varepsilon''| = |\varepsilon'| / \mathrm{tg}\varphi,$$

where ω is the registration frequency, and C_0 is the capacity of the empty measuring cell.

It was possible to calculate, at the subsequent stage, the value of Maxwell relaxation time

$$\tau_M = R_x C_x = |\varepsilon'| / |\varepsilon''| \omega.$$

At the last stage the values of $R_x = \tau_M / C_0 |\varepsilon'|$ and $C_x = \tau_M / R_x$ were calculated.

III. Results of the Experiment

Measurements were carried out on the samples prepared in an ordinary way, and this guaranteed the reproducibility of the results. Namely, at first the sample was heated up from the room temperature to +150 °C with the purpose of emptying the traps of various types. After that the sample was cooled up to −50 °C, and after that it was illuminated during 20 min with photoactive light (λ = 470 nm) of constant intensity. Further, the sample was kept in darkness without illumination for 20 min to except the influence of activity of super shallow traps. After that the measurements of electric parameters of the sample were carried out at heating with a constant speed of 5 °C/min in the range from −50 °C to +150 °C.

The temperature dependences of the conductivity and dielectric loss tangent of BSO samples at the frequencies of 100 Hz and 10 Hz are shown in Fig. 1, *a* and *b*, accordingly. In Fig. 2, *a* and *b*, the dielectric spectra at temperature 0 °C of not illuminated and illuminated samples are shown.

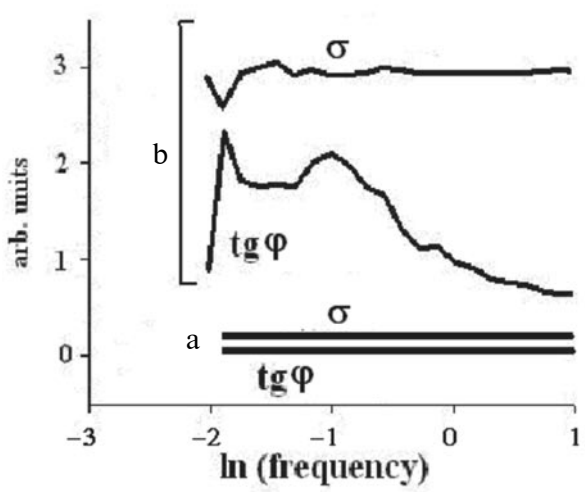

Fig. 2. Spectra of the conductivity σ and dielectric loss tangent tg φ of BSO-samples at 0 °C obtained before (a) and after (b) photoactive illumination

The temperature dependence of Maxwell relaxation time of preliminary illuminated BSO samples is shown in Fig. 3.

In Fig. 1, *a* and *b*, in the range from −50 °C up to +15 °C, we can see two TSC maxima at the temperatures of −40 °C (233 K) and −2 °C (271 K).

The comparison of Fig. 1, *a* and *b* shows that the change of the frequency of registration from 10 Hz to 100 Hz does not lead to the maxima parameters changes. The reason is that small concentration of free electrons $n(t)$ in a conductivity band at TSC measurement is realized. Under these conditions the Maxwell relaxation time τ_M is very large and is fixed in the range from tens up to hundreds of seconds. That is why the working frequencies of 10 Hz and 100 Hz used in our research are many times more than the value $1/\tau_M$ and, consequently, the deduced results of TSC measurements reflect the undistorted value $n(t)$. Such conclusion is confirmed by the comparison of the dielectric spectra of Fig. 2, *a* and *b* obtained before and after photoactive illumination. Namely, only at the frequencies less than one Hertz, the influence of illumination on the dielectric spectrum is observed.

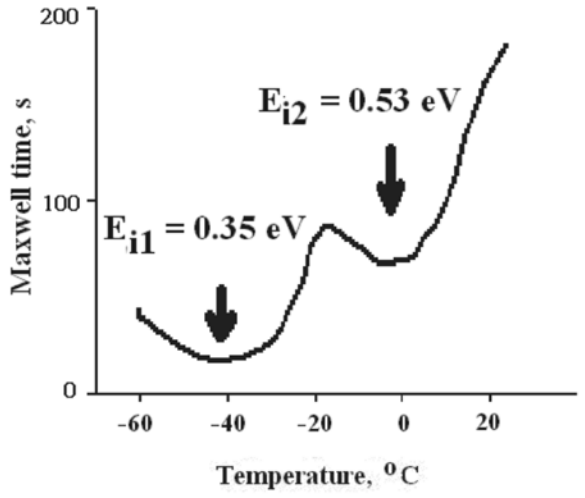

Fig. 3. Temperature dependence of Maxwell relaxation time of BSO-samples

IV. Discussion of the Results

A. Qualitative Model

BSO crystal is a high-resistance photoconductor, electrooptical (EO) properties of which allow observing evolution of spatial charge area in the volume of crystal [6]. In Ref. [6] the evolution of a spatial charge zone of BSO crystal after photoactive illumination was observed. On the basis of this information we can say the following.

It is known [1] that in the gap of BSO crystals there are levels of traps and levels of the deep recombination centers. We have experimentally found out two TSC maxima. For this reason, at the analysis of our experimental results we consider the energy circuit (Fig. 4) that has two levels of tr1 and tr2 traps and one deep recombination *R* level.

According to executing the algorithm of our experiment, preliminary warming the sample up to 150 °C led to full emptying the traps and to the recombination of electrons with holes on *R* centers. Heating up to 150 °C, cooling of the sample in darkness up to −50 °C and keeping the sample at −50 °C without illumination provided reproducibility of the results.

Illumination of a BSO sample with photoactive light (λ = 470 nm) at low temperatures (−50 °C) within 20 min caused the transitions of electrons from the *R* centers through the gap to the traps (Fig. 4, *a*). Subsequent keeping the sample in darkness fixed metastable quasi-equilibrium station at which the concentration of electrons in the

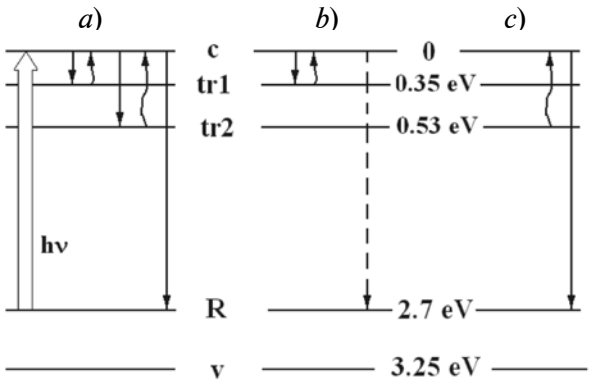

Fig. 4. The scheme of the levels of local centers in BSO: *a* – preliminary illumination of the sample at low temperature $T = -50$ °C; *b* – the scheme of electronic transitions in the range of the first (low temperatures) TSC-maximum; *c* – the scheme of electronic transitions in the range of the second (high temperatures) TSC-maximum

conduction band was small. For this reason, when an external alternate voltage was applied to the crystal, the registered current was small too. By rising the temperature at constant speed $b = 5$ °C/min, the shallow tr1 traps were ionized at first. It generated charge carriers in a conduction band and that is why a thermo-stimulated current (TSC) is now visible.

Initial range of TSC maximum was generated by approaching kT (k – Boltzmann constant) to the ionization energy (E_{i1}) of tr1 traps. According to electrooptical data [6] for tr1 traps, the drift of free electrons in an external electric field is accompanied by effective reoccupation and weak recombination processes (see Fig. 4, *b*). It provided in EO experiments the expansion of the spatial charge area. Such expansion is typical for strong reoccupation of the traps by electrons at weak recombination processes. By continued rise of the temperature, the recombination processes empty the tr1 centers despite effective reoccupation and cause the decrease of TSC with the formation of low temperature TSC maximum. Shallow tr1 traps are empty. It is necessary to notice that tr2 traps remain filled with electrons.

Ionization of electrons from deep tr2 traps begins with continued rise of temperature. It creates high-temperature TSC maximum. For tr2 traps, in contrast to tr1 traps, reoccupation of carriers is small (Fig. 4, *c*). It is established in electrooptical experiments [6]. Namely, for tr2 traps, narrowing the spatial charge area was observed [6], but an expansion did not appear.

B. Mathematical TSC Description

According to our model, the results of TSC measurements are described by the system of equations (1). The system (1) describes the change of electronic concentration in conduction band $n(t)$ and electrons concentration $n_{tr}(t)$ in the traps. The temperature T is fixed. We can write:

$$\begin{aligned} dn(t)/dt &= An_{tr}(t) - Bn(t) - Cn(t); \\ dn_{tr}(t)/dt &= Bn(t) - An_{tr}(t). \end{aligned} \qquad (1)$$

Here $A = 1/\tau_T$ is the probability of thermal ionization of the traps, $B = 1/\tau_{tr}$ – the probability of the capture of a free electron by a trap, $C = 1/\tau_R$ is the probability of recombination of free electrons with holes on the R centers.

Generally, the system (1) has an analytical solution with the initial conditions $n_{tr}(0) = n_{tr0}$ and $n(0) = n_0$, and at the assumption that A, B, C do not depend on time:

$$n_{tr}(t) = [(n_{tr0}\lambda_2 - Bn_0 + An_{tr0})/(\lambda_2 - \lambda_1)]\exp(\lambda_1 t) + \\ + [(Bn_0 - n_{tr0} - An_{tr0})/(\lambda_2 - \lambda_1)]\exp(\lambda_2 t);$$

$$n(t) = [(n_{tr0}\lambda_2 - Bn_0 + An_{tr0})/(\lambda_2 - \lambda_1)] \times \\ \times [\exp(\lambda_1 t)](\lambda_1 + A) + [(Bn_0 - n_{tr0} - \\ - An_{tr0})/(\lambda_2 - \lambda_1)][\exp(\lambda_2 t)](\lambda_2 + A),$$

where

$$\lambda_1 = (1/2)\{-(A + B + C) + \\ + [(A + B + C)^2 - 4AC]^{1/2}\};$$

$$\lambda_2 = (1/2)\{-(A + B + C) - \\ - [(A + B + C)^2 - 4AC]^{1/2}\}.$$

In a limiting case, when strong reoccupation of carriers is small, that is at $B >> C$ ($\tau_R >> \tau_{tr}$), the system (1) becomes simpler. In initial range of a TSC maximum, its solution looks:

$$n(T) = n_{tr}(0)\tau_{tr}/\tau_T = t_{tr}\omega T n_{tr}(0)\exp(-E_i/kT), \qquad (2)$$

where $1/\tau_T = \omega_T \exp(-E_i/kT)$.

The formula (2) does not describe completely the form of TSC maximum. The reason for this is that the neglect of recombination processes is powerless at the top and slope of a TSC maximum.

In the other limiting case at strong recombination $C >> B$ ($t_R << t_{tr}$) without reoccupation processes, the system of Eq. (1) becomes simpler too. With the assumption $t = (T - T_0)/b$, (b is the speed of heating), the expression for electronic concentration in the conduction band looks like

$$n(T) = (\tau_R/\tau_T)n_{tr}(0)\exp[-(T - T_0)/(b\tau_T)]. \quad (3)$$

The system of Eq. (1) has the generally analytical solution with the assumption, as has already been told, that probabilities $A = 1/\tau_{tr}$, $B = 1/\tau_T$, $C = 1/\tau_R$ do not depend on time. This solution allows performing the full description of the process of TSC occurrence. The comparison of the theory with the experiment can be performed with the use of computer software packages. However, at the initial stage of processing of the results, it is reasonable to use the expressions (2) and (3).

C. Processing the Experimental Results

Fig. 5 shows the result of definition E_i in initial temperature ranges of TSC maxima. The low temperature maximum 1 accords with the case of a strong reoccupation of electrons by shallow tr1 traps and small recombination probability of electrons on the R centers. Thus, it corresponds to the case of deep tr2 traps inaction. For the low temperature maximum 1, from expression (2) it follows that

$$\ln[n_1(T)] = -E_{itr1}/kT + \ln[\tau_{tr1}\omega_T n_{tr1}(0)].$$

Using Arrenius coordinates leads to linearization of the initial range. By means of the tangent of an angle of inclination of a linear site we determine the ionization energy of shallow traps E_{i1} = 0.35 eV. The high-temperature maximum 2 accords to the case of thermal ionization of deep tr2 traps. After ionization from tr2 traps, electrons recombine with holes on R centers. Repeated capture of electrons on tr2 traps is absent. Shallow traps tr1 are completely empty.

The analysis of the initial range of the second TSC maximum gives

$$\ln[n_2(T)] = -E_{i2}/kT + \ln[\tau_R\omega_T n_{tr2}(0)].$$

In Arrenius coordinates, we determine energy E_{i2} of the ionization of tr2 traps: E_{i2} = 0.53 eV. Notice that the methods of

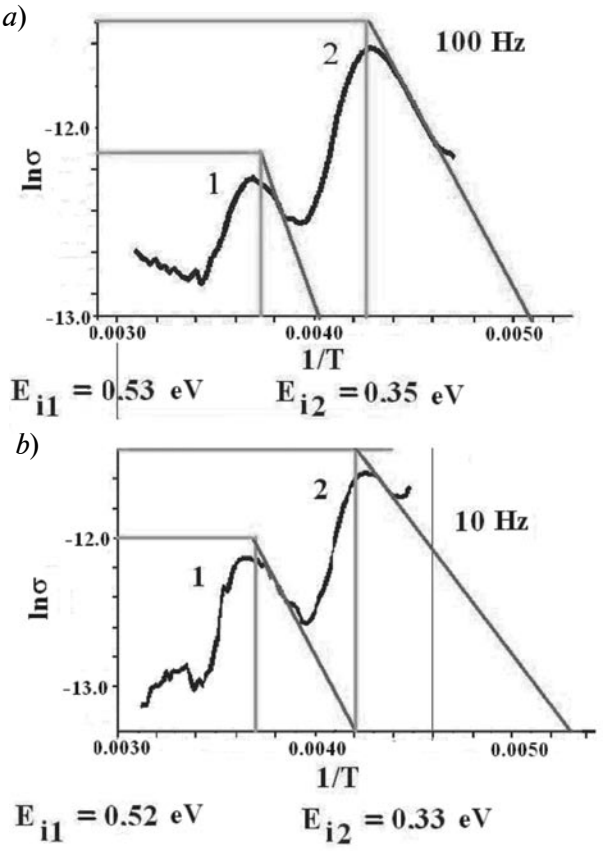

Fig.5. Definition of E_i (ionization energy) of the impurity centers (traps) in BSO crystals by TSC method on the base of dielectric spectroscopy data for frequencies100 Hz (*a*) and 10 Hz (*b*)

defining E_i in the initial range of TSC maxima accord with the methods described in Ref. [5].

The method of the analysis of an initial range allows estimating the relation of probabilities $B = 1/\tau_{tr}$ and $C = 1/\tau_R$. Actually, from the Eq. (2) and (3) in view of crossing points $\ln[n_1(T \to \infty)]$ and $\ln[n_2(T \to \infty)]$ by the linear sites of an ordinates axis ($1 / kT \to 0$), we have the following:

$$\ln[n_1(T)] - \ln[n_2(T)] = \ln[\tau_{tr1}\omega_T n_{tr1}(0)] - \\ - \ln[\tau_R\omega_T n_{tr2}(0)] = 2.4.$$

From here follows $C/B = \tau_{tr1}/\tau_R = 3$. The relation $n_{tr1}(0)/n_{tr2}(0)$ of degrees of initial filling the tr1 and tr2 traps at illumination is equal to 3. This value is determined using the area relation covered with 1 and 2 TSC maxima. τ_{tr1}/τ_R parameter derived in such measurements is important for the estimation of optoelectronic properties of sillenits. This parameter

directly reflects mutual ability of the impurity centers to capture electrons.

V. Conclusion

In the present work we demonstrate the possibility of application of dielectric spectroscopy to estimating Maxwell relaxation time of high-resistance semiconductors with the use of ε(ν) and tg φ spectra. It is shown that the reasonable choice of frequency of registration allows determining key parameters of impurity centers. The algorithm of starting preparation of the samples, excluding the distortion of the data is developed. It is essentially important in the area of using sillenits as sensors of physical parameters.

REFERENCES

1. **Osugi Y., Minemoto T.** Increase the size of Bi12Si020 real-time hologram for three-dimensional display. *Optical Review*, Vol. 3, No. 6B (1996), pp. 552–555.

2. **Petrov M.R., Stepanov S.I., Khomenko A.V.** Fotochuvstvitel'nye elektroopticheskie sredy v golografii i opticheskoi obrabotke informatsii. Leningrad, Nauka, 1983, 270 p. (rus)

3. **Ilinskyi A.V., Castro R.A., Nabiullina L.A., Pashkevich M.E., Shadrin E.B.** Magneto-optical effects in undoped bismuth silicate crystals. *St. Petersburg State Polytechnical University Journal: Physics and Mathematics*, 2013, No. 4-1(182), pp. 9–20. (rus)

4. **Nabiullina L., Shadrin E.** Magnetic resonance properties of single crystals $Bi_{12}SiO_{20}$:Fe. *Izvestia: Herzen University Journal Of Humanities & Sciences*, 2012, No. 147, p. 63–72.

5. **Bordovskii G.A., Castro R.A.** Photoinduced changes in optical and contact properties of chalcogenide glasses. *Optics and Spectroscopy*, 2001, Vol. 90, Iss. 6, pp. 884–886.

6. **Castro R.A. Bordovsky G.A., Bordovsky V.A., Anisimova N.I.** Correlation between bismuth concentration and distribution of relaxators in As_2Se_3(Bi)(x) layers. *Journal of Non-Crystalline Solids*, 2006, Vol. 352, Iss. 9–20, pp. 1560–1562.

7. **Astratov V.I., Il'inskii A.V., Furman A.S.** Dinamika ekranirovaniia elektricheskogo polia v fotorefraktivnykh kristallakh $Bi_{12}SiO_{20}$. *Technical Physics Letters*, 1988, Vol.14, Iss.14. (rus)

8. **Gorokhovatskii Yu.A., Bordovsky G.A.** Termoaktivatsionnaia tokovaia spektroskopiia vysokoomnykh poluprovodnikov i dielektrikov. Moscow, Nauka, 1991, 245 p. (rus)

СПИСОК ЛИТЕРАТУРЫ

1. **Osugi Y., Minemoto T.** Increase the size of Bi12Si020 real-time hologram for three-dimensional display. *Optical Review*, Vol. 3, No. 6B (1996), pp. 552–555.

2. **Петров М.Р., Степанов С.И., Хоменко А.В.** Фоточувствительные электрооптические среды в голографии и оптической обработке информации. Л.: Наука, 1983. 270 с.

3. **Ильинский А.В., Кастро Р.А., Набиуллина Л.А., Пашкевич М.Э., Шадрин Е.Б.** Магнитооптические эффекты в недопированных кристаллах силиката висмута // Научно-технические ведомости СПбГПУ. Физико-математические науки. 2013. № 4-1(182). С. 9–20.

4. **Набиуллина Л.А., Шадрин Е.Б.** Магниторезонансные свойства монокристаллов $Bi_{12}SiO_{20}$: Fe // Известия РГПУ им. А.И. Герцена. 2012. № 147. С. 63–72.

5. **Бордовский Г.А., Кастро Р.А.** Фотоиндуцированные изменения оптических и контактных свойств халькогенидных стекол // Оптика и спектроскопия. 2001. Т. 90. Вып. 6. С. 884–886.

6. **Castro R.A. Bordovsky G.A., Bordovsky V.A., Anisimova N.I.** Correlation between bismuth concentration and distribution of relaxators in As_2Se_3(Bi)(x) layers. *Journal of Non-Crystalline Solids*, 2006, Vol. 352, Iss. 9–20, pp. 1560–1562.

7. **Астратов В.Н., Ильинский А.В., Фурман А.С.** Динамика экранирования электрического поля в фоторефрактивных кристаллах $Bi_{12}SiO_{20}$ // Письма в Журнал технической физики. 1988. Т. 14. Вып. 14. С. 1330–1334.

8. **Гороховатский Ю.А., Бордовский Г.А.** Термоактивационная токовая спектроскопия высокоомных полупроводников и диэлектриков. М.: Наука, 1991. 245 с.

ИЛЬИНСКИЙ Александр Валентинович – *доктор физико-математических наук, старший научный сотрудник Физико-технического института им. А.Ф. Иоффе РАН.*

194021, Россия, г. Санкт-Петербург, Политехническая ул., 26

ilinskiy@mail.ioffe.ru

КАСТРО Арата Рене Алехандро – *доктор физико-математических наук, профессор кафедры физической электроники Российского государственного педагогического университета им. А.И. Герцена.*
191186, Россия, г. Санкт-Петербург, наб. реки Мойки, 48
recastro@mail.ru

НАБИУЛЛИНА Лилия Ансафовна – *аспирантка Российского государственного педагогического университета им. А.И. Герцена.*
191186, Россия, г. Санкт-Петербург, наб. реки Мойки, 48

ПАШКЕВИЧ Марина Эрнстовна – *старший преподаватель кафедры высшей математики Санкт-Петербургского государственного политехнического университета.*
195251, Россия, г. Санкт-Петербург, Политехническая ул., 29
marpash@yandex.ru

ШАДРИН Евгений Борисович – *доктор физико-математических наук, заведующий лабораторией физики фазовых переходов в твердых телах Физико-технического института им. А.Ф. Иоффе РАН.*
194021, Россия, г. Санкт-Петербург, Политехническая ул., 26
shadr.solid@mail.ioffe.ru

UDC 537.226:544.163.2

T.P. Stepanova [1], T.D. Anan'eva [1],
E.D. Karpenko [2], V.M. Kapralova [2]

[1] Institute of Macromolecular Compounds RAS
31 Bolshoy Ave. V.O., St. Petersburg, 199004, Russia
[2] St. Petersburg State Polytechnical University,
29 Politekhnicheskaya St., St. Petersburg, 195251, Russia

A DIPOLE MOMENT AND CONFORMATIONS OF POLY-N-VINYLPYRROLIDONE AND OF ITS COMPLEX WITH C_{60} FULLERENE IN AQUEOUS SOLUTIONS

Т.П. Степанова, Т.Д. Ананьева,
Е.Д. Карпенко, В.М. Капралова

ДИПОЛЬНЫЙ МОМЕНТ И КОНФОРМАЦИОННЫЕ СВОЙСТВА ПОЛИВИНИЛПИРРОЛИДОНА И ЕГО КОМПЛЕКСА С ФУЛЛЕРЕНОМ C_{60} В РАСТВОРЕ В ВОДЕ

The study of temperature dependences of dipole moments and conformational properties of poly-N-vinylpyrrolidone (PVP) and polymer complex of PVP with C_{60} fullerene (PVP + FC_{60}) was carried out in dilute aqueous solutions at 293−313 K. It was shown that dipole moment values for PVP and PVP + FC_{60} were 24−32 D and 18 D, correspondingly. The presence of the molecular group −N−C=O in each monomer unit near the macromolecule backbone promotes the formation of helical blocks in macromolecular coils. In external electric field, the non-alternating projections on the direction of this field and on the vectors connecting the neighboring segments of the macromolecule appear. It was demonstrated that the changes in the characteristics of the dielectric polarization could be explained by structuring in the coils of PVP and PVP + FC_{60} in aqueous solutions.

DIELECTRIC PERMITTIVITY, DIPOLE MOMENT, HELICAL BLOCKS IN COILS, ASSOCIATION, SOLUTION.

Проведено исследование дипольных моментов поли-N-винилпирролидона (ПВП) и на его основе полимерного комплекса с фуллереном C_{60} (ПВП + C_{60}). Показано, что значения дипольного момента ПВП и ПВП + C_{60} в водных растворах в условиях бесконечного разбавления велики и составляют 24 − 32 Д и 18 Д (T = 293 − 313 K) соответственно. Анализ экспериментальных результатов указывает на специфические конформационные свойства макромолекул исследованных полимеров. Наличие молекулярной группы −N − C = O в каждом мономерном звене у хребта макромолекулы обусловливает возникновение спирализованных блоков внутри макромолекулы. В этом случае во внешнем электрическом поле возникает неальтернирующая составляющая дипольного момента на направление спирали. Суммарный эффект векторного сложения этих дипольных моментов и взаимоориентация спирализованных блоков в статистическом клубке определяют высокие значения дипольных моментов ПВП и ПВП + C_{60} в водных растворах.

ДИЭЛЕКТРИЧЕСКАЯ ПРОНИЦАЕМОСТЬ, ДИПОЛЬНЫЙ МОМЕНТ, СПИРАЛИЗОВАННЫЕ БЛОКИ, АССОЦИАЦИЯ, РАСТВОР.

Polyvinylpyrrolidone (PVP) is known to be one of amphiphilic polymers which are inclined to self-organization into various aggregates in both polar and non-polar environment [1]. Stable aggregate formation in the solutions of amphiphilic polymers is due to hydrophobic

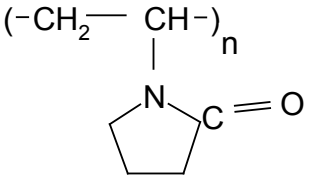

PVP structure

and ionic interactions resulting in H-bonds, charge transfer complexes, coordination complexes, etc. PVP ability to form complexes as well as its other physical, chemical and biological properties make this polymer suitable for technological and biomedical applications. PVP structural formula is given in scheme. The PVP solubility in water is mostly due to the lactam cycle.

Recently, the synthesis of PVP with biological or technogenic inclusions of macromolecular scale has been described, and the main attention was paid to PVP and fullerene C_{60} (FC_{60}) complexes using in medical applications. The use of fullerenes in medicine faces significant difficulties because of their almost total water insolubility, though it could be overcome by using fullerene non-covalent complexes with water soluble polymers like PVP. In this case, the electronic structure and therefore the properties of fullerene molecular clusters are disturbed minimally in contrast to covalent bonding. It is obvious that physical and chemical properties of non-covalent complexes are determined by the proportion of fullerenes and polymer in the complex [2]. It is well-known that fullerene molecule has a form of truncated icosahedron with the surface consisting of hexagons and pentagons connected by single and double bonds. The molecule FC_{60} diameter is shown to be approximately 10.2 Å [3].

The purpose of the present paper is to investigate and compare the dipole moments and conformational properties of PVP and PVP + FC_{60} complexes in aqueous solutions under the conditions of infinite dilution.

To produce the PVP + FC_{60} complex, PVP with molecular mass of 24000 produced by «Fluka» and C_{60} fullerene from the company «Fullerene technologies» (St.-Petersburg) with fullerene content of 99.5 % were used [4 – 7]. PVP used for this work is the white-yellow powder with softening temperature as high as 160 °C, density $d_{20} = 1.9$ g/cm^3 [1] and refraction index $n_{D20} = 1.58$ (for a film).

The solutions of PVP in chloroform (50 mg/ml) and of fullerene in *o*-dichlorobenzene (0.8 mg/ml) were mixed with the volume proportion 2 : 1, then the solvents were evaporated in vacuum at 35 – 40 °C, and the solid residual was dried. To remove free fullerenes, the solid residual was stirred into water and filtered through the filter paper. This procedure was followed by water vacuum evaporation at the same temperature.

Fullerene concentration in the complex was estimated by complex destruction in 2 mg/ml solution in the mixture of ethanol and toluene 1 : 9. Fullerene concentration in the mixture of solvents was measured by UV spectroscopy method [7] and brought into correlation with PVP concentration.

The capacity of solution was measured in the cell with platinum electrodes [9] using measuring the bridge E7-12 at the frequency of 1 MHz with the error of 0.001 pf. The capacity of the used cell was 4.53 pf.

The solutions of PVP and PVP + FC_{60} in distilled water for further measurements were prepared using gravimetrical method.

Dipole moments of PVP molecules and PVP + FC_{60} complexes in aqueous solutions were estimated according to Buckingham theory of statistical polarization [8] for two-component systems:

$$\frac{(\varepsilon_{12}-1)(2\varepsilon_{12}+1)}{3\varepsilon_{12}}V_{12} - \frac{(n_1^2-1)(2\varepsilon_{12}+1)}{\left(2\varepsilon_{12}+n_1^2\right)}V_1x_1 - \frac{(n_2^2-1)(2\varepsilon_{12}+1)}{(2\varepsilon_{12}+n_2^2)}V_2x_2 = \left(\frac{4\pi N_A}{3kT}\right)\mu_{1ef}^2x_1 + \mu_{2ef}^2x_2. \quad (1)$$

Here ε is dielectric permittivity; n – refraction index; V – molar volume, $V = Mv_s$ (v_s – specific volume, M – molar mass); x – mole per cent, T – absolute temperature, N_A – Avogadro number, k – Boltzmann constant, μ_{ef} – effective dipole moment (indexes 1, 2 и 12 are for solvent, dissolved substance and solution, accordingly).

According to the statistical theory of dielectric polarization,

$$M_{ef}^2 = \mu^2 g, \quad (2)$$

where g is a correlation parameter for dipole moments orientation characterizing short-range interactions; μ – dipole moment of a polar molecule related to its dipole moment in vacuum μ_0 by

$$\mu = \frac{n^2+2}{3} \cdot \frac{2\varepsilon+1}{2\varepsilon+n^2} \cdot \mu_0. \quad (3)$$

Dipole moments μ_{1ef} and μ_{2ef} were calculated graphically by extrapolation of the concentration dependence of summary orientation polarization S_{12} to infinite dilution:

$$S_{12} = \mu_{1ef}^2 x_1 + \mu_{2ef}^2 x_2; \quad (4)$$

$$S_{12} = \mu_{1ef}^2 + (\mu_{2ef}^2 - \mu_{1ef}^2) x_2 = a + bx. \quad (5)$$

Dipole moments $(\mu_{1ef})^2|_{x_2=0}$ and $(\mu_{2ef})^2|_{x_2=0}$ were calculated using the parameters a and b by the equations

$$a = (S_{12})|_{x_2=0} = (\mu_{1ef})^2|_{x_2=0}; \quad (6)$$

$$b = \left.\frac{\partial S_{12}}{\partial x_2}\right|_{x_2=0} = \mu_{2ef}^2\big|_{x_2=0} - \mu_{1ef}^2\big|_{x_2=0}; \quad (7a)$$

$$(\mu_{2ef})^2|_{x_2=0} = (\mu_{1ef})^2|_{x_2=0} + b. \quad (7b)$$

Taking into account that at infinite dilution $\varepsilon_{12}|_{x_2=0} = \varepsilon_1$, dipole moments of the components 1 and 2 were defined by

$$\mu_1 = (\mu_{0,1}^2 \cdot g_1)^{1/2} = \frac{3(\mu_{1ef}^2\big|_{x_2=0})^{1/2}(2\varepsilon_1 + n_1^2)}{(n_1^2+2)(2\varepsilon_1+1)}; \quad (8)$$

$$\mu_2 = (\mu_{0,2}^2 \cdot g_2)^{1/2} = \frac{3(\mu_{2ef}^2\big|_{x_2=0})^{1/2}(2\varepsilon_1 + n_2^2)}{(n_2^2+2)(2\varepsilon_1+1)}. \quad (9)$$

Using the results of the measurement of permittivity and density of the water used as a solvent, the dipole moment of liquid water molecule μ was calculated by Onsager formula [8]:

$$\frac{(\varepsilon - n^2)(2\varepsilon + n^2)}{\varepsilon(n^2+2)^2} = \frac{4\pi N_A}{3} \cdot \frac{\rho}{M} \cdot \frac{\mu^2}{3kT}. \quad (10)$$

Here ε, n, ρ, M are dielectric permittivity, refraction index, density and molecular mass of water, respectively.

Refraction indexes of the polymer and solvent were determined at fixed temperatures from the molar refraction R_D by

$$R_D = \frac{n^2-1}{n^2+2}\frac{M}{\rho}. \quad (11)$$

Molar refraction was taken as a sum of atomic refractions and bond increments [12].

PVP monomeric unit molecular mass and molecular refraction were estimated to be $M_{PVP} = 111$ and $R_{DPVP} = 27.445$. Molecular mass and molecular refraction of the hypothetical monomeric unit of PVP + FC_{60} complex were calculated as average values for a macromolecule containing PVP and FC_{60} in the proportion of 0.8 mole % FC_{60} to 100g PVP. Also, using values $M_{FC60} = 720$, $R_{DFC60} = 230.4$ [3] for molecular cluster FC_{60}, values for complex $M_{PVP+FC60} = 111.75$ and $R_{DPVP+FC60} = 29.773$ were obtained.

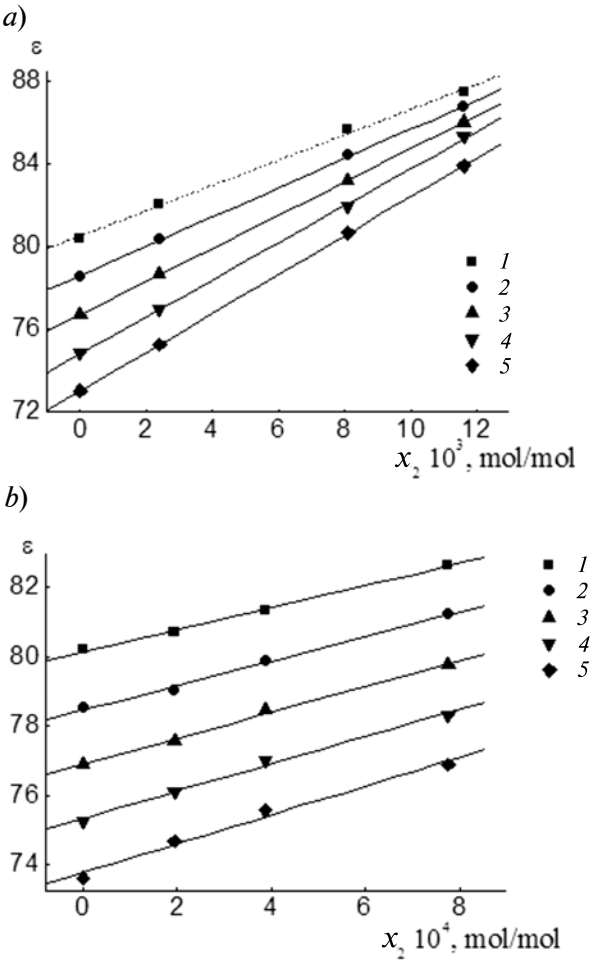

Fig. 1. Dielectric permittivity concentration dependence of PVP (*a*) and PVP+FC_{60} (*b*) aqueous solutions at T °C: 20(*1*); 25(*2*); 30 (*3*); 35(*4*); 40(*5*)

Table 1

Temperature dependences of water, PVP and PVP + FC_{60} characteristics

T °C	v_1, cm³/g	n_1^2	v_2, cm³/g	$n_{2\ PVP}^2$	$n_{2\ PVP+FC60}^2$
20	1.0018	1.7778	0.8333	2.26579	2.40719
25	1.0030	1.7765	0.8343	2.26354	2.40411
30	1.0044	1.7750	0.8353	2.26139	2.40224
35	1.0060	1.7731	0.8363	2.26925	2.39978
40	1.0078	1.7712	0.8373	2.25711	2.39733

Dipole moment estimation total error was $\Delta\mu = \pm 0.05$ D.

Dielectric permittivity concentration dependences for PVP and PVP + FC_{60} aqueous solutions in the temperature range of 20 – 40 °C are given in Fig. 1. Concentrations used are small enough ($x_2 \le 1.16 \cdot 10^{-3}$ mole\mole and $x_2 \le 0.8 \cdot 10^{-3}$ mole\mole respectively) to make it possible to extrapolate ε_{12} to infinite dilution situation and to apply dielectric polarization theories for dipole moment calculations.

Molar orientation polarization S_{12} values were calculated by (1) using permittivity (see Fig. 1), specific volume and refraction indexes (Table 1). As an example, Fig. 2 shows concentration dependences of S_{12} for aqueous solutions of PVP and PVP+FC_{60} at 25 °C. Values

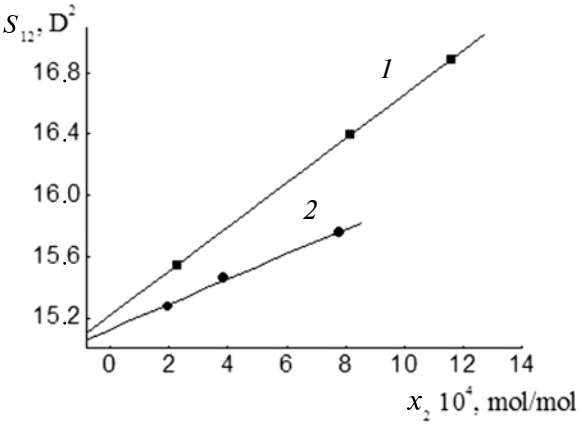

Fig. 2. Molar orientation polarization S_{12} concentration dependence of PVP (*1*) and PVP + FC_{60} (*2*) aqueous solutions at 25 °C

Table 2

Molar orientation polarization S_{12} temperature dependences for PVP and PVP + FC_{60} aqueous solutions

T °C	PVP			PVP+FC_{60}		
	$x_2 = 2.27 \cdot 10^{-4}$	$x_2 = 8.14 \cdot 10^{-4}$	$x_2 = 0.00116$	$x_2 = 1.94 \cdot 10^{-4}$	$x_2 = 3.87 \cdot 10^{-4}$	$x_2 = 7.76 \cdot 10^{-4}$
20	15.592	16.344	16.716	15.326	15.464	15.752
25	15.540	16.394	16.880	15.272	15.461	15.754
30	15.483	16.439	17.044	15.261	15.453	15.749
35	15.416	16.481	17.207	15.242	15.439	15.739
40	15.339	16.516	17.222	15.220	15.417	15.723

Table 3

Dipole moment and Kirkwood factor of water in solutions of PVP and PVP + FC_{60}

T °C	Onsager factor (3)	PVP solution				PVP + FC_{60} solution			
		$(S_{12})\|_{x2=0}$ (6)	μ_{1ef} (6)	μ_1 (8)	Kirkwood factor (2)	$(S_{12})\|_{x2=0}$ (6)	μ_{1ef} (6)	μ_1 (8)	Kirkwood factor (2)
20	1.254	15.327	3.91	3.12	2.88	15.182	3.89	3.10	2.85
25	1.253	15.216	3.90	3.11	2.86	15.126	3.89	3.10	2.84
30	1.253	15.097	3.89	3.10	2.84	15.113	3.89	3.10	2.84
35	1.252	14.967	3.87	3.09	2.82	15.093	3.89	3.10	2.84
40	1.251	14.879	3.86	3.08	2.81	15.067	3.88	3.10	2.83

Table 4

Dipole moment and Onsager factor of PVP and PVP + FC_{60} in the water

T °C	PVP				PVP+FC_{60}			
	$b = [\partial(S_{12})/\partial x_2)]\|_{x2=0}$ (7a)	μ_{2ef}(7b)	Onsager factor (3)	μ_2 (9)	$b = [\partial(S_{12})/\partial x_2)]\|_{x2=0}$ (7a)	μ_{2ef}(7b)	Onsager factor (3)	μ_2 (9)
20	1213.2	35.05	1.412	24.8	733.2	27.37	1.456	18.79
25	1438.6	38.13	1.411	27.0	817.3	28.85	1.456	19.82
30	1668.9	41.04	1.410	29.1	827.3	29.02	1.456	19.93
35	1909.0	43.86	1.410	31.1	842.0	29.28	1.456	20.11
40	2017.4	45.08	1.410	32.0	853.0	29.46	1.456	20.24

of S_{12} at $x_2 = 0$, increments of S_{12} concentration dependences and dipole moments per monomer unit for PVP and PVP+FC_{60} calculated by (2)−(9) are presented in Tables 2 − 4.

Dipole moments and Kirkwood factor temperature dependences of PVP and PVP + FC_{60} as well as of water and N-methylpyrrolidone (NMP) which is low molecular weight analog of PVP monomeric unit are compared in Fig. 3, 4.

It is significant that the values of dipole moments and Kirkwood factor for liquid water calculated according to Buckingham theory are in good agreement with earlier published values. Thus, calculated dipole moments are to be considered correct and adequate.

Dipole moment and Kirkwood factor temperature dependences were discussed in the previous paper [10]. Dipole moments of NMP in the water (4.12 D) and non-polar solvents dioxane (4.06 D) and benzene (4.09 D) at 20 °C are close to each other within the experimental error confirming the fact that the NMP molecules do not disturb the local structure of water. The life time of hydrated shell seems to be too short to lead to significant polarization effects.

Dipole moments of macromolecules of PVP and PVP + FC_{60} are rather large being 25 and 18 D, respectively. It can be seen from Fig. 3 that the dipole moments of PVP increase noticeably with temperature, then reach a plateau of approximately 30 D at 40 °C whereas the dipole moments of PVP + FC_{60} complex stay nearly constant. We suppose that the groups −N−C=O− located in each monomeric unit near the macromolecule main chain, mostly in *trans*-conformation, determine the formation of helical blocks stabilized by donor-acceptor interactions inside the macromolecular coils.

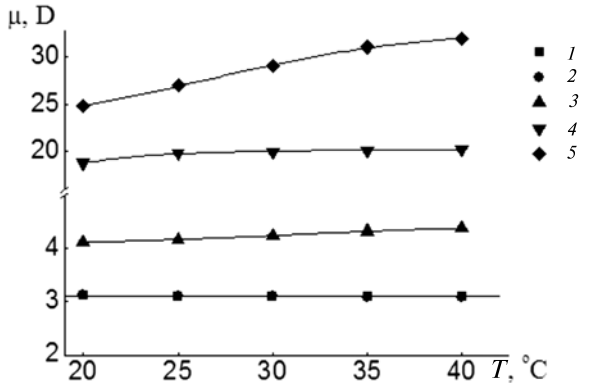

Fig. 3. Dipole moment temperature dependence of water (*1*, *2*) (see also Table 3); N-methylpyrrolidone aqueous solution (*3*) [11]; PVP + FC_{60} (*4*) and PVP (*5*) (Table 4).

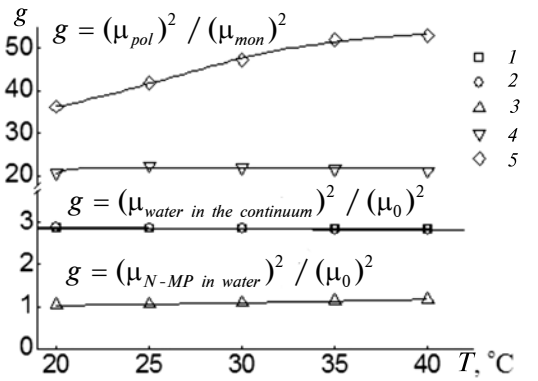

Fig. 4. Kirkwood factor $g = \mu^2 / \mu_0^2$ temperature dependence for water in solutions of PVP and PVP + FC_{60} at infinite dilution (*1*, *2*); NMP (*3*) [11], PVP+FC_{60} (*4*) and PVP (*5*) in the water

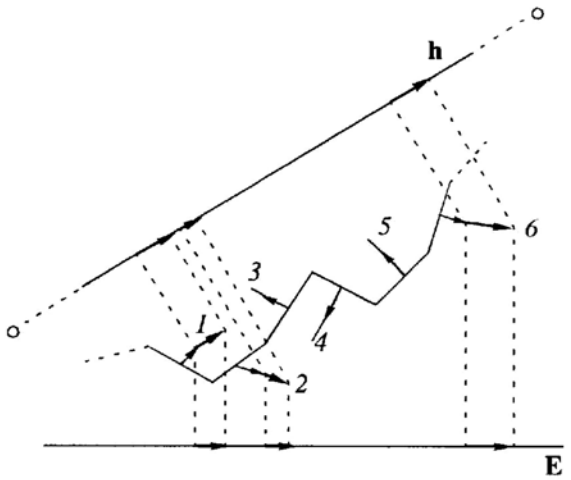

Fig. 5. Formation of non-alternating projections of dipole moment **μ** on helix axis vector **h** and electrical field vector **E** for the chain segment with $-^{+}N-C-O^{-}$group trans-conformation. Thin arrows depict constant dipole moment of $-N-C=O-$ groups near the main chain, bold arrows – induced dipole moments of these groups in donor-acceptor form directions (*1*, *2*, *6*); thin lines – movement fluctuation direction of dipole moments of $-N-C=O-$ groups which do not create induced dipole moments (*3*, *4*, *5*)

In this case, non-alternating projection of the $-N^{+}-C=O^{-}$ group dipole moment on the helix axis appears in the external electrical field as depicted in Fig. 5 similar to the matter discussed in [15]. As the temperature rises, hydrophobic interactions tend to become stronger due to H-bonds of hydrophilic segments, and water molecules life time decreases. Further structuring inside the coil takes place because of the helical blocks orientation ordering. Large values of PVP and PVP+FC_{60} dipole moments in aqueous solutions are determined by induced dipole moments vectorial addition and helical blocks association.

Less values of PVP + FC_{60} complex dipole moment are caused by fullerene molecules implantation into macromolecular coils, which makes helical blocks formation more difficult. In the macromolecular coil of PVP + FC_{60}, complex helical blocks seem to be shorter than in PVP macromolecules. Distinctive for fullerene, donor-acceptor interactions [16] with PVP monomeric units (so called lactam traps) lead to monomeric unit dipole moments compensation, helical blocks shortening and, thus, macromolecule dipole moment decrease. Coordination number of polar groups taking part in correlating orientation can be evaluated by Kirkwood factor (see Fig. 4) as approximately 3 for liquid water, approximately 1 for liquid NMP or NMP aqueous solution, 36 for PVP and 24 for PVP + FC_{60} infinitely diluted aqueous solutions.

REFERENCES

1. **Kirsh Yu.E.** Poli-N-vinilpirrolidon i drugie poli-N-vinilamidy. Moscow, Nauka, 1998. (rus)

2. **Kamalova D.I., Koliadko I.M., Remizov A.B.** Konformatsionnye zondy v izuchenii lokal'noi molekuliarnoi dinamiki razvetvlennogo polimetilmetakrilata i ego fullerensoderzhashchego analoga. XX Vseross. Konf. «Struktura i dinamika molekuliarnykh sistem» i 11-ia Mezhdunarodnaia shkola molodykh uchenykh «Sintez, struktura i dinamika molekuliarnykh sistem». 24-29 iiunia 2013g. ozero Ial'chik. Sb. tez-v, dokl. i soobshch. 106 p. (rus)

3. **Khairullin A.R., Stepanova T.P., Rozhkova N.N., Gladchenko S.V., Krakoviak M.G., Anufrieva E.V., Piotrovskii L.B., Anan'eva T.D., Nekrasova T.N.** Vodorastvorimye kompleksy fullerena s poli-N-vinilpirrolidonom i sposob polucheniia etikh kompleksov. Patent RF No. 2255942. Opubl. Biul. No. 19. 2005. (rus)

4. **Krakoviak M.G., Anufrieva E.V., Anan'eva T.D., Nekrasova T.N.** Vodorastvorimye kompleksy poli-N-vinilamidov var'iruemogo stroeniia s fullerenami C_{60} i C_{80}. *Vysokomolekuliarnye soedineniia*, 2006, Series A, Vol. 48, No. 5, pp.1–7. (rus)

5. **Moravsky A.P., Fursikov P.V., Kiryakov N.V., Ryabenko A.G.** Mol. Mat. 1996, Vol. 7, pp. 241–246. (rus)

6. **Stepanova T.P., Burshtein L.L.** *Izmeritel'naia iacheika*, 1983, No.22. 105 p. (rus)

7. **Buckingham A.D.** A Theory of the dielectric polarization of polar substances. *Proc. Roy. Soc. A. Mathem. and Phys. Sci.* 1956, Vol. A 38, No. 1213, pp. 235–244.

8. **Onsager L.** Electrical moments of molecules in liquids. *J. Amer. Chem. Soc.* 1936, Vol. 58, No. 8, pp. 1468–1493.

9. **Vol'kenshtein M.V.** Stroenie i fizicheskie svoistva molekul. Moscow, Leningrad, Iz-vo AN SSSR, 1955. (rus)

Stepanova T.P., Karpenko E.D., Kapralova V.M. Dipole moments of N-methylpyrrolidone in liquid state and in dilute aqueous solution. *St. Petersburg*

Polytechnical University Journal: Physics and mathematics, 2013, No. 4-1(182) pp. 112–116. (rus)

11. **Lee C.M., Kumler W.D.** The dipole moment and structure of five- and six- membered lactams. *JACS*, 1961, Vol.83, No. 22, pp.4593–4596.

12. **Frolov V.I., Stepanova T.P.,.Borisova T.I, Filippova O.E., Khokhlov. A.R.** Dinamika ionnoi atmosfery gelei polimetakrilata natriia v metanole v radiochastotnom diapazone. *Vysokomolekuliarnye soedineniia*, 2002, A, Vol. 44, No. 4, pp. 597–604. (rus)

13. **Badamshina E.R., Gafurova M.P.** Modifikatsiia svoistv polimerov putem dopirovaniia fullerenom C_{60}. *Vysokomolekuliarnye soedineniia*, 2008, Seriia B, Vol. 50, No. 8, pp.1572–1584. (rus)

14. **Changchun Wang, Zhi-Xin Guo, Shoukuan Fu, Wei Wu, Daoben Zhu.** Polymers containing fullerene or carbon nanotube structures. *Prog. Polym. Sci.* 2004, No. 29, pp. 1079–1141.

15. **Evlampieva N.P., Lavrenko P.N, Melenevskaia E.Yu., Vinogradova L.V., Ryuntev E.I., Zgonnik V.N.** Molekuliarnye svoistva kompleksov tsiklosoderzhashchikh polimerov s fullerenom C_{60} v rastvorakh. *Fizika tverdogo tela*, 2002, Vol. 44, Iss. 3, pp. 537–540. (rus)

16. **Vinogradova L.V., Melenevskaia E.Yu., Khachaturov A.S.** Vodorastvorimye kompleksy fullerena C_{60} s poli-N-vinilpirrolidonom. *Vysokomolekuliarnye soedineniia*, Seriia A, 1998, Vol. 40, No. 11, p. 1854. (rus)

СПИСОК ЛИТЕРАТУРЫ

1. **Кирш Ю.Э.** Поли-N-винилпирролидон и другие поли-N-виниламиды. М.: Наука, 1998. 252 с.

2. **Камалова Д.И., Колядко И.М., Ремизов А.Б.** Конформационные зонды в изучении локальной молекулярной динамики разветвленного полиметилметакрилата и его фуллереносодержащего аналога // XX Всерос. конф. «Структура и динамика молекулярных систем» и 11-я Междунар. школа молодых ученых «Синтез, структура и динамика молекулярных систем». 24 – 29 июня 2013 г. Озеро Яльчик . Сб. тезисов и сообщений. 106 с.

3. **Хайруллин А.Р., Степанова Т.П., Рожкова Н.Н., Гладченко С.,В., Краковяк М.Г., Ануфриева Е.В., Пиотровский Л.Б., Ананьева Т.Д., Некрасова Т.Н.** Водорастворимые комплексы фуллерена с поли-N-винилпирролидоном и способ получения этих комплексов. Патент РФ. № 2255942. Опубл. Бюл. № 19, 2005 г.

4. **Краковяк М.Г., Ануфриева Е.В., Ананьева Т.Д., Некрасова Т.Н.** Водорастворимые комплексы поли-N-виниламидов варьируемого строения с фуллеренами C_{60} и C_{80} // Высокомолекулярные соединения. 2006. Сер. А. Т. 48. № 5. С. 926–932.

5. **Моравский А.П., Фурсиков П.В., Кирьяков Н.В., Рябенко А.Г.** // Мол. мат. 1996. Т. 7., 241 с.

6. **Степанова Т.П., Бурштейн Л.Л.** Измерительная ячейка. А.с. № 10232331983. 1983 г.

7. **Buckingham A.D.** A theory of the dielectric polarization of polar substances. *Proc. Roy. Soc. A., Mathem. a. Phys. Sci.* 1956, Vol. A 38, No. 1213, pp. 235–244.

8. **Onsager L.** Electrical moments of molecules in liquids. *J. Amer. Chem. Soc.* 1936, Vol. 58, No. 8, 1468 p.

9. **Волькенштейн М.В.** Строение и физические свойства молекул. М.Л.: Изд-во АН СССР, 1955. 638 с.

10. **Степанова Т.П., Карпенко Е.Д., Капралова В.М.** Дипольные моменты N-винилпирролидона в жидком состоянии и в разбавленном водном растворе // Научно-технические ведомости СПбГПУ. Физико-математические науки. 2013. № 4-1 (182). С. 112–116.

11. **Lee C.M., Kumler W.D.** The dipole moment and structure of five- and six- membered lactams. *JACS*, 1961, Vol.83, No. 22, pp. 4593–4596.

12. **Фролов В.И., Степанова Т.П., Борисова Т.И., Филиппова О.Е., Хохлов А.Р.** Динамика ионной атмосферы гелей полиметилметакрилата натрия в метаноле в радиочастотном диапазоне // Высокомолекулярные соединения. 2002. А. Т. 44. № 4. С. 597– 604.

13. **Бадамшина Е.Р., Гафурова М.П**. Модификация свойств полимеров путем допирования фуллереном C_{60} // Высокомолекулярные соединения. 2008. Сер. Б. Т. 50. № 8. С. 1572–1584.

14. **Changchun Wang, Zhi-Xin Guo, Shoukuan Fu, Wei Wu, Daoben Zhu.** Polymers containing fullerene or carbon nanotube structures. *Prog. Polym. Sci.* 2004, No. 29, pp. 1079–1141.

15. **Евлампиева Н.П., Лавренко П.Н., Меленевская Е.Ю., Виноградова Л.В., Рюмцев Е.И., Згонник В.Н.** Молекулярные свойства комплексов циклосодержащих полимеров с фуллереном C_{60} в растворах // Физика твердого тела. 2002. Т. 44. Вып. 3. С. 537–540.

16. **Виноградова Л.В., Меленевская Е.Ю., Хачатуров А.С.** Водорастворимые комплексы фуллерена C_{60} с поли-N-винилпирролидоном // Высокомолекулярные соединения. 1998. Сер. А. Т. 40. № 11. С. 1854.

СТЕПАНОВА Тамара Павловна – *кандидат физико-математических наук, старший научный сотрудник Института высокомолекулярных соединений РАН.*
199004, Россия, г. Санкт-Петербург, Большой пр. В.О., 31
t_stepanova2005@mail.ru

АНАНЬЕВА Татьяна Дмитриевна – *кандидат химических наук, старший научный сотрудник Института высокомолекулярных соединений РАН.*
199004, Россия, г. Санкт-Петербург, Большой пр. В.О., 31
anthracene@hq.macro.ru

КАРПЕНКО Елена Драгановна – *студентка Санкт-Петербургского государственного политехнического университета.*
195251, Россия, г. Санкт-Петербург, Политехническая ул., 29.
ele62461401@yandex.ru

КАПРАЛОВА Виктория Маратовна – *кандидат физико-математических наук, доцент кафедры интегральной электроники Санкт-Петербургского государственного политехнического университета.*
195251, Россия, г. Санкт-Петербург, Политехническая ул., 29.
kapralova2006@yandex.ru

UDC 538.958

L.E. Vorobjev, D.A. Firsov, V.Yu. Panevin,
A.N. Sofronov, R.M. Balagula, I.S. Makhov

St. Petersburg State Polytechnical University,
29 Politechnicheskaya St., St. Petersburg, 195251, Russia

NEAR- AND FAR-INFRARED EMISSION FROM GaAs/AlGaAs QUANTUM WELLS UNDER INTERBAND OPTICAL EXCITATION

Л.Е. Воробьев, Д.А. Фирсов, В.Ю. Паневин,
А.Н. Софронов, Р.М. Балагула, И.С. Махов

ИЗЛУЧЕНИЕ БЛИЖНЕГО И ДАЛЬНЕГО ИНФРАКРАСНОГО ДИАПАЗОНА ИЗ КВАНТОВЫХ ЯМ GaAs/AlGaAs ПРИ МЕЖЗОННОМ ОПТИЧЕСКОМ ВОЗБУЖДЕНИИ

The results of experimental studies of low-temperature impurity-assisted photoluminescence of *n*-doped GaAs/AlGaAs quantum well structures both in near- and far-infrared (terahertz) spectral ranges under interband optical excitation are presented. In the near-infrared photoluminescence spectra the optical electron transitions from the donor ground state to the hole subband are revealed. The depopulation of the impurity ground states due to these transitions allowed us to observe photoluminescence in terahertz spectral range related to electron transitions from the first electron subband to the donor state as well as to intracenter optical transitions. Experimental results in near- and far-infrared spectral ranges are well-consistent with the results on terahertz photoconductivity and theoretical calculations.

IMPURITIES, QUANTUM WELLS, TERAHERTZ RADIATION, PHOTOLUMINESCENCE.

В настоящей работе представлены результаты экспериментальных исследований низкотемпературной примесной фотолюминесценции (ФЛ) из структур с квантовыми ямами (КЯ) GaAs/AlGaAs *n*-типа в ближней и дальней инфракрасной (ИК) областях спектра. В спектрах ФЛ в ближнем ИК диапазоне проявляются оптические переходы из основного состояния донора в КЯ в нижнюю подзону дырок в КЯ. Опустошение основного состояния донора благодаря этим переходам позволило нам наблюдать фотолюминесценцию в терагерцовом диапазоне, связанную с переходами электронов из первой электронной подзоны на состояния донора, а также с внутрицентровыми оптическими переходами. Результаты исследования ФЛ в ближнем и дальнем ИК диапазонах дополняют друг друга и хорошо согласуются с результатами исследования терагерцовой фотопроводимости и теоретическими расчетами.

ПРИМЕСИ, КВАНТОВЫЕ ЯМЫ, ТЕРАГЕРЦОВОЕ ИЗЛУЧЕНИЕ, ФОТОЛЮМИНЕСЦЕНЦИЯ.

I. Introduction

Development of effective emitters operating in terahertz (far-infrared) spectral range is considered as an important and urgent task because of the wide range of potential applications of various terahertz devices in information technologies, medicine, chemistry, physics, nanotechnology and other demanding areas [1]. The energies of intracenter carrier transitions in doped semiconductors and semiconductor nanostructures correspond to terahertz spectral ranges. Development of lasers using shallow impurity levels in the lasing scheme is a promising alternative to the well-known quantum cascade lasers [2] of a very complicated technology. That is why the optical studies of impurity related carrier transitions attract particular interest with respect to developing new types of terahertz radiation sources.

There are some mechanisms suggested for obtaining the impurity related terahertz emission. In Ref. [3] spontaneous emission in the THz range was observed from electrically pumped bulk silicon doped with phosphorus. Another way to create nonequilibrium carriers and to use intracenter carrier transitions can be realized with the impurity-band optical excitation by the radiation of CO_2 laser (see, for example, [4] where THz lasing was observed in bulk silicon doped with phosphorus).

Low-temperature interband photoluminescence in doped semiconductors can be used for the depopulation of the ground impurity states due to processes of impurity-band recombination. In Ref. [5] terahertz luminescence under the interband photoexcitation of bulk *n*-GaAs and *p*-Ge semiconductors at low temperatures was reported. The terahertz photoluminescence was caused by intraband radiative carrier transitions, which accompanied the capture of nonequilibrium carriers by impurity centers. The depopulation of impurity ground states was achieved due to the impurity-assisted electron-hole recombination.

In this work we present the investigation of impurity-related THz emission in nanostructures with quantum wells (QW). QW structures are of considerable interest because the energy differences between impurity levels can be changed easily with changing the QW structure parameters. Previously, terahertz emission in *n*-GaAs/AlGaAs quantum well structure was observed under impurity breakdown in strong electric field [6]. This emission was related mainly to electron intracenter optical transitions between resonant and bound donor states. In the present work we used optical interband excitation of nonequilibrium carriers in donor-doped GaAs/AlGaAs QW structures to initiate THz emission. After optical excitation, the electrons on the ground donor state radiatively recombine with nonequilibrium holes. Nonequilibrium electrons can be captured on the ground states of positively charged donors with the emission of terahertz photons. Nonequilibrium electrons can also be captured on excited states of donors and then fall on donor ground states with emission of photons.

In this work we present spectra of both intraband terahertz (far-infrared) radiation and interband near-infrared emission (photoluminescence). It is shown that the features in the measured spectra are related to impurity-assisted electron transitions in quantum wells.

II. Samples and Experimental Techniques

The samples for optical studies were MBE grown on GaAs semi-insulating substrate placed on a 0.2 μm GaAs buffer layer and they consisted of 50 layers of 30 nm GaAs quantum wells separated with 7 nm $Al_{0.3}Ga_{0.7}As$ barriers. Quantum wells were doped in the 4 nm layer with surface donor (Si) concentration of $3 \cdot 10^{10}$ cm^{-2}. Doped region was shifted by 6 nm from the QW center. The samples had a 20 nm GaAs cap layer doped up to the level of $5 \cdot 10^{17}$ cm^{-3} with a silicon.

The sample was mounted in a low vibration closed cycle cryostat Janis PTCM-4-7 based on the pulse tube thermodynamic cycle. Its temperature could be varied from ~4 to 320 K. Interband optical excitation of the sample was attained with solid state CW laser with diode pumping (λ = 532 nm, P = 8 mW). We used fused silica window, mirrors and lens to direct the laser beam to the sample inside the cryostat with an incidence angle of approximately 45 ° to the growth axis. Far-infrared (IR) emission as well as near-IR one was collected from the surface of the QW structure in the growth axis direction. Near-IR emission was studied through the fused silica cryostat window, far-IR emission was studied through the polymethylpentene (TPX) window.

Far-IR photoluminescence spectra were studied with Fourier transform technique using vacuum Fourier transform infrared (FTIR) spectrometer Bruker Vertex 80v operating in step-scan mode. FTIR spectrometer had a polyethylene (PE) entrance window and a kit of exchangeable terahertz beamsplitters. There was a distance about 2 cm between the cryostat TPX window and the spectrometer PE window. Here we put ~100 μm black PE filter to block the pumping light. The intensity of the far-IR emission was measured with Si bolometer system (made by Infrared Laboratories, Inc.) cooled with liquid helium. The bolometer cryostat had a vacuum optical coupling with the FTIR spectrometer. Bolometer had a PE window and two internal interchangeable fil-

ters, namely, 0.5 mm thin PE filter and 1 mm thick crystalline quartz filter. Pre-amplified and filtered bolometer photoresponse was measured by a lock-in amplifier SR-830 on a pump laser driven frequency (laser current was modulated with the frequency of 87 Hz, 50% duty cycle). Lock-in output signal was digitized by a 14-bit ADC. Bruker software OPUS triggered measurement cycle for each FTIR spectrometer mirror position and performed Fourier transform of the resulting interferogram.

We have used two optical configurations of the FTIR setup with different spectral throughputs. The combination of 6 μm multilayer Mylar beamsplitter with 0.5 mm PE bolometer filter allowed us to investigate as wide spectral range as 4 – 85 meV. The combination of 25 μm Mylar beamsplitter with a crystalline quartz bolometer filter significantly increased setup transmission in 2 – 14 meV spectral range but blocked higher frequencies.

Near-IR photoluminescence spectra were studied with grating monochromator Horiba Jobin Yvon FHR-640 operating in a spectrograph mode with a holographic grating of 1200 groves per mm and a liquid nitrogen cooled CCD camera.

III. Experimental Results and Discussion

In the conditions of low temperature (about 4 K) and interband optical excitation of *n*-doped QW nanostructures, the recombination of nonequilibrium holes and electrons initially localized at non-ionized donors can exist along with exciton recombination. That is why in the present work we had a pleasure to observe both near-IR emission and terahertz radiation. Near-IR emission was related to exciton recombination and electron transitions from donor states to the valence band. The terahertz radiation was related to electron transitions from the conduction band to donor states and probably to intracenter electron transitions accompanying the process of nonequilibrium electron capture by ionized donors.

The results of photoluminescence (PL) investigations in the *n*-doped QW nanostructure in the far-IR spectral range are shown in Fig. 1. PL spectrum of the substrate is also shown there. It should be noted that the real emission spectra can slightly differ from the spectra presented in our paper because of spectral dependency of photodetector sensitivity and windows and beamsplitter transmission. Anyway, Fig. 1 allows one to distinguish the difference in photoluminescence spectra of QW structure and its substrate. Really, the wide emission band 13 – 30 meV is presented in both spectra. This fact probably means, that in this spectral range we deal with some impurity related emission from the bulk layers of the sample such as semi-insulated (probably compensated) substrate and the cap or barrier layers. It is well known that the energies of intracenter hole transitions, for example, in Be-doped bulk GaAs, lie in this spectral range [7]. The thickness of QW layers is not too high, so the exciting laser radiation can reach the substrate and produce impurity involved optical transitions according to the mechanism described for donors in QW.

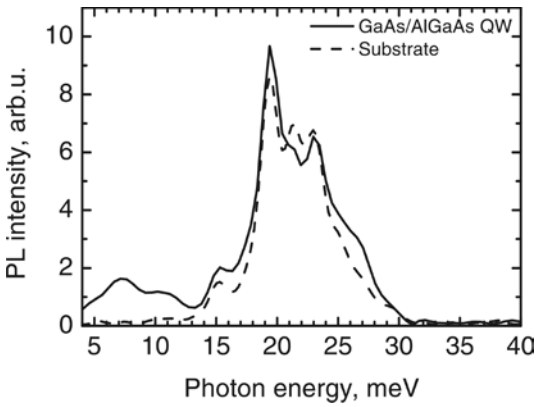

Fig. 1. Terahertz emission spectrum of optically excited GaAs/AlGaAs QW structure – solid line. Dashed line corresponds to substrate emission spectrum. $T = 4.4$ K

It should be noted that the weaker emission band near 4 – 13 meV is a feature of the QW spectrum only. Some changes of the optical path allow us to improve the throughput of our experimental setup in 2 – 14 meV spectral range and to study QW emission spectral features more elaborately at two temperatures (see Fig. 2). Beyond the above-mentioned spectral range, the throughput of the experimental setup is equal to zero.

In accordance with the results of electron energy spectrum calculations for our QW structure (see Ref. [6]), the energies of electron transitions between the first electron subband

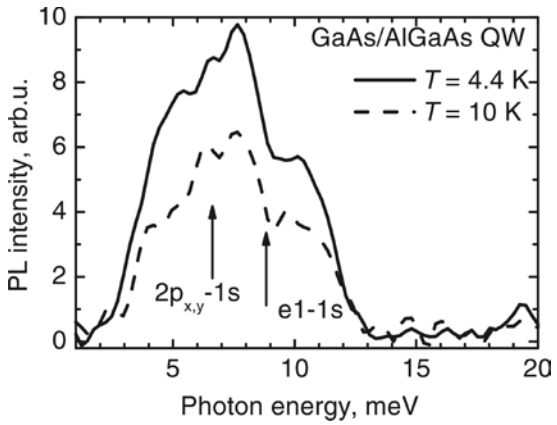

Fig. 2. Long wavelength part of QW emission spectrum measured at two temperatures. Energies of some allowed electron optical transitions are shown with arrows

and the impurity ground state $e1 \rightarrow 1s$, and between the excited and ground impurity states $2p_{x,y} \rightarrow 1s$ are 8.8 and 6.5 meV, respectively. Note, that these calculated values agree well with experimental photoconductivity spectra also presented in Ref. [6]. Energies of these transitions are shown by arrows in Fig. 2. One should not wonder that in our spectra different impurity related transitions are broadened and cannot be resolved clearly. It is well known that narrow impurity lines could only be observed in «pure» samples, with doping level significantly less then in our QW structure (see, for example, Ref. [7]). Thus, we can conclude that our 4 – 13 meV emission band can be connected exactly with band-impurity and intracenter transition in the QW. The observed decrease of photoluminescence intensity by 1.5 times with temperature increase from 4.4 K to 10 K can be explained with a variety of factors, such as ionized donor capture probability decrease or the increase of the carrier ejection from the neutral donor with temperature increase. Earlier, the similar temperature quenching of terahertz luminescence was observed in Ref. [5] in bulk semiconductors.

The results of photoluminescence investigations of the *n*-doped QW nanostructure, as well as of its substrate, in the near-IR spectral range are substantially supporting our conception pronounced above about the origin of the observed terahertz emission. As a rule, at low temperature, in the interband photoluminescence spectra of the doped semiconductor or nanostructures, one can observe series of emission lines associated with radiative recombination of the free heavy and light excitons (the latter can be observed in QW structures at higher temperatures), radiative recombination of the impurity-bound excitons and radiative electron-hole recombination via impurity states (see, for example, Ref. [8 – 10]).

The results of investigations of the interband excitonic and impurity assisted near-IR radiation under interband optical pumping in our QW structure are shown in Fig. 3.

According to the calculation of electron (*e*) and heavy hole (*hh*) energy states in our QW, we expect the interband energy separation between the first electron and hole QW levels $e1 - hh1$ to be of about 1.526 eV. Direct optical transitions between the electron and hole states are not observed in our spectra because of excitonic formation effects. The exciton binding energy in bulk GaAs is about 4.2 meV [11]. For such a wide QW as our one, the exciton binding energy value should not be significantly more. Thus, the emission line marked in Fig. 3 with the arrow Xe1-hh1 could be connected with free heavy exciton for the first QW subbands.

The emission line marked with the arrow Si-X in Fig. 3 could be connected with the donor bound exciton.

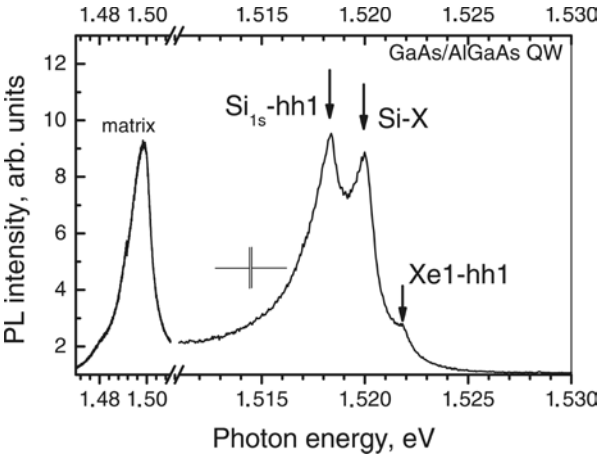

Fig. 3. Near-IR luminescence spectra of the GaAs/AlGaAs QW structure under interband optical excitation; $T = 4$ K. Arrows show the main emission lines (see discussion in the text). Spectral resolution is shown in the plot

Finally, as we expected for interband recombination via 1*s* donor state, we have observed optical transition marked as Si_{1s}-*hh*1 for the photon energy about 1.5183 eV.

As we have pointed above, that transition foregoes the *e*1 − 1*s* transition observed in far-IR PL spectra.

The low frequency part of near-IR spectrum with the main power concentrated between 1.49 eV and 1.50 eV (marked «matrix» in Fig. 3) lies at the distance of about 20 − 30 meV from GaAs energy gap (1.519 eV) and could be connected with some impurity transitions in the sample substrate which as well could give their impact on far-IR spectra described above.

IV. Summary

Finally, in the present paper, the emission of terahertz radiation related to band-impurity and intracenter optical transition under optical interband excitation in silicon-doped *n*-GaAs/AlGaAs quantum well structures has been observed and investigated.

Acknowledgements

The reported study was partially supported by RFBR, research projects No. 12-02-01155 a, by Russian Federal Program «Kadry» for 2009 − 2013, Russian President grant and the German-Russian Program of the Federal Ministry of Education and Research (BMBF).

REFERENCES

1. **Tonouchi M.** Cutting-edge terahertz technology. *Nature Photonics*, 2007, Vol. 1, No. 2, pp. 97−105.

2. **Kohler R., Tredicucci A., Beltram F., Beere H.E., Linfield E.H., Davies A.G., Ritchie D.A., Iotti R.C., Rossi F.** Terahertz semiconductor − heterostructure laser. *Nature*, 2002, Vol. 417, No. 6885, 156 p.

3. **Lv P.-C., Troeger R.T., Adam T.N., Kim S., Kolodzey J., Yassievich I.N., Odnoblyudov M.A., Kagan M.S.** Electroluminescence at 7 terahertz from phosphorus donors in silicon. *Applied Physics Letters*, 2004, Vol. 85, No. 1, pp. 22−24.

4. **Pavlov S.G., Zhukavin R.Kh., Orlova E.E., Shastin V.N., Kirsanov A.V., Hübers H.-W., Auen K., Riemann H.** Stimulated emission from donor transitions in silicon. *Phys. Rev. Lett.*, 2000, Vol. 84, No. 22, pp. 5220−5223.

5. **Andrianov A.V., Zakhar'in A.O., Ivanov Yu.L., Kipa M.S.** Terahertz impurity luminescence under the interband photoexcitation of semiconductors. *JETP Lett.*, 2010, Vol. 91, No.2 , pp. 96−99.

6. **Firsov D.A., Shalygin V.A., Panevin V.Yu., Melentyev G.A., Sofronov A.N., Vorobjev L.E., Andrianov A.V., Zakhar'in A.O., Mikhrin V.S., Vasil'ev A.P., Zhukov A.E., Gavrilenko L.V., Gavrilenko V.I., Antonov A.V., Aleshkin V.Ya.** Terahertz emission and photoconductivity in *n*-type GaAs/AlGaAs quantum wells: the role of resonant impurity states. *Semiconductors*, 2010, Vol. 44, No. 11, pp. 1394−1397.

7. **Lewis R.A., Cheng T.S., Henini M., Chamberlain J.M.** Energy states of Be in GaAs. *Phys. Rev. B*, 1996, Vol. 53, No. 19, pp. 12829−12834.

8. **Kundrotas J., Čerškus A., Valušis G., Johannessen A., Johannessen E., Harrison P., Linfield E.H.** Impurity-related photoluminescence line shape asymmetry in GaAs/AlAs multiple quantum wells: Fractional−dimensional space approach. *Journal of Applied Physics*, 2010, Vol. 107, No. 9, 093109.

9. **Kundrotas J., Čerškus A., Nargelienė V., Sužiedėlis A., Ašmontas S., Gradauskas J., Johannessen A., Johannessen E., Umansky V.** Enhanced exciton photoluminescence in the selectively Si-doped GaAs/$Al_xGa_{1-x}As$ heterostructures. *Journal of Applied Physics*, 2010, Vol. 108, No. 6, 063522.

10. **Tabata A., Levine A., Marti Ceschin A., Quivy A.A., Scolfaro L.M.R., Enderlein R., Leite J.R.** Optical properties of GaAs/AlGaAs selectively doped quantum well structures. *Radiation Effects and Defects in Solids: Incorporating Plasma Science and Plasma Technology*, 1998, Vol. 146, No. 1−4, pp. 207−214.

11. **Nam S.B., Reynolds D.C., Litton C.W., Almassy R.J., Collins T.C.** Free-exciton energy spectrum in GaAs. *Phys. Rev. B*, 1976, Vol. 13, No. 2, pp. 761−767.

СПИСОК ЛИТЕРАТУРЫ

1. **Tonouchi M.** Cutting-edge terahertz technology. *Nature Photonics*, 2007, Vol. 1, No. 2, pp. 97−105.

2. **Kohler R., Tredicucci A., Beltram F., Beere H.E., Linfield E.H., Davies A.G., Ritchie D.A., Iotti R.C., Rossi F.** Terahertz semiconductor − heterostructure laser. *Nature*, 2002, Vol. 417, No. 6885, 156 p.

3. **Lv P.-C., Troeger R.T., Adam T.N., Kim S., Kolodzey J., Yassievich I.N., Odnoblyudov M.A., Kagan M.S.** Electroluminescence at 7 terahertz from phosphorus donors in silicon. *Applied Physics Letters*, 2004, Vol. 85, No. 1, pp. 22−24.

4. **Pavlov S.G., Zhukavin R.Kh., Orlova E.E., Shastin V.N., Kirsanov A.V., Hübers H.-W., Auen K., Riemann H.** Stimulated emission from donor

transitions in silicon. *Phys. Rev. Lett.*, 2000, Vol. 84, No. 22, pp. 5220–5223.

5. **Andrianov A.V., Zakhar'in A.O., Ivanov Yu.L., Kipa M.S.** Terahertz impurity luminescence under the interband photoexcitation of semiconductors. *JETP Lett.*, 2010, Vol. 91, No.2 , pp. 96–99.

6. **Фирсов Д.А., Шалыгин В.А., Паневин В.Ю., Мелентьев Г.А., Софронов А.Н., Воробьев Л.Е., Андрианов А.В., Захарьин А.О., Михрин В.С., Васильев А.П., Жуков А.Е., Гавриленко Л.В., Гавриленко В. И., Антонов А.В., Алешкин В.Я.** Излучение и фотопроводимость в квантовых ямах GaAs/AlGaAs *n*-типа в терагерцовой области спектра: роль резонансных состояний// ФТП. 2010. Т.44. Вып. 11. С. 1443 – 1446.

7. **Lewis R.A., Cheng T.S., Henini M., Chamberlain J.M.** Energy states of Be in GaAs. *Phys. Rev. B*, 1996, Vol. 53, No. 19, pp. 12829–12834.

8. **Kundrotas J., Čerškus A., Valušis G., Johannessen A., Johannessen E., Harrison P., Linfield E.H.** Impurity-related photoluminescence line shape asymmetry in GaAs/AlAs multiple quantum wells: Fractional–dimensional space approach. *Journal of Applied Physics*, 2010, Vol. 107, No. 9, 093109.

9. **Kundrotas J., Čerškus A., Nargelienė V., Sužiedėlis A., Ašmontas S., Gradauskas J., Johannessen A., Johannessen E., Umansky V.** Enhanced exciton photoluminescence in the selectively Si-doped GaAs/$Al_xGa_{1-x}As$ heterostructures. *Journal of Applied Physics*, 2010, Vol. 108, No. 6, 063522.

10. **Tabata A., Levine A., Marti Ceschin A., Quivy A.A., Scolfaro L.M.R., Enderlein R., Leite J.R.** Optical properties of GaAs/AlGaAs selectively doped quantum well structures. *Radiation Effects and Defects in Solids: Incorporating Plasma Science and Plasma Technology*, 1998, Vol. 146, No. 1–4, pp. 207–214.

11. **Nam S.B., Reynolds D.C., Litton C.W., Almassy R.J., Collins T.C.** Free-exciton energy spectrum in GaAs. *Phys. Rev. B*, 1976, Vol. 13, No. 2, pp. 761–767.

ВОРОБЬЕВ Леонид Евгеньевич – *доктор физико-математических наук, профессор кафедры физики полупроводников и наноэлектроники Санкт-Петербургского государственного политехнического университета.*
195251, Россия, Санкт-Петербург, Политехническая ул., 29
LVor@rphf.spbstu.ru

ФИРСОВ Дмитрий Анатольевич – *доктор физико-математических наук, профессор, заведующий кафедрой физики полупроводников и наноэлектроники Санкт-Петербургского государственного политехнического университета.*
195251, Россия, Санкт-Петербург, Политехническая ул., 29
DmFir@rphf.spbstu.ru

СОФРОНОВ Антон Николаевич – *кандидат физико-математических наук, доцент кафедры физики полупроводников и наноэлектроники Санкт-Петербургского государственного политехнического университета.*
195251, Россия, Санкт-Петербург, Политехническая ул., 29
Sofronov@rphf.spbstu.ru

ПАНЕВИН Вадим Юрьевич – *старший преподаватель кафедры физики полупроводников и наноэлектроники Санкт-Петербургского государственного политехнического университета.*
195251, Россия, Санкт-Петербург, Политехническая ул., 29
PVYu@rphf.spbstu.ru

БАЛАГУЛА Роман Михайлович – *аспирант кафедры физики полупроводников и наноэлектроники Санкт-Петербургского государственного политехнического университета.*
195251, Россия, Санкт-Петербург,. Политехническая ул., 29
RMBal@spbstu.ru

МАХОВ Иван Сергеевич – *студент Санкт-Петербургского государственного политехнического университета.*
195251, Россия, Санкт-Петербург,. Политехническая ул., 29
Makhoviv@gmail.com

UDC 538.951:53.097

E.N. Shubina [1], P.A. Karaseov [1], M.V. Mishin [1],
V.S. Protopopova [1], A.Ya. Vinogradov [2], N.N. Karaseov [3],
A.V. Arkhipov [1], A.L. Shakhmin [1], O.A. Podsvirov [1], A.I. Titov [1]

[1] St. Petersburg State Polytechnical University,
29 Politekhnicheskaya St., St. Petersburg, 195251, Russia
[2] Ioffe Physical Technical Institute,
26 Politekhnicheskaya St., St. Petersburg, 194021, Russia
[3] St. Petersburg State University of Information Technologies, Mechanics and Optics
49 Kronverkskiy Ave., St. Petersburg, 197101, Russia

EFFECT OF TEMPERATURE ON PROPERTIES OF DLC FILMS AND DLC-Ni:C SANDWICH GROWTH

Е.Н. Шубина, П.А. Карасёв, М.В. Мишин,
В.С. Протопопова, А.Я. Виноградов, Н.Н. Карасёв,
А.В. Архипов, А.Л. Шахмин, О.А. Подсвиров, А.И. Титов

ВЛИЯНИЕ ТЕМПЕРАТУРЫ НА СВОЙСТВА DLC-ПЛЕНОК И НА РОСТ СЭНДВИЧ-СТРУКТУРЫ DLC-Ni:C

A possibility of formation of sandwich structures comprising of both DLC and nano-crystalline Ni-carbon films on silicon substrate is presented. The influence of DLC film exposition to high temperature during preparation of Ni:C layers on its properties has been investigated by means of isochronal thermal annealing in carrying gas used. All structures obtained were examined by atomic force microscopy, scanning electron microscopy and X-ray photoelectron spectroscopy. It has been established that annealing leads to decrease of the internal residual stress in the DLC films as well as causes swelling of samples with temperature rise. The fraction of sp^3 hybridized bonds increases and the sp^2 fraction symmetrically decreases with increase of annealing temperature. The different sequences of growth processes to obtain DLC-Ni:C-DLC sandwich structure were investigated. The best way to get good structure quality is to grow initial DLC film at 200 V and 100 W and Ni:C layer at 500 °C.

DIAMOND-LIKE CARBON, DLC, NANOCRYSTALLINE NICKEL, THERMAL ANNEALING, INTERNAL RESIDUAL STRESS, SANDWICH STRUCTURE.

Продемонстрирована возможность формирования сэндвич-структур, включающих слои алмазоподобного углерода (DLC) и слои углерода с нанокристаллами никеля на кремниевой подложке (ncNi:C). Исследовано влияние высокотемпературной выдержки DLC-пленки в процессе осаждения слоев ncNi:C на ее свойства. Изохронный отжиг проводился в среде технологического газа, используемого в CVD-процессе осаждения. Все полученные структуры были исследованы методами атомной силовой и сканирующей электронной микроскопии, а также рентгеновской фотоэлектронной спектроскопии. Установлено, что отжиг приводит к снятию внутренних механических напряжений в DLC-пленках, а также вызывает свеллинг образцов. При этом с увеличением температуры отжига возрастает доля sp^3-гибридизованных связей и симметрично снижается доля sp^2-связей. Были изучены различные последовательности процессов получения сэндвич-структуры DLC-Ni:C. Наилучший режим для достижения высокого качества структуры – это использование напряжения 200 В и мощности 100 Вт для выращивания DLC-пленки и получение слоев Ni : C при температуре не выше 500 °C.

АЛМАЗОПОДОБНЫЙ УГЛЕРОД, НАНОКРИСТАЛЛ НИКЕЛЯ, ТЕРМИЧЕСКИЙ ОТЖИГ, ВНУТРЕННЕЕ МЕХАНИЧЕСКОЕ НАПРЯЖЕНИЕ, СЭНДВИЧ-СТРУКТУРА.

I. Introduction

Diamond-like carbon (DLC) thin films have attracted significant attention because of their unique properties namely extremely high hardness, transparency in the infrared range, high density, low friction coefficient, chemical stability, etc. [1, 2]. All these provide a possibility to use the DLC thin films in many applications as protective coating for magnetic recording disks, anti-reflective coating on optics and IR windows, wear-resistant coating on cutting and abrasive tools, etc. Moreover, promising field emission properties of DLC thin films have been reported [3–5]. In this way, DLC films can find applications as electron emitters in vacuum microelectronic devices. The aligned array of conducting nanowires inside highly resistive DLC matrix can be used as nanofilaments in complex electronic devices. The formation of such conducting channels in different carbon matrices by irradiation with swift heavy ions is described in [6, 7]. Moreover, in a recent study, H.-G. Gehrke et al. [8, 9] have shown the fabrication of conducting vertical carbon nanowires in insulating Ta-C matrix together with a built-in self-aligned gate electrode which has potential application as a gated field emission cathode.

The properties of DLC films mainly depend on their microstructure, which is an amorphous mixture of sp^2 and sp^3 hybridized bonds between carbon atoms [1 – 5, 8, 9]. The quality of DLC films and therefore their properties such as internal residual stress, resistance, hardness, friction coefficient, etc. can be changed by tuning the ratio of sp^2/sp^3 phases. One more way to change the film properties is its doping by metal (Fe, Cu, Ag, Sn) or non-metal (B, N, P, S, Si) impurities [10 – 13]. Hydrogenated amorphous carbon (α-C:H) films are grown in the processes with the use of hydrogen containing precursors. Therefore, hydrogen is always incorporated into the film and the amount of it also influences on film properties.

On the other hand, the formation of Ni-nanoparticle containing carbon films obtained by CVD technique has been reported recently [14]. Their field emission properties were investigated [15]. These films containing well separated 20 nm Ni particles showed the best emission properties with the threshold field value close to 2 V/μm.

It is possible to improve the conductivity of nanowires formed by swift heavy ions by incorporating metal phase, in particular nickel nanoparticles. At the same time, more or less thick films could not be obtained by the CVD process used for Ni-nanoparticle formation. Hence, it is necessary to grow structure consisting of alternate layers of pure carbon films (DLC) and NiC.

The growth temperature of Ni-nanoparticle containing carbon films is higher than DLC film preparation temperature. In this study an influence of thermal annealing in a carrying gas utilized for Ni-C layer formation on the properties of grown DLC films as well as the possibility to grow the sandwich structures comprising both DLC and Ni-C films on crystalline silicon substrates are presented.

II. Experiment

DLC films were grown on (1 0 0) silicon substrates of 4.30 mm in size in the RF plasma of methane (CH_4) gas. Plasma-enhanced chemical vapor deposition (PECVD) capacitive system with flat electrodes was used [16]. Positive bias was applied to the same electrode as the RF (40 MHz) power. The samples were mounted on the grounded electrode.

To provide good adhesion, three-step substrate pretreatment procedure was used. The first stage of this procedure was oxygen plasma exposition; at the second one, the substrate was annealed at 350 °C. At the third stage, hydrogen plasma exposition was used during sample cooling from annealing to the deposition temperature. Such a scheme is necessary to prevent exfoliating or bursting diamond-like carbon films. Methane pressure during the film deposition was 30 mTorr, substrate temperature was measured by a thermocouple and kept at 300 °C. It is possible to affect the phase composition and therefore the properties of films by the variation of process parameters such as DC-bias voltage in the range of 50 – 500 V, RF-power in the range of 50 – 450 W, and substrate temperature from room to 350 °C [17, 18]. The thickness of grown DLC films was measured by atomic-force microscopy at the film edge after the deposition and was 0.08 ± 0.01 μm.

The set of DLC film samples was annealed in argon ambient at the temperature of 400 – 600 °C using isochronal steps of 60 min. Thermal annealing was carried out using the same setup as for Ni-C film growth.

Ni-nanoparticles containing carbon films were prepared by chemical vapor deposition (CVD) technique with bis-(ethylcyclopentadienyl) nickel ((EtCp)2Ni) as a precursor [14]. The deposition process was carried out in hot-wall horizontal low-pressure silica tube reactor. The temperature range was 500 – 600 °C, the deposition time was 5 min. Argon or hydrogen were used as a carrying gas. (EtCp)2Ni partial pressure was 75 Pa. The total pressure in the reactor was 840 Pa. The obtained layers contained 10 – 20 nm Ni particles (presumably coated by nickel carbide shells), either isolated from each other or comprised into continuous coverage (it depended on some technological parameters, such as deposition time and substrate temperature).

Relative contents of the sp^2 and sp^3 phases in the obtained films were determined using *X*-ray photoelectron spectra measured by NANOFAB-25 system (NT-MDT). The curvature of the silicon wafer was measured using an interferometry method before and after film deposition, and after annealing. Internal residual stress in the film was determined with the use of Stoney equation [19]. All the grown films were compressed. The morphology of the deposited structures was examined using a scanning electron microscope Supra 55 VP. The film thickness was determined after deposition and annealing by atomic force microscopy with Nano-DST (Pacific Nanotechnology) machine.

III. Results

To investigate the influence of thermal annealing on DLC film properties, we prepared a series of samples at 300 °C. DC-bias voltage and RF-power were 200 V and 100 W, correspondingly. The thickness of as-grown films was 70 – 90 nm. In our previous work it was shown that annealing in air in the temperature range of 250 – 350 °C had no effect on the properties of DLC films [17]. Here we present investigating the influence of isochronal annealing in argon ambient in the temperature range of 400 – 600 °C (see Fig. 1) on DLC film properties. These temperatures are typical in the CVD process used to get Ni containing carbon films.

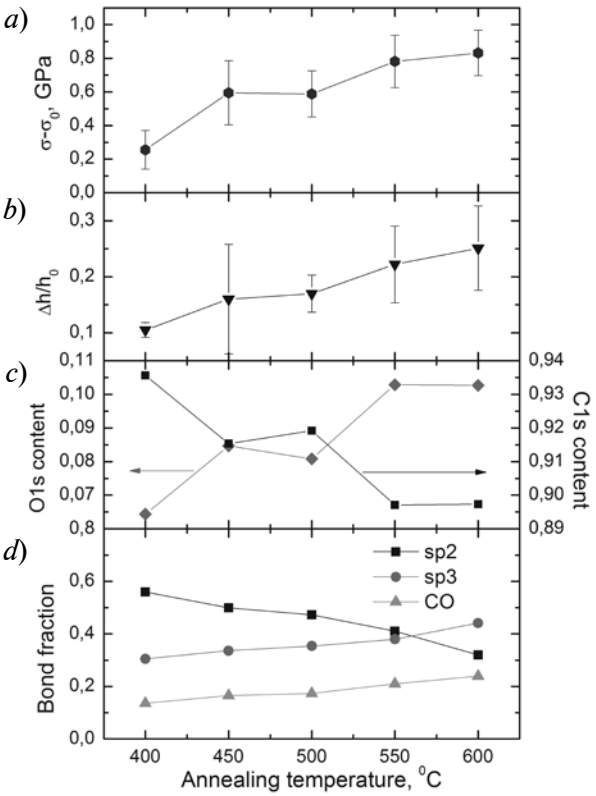

Fig. 1. Dependence of the stress change in the DLC films (*a*), the relative increase of the film thickness (*b*) and the change in the O and C content (*c*) and fraction of sp^2 and sp^3 hybridized bonds (*d*) after isochronal annealing in argon ambient as a function of temperature

In Fig. 1, *a* we present internal residual stress in the DLC film, initial stress value being preliminarily subtracted from the whole value ($\sigma - \sigma_0$), as a function of annealing temperature. As it was pointed out above, all as-grown films were stressed. Fig. 1, *a* shows that the stress value decreases with temperature.

The influence of thermal annealing on the DLC film thickness is presented in Fig. 1, *b*. Almost linear temperature dependence of the film swelling is observed. The film thickness increases up to 25 % of initial thickness. Interestingly, internal stress as well as film thickness exhibit similar trends with the increase of accelerated ion fluence, as it was shown in

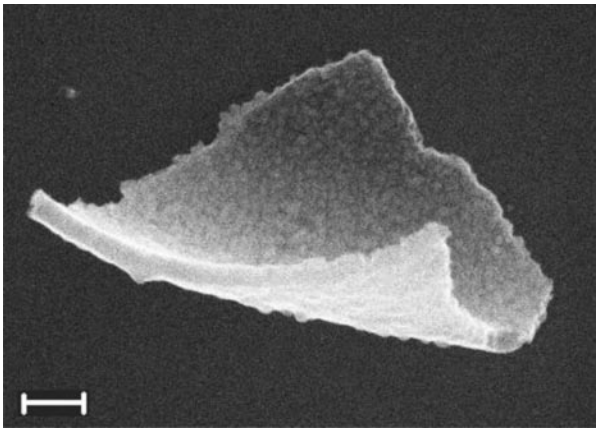

Fig. 2. SEM micrograph of peeled flake of NiC-DLC structure.
Marker length is 200 nm

Ref. [20]. This finding let us conclude that the mechanisms of the film properties change are very close. To support this idea we need to investigate the change in film structure.

Influence of annealing on the film structure was studied by *X*-ray photoelectron spectroscopy. This technique lets us investigate content and bond fraction in ~5 nm thick subsurface layer. The contents of carbon and oxygen in the films are presented in Fig. 1, *c*. C1*s* peak was decomposed into components corresponding to graphite, diamond phases and C—O bond. The positions of corresponding maxima were kept close to 284.6, 285.2, 286.7 eV according to data from Ref. [1]. The results are presented in Fig. 1, *d*. With the rise of annealing temperature, the fraction of sp^3 hybridized bonds increases, and simultaneously the sp^2 phase symmetrically decreases. Moreover, it is seen that the oxygen content at the sample surface increases with the increase of annealing temperature. We explain this high oxygen content as follows. The increase of C—O bond fraction could be associated with the oxidation of the surface when DLC films were taken out the reactor. The driving reason for oxygen trapping can be activation of carbon bonds due to the hydrogen loss during film annealing.

For the preparation of sandwich structures we used two reverse sequences of the film growth processes: Ni : C-DLC and DLC-Ni : C. In the first case, after the deposition of DLC film grown without pretreatment procedure, the Ni : C layer peeled off the substrate. SEM micrograph of a piece of the sample is presented in Fig. 2. The figure shows that the stressed DLC film fixes a Ni nanoparticle containing carbon film, rolls up and peels off. To improve adhesion, the three-step substrate pretreatment procedure was used. But it led to the oxidization of Ni nanoparticles. Thus we were not able to obtain the sandwich structure by this method.

In the second case, we prepared two series of DLC films at 300 °C and different values of RF-power and DC-bias voltage: 100 W, 200 V and 400 W, 400 V, which gave high and low values of compressive stress in the DLC films [17, 18]. The morphology of the films grown at 400 W and 400 V was nonuniform. Partial peeling on the edges of some samples was observed.

a) *b*)

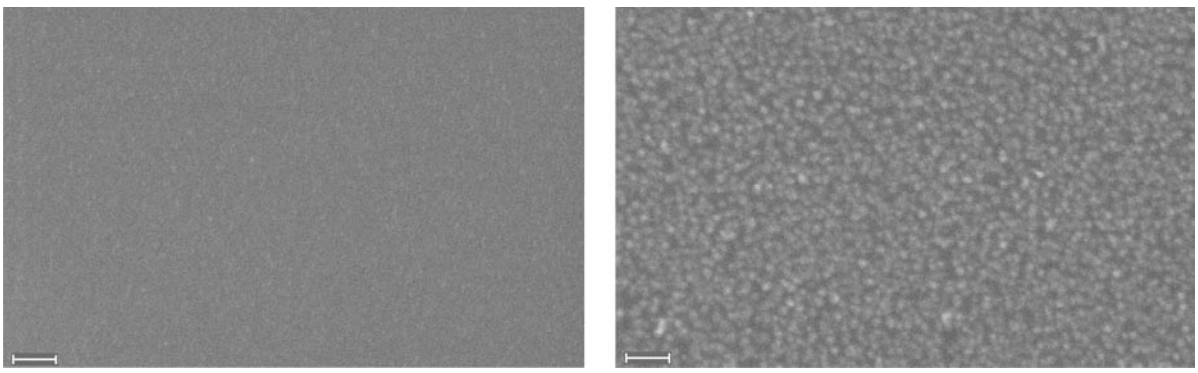

Fig. 3. SEM micrograph of DLC-NiC structure.
DLC film was grown at 100 W and 200 V, Ni-C layer was grown using argon as a carrying gas at 500 °C (*a*) and 570 °C (*b*).
Marker length is 100 nm

The Ni-C layers were grown on the top of the DLC films at different temperatures (500 or 570 °C) and carrying gases (argon or hydrogen).

The growth of Ni-nanoparticle containing carbon film was successful at all cases. The size and concentration of Ni nanocrystals did not depend on the type of underlying DLC film but changed with the parameters of CVD process, namely the carrying gas and process temperature. Moreover, if we used hydrogen as carrying gas, the concentration of Ni nanoparticles increased with temperature while their size did not change. For the case of argon as a carrying gas, the size and concentration of nanocrystals increased with temperature (Fig. 3). At the same time, the CVD process temperature had significant influence on DLC sublayer, as described above. Capping DLC layers were grown on all the samples using the same process parameters as were used for initial DLC layer growth. The upper layer of DLC film was grown without pretreatment procedure. Only hydrogen plasma exposition during 1 – 2 min was used to remove oxygen from the surface. Partial peeling and formation of blisters were observed after the capping layer growth in all the cases if high temperature CVD was utilized. The initial DLC films grown at 400 W and 400 V had some cleavages. Moreover, the area and quantity of such cleavages significantly increased after the growth of the third layer (Fig. 4). Thus, it was very difficult to obtain uniform films using these conditions. In the case of Ni-C layer grown at low temperature and the initial DLC film grown at 100 W and 200 V, the obtained structures were uniform and of good adhesion (Fig. 5). Therefore, these conditions corresponded to the best results of growing a sandwich structure.

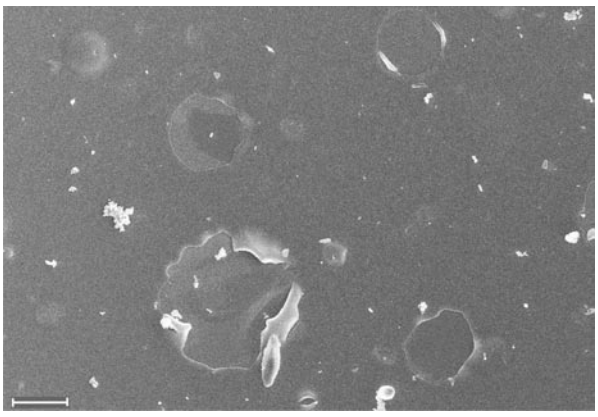

Fig. 4. SEM micrograph of DLC-NiC-DLC structure. DLC film was grown at 400 W and 400 V, Ni-C layer was grown using hydrogen as a carrying gas at 570 °C. Marker length is 10 μm

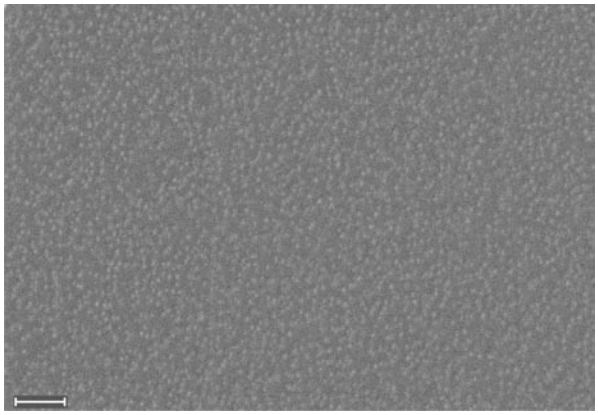

Fig. 5. SEM micrograph of DLC-NiC-DLC structure. DLC film was grown at 100 W and 200 V, Ni-C layer was grown using argon as a carrying gas at 500 °C. Marker length is 100 nm

IV. Conclusion

It has been found that isochronal annealing in argon ambient leads to the decrease of the internal residual stress in DLC films. Moreover, with the rise of annealing temperature, the relative concentration of sp^3 hybridized bonds increases, and simultaneously the sp^2 phase symmetrically decreases. Also, annealing causes sample swelling. Film growth in sequence NiC-DLC leads to peeling the whole structure off the substrate. For the reverse sequence, the size and concentration of Ni nanocrystals do not depend on the type of the underlying DLC film (with high or low stresses) but depend on the process parameters such as carrying gas and temperature. For both hydrogen and argon carriers, the Ni nanocrystal concentration increases with temperature. Moreover, if we use hydrogen as carrying gas, the size of Ni-nanoparticles does not change while in the case of argon their size increases with temperature. The rise of temperature during the growth of NiC layer leads to all the structure peeling irrespectively of the initial DLC film. We have found that the sequence DLC-NiC-DLC, where the initial DLC film is of high stress and NiC layer

is deposited at low temperature, is the best way to grow a good sandwich structure.

This work was supported by Russian RFBR grants 12-08-01197 and 13-02-92709.

REFERENCES

1. **Robertson J.** Diamond-like amorphous carbon. *Materials Science and Engineering: R: Reports*, 2002, Vol. 37, No. 4, pp. 129–281.

2. **McKenzie D.R.** Tetrahedral bonding in amorphous carbon. *Reports on Progress in Physics*, 1996, Vol. 59, No. 12, 1611.

3. **Amaratunga G.A., Silva S.R.P.** Nitrogen containing hydrogenated amorphous carbon for thin film field emission cathodes. *Applied Physics Letters*, 1996, Vol. 68, No. 18, pp. 2529–2531.

4. **Mammana V.P., Santos T.E.A., Mammana A.P., Baranauskas V., Ceragioli H.J., Peterlevitz A.C.** Field emission properties of porous diamond-like films produced by chemical vapor deposition. *Applied Physics Letters*, 2002, Vol. 81, No. 18, pp. 3470–3472.

5. **Ilie A., Ferrari A.C., Yagi T., Robertson J.** Effect of sp^2-phase nanostructure on field emission from amorphous carbons. *Applied Physics Letters*, 2000, Vol. 76(18), pp. 2627–2629.

6. **Kumar A., Singh F., Tripathi A., Pernot J., Pivin J.C., Avasthi D.K.** Conducting carbon nano-patterns (nanowire) by energetic ion irradiation. *Journal of Physics D: Applied Physics*, 2008, Vol. 41, No. 9, p. 095304.

7. **Koenigsfeld N., Hofsäss H., Schwen D., Weidinger A., Trautmann C., Kalish R.** Field emission enhancement by graphitic nano-scale channels through ta-C layers. *Diamond and Related Materials*, 2003, Vol. 12, No. 3, pp. 469–473.

8. **Gehrke H.G., Nix A.K., Hofsass H., Krauser J., Trautmann C., Weidinger A.** Self-aligned nanostructures created by swift heavy ion irradiation. *Journal of Applied Physics*, 2010, Vol. 107, No. 9, pp. 094305–094305.

9. **Krauser J., Nix A.K., Gehrke H.G., Hofsäss H., Trautmann C., Weidinger A.** Highly conductive ion tracks in tetrahedral amorphous carbon by irradiation with 30 MeV C_{60} projectiles. *New Journal of Physics*,Vol. 13, No. 8, 083023.

10. **Gupta S., Weiner B.R., Morell G.** Role of sp^2 C cluster size on the field emission properties of sulfur-incorporated nanocomposite carbon thin films. *Applied Physics Letters*, 2011, 2002, Vol. 80, No. 8, pp. 1471–1473.

11. **Ahmed S.F., Mitra M.K., Chattopadhyay K.K.** Low-macroscopic field emission from silicon-incorporated diamond-like carbon film synthesized by dc PECVD. *Applied Surface Science*, 2007, Vol. 253, No. 12, pp. 5480–5484.

12. **Kundoo S., Saha P., Chattopadhyay K.K.** Synthesis of tin-incorporated nanocomposite diamond like carbon films by plasma enhanced chemical vapor deposition and their characterization. *Journal of Vacuum Science Technology B: Microelectronics and Nanometer Structures*, 2004, Vol. 22, No. 6, pp. 2709–2714.

13. **Ahmed S., Moon M.W., Lee K.R.** Enhancement of electron field emission property with silver incorporation into diamondlike carbon matrix. *Applied Physics Letters*, 2008, Vol. 92, No. 19, pp. 193502–193502.

14. **Alexandrov S.E., Protopopova V.S.** Chemical vapor deposition of NiC films from bis-(Ethylcyclopentadienyl) nickel. *Journal of Nanoscience and Nanotechnology*, 2011, Vol. 11, No. 9, pp. 8259–8263.

15. **Protopopova V.S., Mishin M.V., Arkhipov A.V., Krel S.I., Gabdullin P.G.** *Nanosystems: Physics, Chemistry, Mathematics.* Accepted for publication.

16. **Vinogradov A.Y., Abramov A.S., Orlov K.E., Smirnov A.S.** Low-temperature plasma-enhanced chemical vapor deposition of hard carbon films. *Vacuum*, 2004, Vol. 73. No. 1, pp. 131–135.

17. **Karasev P.A., Podsvirov O.A., Vinogradov A.Y., Azarov A.Y., Karasev N.N., Smirnov A.S., Poplevkin S.V.** Influence of ion bombardment on residual stresses in diamond-like carbon films. *Journal of Surface Investigation. X-ray, Synchrotron and Neutron Techniques*, 2009, Vol. 3, No. 2, pp. 235–238.

18. **Podsvirov O.A., Karaseov P.A., Vinogradov A.Y., Azarov A.Y., Karasev N.N., Smirnov A.S., Karabeshkin K.V.** Residual stress in diamond-like carbon films: Role of growth conditions and ion irradiation. *Journal of Surface Investigation. X-ray, Synchrotron and Neutron Techniques*, 2010, Vol. 4(2), pp. 241–244.

19. **Stoney G.G.** The tension of metallic films deposited by electrolysis. *Proceedings of the Royal Society of London. Series A, Containing Papers of a Mathematical and Physical Character*, 1999, Vol. 82, No. 553, pp. 172–175.

20. **Karasev P.A., Podsvirov O.A., Titov A.I., Karabeshkin K.V., Vinogradov A.Y., Belyakov V.S., Arkhipov A.V., Nikulina L.M., Shakhmin A.L., Shubina E.N., Karasev N.N.** Vliianie ionnoi bombardirovki na fazovyi sostav i mekhanicheskie svoistva almazopodobnykh plenok. *Journal of Surface Investigation. X-ray, Synchrotron and Neutron Techniques*, 2014, Vol. 8, No. 1, pp. 45–49.

СПИСОК ЛИТЕРАТУРЫ

1. **Robertson J.** Diamond-like amorphous carbon. *Materials Science and Engineering: R: Reports*, 2002, Vol. 37, No. 4, pp. 129–281.

2. **McKenzie D.R.** Tetrahedral bonding in amorphous carbon. *Reports on Progress in Physics*, 1996, Vol. 59, No. 12, 1611.

3. **Amaratunga G.A., Silva S.R.P.** Nitrogen containing hydrogenated amorphous carbon for thin film field emission cathodes. *Applied Physics Letters*, 1996, Vol. 68, No. 18, pp. 2529–2531.

4. **Mammana V.P., Santos T.E.A., Mammana A.P., Baranauskas V., Ceragioli H.J., Peterlevitz A.C.** Field emission properties of porous diamond-like films produced by chemical vapor deposition. *Applied Physics Letters*, 2002, Vol. 81, No. 18, pp. 3470–3472.

5. **Ilie A., Ferrari A.C., Yagi T., Robertson J.** Effect of sp^2-phase nanostructure on field emission from amorphous carbons. *Applied Physics Letters*, 2000, Vol. 76(18), pp. 2627–2629.

6. **Kumar A., Singh F., Tripathi A., Pernot J., Pivin J.C., Avasthi D.K.** Conducting carbon nanopatterns (nanowire) by energetic ion irradiation. *Journal of Physics D: Applied Physics*, 2008, Vol. 41, No. 9, p. 095304.

7. **Koenigsfeld N., Hofsäss H., Schwen D., Weidinger A., Trautmann C., Kalish R.** Field emission enhancement by graphitic nano-scale channels through ta-C layers. *Diamond and Related Materials*, 2003, Vol. 12, No. 3, pp. 469–473.

8. **Gehrke H.G., Nix A.K., Hofsass H., Krauser J., Trautmann C., Weidinger A.** Self-aligned nanostructures created by swift heavy ion irradiation. *Journal of Applied Physics*, 2010, Vol. 107, No. 9, pp. 094305–094305.

9. **Krauser J., Nix A.K., Gehrke H.G., Hofsäss H., Trautmann C., Weidinger A.** Highly conductive ion tracks in tetrahedral amorphous carbon by irradiation with 30 MeV C_{60} projectiles. *New Journal of Physics*,Vol. 13, No. 8, 083023.

10. **Gupta S., Weiner B.R., Morell G.** Role of sp^2 C cluster size on the field emission properties of sulfur-incorporated nanocomposite carbon thin films. *Applied Physics Letters*, 2011, 2002, Vol. 80, No. 8, pp. 1471–1473.

11. **Ahmed S.F., Mitra M.K., Chattopadhyay K.K.** Low-macroscopic field emission from silicon-incorporated diamond-like carbon film synthesized by dc PECVD. *Applied Surface Science*, 2007, Vol. 253, No. 12, pp. 5480–5484.

12. **Kundoo S., Saha P., Chattopadhyay K.K.** Synthesis of tin-incorporated nanocomposite diamond like carbon films by plasma enhanced chemical vapor deposition and their characterization. *Journal of Vacuum Science Technology B: Microelectronics and Nanometer Structures*, 2004, Vol. 22, No. 6, pp. 2709–2714.

13. **Ahmed S., Moon M.W., Lee K.R.** Enhancement of electron field emission property with silver incorporation into diamondlike carbon matrix. *Applied Physics Letters*, 2008, Vol. 92, No. 19, pp. 193502–193502.

14. **Alexandrov S.E., Protopopova V.S.** Chemical vapor deposition of NiC films from bis-(Ethylcyclopentadienyl) Nickel. *Journal of Nanoscience and Nanotechnology*, 2011, Vol. 11, No. 9, pp. 8259–8263.

15. **Protopopova V.S., Mishin M.V., Arkhipov A.V., Krel S.I., Gabdullin P.G.** *Nanosystems: Physics, Chemistry, Mathematics.* Accepted for publication.

16. **Vinogradov A.Y., Abramov A.S., Orlov K.E., Smirnov A.S.** Low-temperature plasma-enhanced chemical vapor deposition of hard carbon films. *Vacuum*, 2004, Vol. 73. No. 1, pp. 131–135.

17. **Карасёв П.А., Подсвиров О.А., Виноградов А.Я., Азаров А.Ю., Карасёв Н.Н., Смирнов А.С., Титов А.И., Коркин И.В., Поплёвкин С.В.** Влияние облучения ионами на остаточные напряжения в алмазоподобных пленках// Поверхность. Рентгеновские, синхротронные и нейтронные исследования. 2009. № 3. С. 80–83.

18. **Подсвиров О.А., Карасёв П.А., Виноградов А.Я., Азаров А.Ю., Карасёв Н.Н., Смирнов А.С., Титов А.И., Карабешкин К.В.** Механические напряжения в алмазоподобных пленках: роль условий осаждения и ионного облучения// Поверхность. Рентгеновские, синхротронные и нейтронные исследования. 2010. № 3. С. 81–84.

19. **Stoney G.G.** The tension of metallic films deposited by electrolysis. *Proceedings of the Royal Society of London. Series A, Containing Papers of a Mathematical and Physical Character*, 1999, Vol. 82, No. 553, pp. 172–175.

20. **Карасёв П.А., Подсвиров О.А., Титов А.И., Карабешкин К.В., Виноградов А.Я., Беляков В.С., Архипов А.В., Никулина Л.М., Шахмин А.Л., Шубина Е.Н., Карасёв Н.Н.** Влияние ионной бомбардировки на фазовый состав и механические свойства алмазоподобных пленок // Поверхность. Рентгеновские, синхротронные и нейтронные исследования. 2014. № 1. С. 45–49.

ШУБИНА Екатерина Николаевна – *аспирантка кафедры физической электроники Санкт-Петербургского государственного политехнического университета.*
195251, Россия, г. Санкт-Петербург, Политехническая ул., 29
katerinashubuna@gmail.com

КАРАСЁВ Платон Александрович – *кандидат физико-математических наук, доцент кафедры физической электроники Санкт-Петербургского государственного политехнического университета.*
195251, Россия, г. Санкт-Петербург, Политехническая ул., 29
Platon.Karaseov@rphf.spbstu.ru

МИШИН Максим Валерьевич – *кандидат физико-математических наук, доцент кафедры физико-химии и технологии микросистемной техники Санкт-Петербургского государственного политехнического университета.*
195251, Россия, г. Санкт-Петербург, Политехническая ул., 29

ПРОТОПОПОВА Вера Сергеевна – *аспирантка кафедры физико-химии и технологии микросистемной техники Санкт-Петербургского государственного политехнического университета.*
195251, Россия, г. Санкт-Петербург, Политехническая ул., 29

ВИНОГРАДОВ Андрей Яковлевич – *старший научный сотрудник ФТИ им. А.Ф. Иоффе РАН.*
195251, Россия, г. Санкт-Петербург, Политехническая ул., 26

КАРАСЁВ Никита Николаевич – *кандидат технических наук, доцент Санкт-Петербургского государственного университета информационных технологий, механики и оптики.*
197101, Россия, г. Санкт-Петербург, Кронверкский пр., 49

АРХИПОВ Александр Викторович – *кандидат физико-математических наук, доцент кафедры физической электроники Санкт-Петербургского государственного политехнического университета.*
195251, Россия, г. Санкт-Петербург, Политехническая ул., 29

ШАХМИН Александр Львович – *кандидат физико-математических наук, доцент кафедры физико-химии и технологии микросистемной техники Санкт-Петербургского государственного политехнического университета.*
195251, Россия, г. Санкт-Петербург, Политехническая ул., 29

ПОДСВИРОВ Олег Алексеевич – *доктор физико-математических наук, профессор кафедры физической электроники Санкт-Петербургского государственного политехнического университета.*
195251, Россия, г. Санкт-Петербург, Политехническая ул., 29

ТИТОВ Андрей Иванович – *доктор физико-математических наук, профессор кафедры физической электроники Санкт-Петербургского государственного политехнического университета.*
195251, Россия, г. Санкт-Петербург, Политехническая ул., 29
andrei.titov@rphf.spbstu.ru

UDC 537.533.2

A.V. Arkhipov, S.I. Krel, M.V. Mishin, A.A. Uvarov

St. Petersburg State Polytechnical University,
29 Politekhnicheskaya St., St. Petersburg, 195251, Russia

CORRELATIONS IN FIELD ELECTRON EMISSION CURRENT FROM LOCAL SPOTS AT NANOPOROUS CARBON FILMS

А.В. Архипов, С.И. Крель, М.В. Мишин, А.А. Уваров

КОРРЕЛЯЦИЯ ТОКОВ ПОЛЕВОЙ ЭМИССИИ ИЗ ЛОКАЛЬНЫХ УЧАСТКОВ ПЛЕНОК НАНОПОРИСТОГО УГЛЕРОДА

Heterogeneous nanocarbon materials including both diamond and graphite phase domains demonstrate enhanced efficiency of electron emission that often remains unexplained by theory. Characteristic features of the actual mechanism of facilitated emission were searched for via position-resolved investigation of emission current fluctuations. The reported studies were performed with nanoporous carbon chemically derived from SiC. Partially ordered and spatially correlated character of fluctuations observed in the experiment allows to presume involvement of self-sustaining non-stationary electric field as a possible factor of emission enhancement.

FIELD-INDUCED ELECTRON EMISSION, NANOPOROUS CARBON, CORRELATION ANALYSIS.

Наноматериалы, содержащие углерод как в алмазоподобном, так и в графитоподобном состоянии, зачастую демонстрируют остающуюся пока не вполне объясненной способность к эффективной полевой эмиссии электронов. Для уточнения механизма эмиссии, реализующегося для таких материалов, мы исследовали флуктуации эмиссионных токов с высоким пространственным разрешением. Объектом исследования служили образцы нанопористого углерода, полученного химической обработкой SiC. Наблюдавшийся в экспериментах частично упорядоченный и пространственно коррелированный характер токовых флуктуаций позволяет предположить, что одним из факторов увеличения эмиссионной эффективности может служить присутствие самоподдерживающееся нестационарного электрического поля.

АВТОЭЛЕКТРОННАЯ ЭМИССИЯ, НАНОПОРИСТЫЙ УГЛЕРОД, КОРРЕЛЯЦИОННЫЙ АНАЛИЗ.

I. Introduction

High efficiency of electron emission from nanocarbon materials comprised of low-aspect-ratio particles remains unexplained [1 – 5]. In many cases, the measured emission current greatly exceeded Fowler – Nordheim (FN) law predictions based on known surface morphology and electron structure. In previous works [6, 7], we studied special features of current hysteresis in μs-length pulsed field regime for emitters of this type. Those experimental results allowed proposing a model of two-stage mechanism of emission: accumulation of electrons at «shallow» surface energy states under the effect of nonstationary field at the pulse front and their facilitated transition from these states

to vacuum. Our present research is aimed to investigate whether a similar mechanism can be responsible for enhanced emission in the case of constant extracting field. Even in this regime, the emission process can be affected (stimulated) by nonstationary field component associated with local fluctuations of current. On the other hand, the increased level of fluctuations in the system can be sustained by field interaction between active centers of emission. Thus, high efficiency of emission from nanocarbons in this scenario is maintained as a result of dynamic processes (auto-oscillations) developing in the emitter.

This paper presents early results of experimental study of fluctuations of emission current distribution, performed to examine the role of self-maintaining nonstationary field component in the actual emission mechanism. If this role is negligible and the emission process complies in general with FN model, fluctuations of current density measured in different emitter areas are expected to be purely statistical and independent. In the contrary case, we will observe fluctuations associated with a dynamic process. Most probably, they will be (at least, partially) ordered and correlated. Experimental definition of quantitative parameters of such an ordered oscillatory state (peak frequencies, correlation lag times, etc.) can also give new information on the nature and interaction of emission centers.

II. Experimental Setup and Techniques

The described experiments were performed with nanocarbon film samples of the type used in previous studies [5 – 7], comprised of μm-size grains of nanoporous carbon (NPC). This material represents a derivative of SiC produced by chemical removal of silicon atoms (manufacturer – RSC «Applied Chemistry», St. Petersburg; for more details, see Ref. [5]). An NPC powder sample at a niobium plate was fixed behind an opening in the cathode electrode of a wide (2.5 mm) quasi-planar field gap (Fig. 1). Electrons emitted from the central part of the sample were directed through an aperture in the anode onto the phosphor screen covering the end plane of an optic fiber bunch to visualize spatial distribution of the emission current. The optic bunch served to transfer the emission image outside of vacuum chamber ($(1 - 7)\cdot10^{-7}$ Torr). At its atmospheric-pressure end, the light fluxes from a few elements («pixels») of the image were collected with adjustable 50 μm-diameter single-fiber probes for analysis of fluctuations. Phosphor screen after-glow was the principle factor limiting the data channel time resolution at approximately 0.1 μs. Though, for the frequency range of our primary interest lying below 1 MHz [6, 7], this limitation was inessential. The spatial resolution was determined by 50 μm diameter of the optic fibers. In comparison with characteristic dimensions of nanocarbon structure, the resolved area was very large and presumably covered with more than one active emission center. Improvement of the resolution was technically possible, but would cause the corresponding reduction of the measured light fluxes magnitudes to only a few photons per sampling interval, and hence to drastic increase of the shot noise component in the spectra. This problem was especially severe because we preferred to keep the full current extracted from the whole specimen below 3 μA (to avoid surface degradation) and investigated properties of both active emission sites and «darker» image areas. The chosen fiber cross-section provided an acceptable balance between negative statistical effects associated with light flux (current) discontinuity and the loss of data localization.

The light fluxes corresponding to 2 or 4 selected pixels of emission image were converted, with a set of photomultipliers, into electric signals and digitized as 2048- or 4096-point oscillograms with the sampling step of 0.1 – 1.6 μs. A typical data series measure for a fixed regime and probe positions consisted of 100 of such waveform sets. For each series, various statistical distributions were calculated, including functions of self- and cross-correlation, individual and series-averaged frequency spectra. In the case of purely statistical or chaotic fluctuations (such as «$1/f$» or shot noise), all these functions are expected to be uniform. Any statistically significant deviations from uniformity (prominent peaks in spectra, intervals of temporary regularization in waveforms, delayed cross-correlation between signals, etc.) were noted as signs of ordering.

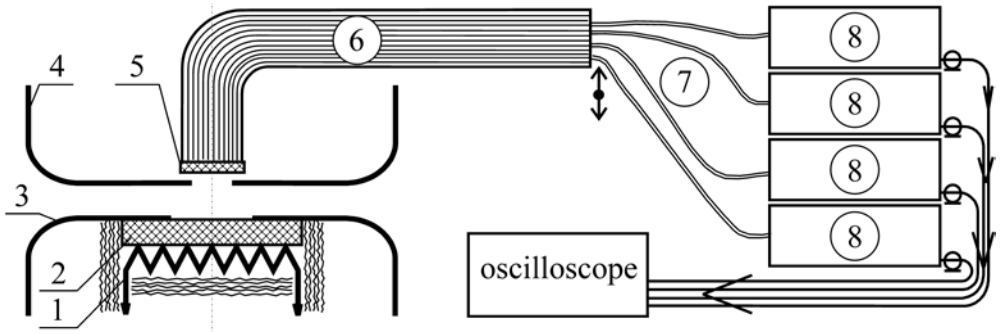

Fig. 1. Experimental setup scheme:
1 – cathode heater; *2* – emitter sample; *3* – cathode cover; *4* – anode; *5* – phosphor screen; *6* – evacuated optic bunch; *7* – light-guide fiber probes; *8* – photomultipliers
Field gap width is 2.5 mm, openings in the cathode cover and in the anode are 6 and 2 mm in diameter respectively

III. Emission Image Structure and Dynamics

The tested nanocarbon samples demonstrated moderate emission efficiency: 1 μA current was achieved at 12 – 16 kV gap voltage, which corresponds to mean field magnitude 4.8 – 6.4 V/μm. Examined under a microscope, a typical low-current emission pattern was comprised of bright spots of 200 – 400 μm in size with darker intervals between them. The natural assumption that each spot represents a smeared image of a single emission center proved to the wrong, because different pixels belonging to the same spot demonstrated relatively independent behavior in time – they flickered and even «turned off» and «on» separately. Positions of the probe fibers were chosen so as to compare light flux fluctuations for the pixels belonging to different parts of the same spot, or to different spots.

IV. Statistical Properties of Local Emission Waveforms

The measured current density fluctuation data can be roughly divided, in accordance with their statistical properties, into two major groups.

For relatively low-current-density parts of the emissing pattern, such as peripheral pixels surrounding the bright spots, signals with dominating low-frequency spectral components were most typical. The spectra averaged over a data series (100 waveforms) were very smooth, and either had a broad maximum near 30 – 50 kHz (see Probe 1 plot in Fig. 2) or were «1/*f*» type. Individual signal waveforms often represented successions of microsecond-length photon bunches separated by irregular gap time intervals (Fig. 3). In this case, insta-

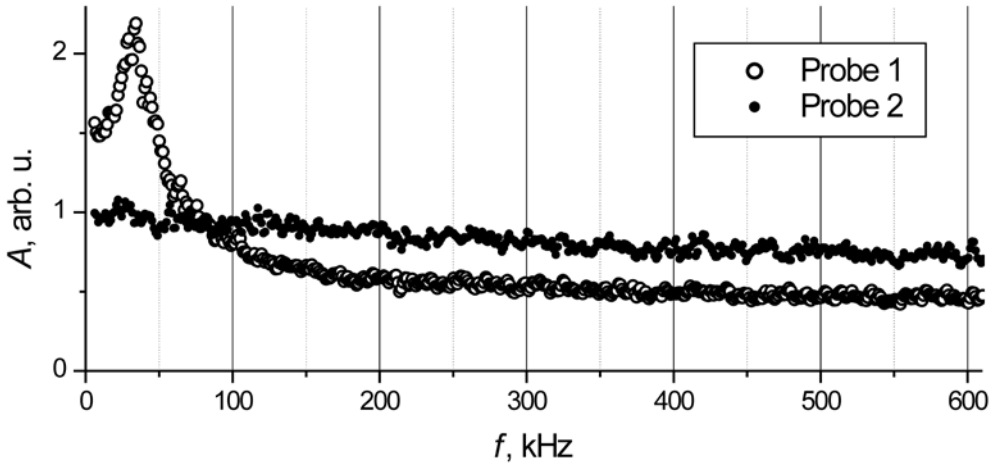

Fig. 2. Series-averaged frequency spectra for two pixels of emission image spaced by 150 μm. Probe 2 is placed near the center of a bright spot, probe 2 – in its peripheral part

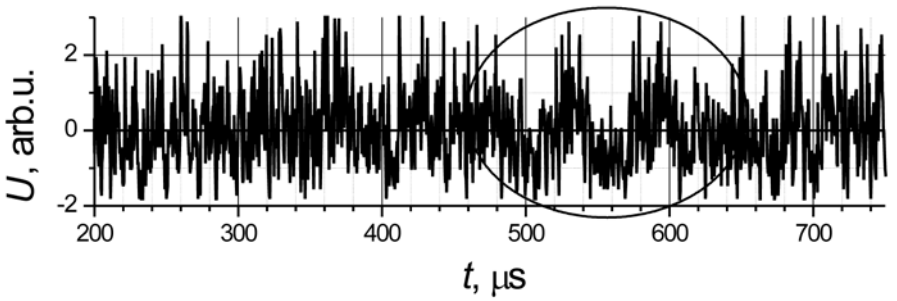

Fig. 3. A typical emission signal waveform with an interval of partial regularization

bility of emission process and dynamical character of its fluctuations are apparent.

For the brighter parts of the emission pattern, averaged frequency characteristics of fluctuation signals usually were practically uniform all over the surveyed range (Probe 2 in Fig. 2). The corresponding waveforms were visibly chaotic over the main part of their lengths, yet occasionally included intervals of more regular behavior – such as the one presented in Fig. 4. During these intervals, quasi-periodic modulation grew simultaneously with reduction of the noise-like component, so that the full energy of the signal remained approximately constant. This feature proves that even when the observed fluctuations are disordered, they have dynamic nature – because the basic statistical noise cannot be suppressed by interference with an ordered signal.

V. Cross-Correlation of Signals

Another notable feature of emission pattern fluctuations consisted of partial correlation of current density signals measured at different positions. No correlations of this sort were ever observed for a pair of pixels belonging to different bright spots comprising the pattern. Signals from different parts of the same spot were definitely correlated for approximately 50 % of acquired data series. Fig. 4 represents series-

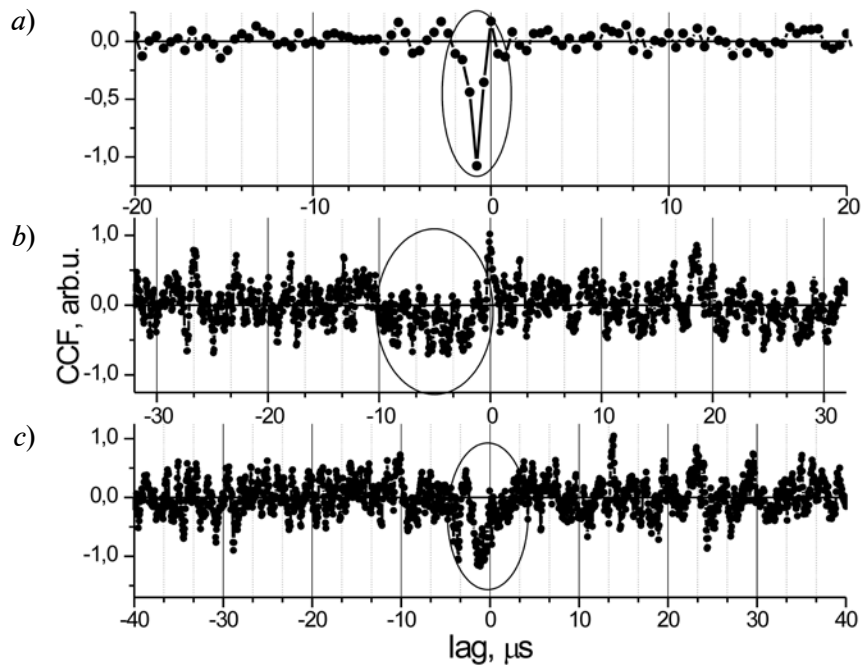

Fig. 4. Series-averaged cross-correlation functions of emission signals displaying statistically significant delayed correlation. In all cases the probe spacing is 150 μm

averaged cross-correlation function (CCF) plots for light flux signals from pixels spaced by 150 μm distance. The upper plot illustrates the case of one-directional suppression of the weaker signal from the peripheral part of a bright spot by high-magnitude signal from the spot core with well-defined lag time close to 1 μs. The effective peak stands far out against the background noise. Absence of zero-lag correlation allows to exclude its attribution to instrumental sources, such as light flux mixing or electric signal interference. The CCF plotted in Fig. 4, *b* gives another example of statistically significant cross-correlation, with characteristic lag times of the effect lying in much broader range between 0 and 10 μs. Fig. 4, *c* demonstrates a case of more «symmetric» mutual suppression developing between emission pattern areas with comparable brightness. The effect is notable for the lag absolute values up to 2 – 3 μs.

Thus, the fact of correlated behavior of field-induced current density fluctuations has been established experimentally for measurement points spaced by distances as large as 100 – 300 μm, which can be interpreted as a sign of involvement of large continuously-active specimen areas in universal wave-like processes. The observed cross-correlation lag times suggest the wave propagation velocity range 10 – 100 m/s. These values look too small for waves of electromagnetic and even acoustic nature, but could be explained by models based on thermal processes [8] or, for instance, electric charge transfer in weakly-conducting μm-grain powder. Currently, we are launching experiments with larger probe arrays to investigate this possibility in more detail and to perform a more accurate measurement of the characteristics of presumably propagating emission waves.

VI. Conclusions

The performed experiments have demonstrated that fluctuations of field-induced emission current from an NPC layer in dc extraction regime have dynamic nature and in some cases are partially correlated for large areas of emitter surface (as much as 100 – 300 μm in size). These properties cannot be adequately explained by any model considering the field emission from materials of the investigated type as an instant and local process. Thus, another indirect confirmation of the role of non-stationary field in emission is found. Typical periods of ordered oscillations and cross-correlation lag times observed in these experiments (1 – 10 μs) agree with our previous results for pulsed-field regime hysteresis [6, 7].

REFERENCES

1. **Forbes R.G.** Field emission: New theory for the derivation of emission area from a Fowler–Nordheim plot. *Journal of Vacuum Science & Technology B: Microelectronics and Nanometer Structures*, 1999, Vol. 17, Iss. 2, pp. 526–533.

2. **Frolov V.D., Karabutov A.V., Pimenov S.M., Konov V.I.** Electronic properties of the emission sites of low-field emitting diamond films. *Diamond and Related Materials*, 2000, Vol. 9, No. 3, pp. 1196–1200.

3. **Obraztsov A.N., Pavlovskii I.Y., Volkov A.P.** Field electron emission in graphite-like films. *Technical Physics*, 2001, Vol. 46, No. 11, pp. 1437–1443.

4. **Okotrub A.V., Bulusheva L.G., Gusel'nikov A.V., Kuznetsov V.L., Butenko Y.V.** Field emission from products of nanodiamond annealing. *Carbon*, 2004, Vol. 42, No. 5, pp. 1099–1102.

5. **Bondarenko V.B., Gabdullin P.G., Gnuchev N.M., Davydov S.N., Korablev V.V., Kravchik A.E., Sokolov V.V.** Emissivity of powders prepared from nanoporous carbon. *Technical physics*, 2004, Vol. 49, No. 10, pp. 1360–1363.

6. **Arkhipov A.V., Mishin M.V., Sominski G.G., Parygin I.V.** Hysteresis of pulsed characteristics of field emission from nanocarbon films. *Technical Physics*, 2005, Vol. 50, No. 10, pp. 1353–1359.

7. **Arkhipov A.V., Mishin M.V., Parygin I.V.** Hysteresis of pulsed characteristics of field emission from nanocarbon materials. *Surface and interface analysis*, 2007, Vol. 39, No. 2–3, pp. 149–154.

8. **Vul A.Y., Eidelman E.D., Dideikin A.T.** Thermoelectric Effect in Field Electron Emission from Nanocarbon. In *Synthesis, Properties and Applications of Ultrananocrystalline Diamond*. Springer Netherlands, 2005, pp. 383–394.

СПИСОК ЛИТЕРАТУРЫ

1. **Forbes R.G.** Field emission: New theory for the derivation of emission area from a Fowler–Nordheim plot. *Journal of Vacuum Science & Technology B: Microelectronics and Nanometer*

Structures, 1999, Vol. 17, Iss. 2, pp. 526–533.

2. **Frolov V.D., Karabutov A.V., Pimenov S.M., Konov V.I.** Electronic properties of the emission sites of low-field emitting diamond films. *Diamond and Related Materials*, 2000, Vol. 9, No. 3, pp. 1196–1200.

3. **Obraztsov A.N., Pavlovskii I.Y., Volkov A.P.** Field electron emission in graphite-like films. *Technical Physics*, 2001, Vol. 46, No. 11, pp. 1437–1443.

4. **Okotrub A.V., Bulusheva L.G., Gusel'nikov A.V., Kuznetsov V.L., Butenko Y.V.** Field emission from products of nanodiamond annealing. *Carbon*, 2004, Vol. 42, No. 5, pp. 1099–1102.

5. **Bondarenko V.B., Gabdullin P.G., Gnuchev N.M., Davydov S.N., Korablev V.V., Kravchik A.E., Sokolov V.V.** Emissivity of powders prepared from nanoporous carbon. *Technical physics*, 2004, Vol. 49, No. 10, pp. 1360–1363.

6. **Arkhipov A.V., Mishin M.V., Sominski G.G., Parygin I.V.** Hysteresis of pulsed characteristics of field emission from nanocarbon films. *Technical Physics*, 2005, Vol. 50, No. 10, pp. 1353–1359.

7. **Arkhipov A.V., Mishin M.V., Parygin I.V.** Hysteresis of pulsed characteristics of field emission from nanocarbon materials. *Surface and interface analysis*, 2007, Vol. 39, No. 2–3, pp. 149–154.

8. **Vul A.Y., Eidelman E.D., Dideikin A.T.** Thermoelectric Effect in Field Electron Emission from Nanocarbon. In *Synthesis, Properties and Applications of Ultrananocrystalline Diamond*. Springer Netherlands, 2005, pp. 383–394.

АРХИПОВ Александр Викторович – *кандидат физико-математических наук, доцент кафедры физической электроники Санкт-Петербургского государственного политехнического университета.*
195251, Россия, Санкт-Петербург, Политехническая ул., 29
arkhipov@rphf.spbstu.ru

КРЕЛЬ Святослав Игоревич – *аспирант кафедры физической электроники Санкт-Петербургского государственного политехнического университета.*
195251, Россия, Санкт-Петербург, Политехническая ул., 29
8svyatoslav8@mail.ru

МИШИН Максим Валерьевич – *доцент кафедры физико-химии и технологий микросистемной техники Санкт-Петербургского государственного политехнического университета.*
195251, Россия, Санкт-Петербург, Политехническая ул., 29
max@mail.spbstu.ru

УВАРОВ Андрей Анатольевич – *доцент кафедры физико-химии и технологий микросистемной техники Санкт-Петербургского государственного политехнического университета.*
195251, Россия, Санкт-Петербург, Политехническая ул., 29

UDC 533.9=111

A.P. Golovitskii

St. Petersburg State Polytechnical University,
29 Politekhnicheskaya St., St. Petersburg, 195251, Russia

ELECTRON ENERGY RELAXATION LENGTH IN CONNECTION WITH THE PROBLEM OF ELECTRON ENERGY DISTRIBUTION LOCALITY IN GLOW DISCHARGE PLASMA IN A XENON-CHLORINE MIXTURE

А.П. Головицкий

ДЛИНА РЕЛАКСАЦИИ ЭНЕРГИИ ЭЛЕКТРОНА И ПРОБЛЕМА ЛОКАЛЬНОСТИ РАСПРЕДЕЛЕНИЯ ЭЛЕКТРОНОВ ПО ЭНЕРГИЯМ В ПЛАЗМЕ ТЛЕЮЩЕГО РАЗРЯДА В СМЕСИ КСЕНОН-ХЛОР

The analytic calculations of relaxation length of electron energy based on a probabilistic approach and numerical calculations of nonlocality effect on the plasma-chemical processes rates have been carried out for plasma of an electronegative glow discharge in a mixture of xenon and chlorine. It is shown, that for total pressure higher than 6 Torr and with amount of chlorine more than 1/25 the effect of electron energy distribution nonlocality is negligibly small and the local approach can be used for modeling such discharges.

GAS DISCHARGE, ENERGY RELAXATION, ELECTRONEGATIVE GASES, ENERGY DISTRIBUTION LOCALITY.

На основе вероятностного подхода выполнены аналитические расчеты длины релаксации энергии электрона, а также численные расчеты влияния нелокальности на скорости плазмохимических процессов в электроотрицательном разряде в смеси ксенона и хлора. Показано, что при общем давлении более 6 Торр и при доле хлора более 1/25 влияние нелокальности энергетического распределения электронов пренебрежимо мало, и для моделирования таких разрядов можно пользоваться локальным приближением.

ГАЗОВЫЙ РАЗРЯД, РЕЛАКСАЦИЯ ЭНЕРГИИ, ЭЛЕКТРООТРИЦАТЕЛЬНЫЕ ГАЗЫ, ЛОКАЛЬНОСТЬ ЭНЕРГЕТИЧЕСКОГО РАСПРЕДЕЛЕНИЯ.

In recent years, there has been significant interest in investigating and modeling the physical processes in middle pressure (5 – 40 Torr) electronegative (EN) discharges in the mixtures of inert gases and halogens because of their practical applicability as effective and powerful sources of ultraviolet radiation [1 – 5].

The physical processes in strongly EN plasmas are extremely complex, and therefore one obtains physical information about these processes mainly from numerical modeling [2, 6 – 8]. The vast majority of EN plasma models use so-called local approach, which means that the electron energy distribution function (EEDF) and also all relevant plasma-chemical processes in the given place can be only expressed in terms of electric field E and neutrals density N being in the same place. We can accept that EEDF is local if

$$\lambda_W(W_e) < \lambda_{E/N} \quad \forall W_e, \qquad (1)$$

where $\lambda_W(W_e)$ – relaxation length of electron energy W_e, $\lambda_{E/N}$ – spatial scale of E/N ratio.

If (1) is not valid, then the kinetic energy of an electron cannot be expressed through the plasma conditions (at particular field E) measured in the place where this electron is located, i. e. EEDF is nonlocal [9, 10], and this fact

should be taken into account while modeling, especially if the field E is spatially nonuniform [10].

In the present paper we estimate the degree of EEDF nonlocality in EN plasmas of a gas mixture containing xenon and chlorine.

It is known that the nonisothermal plasma (at $T_e > T_i$ where T_e, T_i are electron and ion temperatures) of a gas discharge containing both positive and negative ions stratifies across the current direction into two regions with different ion compositions and properties [6 – 8, 11]. In the central region («core»), the densities of positive n_p and negative n_n ions are significantly more than the electron density n_e, i. e. we can speak about an ion-ion (*i-i*) plasma where $n_p \approx n_n >> n_e$. In the case of strong electronegativity the diffusion of electrons in the «core» occurs to be almost free diffusion, the radial profile of n_e is almost flat, and the radial space charge electric field E_r is weak, close to zero. In the outer plasma region («edge»), the density of negative ions is very low $n_p \approx n_e >> n_n$, and we can speak about an electropositive (EP) electron-ion (*e-i*) plasma. In the «edge» area, there is an ambipolar diffusion regime, and the finite radial space charge electric field E_r directed to the wall. The thickness of the «edge» can be estimated for cylindrical geometry as [12]:

$$\delta \approx \frac{\pi}{2} \frac{R_0}{\sqrt{2\sqrt{\alpha} + \alpha}}, \qquad (2)$$

where $\alpha = \nu_a e R_0^2 / (\mu_n T_e)$, ν_a – attachment frequency, μ_n – negative ion mobility, T_e – electron temperature, R_0 – discharge tube radius.

In the narrow transition region between *i-i*- and *e-i*-plasma, there are strong variations of both positive and negative ion concentrations.

The estimation of λ_W and EEDF nonlocality effects has got some difficulties because the value λ_W is not constant but it depends on the electron energy W_e. Therefore, at middle pressure it happens that inequation (1) can be valid for big electron energies (particulary, in pure inert gases where W_e is higher than the first excitation potential) while for lower energies (1) cannot be valid. In such a case, one should derive the kinetic Bolzmann equation taking into account the electric field inhomogeneity which is a difficult task. According to [9, 13], EEDF for EP inert gases can be accepted as local if $pR_0 \geq 10$ Torr·cm (p – gas pressure).

Three considerations prompted us to carry out the presented investigation.

Firstly, the value pR_0 for the part of our discharges is just ≤ 10 Torr·cm [1, 2], and an EEDF nonlocality can be suspected.

Secondly, for EP plasmas there is no stratification, radial field E_r is distributed over the whole plasma cross section, and $\lambda_{E/N} \cong R_0$. But in case of EN plasma, $\lambda_{E/N} \cong \delta$, and corresponding to (2), δ can be ~ $(0.1 - 0.2)R_0$ [8] i. e. $\lambda_{E/N}$ is smaller than R_0. Hence, a criterion (1) of EEDF locality for EP plasmas is weaker than for EN ones, and the problem of EEDF nonlocality in EN plasmas can become even more actual than for EP plasmas.

Thirdly, the gas mixtures considered here contain a noticeable amount of molecular EN gas where the electron energy losses can happen even for small initial energies – due to excitation of low lying vibrational and rotational molecular states and by dissociative attachment [14]. That can lead to a reduction of λ_W in comparison with λ_W in atomic EP gas. By numerical modeling an EN discharge in molecular oxygen [15], it has been shown that EEDF in the tube of 12 mm diameter is local at pressure $p \geq 1$ Torr, which corresponds to $pR_0 \geq 1.2$ Torr·cm. Hence, for discharges in molecular EN gases, the EEDF nonlocality can occur at smaller pressure than in inert gases. This is an encouraging result but, unfortunately, there are no literature data either about $\lambda_W(W_e)$ or about EEDF nonlocality in the discharge plasma containing molecular chlorine.

Before estimating electron energy relaxation length $\lambda_W(W_e)$ itself, let us obtain the expression for the electron free path length $\lambda_e(W_e)$. Definitely,

$$\lambda_e(W_e) = \frac{v_e}{\nu_{ea}(W_e)},$$

where v_e is electron velocity, $\nu_{ea}(W_e)$ is the frequency of any electron-atomic (EA) collisions. Since

$$\nu_{ea}(W_e) = \sigma^{full}(W_e) v_e N,$$

where $\sigma^{full}(W_e)$ – full EA collision cross-sec-

tion for electron energy W_e, we obtain

$$\lambda_e(W_e) = \frac{1}{N\sigma^{full}(W_e)}.$$

If we consider the discharge in a gas mixture, for example in a mixture of xenon and chlorine, then

$$\lambda_e(W_e) = \frac{1}{N_{\mathrm{Xe}}\sigma_{\mathrm{Xe}}^{full}(W_e) + N_{\mathrm{Cl}_2}\sigma_{\mathrm{Cl}_2}^{full}(W_e)}.$$

In one elastic EA collision, an electron losses almost no energy. Therefore, we can accept that the probability of preserving electron initial energy W_e after one EA collision is equal to the probability of elastic collision:

$$a_{el}(W_e) = \sigma^{el}(W_e) / \sigma^{full}(W_e),$$

where $\sigma^{el}(W_e)$ is the cross section for elastic EA collisions.

The same probability for a series of k successive collisions will be

$$a_{el}^{(k)}(W_e) = [a_{el}(W_e)]^k.$$

If the gas mixture contains halogen molecules, then the denominator of $a_{el}(W_e)$ is always bigger than the numerator due to attachment and excitation of low lying molecular states, and the value of $a_{el}(W_e)$ is always smaller than 1 for all W_e. Hence, we can define the fact of relaxation of initial electron energy W_e after k collisions as diminution of $a_{el}^{(k)}(W_e)$ value down to $1/e$, and from the equation

$$\frac{1}{e} = \left[\frac{\sigma^{el}(W_e)}{\sigma^{full}(W_e)}\right]^k$$

we can calculate the value of $k(W_e)$ – the number of collisions needed for the relaxation of electron energy W_e:

$$k(W_e) = \max\left(1, \left\{-\ln\left[\frac{\sigma^{el}(W_e)}{\sigma^{full}(W_e)}\right]\right\}^{-1}\right).$$

As electron motion in any gas at middle pressure is similar to the Brownian motion, the most probable electron displacement from an initial point after $k(W_e)$ collisions corresponds to the desired electron energy relaxation length $\lambda_W(W_e)$:

$$\lambda_W(W_e) = \sqrt{k(W_e)} \cdot \lambda_e(W_e) = \frac{\sqrt{k(W_e)}}{N_{\mathrm{Xe}}\sigma_{\mathrm{Xe}}^{full}(W_e) + N_{\mathrm{Cl}_2}\sigma_{\mathrm{Cl}_2}^{full}(W_e)}. \quad (3)$$

In Fig. 1 the results of the calculations of $\lambda_W(W_e)$, according to Eq. (3), with the use of the cross-section set taken from [14] are presented for a discharge in the mixture of Xe and Cl_2. One can see that if W_e exceeds the first excitation potential of Xe, the value of $\lambda_W(W_e)$ is small and we can state that the EEDF in this energy range is local. If N_{Cl_2} concentration is more than 10^{15} cm^{-3}, then the EEDF is local

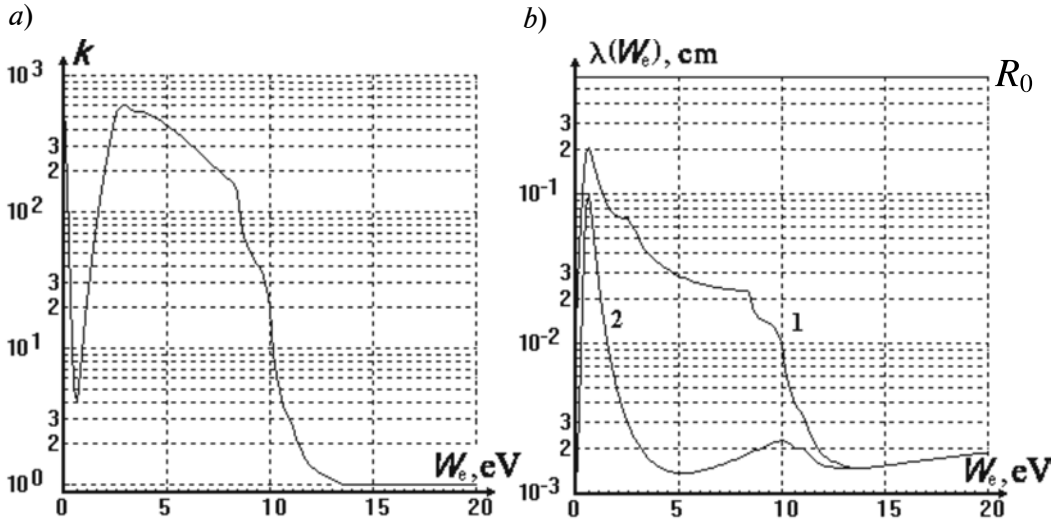

Fig. 1. Dependences on electron energy: *a* – number of collisions needed for energy relaxation; *b*: *1* – energy relaxation length, *2* – free path length; the horizontal line shows the tube radius $R_0 = 6$ mm. Gas mixture is: 6 Torr of Xe and 0.25 Torr of Cl_2, discharge current $I = 10$ mA, $\lambda_{E/N} \approx \delta \approx 0.1$ cm

if $W_e > 2.5$ eV (slightly higher than excitation threshold of the $B^1\Pi_u$ state of Cl_2 molecule). For the slowest electrons with $W_e < 0.5$ eV, the cross-section of dissociative attachment becomes large, and $\lambda_W(W_e)$ becomes small. However, we can see that in the electron energy range $0.5 < W_e < 2$ eV, $\lambda_W(W_e) \approx \lambda_{E/N} \cong \delta$, and expression (1) for these electrons is no more valid. The cross-sections of EA collision processes in this energy range (dissociative attachment, molecular vibrational level excitation) are small, hence the probability of electron energy losses is small as well.

So, the EEDF in discharge plasmas containing inert gases and chlorine can turn out to be nonlocal only in the narrow electron energy range of $0.5 < W_e < 2$ eV.

In discharges in EN gases and mixtures, the strong field inhomogeneity occurs in the «edge» (*e-i* plasma), where the radial field E_r can be large (up to 100 − 400 V/cm at $p \approx 6$ Torr) within the distances of ≤ 0.5 mm from the wall [6, 8]. Radial fields in the «edge» can even exceed the longitudinal field E_z (further in the «core» the radial field E_r quickly reduces to zero). But the outer region contains relatively few electrons [8] and, due to the large total field, the fraction of «hot» electrons with big probability of energy-consuming inelastic collisions is significant. This means that $\lambda_W(W_e)$ for such a fraction is small (see Fig. 1), and «hot» electrons do not penetrate into the region of the «core». Slow electrons can penetrate from the «edge» into the «core» but due to the small concentration of electrons in the «edge», they cannot seriously effect EEDF in the «core».

The radial field in the «core» is small [6, 8], and the total electrical field practically is equal to the longitudinal field E_z which is uniform, and hence there is no difference between local und nonlocal EEDF.

There is one more aspect which should be considered. Together with electron energy relaxation in isotropic Brownian motion, there is a radial drift of electrons to the discharge center in radial field E_r. If electrons during this drift have collisions with small energy losses only, they can receive an additional kinetic energy from the radial field.

But the slowest electrons with $0 < W_e < 0.5$ eV cannot gain energy: $\lambda_W(W_e)$ for such electrons is small (see Fig. 1, *b*, curve *1*) because the attachment cross-section is large in this energy range [16], and in the attachment acts electrons disappear as free particles.

The said receive of kinetic energy from radial field is mostly relevant to the group of electrons with $0.5 \leq W_e < 2$ eV where inelastic cross-sections are small and $\lambda_W(W_e)$ is comparable with δ. But let us notice that it is enough

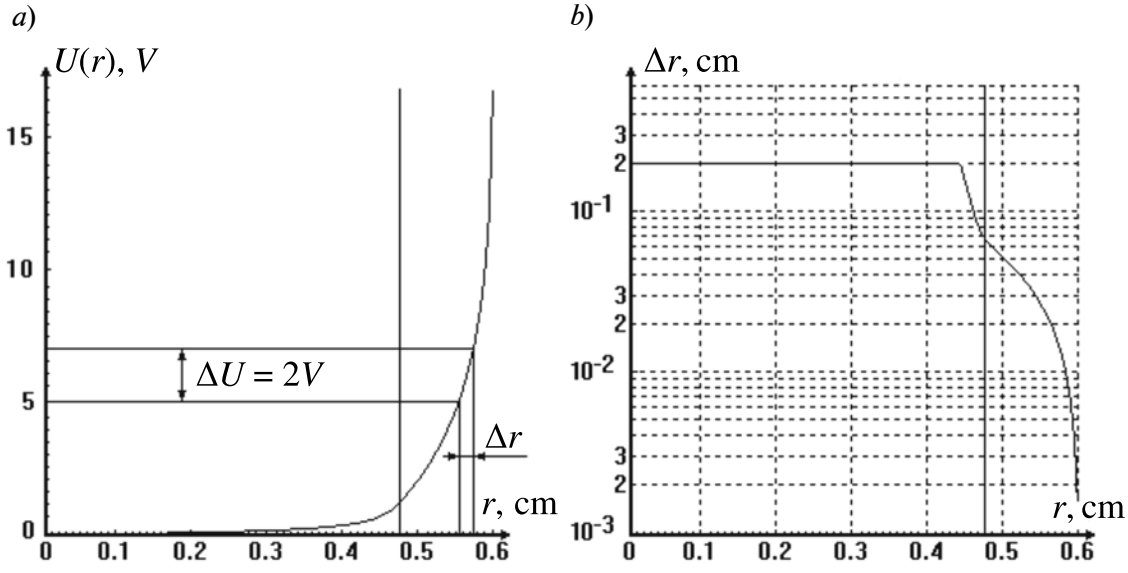

Fig. 2. Radial field potential (*a*) and the value of Δr (*b*), limited above by $\lambda_W \cong 0.2$ cm (see Fig. 1); discharge conditions are the same as in Fig. 1; vertical line shows the boundary between *i-i*- and *e-i*-plasmas

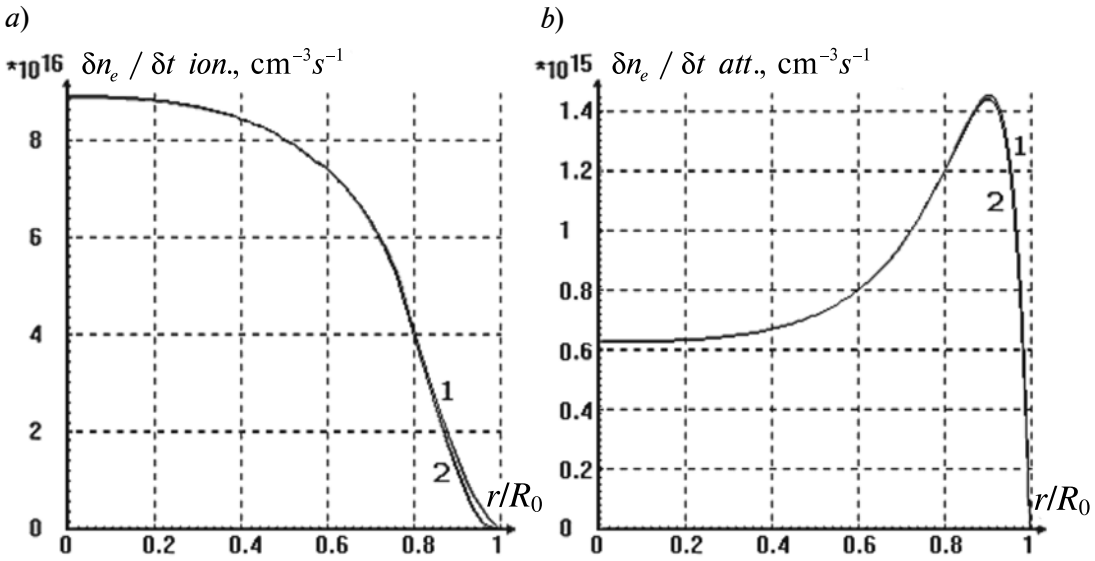

Fig. 3. Spatial distributions of ionization $N_{Xe} n_e \langle \sigma_i v_e \rangle$ (*a*) and attachment $N_{Cl_2} n_e \langle \sigma_a v_e \rangle$ (*b*) rates in local (*1*) and nonlocal (*2*) approach; the discharge conditions are the same as in Fig. 1

for these electrons to gain 2 eV, and their energy relaxation length becomes vanishingly small (see Fig. 1, *b*, curve *1*).

Hence, the real energy relaxation length of electrons with initial energy $0.5 \le W_e < 2$ eV can be defined as the piece of radial coordinate Δr along which the potential of radial field changes by $\Delta U \approx 2$ V (Fig. 2, *a*); more correctly, this length will be $\lambda_W^*(W_e) = \min[\Delta r, \lambda_W(W_e)]$ where $\lambda_W(W_e)$ can be estimated according to (3). In Fig. 2, there is an illustration to Δr computing and the result of such computing: $\Delta r(r) \approx 2 / E_r(r)$, where E_r is in V/cm.

It is seen that in the «edge» (*e-i* plasma), where nearly all the radial potential fall is concentrated, the values of Δr are vanishingly small, and we can hence accept the EEDF in the «edge» as local. Only at the boundary between *e-i*- and *i-i*-plasmas and inside the «core» (where E_r is close to zero), $\lambda_W^*(W_e) \approx \lambda_W(W_e)$, and EEDF in the energy range $0.5 < W_e < 2$ eV is nonlocal. But this group of electrons practically takes no part in plasma interaction processes due to smallness of all collision cross-sections for electrons of said energy range.

Assuming the afore-mentioned, we can suppose that the effect of EEDF nonlocality on properties of our discharges should be not significant. Model calculations [8] confirm this assumption. As an illustration, the results of computing of rates of some plama-chemical processes both in local and nonlocal approach are presented in Fig. 3.

For the mixture of 6 Torr Xe and 0.25 Torr Cl_2, the biggest difference among all collision rates was observed in the ionization rate $N_{Xe} n_e \langle \sigma_i v_e \rangle$, the residual for local and nonlocal approaches was of about 1.6 % with the main deviation taking place just near the tube wall (not more than 0.5 mm from the wall). The reason for such a weak reduction of ionization rate in the nonlocal approach lies in the small relaxation length (< 0.1 mm). As a result, the wall losses of «hot» electrons, which are not only able to produce ionization but also can penetrate through the wall potential barrier and die on the wall, are small.

For the attachment rate $N_{Cl_2} n_e \langle \sigma_a v_e \rangle$ – the most important process for EN discharges – where the process is maintained mainly by slow electrons [16], the residual turned out to be even smaller – about 1 %.

These differences have almost no effect on the spatial distributions of charged particles and excimer molecules densities (the concentration of residuals was less than 1%).

The residuals for the mixtures with higher gas pressure or with higher percentage of chlorine are smaller because $\lambda_W(W_e)$ decreases

proportionally both to total pressure and to amount of molecular chlorine. For the mixture of 18 Torr Xe and 0.7 Torr Cl_2, the residuals for rates of all the processes turned out to be no more than 0.4 %.

Hence, we can state that for gas discharges in a mixture of Xe and Cl_2 with total pressure not less than 6 Torr and with amount of chlorine not less than 1/25, the effect of EEDF nonlocality on properties of discharges is insufficient, and the local approach can be used in modeling such discharges.

REFERENCES

1. **Golovitskii A.P., Kan S.N.** Characteristics of UV excimer radiation from a continuous low-pressure glow discharge. *Opt. Spectrosc.,* 1993, Vol. 75, No. 3, pp. 357–402. (rus)

2. **Golovitskii A.P.** Simulation of gas-discharge UV sources based on a glow discharge in a xenon – chlorine mixture. *Tech. Phys.*, 2011, Vol. 56, No. 3, pp. 371–380.

3. **Skakun V.S., Lomaev M.I., Tarasenko V.F., Shitts D.A., Johnson G.L., Wang F.T.** High-power UV exilamps excited by a glow discharge. *Laser and Particle Beams*, 2003, Vol. 21, pp. 115–119.

4. **Lomaev M.I., Skakun V.S., Sosnin E.A. TarasenkoV.F., Shitts D.A., Erofeev M.V.** Exilamps: efficient sources of spontaneous UV and VUV radiation. *Physics-Uspekhi*, 2003, Vol. 46, No. 2, pp. 193–209. (rus)

5. **Di Lazzaro P., Murra D., Felici G., Fu S.** Spatial distribution of the light emitted by an excimer lamp used for ultraviolet-B photo-therapy: Experiment and modeling. *Rev. Sci. Instrum.*, 2004, Vol. 75, No. 5, pp.1332–1336.

6. **Volynets V.N., Lukyanova A.V., Rakhimov A.T., Slovesky, Suetin N.N.** Experimental and theoretical study of the CF_4 DC glow discharge positive column. *J. Phys. D: Appl. Phys.,* 1993, Vol. 26, pp. 647–656.

7. **Franklin R.N., Daniels P.G., Snell J.** Characteristics of electric discharges in the halogens: the recombination-dominated positive column. *J. Phys. D: Appl. Phys.*, 1993, Vol. 26, pp. 1638–1649.

8. **Golovitskii A.P.** Simulation of the positive column of a glow discharge in an inert gas – chlorine mixture with allowance for the dissociation of chlorine molecules. *Tech. Phys.*, 2011, Vol. 56, No. 3, pp. 361–370.

9. **Tsendin L.D.** Electron kinetics in non-uniform glow discharge plasmas. *Plasma Sources Sci. Technol.*, 1995, Vol. 4, pp. 200–211.

10. **Bernstein I.R., Holstein T.** Electron energy distribution in stationary discharges. *Phys. Rev.*, 1954, Vol. 91, No. 6, pp. 1475–1482.

11. **Tsendin L.D.** Plasma stratification in a discharge in an electronegative gas. *Sov. Phys. Tech. Phys.*, 1989, Vol. 34, No. 1, pp. 11–15. (rus)

12. **Golovitskii A.P., Tsendin L.D.** Simple analytical formulas for an estimation of parameters of a glow discharge positive column in electronegative gases. *Tech. Phys.*, 2014, Vol. 58, No. 2 (in press). (rus)

13. **Bogdanov E.A., Kudryavtsev A.A., Tsendin L.D., Arslanbekov R.R., Kolobov V.I., Kudryavtsev A.A.** The influence of metastable atoms and the effect of the nonlocal character of the electron distribution on the characteristics of the positive column in an argon discharge. *Tech. Phys.*, 2004, Vol. 49, No. 6, pp. 698–706.

14. **Golovitskii A.P.** The coefficient of electron energy losses for collisions in xenon, chlorine and their mixture. *St. Petersburg State Polytechnical University Journal: Physics and Mathematics*, 2008, No. 3, pp. 87–94. (rus)

15. **Bogdanov E.A., Kudryavtsev A.A., Tsendin L.D., Arslanbekov R.R., Kolobov V.I., Kudryavtsev A.A.** Substantiation of the two-temperature kinetic model by comparing within the kinetic and fluid models of the positive column plasma of a DC oxygen discharge. *Tech. Phys.*, 2003, Vol. 48, No. 8, pp. 983–994.

16. **Golovitskii A.P.** Temperature dependence of an electron attachment to chlorine molecules. *Tech. Phys.*, 2000, Vol. 45, No. 5, pp. 532–537.

СПИСОК ЛИТЕРАТУРЫ

1. **Головицкий А.П., Канн С.Н.** Характеристики ультрафиолетового эксимерного излучения непрерывного тлеющего разряда низкого давления // Оптика и спектроскопия. 1993. Т. 75, № 3. С. 604–609.

2. **Golovitskii A.P.** Simulation of gas-discharge UV sources based on a glow discharge in a xenon-chlorine mixture. *Tech. Phys.* 2011, Vol. 56, No. 3, pp. 371–380.

3. **Skakun V.S., Lomaev M.I., Tarasenko V.F., Shitts D.V., Johnson G.L., Wang F.T.** High-power UV exilamps excited by a glow discharge. *Laser and Particle Beams*, 2003, Vol. 21, pp. 115–119.

4. **Ломаев М.И., Скакун В.С., Соснин Э.А., Тарасенко В.Ф., Шитц Д.В., Ерофеев М.В.** Эксилампы – эффективные источники УФ- и ВУФ-излучения // Успехи физических наук. 2003. Т. 173. № 2. С. 201 – 217.

5. **Di Lazzaro P., Murra D., Felici G., Fu S.** Spatial distribution of the light emitted by an excimer lamp used for ultraviolet-B photo-therapy: Experiment and modeling. *Rev. Sci. Instrum.*, 2004, Vol.75, No. 5, pp.1332–1336.

6. **Volynets V.N., Lukyanova A.V., Rakhimov A.T., Slovetsky D.I., Suetin N.V.** Experimental and theoretical study of the CF_4 DC glow discharge positive column. *J. Phys. D: Appl. Phys.,* 1993, Vol. 26, pp. 647–656.

7. **Franklin R.N., Daniels P.G., Snell J.** Characteristics of electric discharges in the halogens: the recombination-dominated positive column. *J. Phys. D: Appl. Phys.*, 1993, Vol. 26, pp. 1638–1649.

8. **Golovitskii A.P.** Simulation of the positive column of a glow discharge in an inert gas – chlorine mixture with allowance for the dissociation of chlorine molecules. *Tech. Phys.*, 2011, Vol. 56, No. 3, pp. 361–370.

9. **Tsendin L.D.** Electron kinetics in non-uniform glow discharge plasmas. *Plasma Sources Sci. Technol.* 1995, V. 4, pp. 200–211.

10. **Bernstein I.R., Holstein T.** Electron energy distribution in stationary discharges. *Phys. Rev.*, 1954, V. 91, No. 6, P. 1475–1482.

11. **Цендин Л.Д.** Расслоение газоразрядной плазмы в электро-отрицательных газах // Журнал технической физики. 1989. Т. 59. Вып. 1. С. 21–28.

12. **Головицкий А.П., Цендин Л.Д.** Простые аналитические формулы для оценки параметров положительного столба тлеющего разряда в электро-отрицательных газах//Журнал технической физики. 2014, Т. 84. Вып. 3 (в печати).

13. **Bogdanov E.A., Kudryavtsev A.A., Tsendin L.D., Arslanbekov R.R., Kolobov V.I., Kudryavtsev V.V.** The influence of metastable atoms and the effect of the nonlocal character of the electron distribution on the characteristics of the positive column in an argon discharge. *Tech. Phys.*, 2004, Vol. 49, No. 6, pp. 698–706.

14. **Головицкий А.П.** Коэффициент потерь энергии электрона при столкновениях в ксеноне, хлоре и их смеси // Научно-технические ведомости СПбГПУ. Основной выпуск. 2008. № 3(59). С. 87–94.

15. **Bogdanov E.A., Kudryavtsev A.A., Tsendin L.D., Arslanbekov R.R., Kolobov V.I., Kudryavtsev V.V.** Substantiation of the two-temperature kinetic model by comparing within the kinetic and fluid models of the positive column plasma of a DC oxygen discharge. *Tech. Phys.*, 2003, Vol. 48, No. 8, pp. 983–994.

16. **Golovitskii A.P.** Temperature dependence of an electron attachment to chlorine molecules. *Tech. Phys.*, 2000, Vol. 45, No. 5, pp. 532–537.

ГОЛОВИЦКИЙ Александр Петрович – *доктор физико-математических наук, доцент кафедры физической электроники Санкт-Петербургского государственного политехнического университета.*

195251, Россия, г. Санкт-Петербург, Политехническая ул., 29

alexandergolovitski@yahoo.com

UDC 537.5

G.G. Sominski[1], V.E. Sezonov[1], E.P. Taradaev[1], T.A. Tumareva[1], E.I. Givargizov[2], A.N. Stepanova [2]

[1] St. Petersburg State Politechnical University, 29 Politechnicheskaya St., St. Petersburg, 195251, Russia
[2] Institute of Crystallography RAS, 59 Leninskiy Pr., 119333, Moscow, Russia

COLD FIELD EMITTERS FOR ELECTRON DEVICES OPERATING IN TECHNICAL VACUUM

Г.Г. Соминский, В.Е. Сезонов, Е.П. Тарадаев, Т.А. Тумарева, Е.И. Гиваргизов, А.Н. Степанова

ХОЛОДНЫЕ ПОЛЕВЫЕ ЭМИТТЕРЫ ДЛЯ ЭЛЕКТРОННЫХ УСТРОЙСТВ, РАБОТАЮЩИХ В ТЕХНИЧЕСКОМ ВАКУУМЕ

The paper describes the field emitters of a new type: multi-tip cathodes with special protective coatings and layered cathodes prepared from the nano-layers of the materials with different work function values. The article presents data on the technology of emitter creation and their operation at technical vacuum conditions.

FIELD EMITTER, HIGH EMISSION CURRENTS, HIGH DURABILITY IN TECHNICAL VACUUM, EXPERIMENT, NUMERICAL COMPUTATION.

В статье описаны эмиттеры нового типа: многоострийные катоды со специальными защитными покрытиями и слоистые катоды, изготовленные из нанослоев материалов с разной работой выхода. Приведены данные о технологии изготовления эмиттеров и об их работе в условиях технического вакуума.

ПОЛЕВОЙ ЭМИТТЕР, БОЛЬШИЕ ЭМИССИОННЫЕ ТОКИ, ВЫСОКАЯ ДОЛГОВЕЧНОСТЬ В ТЕХНИЧЕСКОМ ВАКУУМЕ, ЭКСПЕРИМЕНТ, ЧИСЛЕННЫЙ РАСЧЕТ.

I. Introduction

Interest to the cold field emitters has increased significantly during the last years in connection with the appearance and development of comparatively low-power microwave electron devices operating in the range of terahertz waves. Such devices may be used to implement different types of diagnostics, in particular for some types of medical diagnostic and diagnostic of dense plasma. The miniature cold field emitters are very attractive for such devices. Difficulties in achieving high durability at technical vacuum conditions and obtaining high enough currents prevent the application of field emitters in high voltage microwave electron devices. The authors searched for the methods to create the durable and high current field emitters for microwave devices operating in technical vacuum. Two prospective cathode systems can be proposed for such application. They are multi-tip cathodes with special protective coatings and nano-layered cathodes prepared from materials with greatly different work function values developed by the authors from St. Petersburg State Polytechnic University (SPbSPU) [1, 2].

II. Tip Field Emitters with Fullerene Coatings

Multi-tip silicon systems that we are investigating now provide in pulse regime (1 – 2 μs, 100 – 200 Hz) currents about 100 mA from the square of approximately 1 cm^2. Production of

such systems is organized in Institute of Crystallography RAS (Moscow). But the cathodes of this type usually have low conductivity and provide such a high level of emission only at heightened temperatures, when their conductivity is increased due to the heating. Cathodes of this type are insufficiently steady and usually are destroyed in static regime at significantly lower currents under the action of ponderomotive forces. In addition, silicon cathodes are easily damaged in the presence of an intense ion bombardment. So, one needs to find the ways to increase their conductivity and strength to the action of the ponderomotive forces and ion bombardment to solve the problem of the practical use of silicon cathodes.

The previously performed investigations [3 – 7] of single-tip tungsten field emitters showed that fullerene coatings can be used to protect them from the destructive action of ion bombardment. Fullerene coatings have high work function ($e\varphi \sim 5{,}0 - 5{,}4$ eV). However, creation of a structure including a large amount of roughly equal in size protrusions on the surface of emitters allowed emitters with fullerene coatings to operate at moderate voltages. Additional reduction of the operating voltages was

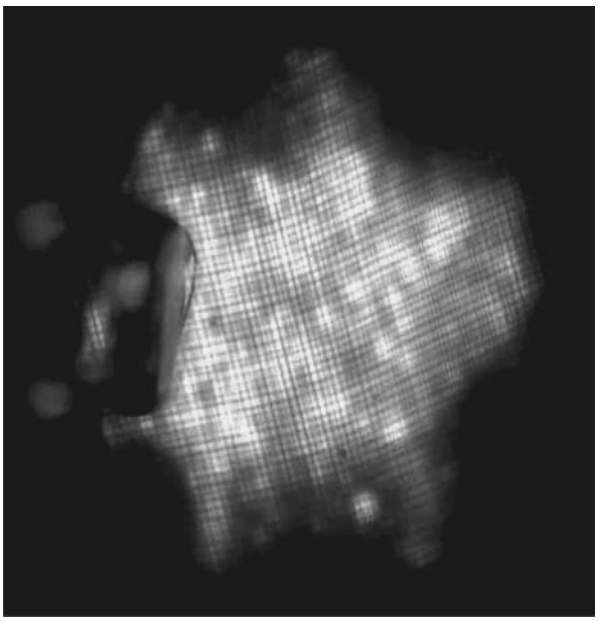

Fig. 1. The image of a single-tip tungsten emitter with activated fullerene coating obtained in the field emitter microscope at residual gas pressure about 10^{-7} Torr

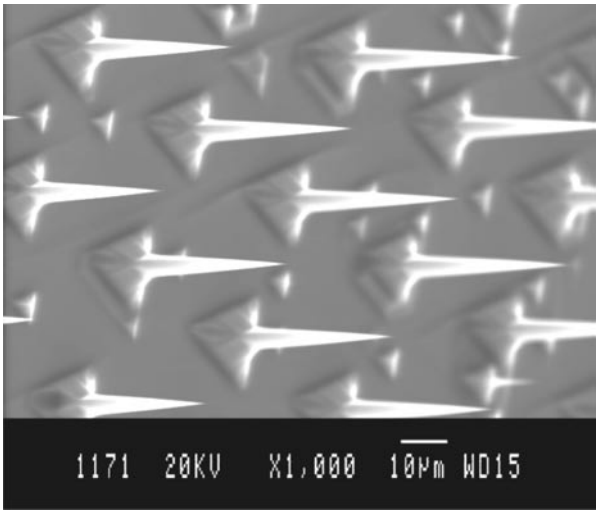

Fig. 2. Multi-tip silicon system

achieved as the result of activating the fullerene coating by a flow of slow (40 eV) potassium ions.

Tungsten tip emitter with activated fullerene coating stably operates at technical vacuum conditions. Fig. 1 demonstrates typical image of a single-tip tungsten emitter obtained in the field emitter microscope at residual gas pressure of about 10^{-7} Torr. The revealed mechanism of fullerene coating self-reproduction in the presence of intensive ion bombardment explains the stable operation of such emitters at technical vacuum conditions [3, 4].

It was important to understand the possibility to use the fullerene coating for shielding silicon tip field emitters from the destructive action of the ion bombardment. We have investigated the functioning of multi-tip silicon system which is demonstrated in Fig. 2. Our measurements showed that application of a thin (two – three monolayer) activated fullerene coating on the surface of the silicon multi-tip field emitter allowed to increase significantly the stability of its operation in a static regime at low (less than 1 – 2 μA) currents, but not prevented its destruction at higher currents. Significantly better results were obtained for the cathodes with more complex evaporated two-layer coating comprising a metal (molybdenum) layer (with thickness of several tens of nm) and a thin (several monolayers) layer of activated fullerene molecules. Cathodes with such coverage allowed to obtain the field emission current

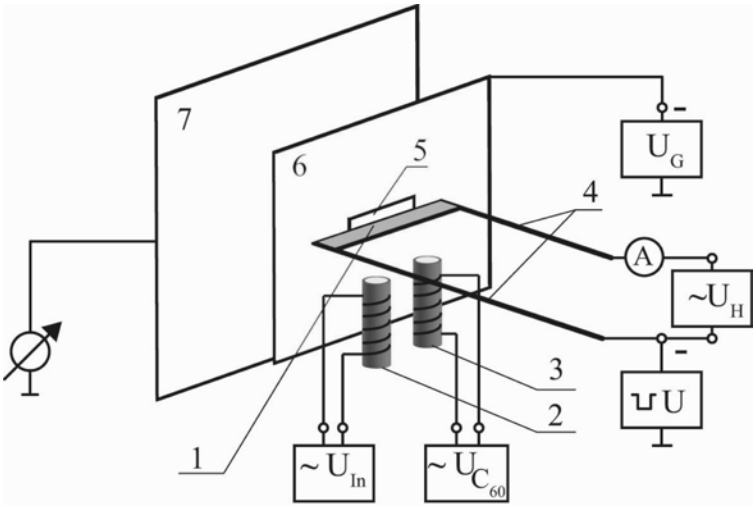

Fig. 3. Triode type system used for the investigation of the layered emitters

density approximately up to 0,1 – 0,5 A/cm^2 without heating. The experiments showed that these cathodes can operate in static regime for a long time at residual gas pressure of the order of 10^{-7} Torr.

III. Nano-Layered Cathodes of New Type

A. Experimental Investigation

Creation and investigation of the layered emitters were performed in a triode type system (Fig. 3). The layers of indium ($e\varphi \sim 3{,}6 - 3{,}8$ eV) and fullerenes ($e\varphi \sim 5{,}0 - 5{,}4$ eV) were deposited alternately from the heated sources *2* and *3* onto the side surface of tungsten substrate – foil *1* (10 μm × 2 mm × 25 mm). Electrons from the frontal surface of the layered cathode reach the collector *7* through the transparent (75 %) grid in the slot *5* (4 × 10 mm) of the anode *6*. Thicknesses of In and C_{60} layers were determined by the measurements of so-called evaporation curves [4, 5]. The thickness of In and C_{60} layers was varied approximately from 1 to 10 nm. Measurements of cathodes emission characteristics were performed in pulse regime (1 – 2 μs, 100 – 200 Hz) in technical vacuum (~ 10^{-7} Torr).

Performed measurements showed that the emission current I increased with the rise of quantity N of pairs In – C_{60} layers. Typical current-voltage characteristics of the cathodes that differ in the quantity N of pairs are shown in Fig. 4. The fields produced by the voltage U near the front of the cathode system can secure only small currents from the substrate *S*. The currents of cathodes *C*1, *C*2 and *C*3 increased with the quantity N of the pairs of layers. This demonstrates the existence of field emission from the nano-contacts of materials with different work functions.

B. Numerical Computation

Numerical computations were performed using the Comsol program. These computations were aimed at determining the regularities and mechanisms of field emission of layered systems prepared of materials with different

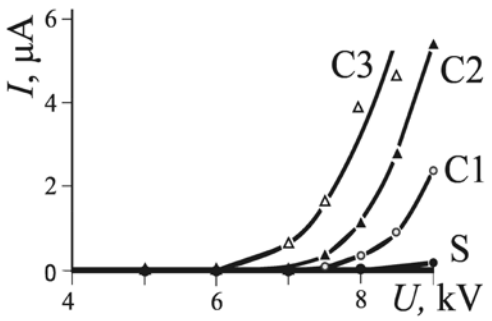

Fig. 4. Typical current-voltage characteristics of cathodes that differ in the quantity N of pairs of layers with different work function values. Cathodes *C*1, *C*2 and *C*3 include correspondingly 1, 2 and 3 pairs of layers. *S* is the current-voltage characteristic of the *W* substrate

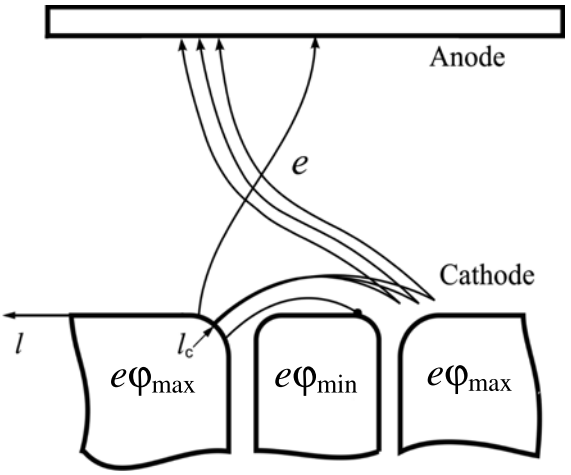

Fig. 5. Typical trajectories of electrons (e) emitted from the material with higher work function ($e\varphi_{max}$) of a layered cathode system.
Here l_c is a critical value of coordinate l that divides the electrons into two main groups: the electrons arriving at the anode, and the electrons returning to the cathode; $e\varphi_{min}$ is the work function of the layer with minimal work function

work functions. Electric field distributions between the layered cathode and flat anode were calculated taking into account not only the «external» field but the fields produced by the contacts of materials with different work functions. These data were used for the calculation of electron trajectories and emission currents.

Typical trajectories of electrons (e) emitted from the material with higher work function ($e\varphi_{max}$) are shown in Fig. 5. Here l_c is a critical value of coordinate l that divides the electrons into two main groups: the electrons arriving at the anode, and the electrons returning to the cathode. The layer with minimal work function is named $e\varphi_{min}$.

The typical distributions of the emission current density $j(l)$ computed at different values of the fullerene layer thickness d_{C60} and at fixed thickness of In layers d_{In} = 5 nm are shown in Fig. 6. The calculations were performed with voltage U = 10 kV for the cathode containing 10 pairs of layers on the substrate of the thickness d_s = 10 μm.

The calculations indicated that the current density j is maximal at $l = l_c$. The value of j increased with the decrease of C_{60} layers thick-

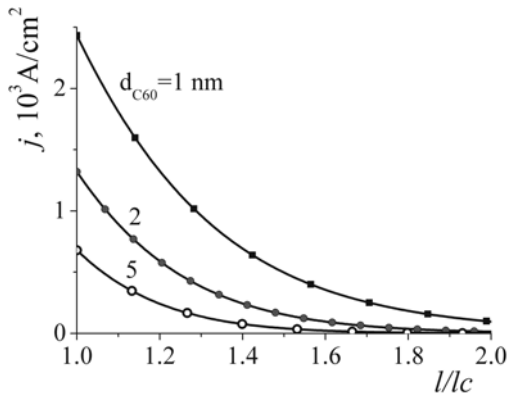

Fig. 6. Dependencies of current density j versus l/l_c measured at voltage U = 10 kV, thickness of substrate d_s =10 μm, d_{In} = 5 nm, $\Delta e\varphi$ = 1.2 eV, $e\varphi_{max}$ = 5.0 eV

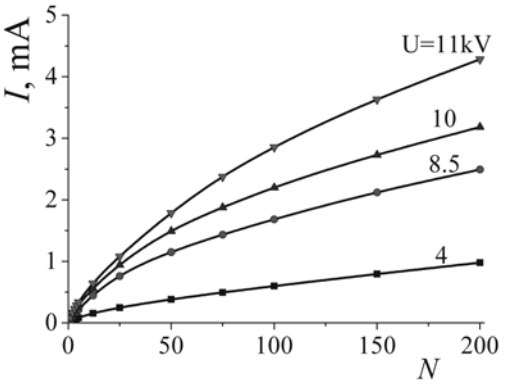

Fig. 7. Dependencies of current I versus quantity N of pairs of layers measured at different values of voltage U; d_s =10 μm, d_{In} = 5 nm, d_{C60} = 1 nm; $\Delta e\varphi$ = 1.5 eV, $e\varphi_{max}$ = 5.3 eV

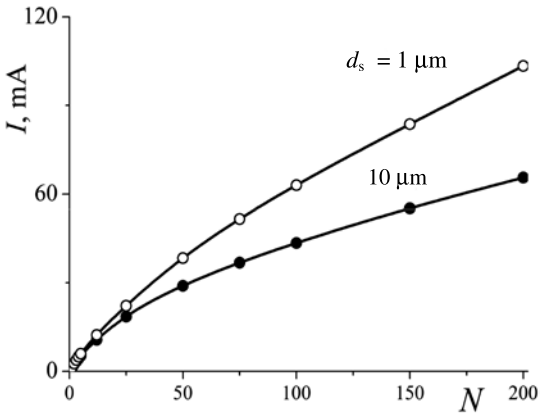

Fig. 8. Dependencies of current I versus quantity N of pairs of layers measured at two values of d_s:1 and 10 μm; U = 11 kV, d_{In} = 5 nm, d_{C60} = 1 nm; $\Delta e\varphi$ = 1.8 eV, $e\varphi_{max}$ = 5.3 eV

ness d_{C60} (see Fig. 6) and with the growth of In layers thickness d_{In}. The value of j increased also with the diminution of the substrate thickness d_s.

The total current of the layered cathode is obtained by integrating emission current density from the area with coordinates $l > l_c$, from which electrons enter the anode. This current is increased with the rise of work function difference $\Delta e\varphi$ for neighboring layers, and also with the rise of voltage U and quantity N of the pairs of layers. Besides, the current is increased with the decrease of the substrate thickness d_s. Fig. 6 – 8 demonstrate the typical changes of emission current at different values of these parameters.

According to calculations, the maximal current about 100 mA can be obtained from the cathode containing 200 pairs of layers on the thin substrate (d_s = 1 μm) at voltage U = 11 kV and at the difference in the work function of neighboring layers $\Delta e\varphi$ = 1.8 eV when optimal thicknesses of the layers d_{In} = 3 – 5 nm and d_{C60} = 1 nm are set.

IV. Conclusion

The main results of the work are the following:

operation of multi-tip silicon field emitters with special two-layer coatings were investigated at technical vacuum conditions, and emission current density up to 0.1 – 0.5 A/cm^2 was derived;

the possibility of field emission from nanocontacts of materials with different work function values was demonstrated in the experiments and computations. The main regularities and mechanisms of such emission were determined;

influence of the layers and substrate thicknesses, quantity of the layers, work function difference and voltage value on the emission current was determined. The possibility to obtain currents of field emission of about 50 – 100 mA from investigated systems was demonstrated.

Performed investigations were supported by the grant of Russian Federation Government (agreement №11.G34.31.0041 with Ministry of education and science) and also by the grant RFBR № 11-02-00425.

REFERENCES

1. **Sominskii G.G., Sezonov V.E., Sakseev D.A., Tumareva T.A.** Influence of the spot field on field emission from composites. *Technical Physics*, 2011, Vol. 56, No. 6, pp. 850–854.

2. **Sominski G.G., Sezonov V.E., Tumareva T.A., Taradaev E.P.** Field emitter. *RF Patent* №118119, 2012. (rus)

3. **Tumareva T.A., Sominskii G.G.** Operation of field emitters with activated fullerene coatings in technical vacuum. *Technical Physics*, 2013, Vol. 58, No. 7, pp. 1048–1051.

4. **Tumareva T.A., Sominski G.G., Veselov A.A.** Field emitters with fullerene coatings for vacuum electronics: formation, achievement of high currents and operating voltage reduction. *ITG-Fachbericht Proceedings* «Displays and Vacuum Electronics» (May 3-4, 2004, Garmisch-Partenkirchen, Germany). VDE Verlag GMBH, Berlin, Offenbach, 2004, No. 183, pp.125–130.

5. **Tumareva T.A., Sominski G.G., Bondarenko A.K., Veselov A.A., Svetlov I.A.** Activation of fullerene coatings on field emitters by potassium atom and ion fluxes. *Technical Physics*, 2006, Vol. 51, No. 7, pp. 898–901.

6. **Tumareva T.A., Sominski G.G.** Development and improvement of field emitters containing carbon-based materials. *Izvestiya VUZOV, Prikladnaya nelineynaya dinamika*, 2009, Vol. 17, No. 3, pp.17–54 (rus).

7. **Tumareva T.A., Sominskii G.G., Svetlov I.A., Panteleev I.S.** Use of ion processing to improve the quality of fullerene-coated field emitters. *Technical Physics*, 2012, Vol. 57, No. 1, pp. 113–118.

СПИСОК ЛИТЕРАТУРЫ

1. **Sominskii G.G., Sezonov V.E., Sakseev D.A., Tumareva T.A.** Influence of the spot field on field emission from composites. *Technical Physics*, 2011, Vol. 56, No. 6, pp. 850–854.

2. **Соминский Г.Г., Сезонов В.Е., Тумарева Т.А., Тарадаев Е.П.** Полевой эмиттер. Патент РФ. ПМ 118119. Начало действия 17.02. 2012.

3. **Tumareva T.A., Sominskii G.G.** Operation of field emitters with activated fullerene coatings in technical vacuum. *Technical Physics*, 2013, Vol. 58, No. 7, pp. 1048–1051.

4. **Tumareva T.A., Sominski G.G., Veselov A.A.** Field emitters with fullerene coatings for vacuum electronics: formation, achievement of high currents and operating voltage reduction. *ITG-Fachbericht Proceedings* «Displays and Vacuum Electronics»

(May 3-4, 2004, Garmisch-Partenkirchen, Germany). VDE Verlag GMBH, Berlin, Offenbach, 2004, No. 183, pp.125–130.

5. **Tumareva T.A., Sominski G.G., Bondarenko A.K., Veselov A.A., Svetlov I.A.** Activation of fullerene coatings on field emitters by potassium atom and ion fluxes. *Technical Physics*, 2006, Vol. 51, No. 7, pp. 898–901.

6. **Соминский Г.Г., Тумарева Т.А.** Разработка и совершенствование полевых эмиттеров на основе содержащих углерод материалов // Известия вузов. Прикладная нелинейная динамика. 2009. Т. 17. № 3. С. 17–54.

7. **Tumareva T.A., Sominskii G.G., Svetlov I.A., Panteleev I.S.** Use of ion processing to improve the quality of fullerene-coated field emitters. *Technical Physics*, 2012, Vol. 57, No. 1, pp. 113–118.

СОМИНСКИЙ Геннадий Гиршевич – *доктор физико-математических наук, профессор кафедры физической электроники Санкт-Петербургского государственного политехнического университета.*
195251, Россия, Санкт-Петербург, Политехническая ул., 29
sominski@rphf.spbstu.ru

СЕЗОНОВ Вячеслав Евгеньевич – *аспирант кафедры физической электроники Санкт-Петербургского государственного политехнического университета.*
195251, Россия, Санкт-Петербург, Политехническая ул., 29
sezonovve@mail.ru

ТАРАДАЕВ Евгений Петрович – *аспирант кафедры физической электроники Санкт-Петербургского государственного политехнического университета.*
195251, Россия, Санкт-Петербург, Политехническая ул., 29
Evgeny_tar@hotmail.com

ТУМАРЕВА Татьяна Алексеевна – *кандидат физико-математических наук, старший научный сотрудник кафедры физической электроники Санкт-Петербургского государственного политехнического университета.*
195251, Россия, Санкт-Петербург, Политехническая ул., 29
tumareva@rphf.spbstu.ru

ГИВАРГИЗОВ Евгений Инвиевич – *доктор физико-математических наук, руководитель лаборатории Института кристаллографии им. А.В. Шубникова РАН.*
119333, Россия, Москва, Ленинский пр. 59
egivargiz@ns.crys.ras.ru

СТЕПАНОВА Алла Николаевна – *кандидат физико-математических наук,ведущий научный сотрудник Института кристаллографии им. А.В. Шубникова РАН.*
119333, Россия, Москва, Ленинский пр. 59
cvdlab@ns.crys.ras.ru

PHYSICAL OPTICS

UDC 535:621.373.8:6

A.V. Kniazkov

St. Petersburg State Polytechnical University,
29 Politekhnicheskaya St., St. Petersburg, 195251, Russia

THE POLARIZATION-OPTICAL METHOD FOR SPECTRAL ANALYSIS OF LIGHT

А.В. Князьков

ПОЛЯРИЗАЦИОННО-ОПТИЧЕСКИЙ МЕТОД СПЕКТРАЛЬНОГО АНАЛИЗА СВЕТА

An analysis of passing the light emission that has Gaussian spectrum through the polarization-optical scheme (POS) with half-wave phase plate has been performed. The results of theoretical calculations of the coherence length of the radiation as a function of the contrast of POS output intensities are obtained for the different widths $\Delta\lambda$ of the Gaussian emission spectrum. The research results of the contrast of POS with $\lambda/2$ phase plate are obtained for the following case: high-power LEDs radiation of red, green and blue spectrum; semiconductor laser red wavelengths; a second harmonic Nd-laser (green wavelength range).

POLARIZE-OPTICAL METHOD, HALF-WAVE PLATE, SPECTRAL ANALYSIS, CONTRAST MODULATION.

В статье представлен спектральный анализ светового потока поляризационно-оптическим методом (ПОМ) с двулучепреломляющей полуволновой пластинкой. Рассмотрены случаи прямоугольного и гауссовского спектра светового потока. Показано, что контрастность ПОМ сильно зависит от ширины спектра света и определяется порядком полуволновой пластинки. Приведены результаты оценки спектра излучения полупроводникового лазера.

ПОЛЯРИЗАЦИОНО-ОПТИЧЕСКИЙ МЕТОД, ПОЛУВОЛНОВАЯ ПЛАСТИНКА, АНАЛИЗ СПЕКТРА, КОНТРАСТНОСТЬ МОДУЛЯЦИИ.

Birefringent (BF) materials are widely used in phase polarization modulation of light. The polarization-optical phase conversion method (POM) of the laser radiation into amplitude modulation is well-known, and it is characterized by high efficiency [1, 2]. This method works in the polarization-optical scheme (POS) (Fig. 1), that consists of the laser *1* with the light of wavelength λ_0 which passes successively through the polarizer *2*, a BF medium *3* of the thickness *l* and birefringence Δn, the analyzer *4*, and then enters the input photo recording device *5*. In POS, collimated radiation of the source *1* passes through the polarizer *2*, the axis orientation of which is relative to the optical axis of the BF material so that the material transforms the light via BF into two orthogonally polarized light waves of equal intensity. These waves, for various values of the refractive index for the ordinary and extraordinary n_e, n_o waves, acquire different phase delays, depending on the path *l* of the BF medium. As a result, the output light after the BF material becomes elliptically polarized. At the output after a quar-

ter-wave plate, the light is circularly polarized, while after a half-wave plate the linear polarization is orthogonal to the input polarization. The transformation of this phase-polarization modulation into amplitude modulation is performed by the analyzer *4*. To register this amplitude modulation photo recording device *5* is used (see Fig. 1). The simplest expression of the phase transformation POS into amplitude modulation was obtained for the optimal orientation of the optical axis relative to the axis of the material BF polarizer-analyzer, when modulated radiation had a single wavelength λ_0 [1 – 3]. The maximal variation of light intensity I of the radiation wavelength λ_0 after its passing the polarization-optical scheme with a crossed-polarizer position of the analyzer axes is described by the following expression:

$$I_{\perp} = I_0 \cdot \sin^2(\pi \Delta n l / \lambda_0),$$

and for the parallel orientation of the polarizer-analyzer axes:

$$I_{\parallel} = I_0 \cdot \cos^2(\pi \Delta n l / \lambda_0) = I_0 \cos^2(\varphi_0).$$

The transformation of the phase-polarization modulation into amplitude modulation POM for radiation sources with finite spectrum of wavelengths is much more difficult. The present work is devoted to the study of polarization-optical method with a half-wave plate used in the spectral analysis of output light in general case of radiation with a finite continuous spectrum.

The real sources of radiation have a finite frequency range. This results is the fact that the extremes of intensity of light after the POS do not reach their maximum or minimum values. All of this can be used as the basis for POM spectral analysis.

Consider the POS with a half-wave plate with crossed/parallel axes of the polarizer-analyzer. The maximum of normalized change in

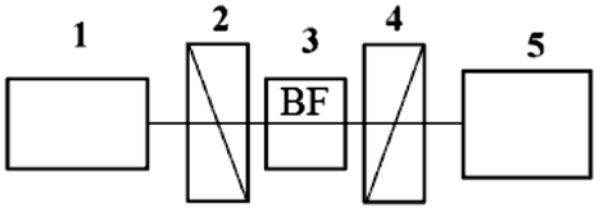

Fig. 1. The polarization-optical scheme (POS)

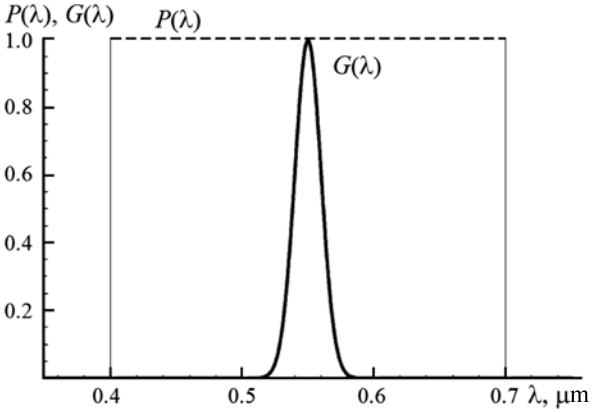

Fig. 2. The rectangular $P(\lambda)$; $\lambda_1 = 0.4$ μm; $\lambda_2 = 0.7$ μm and Gaussian $G(\lambda)$ spectrum. $\lambda_0 = 0.55$ μm, $\sigma = 0.01$ μm

output intensity (1 – 0) or (0 – 1) is taken whenever the orientation of the axes is: polarizer/analyzer: × or ∥, and the phase delay is determined as $\varphi(\lambda_0) = \pi/2$. The maximum depth of the change in intensity is only performed for a specific wavelength λ_0. For the light sources with finite frequency width spectrum of radiation or, in other words, with a finite range of radiated wavelengths: $\Delta\lambda = \lambda_2 - \lambda_1$, the condition of maximum modulation depth is only performed for one wavelength λ_0. For all the other spectral components, this condition is not satisfied, which leads to the reduction of the maximum modulation depth of the radiation.

The amplitude spectral composition of the radiation is described by the spectral density. We will consider two cases of the spectrum: a rectangular spectrum with spectral density $P(\lambda)$ = const, and a Gaussian spectrum with spectral density $G(\lambda)$. LED and laser radiation has a finite frequency spectrum or it has a finite range of wavelengths: $\Delta\lambda = \lambda_2 - \lambda_1$ defining a longitudinal coherence length L_{coh} that for the approximation of a rectangular distribution of the emission spectrum (Fig. 2) can be estimated by the position of the first minimum of the curve of the visibility

$$V = (I_{\max} - I_{\min})/(I_{\max} + I_{\min})$$

of the interference pattern: $L_{coh} = \lambda_0^2/\Delta\lambda$. Conditions of POM of extreme values of intensity $I_{\min,\max}$ ($\varphi = (2N + 1)\pi/2$, where $N = 0, 1, 2, 3, \ldots$ is the wave plate order) are only applied to

a specific wavelength of the emission spectrum λ_0, and they are determined by the thickness l and the magnitude of the birefringence Δn_0, while for the rest of the spectral components this condition is not satisfied. The measurement of the width of the spectrum or of the coherence degree is usually conducted by interference methods of the decay curve of the contrast visibility V of the interference pattern in the different interferometers by changing the phase delay of the interfering beams. Such studies of the laser radiation require carrying out the experiment and processing huge amounts of data interferometric patterns obtained in interferometers with a large difference between the variable shoulders. For example, to study LED radiation, there arise certain difficulties due to the small value of the coherence length (10 – 20 μm).

Our method of estimating the width of the spectrum is based on the measurement of the polarization contrast K of the polarization-optical scheme: K is the measurement of the ratio of maximum to minimum output intensity of POS ($K = I_{\times\max}/I_{\parallel\min}$ for crossed and parallel polarizer-analyzer axes orientation of POS with half-wave phase plate). The intensity of the radiation transmitted in the polarization-optical system with a parallel orientation of the polarizer-analyzer axes $POS_{\parallel}$, will have a minimum value. Its value is determined by integrating the spectral radiation density $P(\lambda)$ and $G(\lambda)$ over the entire width of the spectrum and will be proportional to the width of the spectrum: $I_{\parallel\min} \sim \Delta\lambda$ (zero output intensity is reached only for the one wavelength λ_0). Accordingly, the maximum intensity for $POS_{\times}$ with a half-wave phase plate will be achieved for a crossed orientation of the polarizer-analyzer axes. All of this can be used as a basis of a simple method of estimating the light width of the spectrum by means of measuring the contrast $K = I_{\times\max}/I_{\parallel\min}$ of POS with a half-wave phase plate.

Consider passing the POS with a half-wave plate by radiation of white light with a rectangular spectral density $P(\lambda)$ with a cutoff wavelength $\lambda_1 = 0.4$ μm, $\lambda_2 = 0.7$ μm and by a narrow-band radiation with a Gaussian spectrum

$$G(\lambda) = e^{-(\lambda-\lambda_0)^2/(2\sigma^2)}$$

with the average wavelength $\lambda_0 = 0.55$ μm and a standard deviation $\sigma = 0.01$ μm (Fig. 2). The density of the radiation spectrum $j_{\times P,G}(\lambda)$ at the output of the polarizer-analyzer with the crossed orientation of the axes $POS_{\times}$ for a rectangular radiation spectrum will be:

$$\begin{cases} j_P = 0, \ \lambda < 0.4 \text{ μm}; \\ j_{\times P\max} = j_0 \sin^2\left(\dfrac{\pi \cdot \Delta n_0 \cdot l}{\lambda}\right), \ 0.4 < \lambda < 0.7 \text{ μm}; \\ j_P = 0, \ \lambda > 0.7 \text{ μm}. \end{cases}$$

For a Gaussian spectrum (Fig. 3):

$$j_{\times G\max} = j_0 \sin^2\left(\frac{\pi \cdot \Delta n_0 \cdot l}{\lambda}\right) \cdot G(\lambda). \qquad (3)$$

The density of the radiation spectrum $j_{\parallel P,G}(\lambda)$ at the output of the parallel orientation of the polarizer-analyzer axes $POS_{\parallel}$ for a rectangular radiation spectrum will be:

$$\begin{cases} j_P = 0, \ \lambda < 0.4 \text{ μm}; \\ j_{\parallel P\min} = j_0 \cos^2\left(\dfrac{\pi \cdot \Delta n_0 \cdot l}{\lambda}\right), 0.4 < \lambda < 0.7 \text{ μm}; \\ j_P = 0, \ \lambda > 0.7 \text{ μm}. \end{cases}$$

For a Gaussian spectrum (Fig. 3):

$$j_{\parallel G\max} = j_0 \cos^2\left(\frac{\pi \cdot \Delta n_0 \cdot l}{\lambda}\right) \cdot G(\lambda). \qquad (4)$$

The output intensity is determined as

$$I_{out} = \int_{\lambda_1}^{\lambda_2} j_{P,G}(\lambda)\, d\lambda. \qquad (5)$$

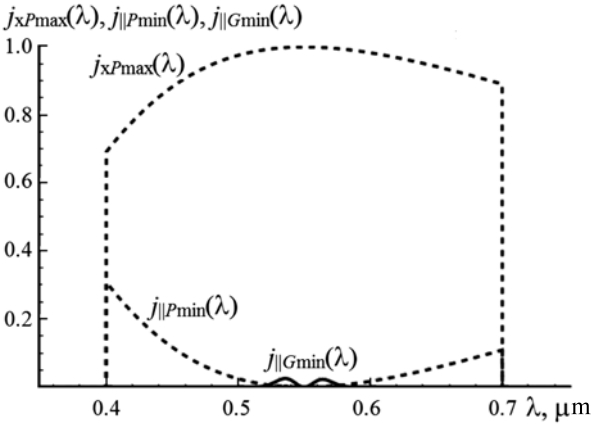

Fig. 3. The density of: the wave with a rectangular spectrum $j_{xP\max}(\lambda)$ after POS_x, the wave with a rectangular spectrum $j_{\parallel P\max}(\lambda)$ after $POS_{\parallel}$, the wave with the Gaussian spectrum $j_{\parallel G\min}(\lambda)$ after POS

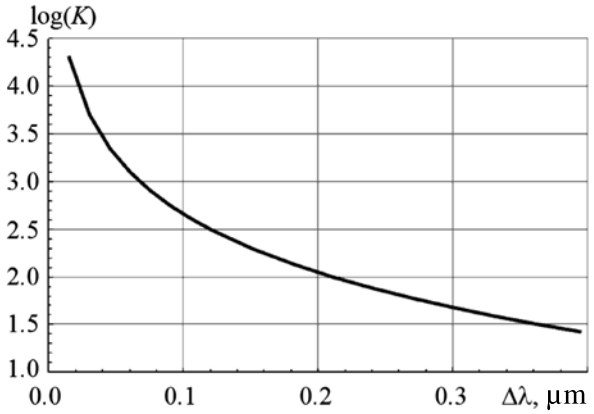

Fig. 4. The logarithm of the contrast intensity POS with zero order half-wave plate from the Gaussian width of the emission spectrum. $\lambda_0 = 0.55$ μm, $\Delta n_0 = 0.04$, $l = 6.88$ μm

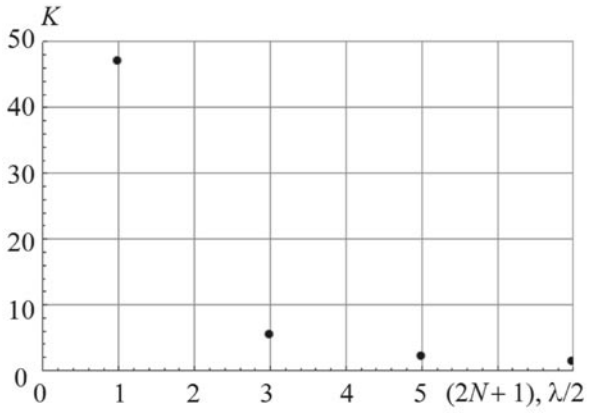

Fig. 5. The dependence of the contrast of the half-wave BF plate from created a path difference of the ordinary and extraordinary waves $\Delta n_0 = 0.04$, the Gaussian spectrum $\lambda_0 = 0.55$ μm, $\sigma = 0.05$ μm

The boundary values of the wavelengths λ_1, λ_2 were determined by the level 0.01 of Gaussian spectrum. The output contrast ratio K of white input light with a rectangular spectrum: $K = 14$, while the contrast of the narrowband modulation in case of Gaussian emission spectrum: $K = 1250$. The modulation depth of white light

$$V = (I_{max} - I_{min})/(I_{max} + I_{min}) = 87\%.$$

Figure 3 shows that the polarization-optical conversion phase modulation into amplitude modulation occurs with the conversion spectrum of the transmitted POS radiation. This is also mentioned in Ref. [4].

The results of theoretical calculations of the logarithm of the contrast intensity POS with zero order half-wave plate from the Gaussian width of the emission spectrum is shown in Fig. 4.

Natural birefringence BF plates, placed in the POS can cause severe transformation of the spectrum of broadband radiation passing POS. Especially clear this phenomenon is for the BF half-wave plates of multiple orders. Zero-order half-wave plates, of the thickness of l_0, creating a path difference $\lambda/2$, a half-wave plate of order N, a thickness of $(2N+1)l_0$, – create a path difference $(2N+1)\lambda/2$. Such plates produce the

a)

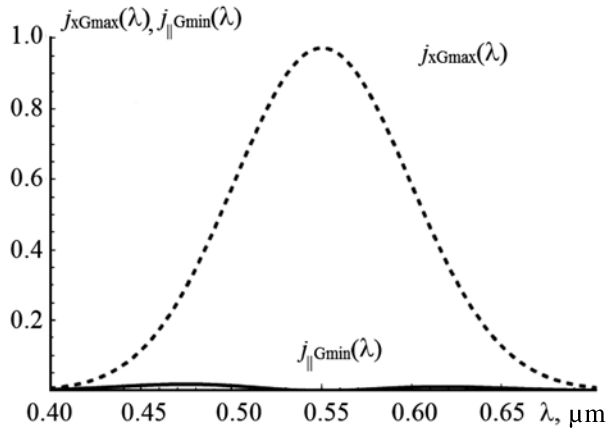

b)

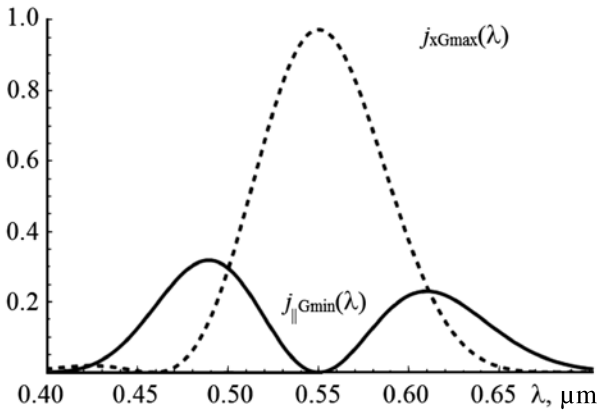

Fig. 6. The spectral density of white Gaussian light spectrum after passing $POS_{x,\|}$ with a half-wave plate: *a* – zero-order ($N = 0$) $\Delta n_0 = 0.04$, thickness $l = 6.88$ μm ($\lambda_0 = 0.55$ μm); *b* – after its passing $POS_{x,\|}$ with a half-wave plate of second order ($N = 2$), $\Delta n_0 = 0.04$, thickness $l = 34.38$ μm

same linear transformation of the input polarization into the orthogonal linearly polarized output radiation. But, the contrast conversion significantly depends on the order of a half-wave plate (Fig. 5). To show this, consider the Gaussian white light emission spectral density

$$G_w(\lambda) = e^{-(\lambda-\lambda_0)^2/(2\sigma^2)}$$

where the average wavelength $\lambda_0 = 0.55$ μm and a standard deviation $\sigma = 0.05$ μm. The spectral density at the output of the POS with a half-wave plate is described by the expression:

$$j^w_{\times,\|G} = \frac{G_w(\lambda)}{2}\left(1 \mp \cos\left(\frac{2\pi \cdot \Delta n_0}{\lambda} l\right)\right). \qquad (6)$$

Natural medium birefringence Δn_0 causes severe aperiodic modulation of the spectrum of white light passing the medium-length BF. Fig. 6 *a*, *b* corresponds to $l = 34.38$ μm ($\Delta n_0 = 0.04$). Note that the intensity of the light which has passed POS, in accordance with (5), is being reduced with increasing order of a half-wave plate. The limit value of this reducing is almost 2. About 50 % is lost due to the spectral modulation.

Estimation of radiation spectrum width as a function of the pump current by polarization-optical method was carried out on the example of semiconductor laser HLDPM10-650-1 ($\lambda = 650$ nm). Fig. 7 shows the width of the spectrum decreasing with the increase of the pump current.

It should be noted that our results would correspond to the polarizer-analyzer and the zero order half-wave plate of a high quality

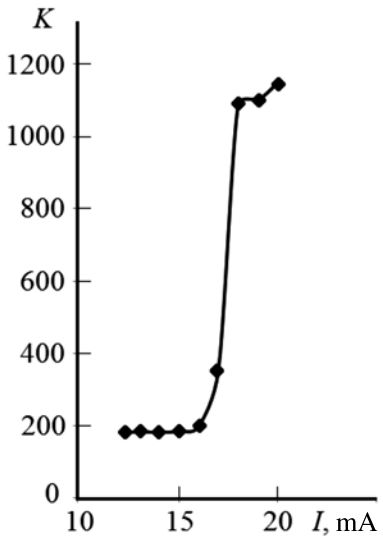

Fig. 7. The dependence of the contrast of the POS with semiconductor laser radiation HLDPM10-650-1 ($\lambda = 650$ nm) in the POS with $\lambda/2$ phase plate on the pump current

only. Usually, a half-wave phase plate, analyzer and polarizer, the quality of workmanship, are far from perfect. These factors can significantly reduce the contrast of the POS with $\lambda/2$ plates. Therefore, the measurement of the width of the emission spectrum of the light source by polarization-optical method with the use of real half-wave plates requires regular calibration by the interference method. The proposed method can be used to quickly estimate the width of the emission spectrum of the light sources.

REFERENCES

1. **Mustel E.R., Parigin V.N.** Modulation and scanning light. Moscow, Nauka, 1970. 96 p. (rus)

2. **Sonin A.S., Vasilevska A.S.** Electro-optic crystals. Moscow, Atomizdat, 1971. 328 p. (rus)

3. **Yariv A., Yuh P.** Optical waves in crystals. Moscow, Mir, 1984. 588 p. (rus)

4. **Berezhnoi A. A., Senichkina O.A.** Wide aperture electro-optic modulator of non-monochromatic light. *Journal of Optical.* 1994. No. 5, pp. 30–34.

СПИСОК ЛИТЕРАТУРЫ

1. **Мустель Е.Р., Парыгин В.Н.** Методы модуляции и сканирования света. М.: Наука, 1970. 296 с.

2. **Сонин А.С., Василевская А.С.** Электрооптические кристаллы. М.: Атомиздат, 1971. 328 с.

3. **Ярив А., Юх П.** Оптические волны в кристаллах. Пер. с англ. Под ред. И.И. Сисакяна. М.: Мир, 1987. 616 с.

4. **Бережной А.А., Сеничкина О.А.** Широкоапертурный электрооптический модулятор немонохроматического света // Оптический журнал. 1994. № 5. С. 30–34.

КНЯЗЬКОВ Анатолий Викторович – *доктор физико-математических наук, доцент кафедры физической электроники Санкт-Петербургского государственного политехнического университета.*

195251, Россия, г. Санкт-Петербург, Политехническая ул., 29.

akniazkov@mail.ru

UDC 57+615.47+621.373.8+535.8

V.E. Privalov [1], *A.Yu. Seteikin* [2], *A.E. Fotiadi* [1]

[1] St. Petersburg State Polytechnical University
29 Politekhnicheskaya St., St. Petersburg, 195251, Russia
[2] Amur State University
21 Ignatievskoe Rd., Blagoveschensk, Amur Oblast, Russia, 675000

SIMULATION OF LASER RADIATION PROPAGATION IN INHOMOGENEOUS MEDIA WITH COMPLEX GEOMETRY

В.Е. Привалов, А.Ю. Сетейкин, А.Э. Фотиади

МОДЕЛИРОВАНИЕ РАСПРОСТРАНЕНИЯ ЛАЗЕРНОГО ИЗЛУЧЕНИЯ В НЕОДНОРОДНЫХ СРЕДАХ СО СЛОЖНОЙ ГЕОМЕТРИЕЙ

A mathematical model has been developed. It makes possible to analyze the process of the three-dimensional propagation of laser radiation in inhomogeneous media with a complex geometry using the proposed modification of the Monte Carlo method. The model also allows to carry out the calculation of the distribution of the absorbed laser energy density in multilayered materials with complex geometry and can be used in solving problems of analysis of thermal fields visualization. Those problems arise in irradiated tissues.

LASER RADIATION, MULTIBIOLOGICAL TISSUE, MONTE CARLO METHOD, INGOMOGENEITY, MULTIPLE SCATTERING.

Построена математическая модель, позволяющая с помощью предложенной модификации метода Монте-Карло анализировать процесс трехмерного распространения лазерного излучения в неоднородных средах со сложной геометрией. Модель позволяет проводить расчет распределения плотности поглощенной энергии лазерного излучения в многослойных материалах сложной геометрии и может использоваться при решении задач анализа визуализации тепловых полей, возникающих в облучаемых тканях.

ЛАЗЕРНОЕ ИЗЛУЧЕНИЕ, МНОГОСЛОЙНАЯ БИОЛОГИЧЕСКАЯ СРЕДА, МЕТОД МОНТЕ-КАРЛО, НЕОДНОРОДНОСТЬ, МНОГОКРАТНОЕ РАССЕЯНИЕ.

I. Introduction

Optical methods of diagnostics of the biological tissues are now becoming more and more widespread. The main advantage of these methods is their non-invasiveness. Using low-intensity laser radiation in the visible and near-IR region as a sounding signal does not have significant damaging effects on the studied biological media. In this context the questions of using mathematical models that would adequately describe the propagation of light in biological tissues, acquire additional relevance. Such models should describe not only the propagation of radiation in terms of the multiple scattering, but they also are supposed to solve the problem of determining the flow of radiation emerging from the medium of the illuminated surface. This is due to the fact that most modern diagnostic methods are based on the detection of reflected and backscattered light.

The theory of radiative transfer is one of the most common theoretical description of light propagation in turbid media. However, the analytical solution of the problem of light propagation in multi-component biological tissues is quite complex, even in simple cases. If we consider heterogeneous tissue or the

tissue of complex geometry, then obtaining an analytical solution is almost impossible. In such cases the required solutions can only be obtained by numerical methods. However, most of the known methods do not allow full determining the changes in the optical and geometrical parameters of the medium due to the presence in it various irregularities. From the point of view of modeling, «visualization» of such objects is to use the most appropriate statistical Monte Carlo (MC) method. It is based on the concept of the radiation propagation in the medium in the form of a flow of model wave packets, each of which being formed by a set of photons of a certain «class» with a given energy and propagation direction. This means that the model package exhibits definite properties such as phase and polarization and is a kind of quasiparticle energy carrier, and is capable of forming an interaction with the medium of similar, but less energetic particles.

The mathematical model of the process of three-dimensional optical radiation propagation in living tissue is described in this paper. It is assumed that the model medium volume is a set of addressable (indexed) volume elements of three-dimensional space. Selecting a possible model for the event package is calculated by its interaction with either the elementary volume or the surface, if the latter is the boundary between the layers with different optical characteristics.

II. Simulation Methods of Laser Radiation Propagation in Complex Tissues

With regard to the problem of light propagation, photons motion in a medium is simulated. In other words, «random path» of photons is simulated on the basis of the laws that determine the radiation distribution in the tissue. The movement trajectory is expressed by the probability density function $p(x)$, which depends on the medium macroscopic optical parameters [1 – 5]. These parameters include the absorption coefficient, the scattering coefficient and the anisotropy parameter. Fresnel law is used to account for the reflection or refraction at the interface of two subdomains. Fig. 1, *a* shows an example of the photon trajectory in the medium. Model is based on the radiative transfer equation.

It is believed that the particles, which are scattered and absorbed, are spherically symmetrical, and therefore the average indicatrix of scattering can be used in our calculations. Using this model and comparison of numerical calculations and experimental results have shown that this approximation satisfactorily describes properties of most biological tissues.

III. The Simulated Experiment Scheme

The action of UV and IR laser radiation on the human epidermis is widely used in medicine. The biological medium is inhomogeneous, and its optical parameters are complex functions of spatial coordinates. However, the medium can be divided into fairly small subregions, within which the optical properties of the medium can be approximately specified. The simplest approximations are those of constant, linear, and quadratic functions. For modeling by Monte Carlo method in three-dimensional space, a very important factor is how to carry out such a division.

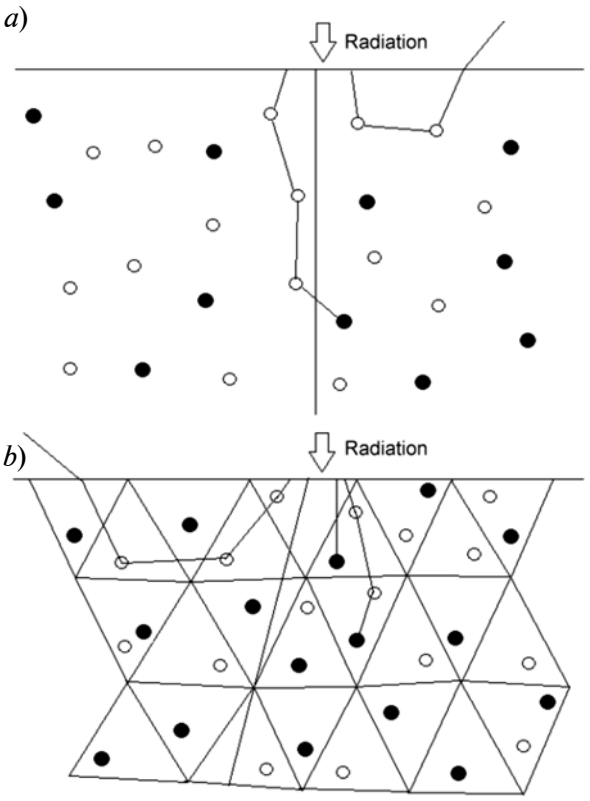

Fig. 1. An example of the photon trajectory in the medium
(The open and shaded circles – respectively absorbing and scattering centers)

The finite-element method provides a convenient set of tools for describing complex media. The geometry of the medium is described in this paper as a finite-element network (Fig. 1, *b*). The use of Monte Carlo method to model radiation propagation with such a specification of the medium has a number of features that are considered in this paper. The simpler the shape of the partitioning elements, the fewer computational resources are required for the calculations. Therefore, the use of tetrahedra as network elements makes it fairly easy to make a transition between elements to go beyond the limits of an element and to find a packet inside a network element. Certain criteria need to be developed to determine the quality of the network. The network by means of which the calculated region is approximated by partitioning into elementary cells is one of the main factors that determine the accuracy and convergence of the numerical solution of the problem.

According to the theory [6], the properties of the network mainly depend on the shape of the partitioning elements. Networks are regarded as high-quality in such an estimate when each element is a regular or close-to-regular tetrahedron. Consequently, a network will be considered low-quality if it contains degenerate or close-to-degenerate elements. With such an approach, the starting geometry of the calculated region can be arbitrary. The case in which the medium contains an internal closed inhomogeneity can be of practical interest. Problems of the propagation of radiation with wavelengths of 400 and 800 nm were therefore chosen as test problems to estimate the accuracy and adequacy of the developed algorithm. Skin has an inhomogeneous structure and accordingly inhomogeneous optical parameters. A medium consisting of several layers: the stratum corneum, the epidermis, and the dermis with a closed inhomogeneity of complex shape – was chosen as the calculation medium. The closed inhomogeneity is modeled in the form of a complex figure bounded by two ellipsoidal surfaces; an additional layer which models air is also introduced.

Fig. 2 shows the geometry of the calculation medium subjected to laser irradiation. The center of the beam is displaced relative to the coordinate origin along the x axis by 0.001 cm and is directed perpendicularly upwards, and its radius is 0.001 cm. The absorption coefficient is fairly high for radiation with wavelength of 400 nm; therefore, it must be strongly absorbed, without penetrating deep inside the medium.

When a photon is deflected by angle θ, it is assumed that it is deflected axially symmetrically relative to the initial propagation direction at azimuthal angle ψ, which is

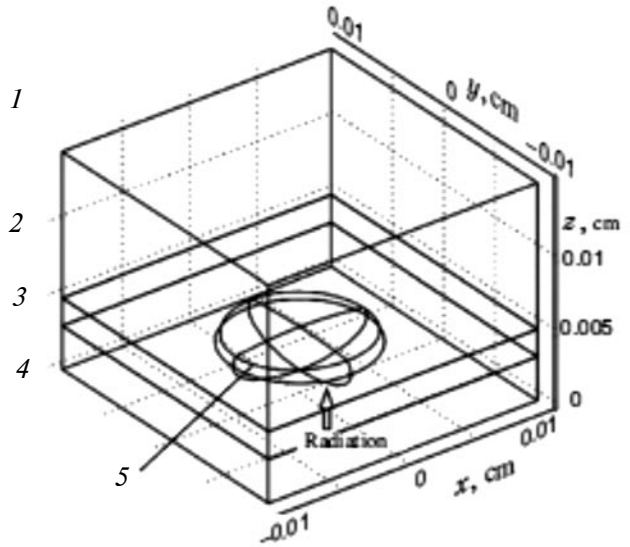

Fig. 2. Geometry of the medium used for calculations. Several layers of medium: *1* – stratum corneum, *2* – epidermis, *3* – dermis with a closed ingomogeneity (*5*), *4* – air

uniformly distributed within the interval [0, 2π]. Asymmetric scattering is not considered in this paper. Probability-density function p is constant and equals $1/2\pi$ [7].

After N photons are launched, we have a certain choice of statistical weights X_1, X_2, ..., X_n for each network node, obtained by the medium in its neighborhood. Statistical processing is carried out for these quantities. The most important ones are the mathematical expectation and the selective dispersion.

Let the weight of all N photons correspond to a certain energy q. Then, the mathematical expectation of the resulting weight by a network node is

$$\overline{X} = (1 / n)\sum_{i=1}^{n} X_i, \qquad (1)$$

where n is the number of absorptions in the neighborhood of the node of interest, and X_i is the statistical weight absorbed in the neighborhood of the i-th node of interest.

The mathematical expectation can be used to compute the energy density as follows:

$$Q = (\overline{X}q) / V, \qquad (2)$$

where V is the volume of the neighborhood of the node of interest, and q is the energy that corresponds to the total statistical weight of N packets of photons.

The method called the implicit photon-capture technique is often used to take into account the absorption [8, 9]. The motion of a packet of photons, rather than of each photon separately, is considered in the modelling. A packet of photons models the motion of a set of photons along similar trajectories. Only some of the photons from a packet are absorbed when they interact with the medium, while the rest continue to move.

A cross-section in the xz plane was chosen for a graphical representation of radiation propagation in the medium. Fig. 3 shows the density distribution of the absorbed energy in this plane for 400-nm radiation.

For 800-nm radiation, the absorption coefficient is significantly less than the scattering coefficient, and a strongly scattering medium is modelled. Consequently, its penetration depth must be greater than in case when UV radiation is used. One more layer is therefore added to the region of calculation – the dermis, 0.05 cm thick. Fig. 4 shows the density distribution of the absorbed energy in the xz plane for radiation with wavelength 800 nm.

The character of the interaction of laser radiation with biological tissue depends on the absorption coefficient for this wavelength. Absorption predominates in the UV region; therefore, the contribution of scattering is

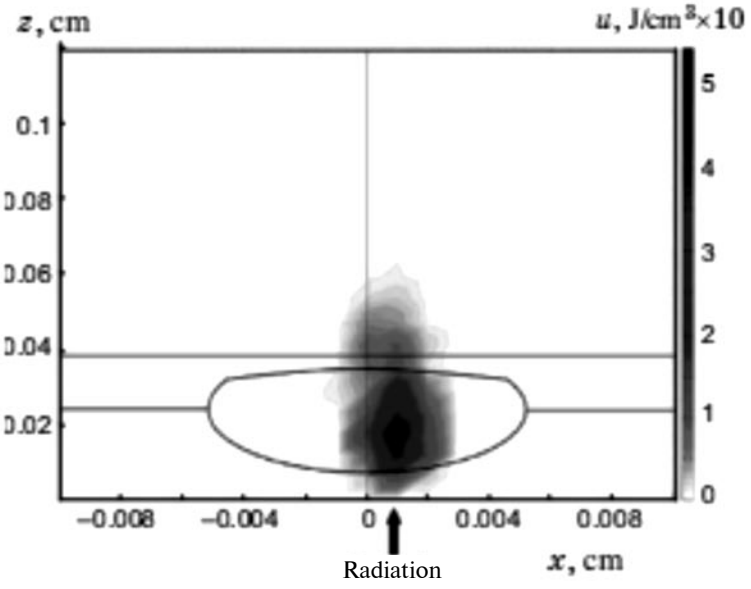

Fig. 3. Density distribution of absorbed energy u in the cross-sectional xz plane for a wavelength of 400 nm

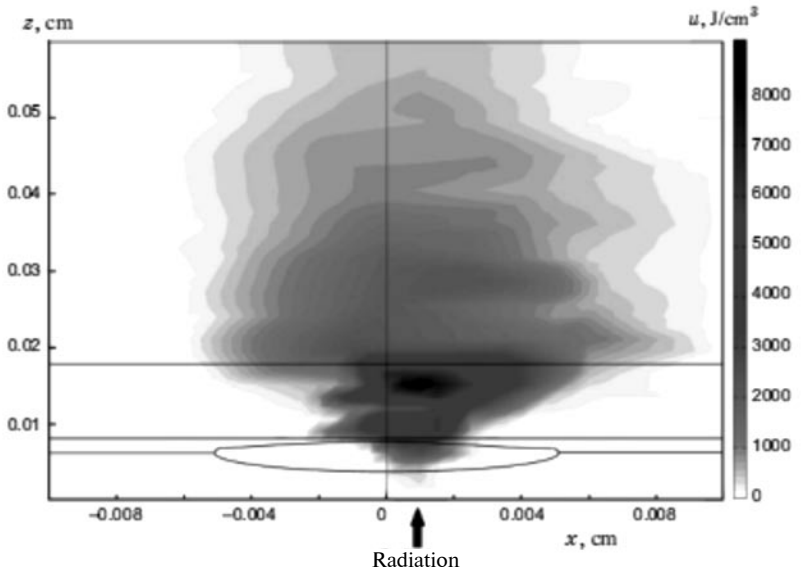

Fig. 4. Density distribution of absorbed energy u in the cross-sectional xz plane for a wavelength of 800 nm

fairly small, and the radiation penetration into the medium is just as shallow. For radiation from 600 to 1500 nm – the so-called terahertz window – in the event that scattering predominates over absorption, and the radiation-penetration depth is significantly greater than that for the UV region.

The laser radiation has the same power and energy in both cases. The penetration depth of UV radiation is slight. Therefore, a great part of the energy will be absorbed in a small volume near skin surface for 400-nm radiation, and the absorbed energy density is significantly greater than in the case of the wavelength of 800 nm [10].

IV. Conclusion

The paper concerns the propagation of optical radiation of different spectral regions in biological tissues. Monte Carlo method has been used in the study. We can simulate all the aspects of biological medium geometry using as the computational domain a grid of tetrahedron elements for 3D modeling or triangles in case of two dimensions. The modeling results give a visual representation of the absorbed energy density distribution in a biological medium. In case of one million packets of photons computational error does not exceed 1 %.

The proposed method is very flexible and well adaptable to the environments of different geometry. It allows obtaining two- and three-dimensional information on the distribution of light in tissue. The algorithms based on MC method can be applied both to diagnosing structural changes in the biological tissue of any closed geometry, and to calculating the temperature field and the boundaries of degradation during laser therapy.

REFERENCES

1. **Jacques S., Wang L.** Monte Carlo modeling of light transport in tissue, In: Welch A.J., Martin J.C., Van Gemert. Optical-thermal response of laser-irradiated tissue. New York: Plenum Press, 1995, Vol. 12, pp.73–100.

2. **Tuchin V.** (ed.). Handbook of optical biomedical diagnostics, Vol. PM107. Washington: SPIE Press, 2002.

3. **Ishimaru A.** Wave propagation and scattering in random media, New York: Academic Press, 1978.

4. **Kumar G., Schmitt J.** Micro-optical properties of tissue. *Advances in Laser and Light Spectroscopy to Diagnose Cancer and Other Diseases III*: *Optical Biopsy*. 1996. Vol. 2679, pp. 106–116.

5. **Doronin A., Meglinski I.** Peer-to-peer Monte Carlo simulation of photon migration in topical applications of biomedical optics. *J. Biomed. Opt.*

2012. Vol. 17, Iss. 9, 090504.

6. **Meglinski I., Doronin A.V.** Monte Carlo modeling for the needs of biophotonics and biomedical optics. Advanced Biophotonics: tissue optical sectioning, Edited by V.V. Tuchin, R.K. Wang, Taylor & Francis, Chapter, 2012.

7. **Wang L.H., Jacques S.L., Zheng L.Q.** MCML: Monte Carlo modeling of photon transport in multylayered tissues. *Comput. Methods Programs Biomed*. 1995. Vol. 47, pp. 131–146.

8. **Wang L.H., Jacques S.L., and Zheng L.Q.** CONV: Convolution for responses to a finite diameter photon beam incident on multilayered tissues. *Comput. Methods Programs Biomed*. 1997. Vol. 54, pp. 141–150.

9. **Krasnikov I., Seteikin A., Drakaki E., Makropoulou M.** Thermal distribution in biological tissue at laser induced fluorescence and photodynamic therapy. *Proc. SPIE* 8337, 2011, 83370E.

10. **Pavlov M.S., Krasnikov I.V., Seteikin A.Yu.** Monte Carlo modeling of optical-radiation propagation in biological media with closed internal inhomogeneities. *Journal of Optical Technology*. 2010. Vol. 77, Iss. 10, pp. 602–605.

СПИСОК ЛИТЕРАТУРЫ

1. **Jacques S., Wang L.** Monte Carlo modeling of light transport in tissue, In: Welch A.J., Martin J.C., Van Gemert. Optical-thermal response of laser-irradiated tissue. New York: Plenum Press, 1995, Vol. 12, pp.73–100.

2. **Tuchin V.** (ed.). Handbook of optical biomedical diagnostics, Vol. PM107. Washington: SPIE Press, 2002.

3. **Ishimaru A.** Wave propagation and scattering in random media, New York: Academic Press, 1978.

4. **Kumar G., Schmitt J.** Micro-optical properties of tissue. *Advances in Laser and Light Spectroscopy to Diagnose Cancer and Other Diseases III*: *Optical Biopsy*. 1996. Vol. 2679, pp. 106–116.

5. **Doronin A., Meglinski I.** Peer-to-peer Monte Carlo simulation of photon migration in topical applications of biomedical optics. *J. Biomed. Opt.* 2012. Vol. 17, Iss. 9, 090504.

6. **Meglinski I., Doronin A.V.** Monte Carlo modeling for the needs of biophotonics and biomedical optics. Advanced Biophotonics: tissue optical sectioning, Edited by V.V. Tuchin, R.K. Wang, Taylor & Francis, Chapter, 2012.

7. **Wang L.H., Jacques S.L., Zheng L.Q.** MCML: Monte Carlo modeling of photon transport in multylayered tissues. *Comput. Methods Programs Biomed*. 1995. Vol. 47, pp. 131–146.

8. **Wang L.H., Jacques S.L., and Zheng L.Q.** CONV: Convolution for responses to a finite diameter photon beam incident on multilayered tissues. *Comput. Methods Programs Biomed*. 1997. Vol. 54, pp. 141–150.

9. **Krasnikov I., Seteikin A., Drakaki E., Makropoulou M.** Thermal distribution in biological tissue at laser induced fluorescence and photodynamic therapy. *Proc. SPIE* 8337, 2011, 83370E.

10. **Павлов М.С., Красников И.В., Сетейкин А.Ю.** Моделирование распространения оптического излучения методом Монте-Карло в биологических средах с замкнутыми внутренними неоднородностями// Оптический журнал. 2010. Т. 77. № 10. С. 15–19.

ПРИВАЛОВ Вадим Евгеньевич – *доктор физико-математических наук, профессор кафедры экспериментальной физики Санкт-Петербургского государственного политехнического университета.*

195251, Россия, Санкт-Петербург, Политехническая ул., 29

vaevpriv@yandex.ru

СЕТЕЙКИН Алексей Юрьевич – *кандидат физико-математических наук, доцент кафедры экспериментальной и теоретической физики Амурского государственного университета.*

675027, Россия, Благовещенск, Игнатьевское шоссе, 21

seteikin@mail.ru

ФОТИАДИ Александр Эпаминондович – *доктор физико-математических наук, профессор, заведующий кафедрой физической электроники Санкт-Петербургского государственного политехнического университета.*

195251, Россия, Санкт-Петербург, Политехническая ул., 29

fotiadi@rphf.spbstu.ru

THEORETICAL PHYSICS

UDC 536.421

A.N. Ipatov, V.K. Ivanov, R.G. Polozkov

St. Petersburg State Polytechnical University,
29 Politekhnicheskaya St., St. Petersburg, 195251, Russia

ON STABILITY OF NANOSCALE ELECTRON-POSITRON DROPLETS

А.Н. Ипатов, В.К. Иванов, Р.Г. Полозков

О СТАБИЛЬНОСТИ НАНОРАЗМЕРНЫХ ЭЛЕКТРОН-ПОЗИТРОННЫХ КАПЕЛЬ

This paper presents the results of the total energy calculation for electroneutral electron-positron clusters with closed shells. The calculations were performed within the Random Phase Approximation with Exchange to take into account many-particle correlations that allowed us to reduce the energy per one electron-positron pair below the energy per one pair of dipositronium molecule. The most stable electron-positron clusters are found for the cluster sizes in the interval from 20 to 40 pairs.

CLUSTER, ELECTRON, POSITRON, NANOSCALE DROPLET, RPAE.

В статье представлены результаты вычислений полных энергий электронейтральных электрон-позитронных кластеров с заполненными оболочками. Для учета многочастичных корреляций вычисления проводились в рамках приближения случайных фаз с обменом, которое позволило получить энергию на одну электрон-позитронную пару меньше той же энергии для молекулы дипозитрония. Обнаружено, что наиболее стабильными являются кластеры, содержащие число пар в интервале от 20 до 40.

КЛАСТЕР, ЭЛЕКТРОН, ПОЗИТРОН, НАНОРАЗМЕРНАЯ КАПЛЯ, ПСФО.

I. Introduction

Investigations of a bound state of matter and antimatter, in particular of electron-positron systems, have a long story. Before the experimental observation of the atom-like bound state of an electron and positron in 1951 [1], the probability of formation of the dipositronium molecule – the bound state of two positroniums – was predicted theoretically in 1946 [2]. Then, in 1947, the ground state energy of dipositronium molecule was calculated by solving the four-body Shrodinger equation for two electrons and two positrons [3]. Later on, a set of computations of coupling energy of dipositronium was performed and the lifetime of that system was estimated as well [4 – 6]. Finally, the dipositronium molecule was found experimentally in 2005 [7] that proved the existence of bound state of two electron-positron pairs.

The problem of possible formation of compact bound systems of more than two electron-positron pairs is still open. Recently, it was shown that formation of an electron-positron liquid is possible in particular interval of particle densities and temperatures due to intense Coulomb interaction that correlates the motion of electrons and positrons [8]. So far, one could have expected a formation of electron-

positron droplets similar to the electron-hole droplets in semiconductors [9]. The number of particles in the droplets theoretically can vary from two electron-positron pairs to infinity. In the similar way, as it happens in positronium atom, the motion of electrons and positrons in a finite-size droplets must be quantized. Electrons and positrons move in the self-consistent field formed by both subsystems with the whole system being electrically neutral. It was proposed that the droplets formed by mutual interaction between electron and positron subsystems should have a lot of similarities with alkali metal clusters, where their valence electrons are completely delocalized through the whole volume. Based on this proposal, a new theoretical model for electron-positron droplets was developed [10 – 12]. In particular, in the papers [10 – 12] the electron-positron droplets containing up to 100 particle pairs have been studied. Calculations of internal structure of these systems were performed both within Hartree – Fock (HF) approximation and the Local Density Approximation (LDA). It was found that similarly to metallic clusters [13], the minimal energies per one particle correspond to the systems with «magic» numbers of electron-positron pairs that form closed shells.

It was shown in [10 – 12] that the optimal density distribution of both subsystems corresponding to an absolute minimum of the total energy of electron-positron droplet must satisfy the local electroneutrality condition that provides the local equality of positive and negative charge densities through the whole droplet volume. The similar situation takes place with alkali metal clusters within the optimized jellium model [14].

The previous calculations [10 – 12] show that the energies per one pair resulting from the latter calculations are significantly higher than the energy per pair in dipositronium molecule [4 – 6]. However, one should note that HF and LDA approximations used in these calculations do not take into account the dynamical part of interparticle correlations, in particular the polarization interaction. Moreover, the energies of electron-positron clusters obtained within the density functional theory framework for a part of many-particle correlations [10, 11] are visibly lower than corresponding Hartree-Fock energies [12].

The goal of present work is to study the role of correlation effects in possible formation of stable electron-positron clusters. The correlation corrections to the Hartree-Fock coupling energies of several most stable clusters with «magic» numbers of pairs were calculated using different approximations. The results of preliminary calculations were already presented in [15]. The present paper is devoted to more detailed description of obtained results.

The atomic system of units is used throughout the paper: $\hbar = |e| = m_e = 1$.

II. Theoretical Approach

Let's consider an electrically neutral system of fermions interacting via Coulomb forces. For example, it can be an electron-positron droplet which consists of the same number N of positive and negative charged fermions with equal masses $m_e = m_p = m = 1$. The ground state wave function of the system described by total Hamiltonian $\hat{H}_0$ with pair interaction potential

$$V(\mathbf{r}, \mathbf{r}') = \frac{1}{|\mathbf{r} - \mathbf{r}'|},$$

$$\hat{H}_0 = -\sum_{i=1}^{N} \frac{\Delta_i}{2} - \sum_{a=1}^{N} \frac{\Delta_a}{2} + \sum_{i \neq j} V(\mathbf{r}_i^{(e)} - \mathbf{r}_j^{(e)}) + \\ + \sum_{a \neq b} V(\mathbf{r}_a^{(p)} - \mathbf{r}_b^{(p)}) + \sum_{i,a} V(\mathbf{r}_i^{(e)} - \mathbf{r}_a^{(p)}), \quad (1)$$

can be represented as a product of electron and positron components

$$\Xi(\mathbf{r}_1^{(e)}, \ldots, \mathbf{r}_N^{(e)}, \mathbf{r}_1^{(p)}, \ldots, \mathbf{r}_N^{(p)}) = \\ = \Psi^{(e)}(\mathbf{r}_1^{(e)}, \ldots, \mathbf{r}_N^{(e)}) \Phi^{(p)}(\mathbf{r}_1^{(p)}, \ldots, \mathbf{r}_N^{(p)}). \quad (2)$$

In this case, the following normalization condition is fulfilled:

$$\left\langle \Psi^{(e)} \middle| \Psi^{(e)} \right\rangle = \left\langle \Phi^{(p)} \middle| \Phi^{(p)} \right\rangle = 1.$$

Here and more throughout the text, indexes i, j correspond to occupied and m, n – non-occupied (virtual) one-particle states, respectively; $\mathbf{r}^{(e)}$, $\mathbf{r}^{(p)}$ – electron- and positron-position vectors.

Within Hartree-Fock approximation, the total electron and positron wave functions are presented by Slater determinants:

$$\Psi^{(e)} = \frac{1}{\sqrt{N!}} \sum_P (-1)^P \varphi_1(\mathbf{r}_1^{(e)}) \times \quad (3)$$

$$\times \varphi_2(\mathbf{r}_2^{(e)}) \cdot \ldots \cdot \varphi_N(\mathbf{r}_N^{(e)});$$
$$\Phi^{(p)} = \frac{1}{\sqrt{N!}} \sum_P (-1)^P \phi_1(\mathbf{r}_1^{(p)}) \times \quad (3)$$
$$\times \phi_2(\mathbf{r}_2^{(p)}) \cdot \ldots \cdot \phi_N(\mathbf{r}_N^{(p)}),$$

composed of one-particle wave functions obtained by solving the system of Hartree-Fock equations:

$$-\frac{\Delta_i}{2}\varphi_i(\mathbf{r}) + (U_{\text{H}}^{(e)}(\mathbf{r}) - U_{\text{H}}^{(p)}(\mathbf{r}) + U_{ex}^{(e)}(\mathbf{r}))\varphi_i(\mathbf{r}) = \varepsilon_i^{(e)}\varphi_i(\mathbf{r});$$
$$-\frac{\Delta_a}{2}\phi_a(\mathbf{r}) + (U_{\text{H}}^{(p)}(\mathbf{r}) - U_{\text{H}}^{(e)}(\mathbf{r}) + U_{\text{ex}}^{(p)}(\mathbf{r}))\phi_a(\mathbf{r}) = \varepsilon_a^{(p)}\phi_a(\mathbf{r}). \quad (4)$$

Here $U_{\text{H}}^{(e)}$ and $U_{\text{H}}^{(p)}$ are the corresponding Hartree's potentials defined as

$$U_{\text{H}}^{(e)}(\mathbf{r}) = \int \frac{\rho^{(e)}(\mathbf{r}')}{|\mathbf{r}-\mathbf{r}'|} d\mathbf{r}';$$
$$U_{\text{H}}^{(p)}(\mathbf{r}) = \int \frac{\rho^{(p)}(\mathbf{r}')}{|\mathbf{r}-\mathbf{r}'|} d\mathbf{r}', \quad (5)$$

where

$$\rho^{(e)}(\mathbf{r}) = 2\sum_i^{occ} \varphi_i^*(\mathbf{r})\,\varphi_i(\mathbf{r});$$
$$\rho^{(p)}(\mathbf{r}) = 2\sum_a^{occ} \phi_i^*(\mathbf{r})\,\phi_i(\mathbf{r}) \quad (6)$$

are the densities of electron and positron subsystems. The non-local exchange potentials $U_{ex}^{(e)}$, $U_{ex}^{(p)}$ in (4) can be written in the following form:

$$U_{ex}^{(e)}(\mathbf{r})\varphi_i(\mathbf{r}) = -\sum_j^{occ} \int \frac{\varphi_j^*(\mathbf{r}')\varphi_i(\mathbf{r}')}{|\mathbf{r}-\mathbf{r}'|} d\mathbf{r}'\,\varphi_j(\mathbf{r});$$
$$U_{ex}^{(p)}(\mathbf{r})\phi_a(\mathbf{r}) = -\sum_b^{occ} \int \frac{\phi_b^*(\mathbf{r}')\phi_a(\mathbf{r}')}{|\mathbf{r}-\mathbf{r}'|} d\mathbf{r}'\,\phi_b(\mathbf{r}). \quad (7)$$

Note, that in the case of central symmetry one-particle wave function can be composed as a product of radial, angular and spin components:

$$\varphi(\mathbf{r},\sigma) = \frac{P_{nl}(r)}{r} Y_{lm}(\theta,\varphi)\chi_\mu(\sigma) \quad (8)$$

and characterized by well-known quantum number set n, l, m, μ [16].

It was shown [15, 17] that in the case of equal masses of interacting particles $m_e = m_p = m$ the minimal value of the total energy corresponds to the equality of local Hartree potentials

$$U_{\text{H}}^{(e)}(\mathbf{r}) = U_{\text{H}}^{(p)}(\mathbf{r}) \quad (9)$$

and the local electrical neutrality of the system

$$\rho^{(e)}(\mathbf{r}) - \rho^{(p)}(\mathbf{r}) = 0. \quad (10)$$

So, Hartree-Fock equations are transformed to the following form [14, 15]:

$$-\frac{\nabla_i^2}{2}\varphi_i(\mathbf{r}) - \sum_j^{occ} \int \frac{\varphi_j^*(\mathbf{r}')\varphi_i(\mathbf{r}')}{|\mathbf{r}-\mathbf{r}'|} d\mathbf{r}'\,\varphi_j(\mathbf{r}) = \varepsilon_i\varphi_i(\mathbf{r}). \quad (11)$$

and the interaction between the particles is only presented by the exchange term (7). Note that the equations (11) are equally suitable for both electron and positron subsystems.

The total energy of the droplet E_{tot} consisting of N electron-positron pairs is determined by the total energies of electron E_e and positron E_p subsystems and the energy of interaction between them E_{e-p}. It can be shown that within the HF approach, the total energy of the droplet is represented by the following expression [12]:

$$E_{tot} = 2\left(\sum_{i=1}^{occ} \varepsilon_i + E_{exch}\right). \quad (12)$$

Here, the values ε_i are one-particle energies of occupied states which are the eigenvalues of HF equation system (11), E_{exch} is the exchange interaction energy

$$E_{exch} = \frac{1}{2}\sum_{i,j=1}^{occ} \langle ij|V|ji\rangle, \quad (13)$$

where $\langle\alpha\beta|V|\gamma\delta\rangle$ is the Coulomb matrix element:

$$\langle\alpha\beta|V|\gamma\delta\rangle = \delta_{\sigma_\alpha\sigma_\gamma}\delta_{\sigma_\beta\sigma_\delta} \times \iint d\mathbf{r}d\mathbf{r}' \frac{\varphi_\alpha^*(\mathbf{r})\varphi_\beta^*(\mathbf{r}')\varphi_\gamma(\mathbf{r})\varphi_\delta(\mathbf{r}')}{|\mathbf{r}-\mathbf{r}'|}. \quad (14)$$

The indexes $\sigma_\alpha, \sigma_\beta, \sigma_\gamma, \sigma_\delta$ correspond to the spin projections of the one-particle states.

Using the HF approximation, one should understand that this approximation underestimates the cluster total energy as soon as it

Table 1

Total energies per pair for electron-positron clusters with different numbers N of pairs obtained within the HF [12] and LDA [11] approaches

N	$E_{tot}^{(HF)}/N$	$E_{tot}^{(LDA)}/N$
	eV	
2	−2.96	−5.12
8	−2.76	−5.44
18	−2.70	−5.56
20	−2.68	−5.60
34	−2.68	−5.64
40	−2.64	−5.72
58	−2.66	−5.70
92	−2.62	−5.60
106	−2.60	−5.58

neglects the many-electron correlations, in particular the polarization interaction [18]. Indeed, the calculations performed within the LDA framework, that effectively takes into account the static part of many-particle correlations [11], lead to essential reduction of the total energy in comparison with the HF results [12]. The corresponding comparison is shown in Table 1.

On the other hand, starting from the HF approach, one can take into account the polarization interaction using Möller − Plesset approximation (MP2) [19], i. e. the second order of the perturbation theory. The corresponding correction of the total energy can be composed of three components

$$\Delta E^{(MP2)} = E_{e-e}^{(MP2)} + E_{p-p}^{(MP2)} + E_{e-p}^{(MP2)} \qquad (15)$$

where

$$E_{e-e}^{(MP2)} = E_{p-p}^{(MP2)} = \\ = -\frac{1}{2}\sum_{ij,mn}\left(\frac{2\langle ij|V|mn\rangle\langle mn|V|ij\rangle}{\varepsilon_m + \varepsilon_n - \varepsilon_i - \varepsilon_j} - \right. \\ \left. - \frac{\langle ij|V|nm\rangle\langle mn|V|ij\rangle}{\varepsilon_m + \varepsilon_n - \varepsilon_i - \varepsilon_j}\right); \qquad (16)$$

$$E_{e-p}^{(MP2)} = -\sum_{ij,mn}\frac{2\langle ij|V|mn\rangle\langle mn|V|ij\rangle}{\varepsilon_m + \varepsilon_n - \varepsilon_i - \varepsilon_j}. \qquad (17)$$

The factor «2» in the formulae (16), (17) results from summation over spin variables in matrix elements (14). Substituting (16), (17) into (15) one obtains the correction to the total energy of the droplet within MP2 approximation:

$$\Delta E^{(MP2)} = -\sum_{ij,mn}\left(\frac{4\langle ij|V|mn\rangle\langle mn|V|ij\rangle}{\varepsilon_m + \varepsilon_n - \varepsilon_i - \varepsilon_j} - \right. \\ \left. - \frac{\langle ij|V|nm\rangle\langle mn|V|ij\rangle}{\varepsilon_m + \varepsilon_n - \varepsilon_i - \varepsilon_j}\right). \qquad (18)$$

The results of the calculations of the total energy per electron-positron pair

Table 2

The total energies per pair for electron-positron clusters with different number N of pairs obtained within the HF approach [12], and with accounting for the correlations within Möller-Plesset approximation and RPAE (present work)

N	$E_{tot}^{(HF)}/N$	$(E_{tot}^{(HF)} + \Delta E^{(MP2)})/N$	$(E_{tot}^{(HF)} + \Delta E^{(RPAE)})/N$
	eV		
2	−2.96	−4.63	−6.20
8	−2.76	−5.06	−7.22
18	−2.70	−5.26	−7.50
20	−2.68	−5.36	−7.68
34	−2.68	−5.38	−7.62
40	−2.64	−5.50	−7.94
58	−2.66	−5.38	−7.48
92	−2.62	−5.40	−7.13
106	−2.60	−5.42	−7.14

$(E_{tot}^{(HF)} + \Delta E^{(MP2)}) / N$ for the series of clusters with closed shells are presented in Table 2. Accounting for polarization interaction within the MP2 decreases the energies per pair and brings the obtained values closer to the LDA results.

However, as it was shown earlier in [15, 17], the Möller – Plesset approximation is still not able to include all correlation effects in the strongly interacting many-body systems. For the proper outline, it is necessary to consider the higher orders of perturbation theory. For this purpose, we use the Random Phase Approximation with Exchange (RPAE) which takes into account so-called «ring» Feynman diagrams of infinite order [18].

The correlated excited state can be represented within the RPAE as

$$\left|\Phi_\nu\right\rangle = \sum_{im} (X_{im}^\nu \hat{a}_m^+ \hat{a}_i - Y_{ia}^\nu \hat{a}_i^+ \hat{a}_m) \left|\Phi_0\right\rangle, \quad (19)$$

where $\Phi_0 = \frac{1}{\sqrt{N!}} \mathrm{Det}\{\varphi_i(\mathbf{r}_j)\}$ is the ground state wave function within the HF approximation, $\hat{a}_\alpha^+$ и $\hat{a}_\beta$ are one-particle Fermi creation and annihilation operators. The coefficients X_{mi}^ν and Y_{mi}^ν called the «time forward» and «time reverse» amplitudes, respectively, are responsible for contributing the determinants $\hat{a}_m^+ \hat{a}_i \left|0\right\rangle$ and $\hat{a}_i^+ \hat{a}_m \left|0\right\rangle$ into the state (19). Note, that due to the local electrical neutrality of an electron-positron droplet [10 – 12], the expression (19) equally describes both the wave functions of electron and positron subsystems. It was shown [17] that the components of $\mathbf{X}^\nu$ and $\mathbf{Y}^\nu$ vectors can be found by solving the following RPAE matrix equation:

$$\begin{pmatrix} \mathbf{A}^{(e)} & \mathbf{B}^{(e)} & \mathbf{C} & \mathbf{D} \\ \mathbf{B}^{(e)*} & \mathbf{A}^{(e)*} & \mathbf{D}^* & \mathbf{C}^* \\ \mathbf{C} & \mathbf{D} & \mathbf{A}^{(p)} & \mathbf{B}^{(p)} \\ \mathbf{D}^* & \mathbf{C}^* & \mathbf{B}^{(p)*} & \mathbf{A}^{(p)*} \end{pmatrix} \begin{pmatrix} \mathbf{X}^{(e)} \\ \mathbf{Y}^{(e)} \\ \mathbf{X}^{(p)} \\ \mathbf{Y}^{(p)} \end{pmatrix} = \Omega \begin{pmatrix} \mathbf{X}^{(e)} \\ -\mathbf{Y}^{(e)} \\ \mathbf{X}^{(p)} \\ -\mathbf{Y}^{(p)} \end{pmatrix}, \quad (20)$$

which has $2(N_{eh} + N_{ph})$ independent solutions, where $N_{eh} = N_{ph}$ is the number of one-particle electron-hole and positron-hole pairs. The elements of Hermitian matrixes **A** and **B**, including electron-electron (and positron-positron) interaction only, are described as

$$\begin{aligned} A_{im,jn}^{(e)} &= \delta_{ij}\delta_{mn}\omega_{im}^{(e)} + \left\langle in \right|\left| mj \right\rangle; \\ B_{im,jn}^{(e)} &= \left\langle ij \right|\left| mn \right\rangle; \\ A_{as,bt}^{(p)} &= \delta_{ab}\delta_{st}\omega_{as}^{(p)} + \left\langle at \right|\left| sb \right\rangle; \\ B_{as,bt}^{(p)} &= \left\langle ab \right|\left| st \right\rangle, \end{aligned} \quad (21)$$

where indexes *i*, *j*, *a*, *b* correspond to the occupied and *m*, *n*, *s*, *t* – to virtual one-particle states.

Each matrix element $\left\langle \alpha\beta \right|\left| \gamma\delta \right\rangle = 2\left\langle \alpha\beta \right| V \left| \gamma\delta \right\rangle - \left\langle \alpha\beta \right| V \left| \delta\gamma \right\rangle$ consists of «direct» and «exchange» parts defined by (14), and the factor «2» in the direct part arises from summation over spin projections.

The matrixes **C** and **D** correspond to the electron-positron interaction and therefore include direct interaction part only:

$$\begin{aligned} C_{im,as} &= -2\left\langle is \right| V \left| ma \right\rangle, \\ D_{im,as} &= -2\left\langle ia \right| V \left| ms \right\rangle. \end{aligned} \quad (22)$$

In case when one of the subsystems (for example, positrons) is «frozen» with respect to small deviation, i. e. $\delta\rho^{(p)}(\mathbf{r}) = 0$, the equation (20) reduces to the form of standard RPAE equation [18]:

$$\begin{pmatrix} \mathbf{A} & \mathbf{B} \\ \mathbf{B}^* & \mathbf{A}^* \end{pmatrix} \begin{pmatrix} \mathbf{X} \\ \mathbf{Y} \end{pmatrix} = \Omega \begin{pmatrix} \mathbf{X} \\ -\mathbf{Y} \end{pmatrix}. \quad (23)$$

The elements of the eigenvectors of matrix of equation (20) satisfy the following orthonormality conditions:

$$\begin{aligned} \sum_{mi} (X_{mi}^\nu X_{mi}^\mu - Y_{mi}^\mu Y_{mi}^\mu) &= \delta_{\nu\mu}; \\ \sum_{\nu} (X_{mi}^{\nu\,*} X_{nj}^\nu - Y_{mi}^{\nu\,*} Y_{nj}^\nu) &= \delta_{mn}\delta_{ij}, \end{aligned} \quad (24)$$

where index ν corresponds to an eigenvector with eigenvalue Ω_ν that equals to the transition frequency between the ground state and ν-th excited one.

Due to the symmetry of equation (20), there are two solutions with eigenvalues Ω_ν and $-\Omega_\nu$ and eigenvectors $(\mathbf{Y}_\nu^{(e)}, \mathbf{X}_\nu^{(e)}, \mathbf{Y}_\nu^{(p)}, \mathbf{X}_\nu^{(p)})$ and $(\mathbf{X}_\nu^{(e)}, \mathbf{Y}_\nu^{(e)}, \mathbf{X}_\nu^{(p)}, \mathbf{Y}_\nu^{(p)})$, respectively. This means that one should consider only $(N_{eh} + N_{ph})$ solutions with positive eigenvalues.

Besides, if the masses of particles are equal ($m_e = m_p = m$), then, due to the symmetry between two subsystems

$$\begin{aligned} \mathbf{A}^{(e)} &= \mathbf{A}^{(p)}, \\ \mathbf{B}^{(e)} &= \mathbf{B}^{(p)}, \end{aligned} \tag{25}$$

one can distinguish two following types of the solutions of equation (20): the symmetric modes, that match the conditions $\mathbf{X}^{(e)} = \mathbf{X}^{(p)}$, $\mathbf{Y}^{(e)} = \mathbf{Y}^{(p)}$, and the antisymmetric ones with the relations $\mathbf{X}^{(e)} = -\mathbf{X}^{(p)}$, $\mathbf{Y}^{(e)} = -\mathbf{Y}^{(p)}$. The solutions of the first type correspond to «acoustic» type of oscillations of the particle density, which retains the local electrical neutrality of the whole system. Thus, in the calculations of optical characteristics of electron-positron droplets, we should take into account only antisymmetric (dipole or «optical») modes. This allows us to transform the equation (20) into the equivalent form with matrix size $2N_{eh} \times 2N_{eh}$ with N_{eh} independent solutions [15, 17]:

$$\begin{pmatrix} \tilde{\mathbf{A}} & \tilde{\mathbf{B}} \\ \tilde{\mathbf{B}}^* & \tilde{\mathbf{A}}^* \end{pmatrix} \begin{pmatrix} \mathbf{X} \\ \mathbf{Y} \end{pmatrix} = \Omega^{(RPAE)} \begin{pmatrix} \mathbf{X} \\ -\mathbf{Y} \end{pmatrix}, \tag{26}$$

where

$$\begin{aligned} \tilde{A}_{im,jn} &= A_{im,jn} + C_{im,jn} = \\ &= \omega_{im}\delta_{ij}\delta_{mn} + 4\langle in|V|mj\rangle - \langle in|V|jm\rangle, \\ \tilde{B}_{im,jn} &= B_{im,jn} + D_{im,jn} = \\ &= 4\langle ij|V|mn\rangle - \langle ij|V|nm\rangle. \end{aligned} \tag{27}$$

Note, that the orthonormality conditions (24) for eigenvectors of equation (26) remain intact.

The coefficients Y^{ν}_{mi} obtained by solving the equation (26) assess the contribution of the correlations to the ground HF state. Finally, the correlation correction to the HF ground state energy within RPAE can be written as [21]

$$\Delta E^{(RPAE)} = -\sum_{im,\nu} \Omega^{(RPAE)}_{\nu} \left|Y^{\nu}_{im}\right|^2, \tag{28}$$

where the summation is performed over all excited states $|\Phi_{\nu}\rangle$, the energies $\Omega^{(RPAE)}_{\nu}$ are the eigenvalues of equation (26).

Note that the same result can be obtained within Tamm – Dancoff approximation [21]

$$\Delta E^{(RPAE)} = -\frac{1}{2}\sum_{\nu} (\Omega^{(RPAE)}_{\nu} - \Omega^{(TDA)}_{\nu}) \tag{29}$$

where $\Omega^{(TDA)}_{\nu}$ are the eigenfrequencies of the corresponding Tamm – Dancoff equation

$$\tilde{\mathbf{A}}\mathbf{X} = \Omega^{(TDA)}\mathbf{X}. \tag{30}$$

Besides the correlation contribution to the ground state energy, the correlations significantly affect the optical properties of many-particle system. Indeed, the static dipole polarizability of an electrically neutral electron-positron droplet can be calculated as [15, 17]

$$\alpha^{(e+p)} = \sum_{\nu} \frac{f_{\nu}}{\mu\Omega^2_{\nu}}. \tag{31}$$

Here the summation is over all excited states of the system, μ is the reduced mass of the electron-positron pair

$$\mu = \frac{m_e m_p}{m_e + m_p} = \frac{m}{2},$$

f_{ν} are the dipole transition oscillator strengths between the ground state and the ν-th excited many-particle state with frequency Ω_{ν}.. The oscillator strengths are defined by the following expression:

$$f_{\nu} = \frac{4}{3}\mu\Omega_{\nu}D^2_{\nu}. \tag{32}$$

They satisfy the sum rule $\sum_{\nu} f_{\nu} = N$ [18, 21]. The transition matrix elements D_{ν} are calculated by summation over all the one-particle excited states:

$$D_{\nu} = \sum_{im} (X^{\nu}_{im}d_{im} + Y^{\nu}_{im}d_{mi}), \tag{33}$$

where d_{im} are the single-particle dipole amplitudes in the length gauge [18]:

$$d_{im} = \int P_{n_i l_i}(r) r P_{n_m l_m}(r) dr, \ ..., \ l_m = l_i \pm 1. \tag{34}$$

III. Results of Calculations

In order to solve the equations (20) and (26) it is necessary to have a complete basis of the one-particle wave functions (8) including both discrete and continuum spectra states. To perform the numerical calculations, we use replacing the true virtual one-particle states by the discrete spectrum of pseudostates. This approach is based on the representation of the radial wavefucntions (8) as a linear combination of the piecewise continuous polynomials defined on a sufficiently large radial interval [0, $R_{\max}$], so-called B-splines [22]. The new rede-

fined functions $P_{nl}(r)$ satisfy the boundary conditions $P_{nl}(0) = P_{nl}(R_{\max}) = 0$, i. e. the system is supposed to be placed in the spherical potential well with the walls of infinite height. This approach allows us to carry out summation over a finite number of discrete pseudostates instead of integrating over continuous part of the spectrum.

In our calculations we use 50 B-splines of the order 7 for each orbital quantum number l, and implement the summation over transferred angular momenta up to $l = 10$. The partial contributions of the terms with different transferred angular momenta to the correlational part of the energy are shown in Fig. 1 for the electron-positron clusters of different sizes. One can see that for small clusters the main contribution comes from the dipole term while the contributions with larger transferred momenta rapidly decrease. At the same time, for clusters with $N > 20$ the terms with larger transferred momenta play more significant role and their contributions decrease more slowly with l.

The results of the calculations of the total energies per electron-positron pair for the clusters of different size are presented in Table 2 and Fig. 2. For comparison, we present the results obtained within the HF approximation, the LDA, the second order

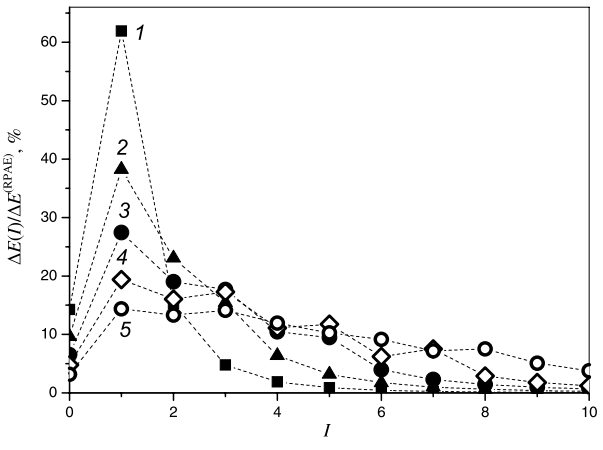

Fig. 1. The partial contributions to the correlation energy of electron-positron clusters as a function of transferred angular momentum for the systems with different number of electron-positron pairs: $N = 2$ (*1*), $N = 8$ (*2*), $N = 20$ (*3*), $N = 40$ (*4*), $N = 92$ (*5*)

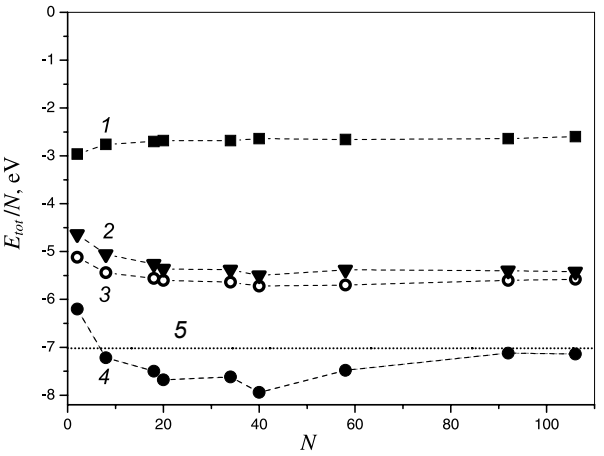

Fig. 2. The total energies of clusters per electron-positron pair as a function of cluster size obtained within the different theoretical approaches: *1* – HF_[12], *2* – LDA_[11], *3* – MP2, *4* – RPAE; *5* – the result of *ab initio* calculations of dipositronium molecule [4]

Möller – Plesset approximation (MP2) and the RPAE as well.

As it can be seen from Table 2, as well as from Fig. 2, the closed-shell clusters containing 20, 34 and 40 electron-positron pairs have the lowest values of the energy. There is a conspicuous minimum of the total energy calculated with the correlation corrections, while the

Table 3

Reduced static dipole polarizabilities $\alpha^{(e+p)}/R^3$ for the clusters consisting of the different numbers of electron-positron pairs N. For comparison, there are reduced polarizabilities of electron subsystem presented here and obtained in a frozen positively charged core $\alpha^{(e)}/R^3$

N	$\alpha^{(e+p)}/R^3$	$\alpha^{(e)}/R^3$
2	1.40	1.24
8	1.58	1.39
18	1.46	1.29
20	1.54	1.38
34	1.39	1.25
40	1.50	1.37
58	1.33	1.21
92	1.30	1.20
106	1.31	1.21

energies within Hartree – Fock approximation have approximately equal values for almost all of the clusters considered (except for the case of $N = 2$). Besides, the calculations with the correlation corrections $(E_{tot}^{(HF)} + \Delta E^{(RPAE)})/N$ show that the pair energy of two electron-positron cluster is higher than half of the total energy of the molecule dipositronium (7.02 eV) obtained in the *ab initio* calculations [4], while the pair energies of other systems are visibly lower.

Thus, it can be assumed that formation of a cluster consisting of two electron-positron pairs bound by exchange-correlation interaction is energetically unfavorable in comparison with the positronium molecule the structure of which is determined by van der Waals interaction [8].

As for the larger systems, the cluster structure of an electron-positron droplet becomes more beneficial. In favor of the latter statement, the behavior of the reduced static dipole polarisability with cluster size reveals the maximum values for $N = 8 - 40$. Table 3 presents the ratios of the static dipole polarizability of electron-positron droplets calculated in RPAE, to the value of the effective cluster radius in the third degree. The effective radius is calculated by the simple formulae

$$R = \sqrt[3]{\frac{3}{4\pi\,\bar{n}}}, \qquad (35)$$

where $\bar{n}$ is the average concentration of electron-positron pairs in the system:

$$\bar{n} = \frac{1}{N}\int \rho_e(\mathbf{r})\rho_p(\mathbf{r})d\mathbf{r}. \qquad (36)$$

For the systems of medium size $N = 8 - 40$ there is an admittedly optimal proportion of the particles in surface area, that give the main contribution to the polarization interaction, with respect to the volume area particles.

It should be noted that, as one may see from Table 3, the polarizability of mutually correlated electron-positron droplets $\alpha^{(e+p)}$ for all N is somewhat higher than the corresponding values calculated in the frozen core of one of the subsystems $\alpha^{(e)}$.. It means that the correlations between the particles constituting the cluster subsystems influence not only the stability of the electron-positron droplets as a whole, but also their optical properties.

IV. Concluding Remarks

This work presents the results of the total energy calculations as well as the static polarisability of electron-positron clusters with closed shells. The calculations fulfilled show that the single-particle approximations like Hartree – Fock one and the Local Density Approximations are not able to provide a stable state of such systems. The total energies obtained within HF and LDA calculations are higher than the corresponding energies of electron-positron systems bound by van der Waals interactions.

However, using HF approximation as a zero guess, it is possible to take into account additional correlations aroused by the strong polarization interaction of electron-positron system. The calculations with accounting for the second order of perturbation theory and within the RPAE reveal the significant decrease of the total energies.

In particular, the RPAE results for the clusters with the number of pairs $N \geq 8$ are below the energy level of −7.02 eV, which is equal to the total energy per pair of positronium molecule [4]. The calculations reveal the minimum of the total energy per pair for the numbers of N in the range between 20 and 40, and this corresponds to the most stable electron-positron clusters. This minimum could be understood if one considered the behavior of reduced static dipole polarizability of electron-positron systems, which also has a visible maximum in the same size region.

The existence of stable electron-positron clusters could be investigated experimentally. These objects can be created during condensation or density collapse of electrons and positrons in a certain volume. The necessary conditions for such process can be obtained in experiments with electron and positron aligned beams of high density and of equal energy. The stable clusters can be determined by the methods of optical spectroscopy. Indeed, the relevant time corresponding to the frequency of dipole resonance is about ~1.5 fs [17] while the lifetime of the annihilation decay of dipositronium molecular is the five orders of magnitude larger [5]. This condition can provide one with enough life time of electron-positron cluster to study its optical properties.

REFERENCES

1. **Deutsch M.** Evidence for the formation of positronium in gases. *Phys. Rev.* 1951. Vol. 82, pp. 455–456.

2. **Wheeler J.A.** Polyelectrons, *Annals of the New York Academy of Sciences.* 1946. Vol. 48, pp. 219–238.

3. **Hylleraas E.A., Ore A.** Binding energy of the positronium molecule. *Phys. Rev.* 1947. Vol. 71, pp. 493–496.

4. **Kinghorn D.B., Poshusta R.D.** Nonadiabatic variational calculations on dipositronium using explicitly correlated Gaussian basis functions. *Phys. Rev. A.* 1993. Vol. 47, pp. 3671–3681.

5. **Kozlovski P.M., Adamowicz L.** Lifetime of positronium molecule. Study with Boy's explicitly correlated Gaussians. *J. Phys. Chem.* 1996. Vol. 100, pp. 6266–6271.

6. **Rebane T.K., Zotev V.S.** Calculation of energy and properties of a positronium molecule. *Optics and spectroscopy*, 1996. Vol. 80, pp. 355–359.

7. **Cassidy D.B., Mills A.P. Jr.** The production of molecular positronium. *Nature.* 2007. Vol. 449, pp. 195–197.

8. **Yabu H.** Many positron and positronium interactions. *Nucl. Instr. and Meth. in Phys. Res. B.* 2004. Vol. 221, pp. 144–148.

9. **Keldysh L.V.** Electron-hole drops in semiconductors. *Sov. Phys. Us.* 1970. Vol. 13, pp. 292–294. (rus)

10. **Keldysh L.V.** The electron-positron-hole liquid in semiconductors. *Contem. Phys.* 1986. Vol. 27, pp. 395–428.

11. **Solov'yov A.V., Ivanov V.K., Polozkov R.G.** Electron-positron quantum droplets. *Eur. Phys. J. D.* 2006. Vol. 40, pp. 313–316.

12. **Ivanov V.K., Polozkov R.G., Solov'yov A.V.** Electron-positron clusters: structure and stability. Latest Advances in Atomic Cluster Collisions: Structure and Dynamics from the Nuclear to the Biological Scale; ed. J.-P. Connerade and A.V. Solov'yov, Imperial College Press, 2008, pp. 297–310.

13. **Yatsyshin P.I., Polozkov R.G., Ivanov V.K. and Solov'yov A.V.** Structure of electron-positron clusters and Hartree – Fock approximation. *Phys. Scr.* 2009. Vol. 80(4), pp. 048126(1)–048126(4).

14. **Yatsyshin P.I., Ivanov V.K., Polozkov R.G., Solov'yov A.V.** The structure of electron-positron clusters. Hartree – Fock approximation. *St. Petersburg State Polytechnical University Journal: Physics and Mathematics.* 2009. No. 1(73), pp. 9–17. (rus)

15. **de Heer W.A.** The physics of simple metal clusters: experimental aspects and simple models. *Rev. Mod. Phys.* 1993. Vol. 65, pp. 611–676.

16. **Ivanov V.K., Kharchenko V.A., Ipatov A.N., Zhizhin M.L.** Optimized jellium model for metal clusters. *JETP Letters*, 1994, Vol. 60, pp. 353–359.

17. **Ipatov A.N., Ivanov V.K., Polozkov R.G.** Effect of multiparticle correlations on the stability of electron-positron clusters. *JETP.* 2013. Vol. 117, pp. 631–634.

18. **Landau L.D., Lifshitz E.M.** Quantum mechanics. Non-relativistic theory, 3rd Ed. New York: Pergamon Press, 1965. 691 p. (rus)

19. **Ipatov A.N.** Influence of interparticle interaction on the optical properties of fermionic systems. *St. Petersburg State Polytechnical University Journal: Physics and Mathematics*, 2013. No. 1(165), pp. 60–70.

20. **Amusia M.Ja., Chernysheva L.V.** Computation of atomic processes. Bristol and Philadelphia: IOPublishing, 1997. 316 p.

21. **Möller C., Plesset M.S.** Note on an approximation treatment for many-electron systems. *Phys. Rev.* 1934, Vol. 46, No. 7, pp. 618–622.

22. **Guet C., Blundell S.A.** Correlation energy in small jellium. *Surf. Rev. Lett.* 1996. Vol. 3, pp. 395–397.

23. **Ring P., Schuck P.** The nuclear many-body problem. Berlin: Springer-Verlag, 2004. 717 p.

24. **de Boor C.** A practical guide to splines. New York: Springer-Verlag, 1978. 346 p.

СПИСОК ЛИТЕРАТУРЫ

1. **Deutsch M.** Evidence for the formation of positronium in gases. *Phys. Rev.* 1951. Vol. 82, pp. 455–456.

2. **Wheeler J.A.** Polyelectrons, *Annals of the New York Academy of Sciences.* 1946. Vol. 48, pp. 219–238.

3. **Hylleraas E.A., Ore A.** Binding energy of the positronium molecule. *Phys. Rev.* 1947. Vol. 71, pp. 493–496.

4. **Kinghorn D.B., Poshusta R.D.** Nonadiabatic variational calculations on dipositronium using explicitly correlated Gaussian basis functions. *Phys. Rev. A.* 1993. Vol. 47, pp. 3671–3681.

5. **Kozlovski P.M., Adamowicz L.** Lifetime of positronium molecule. Study with Boy's explicitly correlated Gaussians. *J. Phys. Chem.* 1996. Vol. 100, pp. 6266–6271.

6. **Ребане Т.К., Зотев В.С.** Расчет энергии и свойств молекулы позитрония// Оптика и спектроскопия. 1996. Т. 80. № 3. С. 402 – 406.

7. **Cassidy D.B., Mills A.P. Jr.** The production of molecular positronium. *Nature*. 2007. Vol. 449, pp. 195–197.

8. **Yabu H.** Many positron and positronium interactions. *Nucl. Instr. and Meth. in Phys. Res. B*. 2004. Vol. 221, pp. 144–148.

9. **Келдыш Л.В.** Электронно-дырочные капли в полупроводниках // Успехи физических наук. 1970. № 3. С. 514–517.

10. **Keldysh L.V.** The electron-positron-hole liquid in semiconductors. *Contem. Phys.* 1986. Vol. 27, pp. 395–428.

11. **Solov'yov A.V., Ivanov V.K., Polozkov R.G.** Electron-positron quantum droplets. *Eur. Phys. J. D*. 2006. Vol. 40, pp. 313–316.

12. **Ivanov V.K., Polozkov R.G., Solov'yov A.V.** Electron-positron clusters: structure and stability. Latest Advances in Atomic Cluster Collisions: Structure and Dynamics from the Nuclear to the Biological Scale; ed. J.–P. Connerade and A.V. Solov'yov, Imperial College Press, 2008, pp. 297–310.

13. **Yatsyshin P.I., Polozkov R.G., Ivanov V.K. and Solov'yov A.V.** Structure of electron-positron clusters and Hartree – Fock approximation. *Phys. Scr.* 2009. Vol. 80(4), pp. 048126(1)–048126(4).

14. **Яцышин П.И., Иванов В.К., Полозков Р.Г., Соловьёв А.В.** Структура электрон-позитронных кластеров. Приближение Хартри – Фока // Научно-технические ведомости СПбГПУ. Физико-математические науки. 2009. № 1 (73). С. 9–17.

15. **de Heer W.A.** The physics of simple metal clusters: experimental aspects and simple models. *Rev. Mod. Phys.* 1993. Vol. 65, pp. 611–676.

16. **Ivanov V.K., Kharchenko V.A., Ipatov A.N., Zhizhin M.L.** Optimized jellium model for metal clusters. *JETP Letters*, 1994, Vol. 60, pp. 353–359.

17. **Ipatov A.N., Ivanov V.K., Polozkov R.G.** Effect of multiparticle correlations on the stability of electron-positron clusters. *JETP*. 2013. Vol. 117, pp. 631–634.

18. **Ландау Л.Д., Лифшиц Е.М.** Квантовая механика. Нерелятивистская теория. Изд. 2-е, испр. и доп. М.: Наука, 1963. 704 с.

19. **Ипатов А.Н.** Влияние межчастичного взаимодействия на оптические свойства систем фермионов // Научно-технические ведомости СПбГПУ. Физико-математические науки. 2013. № 1 (165). С. 60–70.

20. **Amusia M.Ja., Chernysheva L.V.** Computation of atomic processes. Bristol and Philadelphia: IOPublishing, 1997. 316 p.

21. **Möller C., Plesset M.S.** Note on an approximation treatment for many-electron Systems. *Phys. Rev.* 1934, Vol. 46, No. 7, pp. 618–622.

22. **Guet C., Blundell S.A.** Correlation energy in small jellium. *Surf. Rev. Lett.* 1996. Vol. 3, pp. 395–397.

23. **Ring P., Schuck P.** The nuclear many-body problem. Berlin: Springer-Verlag, 2004. 717 p.

24. **de Boor C.** A practical guide to splines. New York: Springer-Verlag, 1978. 346 p.

ИПАТОВ Андрей Николаевич – *доктор физико-математических наук, профессор кафедры экспериментальной физики Санкт-Петербургского государственного политехнического университета.*
195251, Россия, г. Санкт-Петербург, Политехническая ул., 29
andrei_ipatov@mail.ru

ИВАНОВ Вадим Константинович – *доктор физико-математических наук, профессор кафедры экспериментальной физики Санкт-Петербургского государственного политехнического университета.*
195251, Россия, г. Санкт-Петербург, Политехническая ул., 29
ivanov@physics.spbstu.ru

ПОЛОЗКОВ Роман Григорьевич – *кандидат физико-математических наук, доцент кафедры экспериментальной физики Санкт-Петербургского государственного политехнического университета.*
195251, Россия, г. Санкт-Петербург, Политехническая ул., 29
polozkov@tuexph.stu.neva.ru

UDC 519.622

E.A. Novikov

Institute of Computational Modeling SB RAS
50 Akademgorodok, ICM SD RAS, 660036, Krasnoyarsk, 660036, Russia

A SECOND-ORDER METHOD FOR ADDITIVE STIFF PROBLEMS

E.A. Новиков

МЕТОД ВТОРОГО ПОРЯДКА ДЛЯ РЕШЕНИЯ АДДИТИВНЫХ ЖЕСТКИХ ЗАДАЧ

A second-order accuracy method for additive stiff systems of ordinary differential equations is developed. Inequalities for accuracy control are obtained. Numerical results are presented.

STIFF ADDITIVE PROBLEM, (M,K)-METHOD, ERROR ESTIMATION.

Построен метод второго порядка точности для решения жестких аддитивных систем обыкновенных дифференциальных уравнений. Получено неравенство для контроля точности вычислений. Приведены результаты расчетов.

ЖЕСТКАЯ АДДИТИВНАЯ ЗАДАЧА, (М,К)-МЕТОД, ОЦЕНКА ОШИБКИ

I. Introduction

For the numerical solution of the Cauchy problem

$$y' = f(t, y), \quad y(t_0) = y_0, \quad t_0 \le t \le t_k, \qquad (1)$$

for a stiff system of ordinary differential equations, L-stable methods are usually applied. Here y and f are real vector functions of dimension N, t is an independent variable.

For a large-scale problem (1), the total computational cost of a method with the unbounded stability domain in fact is completely defined by the time of the calculation and decomposition of Jacobi matrix of the system (1). In a number of algorithms, Jacobi matrix is frozen, i. e. one and the same matrix is used at several integration steps. This enables one to decrease a computational cost considerably. This approach is widely used when implementing semi-implicit and implicit methods of Runge – Kutta type and multistep methods of Adams and Gear type (see, for example, Ref. [9]). However, for iteration-free methods [2, 5, 8] the problem of the freezing or any other approximation of Jacobi matrix is rather more complicated. On the other hand, the problem (1) can be written in the form [1, 6]:

$$y' = [f(t, y) - By] + By,$$
$$y(t_0) = y_0, \quad t_0 \le t \le t_k, \qquad (2)$$

where B is an approximation of Jacobi matrix.

Assuming that the term By is completely responsible for stiffness, the expression in the brackets can be considered as a non-stiff part. Taking into account this fact when constructing an iteration-free method enables one, in particular, to freeze Jacobi matrix, which can be calculated analytically as well as numerically, in integration algorithms. For some problems, the symmetric part of Jacobi matrix or its diagonal approximation can be taken as the matrix B. Here we propose a second-order accuracy method which admits different types of approximation of Jacobi matrix. An error estimate and an inequality for the calculation accuracy control are obtained. Numerical results are presented.

II. A Numerical Scheme for Autonomous Problems

We consider the Cauchy problem for an autonomous system of the form

$$y' = \varphi(y) + g(y), \quad y(t_0) = y_0, \quad t_0 \le t \le t_k, \quad (3)$$

where y, φ, and g are real vector functions of dimension N, and t is an independent variable.

We assume that the function $g(y)$ is completely responsible for stiffness and $\varphi(y)$ is a non-stiff part. For (3), we consider a method of the form

$$\begin{gathered} y_{n+1} = y_n + \sum_{i=1}^{4} p_i k_i; \quad D_n = E - ahg'_n; \\ k_1 = h\varphi(y_n); \quad Dk_2 = h[\varphi(y_n) + g(y_n)]; \\ Dk_3 = k_2; \\ k_4 = h\varphi(y_n + \beta_{41}k_1 + \beta_{42}k_2 + \beta_{43}k_3), \end{gathered} \quad (4)$$

where E is the identity matrix; $g'_n = \partial g(y_n)/\partial g$; k_i, $1 \le i \le 4$ are the stages of the method; a, p_i, β_{4j}, k_i, $1 \le i \le 4$, $2 \le j \le 3$ are numerical coefficients which define accuracy and stability properties of (4).

To study the scheme (4), we substitute Taylor expansion of the stages k_i, $1 \le i \le 4$ in the first formula of (4). This gives

$$\begin{gathered} y_{n+1} = y_n + (p_1 + p_2 + p_3 + p_4)h\varphi_n + \\ + (p_2 + p_3)hg_n + (\beta_{41} + \beta_{42} + \beta_{43})p_4h^2\varphi'_n\varphi_n + \\ + (\beta_{42} + \beta_{43})p_4h^2\varphi'_n g_n + a(p_2 + 2p_3)h^2g'_n\varphi_n + \\ + a(p_2 + 2p_3)h^2g'_ng_n + O(h^3), \end{gathered}$$

where the elementary differentials φ_n, g_n, $\varphi'_n\varphi_n$, φ'_ng_n, $g'_n\varphi_n$, and g'_ng_n are calculated at an approximate solution y_n.

Taylor expansion of the exact solution $y(t_{n+1})$ is of the form

$$\begin{gathered} y(t_{n+1}) = y(t_n) + h(\varphi + g) + \\ + 0.5h^2(\varphi'\varphi + \varphi' g + g'\varphi + g'g) + O(h^3), \end{gathered}$$

where the elementary differentials φ, g, $\varphi'\varphi$, $\varphi'g$, $g'\varphi$, and $g'g$ are calculated at the exact solution $y(t_n)$. Comparing the above expansions for the condition $y_n = y(t_n)$, we arrive at the second-order conditions for the scheme (4), i. e.

$$\begin{gathered} p_1 + p_2 + p_3 + p_4 = 1, \quad p_2 + p_3 = 1, \\ a(p_2 + 2p_3) = 0.5, \\ (\beta_{41} + \beta_{42} + \beta_{43})p_4 = 0.5, \quad (\beta_{42} + \beta_{43})p_4 = 0.5. \end{gathered}$$

This results in

$$\beta_{41} = 0, \quad p_2 = \frac{4a - 1}{2a}, \quad p_3 = \frac{1 - 2a}{2a},$$

$$p_1 + p_4 = 0, \quad (\beta_{42} + \beta_{43})p_4 = 0.5. \quad (5)$$

Now we study the stability of scheme (4). In this case we may not use the test equation $y' = \lambda y$ with a complex value λ, $\mathrm{Re}(\lambda) < 0$ since there is no sense in splitting the right-hand side of the system of differential equations into stiff and non-stiff parts. Hence, in (3) we put $\varphi(y) = \lambda_1 y$ and $g(y) = \lambda_2 y$ where λ_1 and λ_2 are arbitrary complex numbers. Here λ_1 and λ_2 mean some eigenvalues of the Jacobi matrices of the functions $\varphi(y)$ and $g(y)$, respectively. Applying (4) to the scalar test problem

$$y' = \lambda_1 y + \lambda_2 y, \quad y(0) = y_0, \quad t \ge 0, \quad (6)$$

with the notations $x = \lambda_1 y$ and $z = \lambda_2 y$, we have $y_{n+1} = Q(x,z)y_n$ where

$$\begin{gathered} Q(x,z) = \{1 + (1 - 2a)z + x + \\ + [-2ap_1 - ap_2 + (\beta_{42} + \beta_{43} - 2a)p_4]xz + 0.5x^2 - \\ - a\beta_{42}p_4x^2z + [a^2p_1 + a^2p_4 - a\beta_{42}p_4]xz^2 + \\ + (a^2 - ap_2)z^2\} / (1 - az)^2. \end{gathered}$$

The necessary L-stability condition for the numerical formula (4) with respect to the function $g(y) = \lambda_2 y$ is the relation $Q(x,z) \to 0$ as $z \to -\infty$. From the form of $Q(x,z)$, it follows that this relation is valid provided that $p_2 = a$ and $\beta_{42} = 0$. As a result, taking into account (5), we obtain the set of the coefficients

$$\begin{gathered} \beta_{41} = \beta_{42} = 0, \quad p_2 = a, \quad p_3 = 1 - a, \\ p_4 = -p_1 = 0.5\beta_{43}^{-1} \end{gathered}$$

for the second-order accuracy scheme (4) where β_{43} is a free parameter and a is a root of the equation $a^2 - 2a + 0.5 = 0$. Then, the stability function $Q(x,z)$ of the scheme (4) has the form

$$\begin{gathered} Q(x,z) = [1 + x + 0.5x^2 + (1 - 2a)z + \\ + (1 - 2a)xz] / (1 - az)^2. \end{gathered}$$

For $\varphi(y) = 0$, the scheme (4) coincides with the L-stable (2,1)-method

$$y_{n+1} = y_n + ak_2 + (1 - a)k_3 \text{ [7]}$$

with the stability function $Q(0, z)$ of the form

$$Q(0, z) = [1 + (1 - 2a)z]/(1 - az)^2$$

and the local error $\delta_{n,L}$ of the form

$$\delta_{n,L} = (a - 1/3)h^3g'^2g + h^3g''g^2/6 + O(h^4).$$

The equation

$$a^2 - 2a + 0.5 = 0$$

has two roots $a_1 = 1 - 0.5\sqrt{2}$ and $a_2 = 1 + 0.5\sqrt{2}$. We take $a = a_1$ since in this case the coefficient of the principal term of the local error of the (2,1)-scheme is smaller. For $g(y) = 0$, (4) is degenerated into an explicit method of the Runge – Kutta type of the form

$$y_{n+1} = y_n + (1 - 0.5/\beta_{43})k_1 + 0.5k_4/\beta_{43}.$$

Notice that the local error $\delta_{n,RK}$ of this scheme can be written in the form

$$\delta_{n,RK} = h^3[\varphi'^2\varphi / 6 + \\ +(1/6 - 0.25/\beta_{43})\varphi''\varphi^2] + O(h^4).$$

Hence, the local error of the explicit formula is minimal provided that $\beta_{43} = 2/3$. Finally, we have the coefficients of the second-order accuracy scheme (4), i. e.

$$a = 1 - \sqrt{2}/2, \quad \beta_{41} = \beta_{42} = 0, \quad \beta_{43} = 2/3,$$

$$p_4 = -p_1 = 3/4, \quad p_2 = a, \quad p_3 = 1 - a.$$

III. Calculation Accuracy Control

Calculation control for the scheme (4) is performed with a first-order accuracy method. With the help of the stages of (4), we can construct a family of first-order numerical formulae of the form

$$y_{n+1,1} = y_n + b_1k_1 + b_2k_2 + b_3k_3 + b_4k_4 + b_5k_5, \quad (7)$$

where $k_5 = hg(y_n)$, b_i are numerical coefficients. Using Taylor expansion of the stages, we see that (7) is of first-order accuracy provided that

$$b_1 + b_2 + b_3 + b_4 = 1$$

and

$$b_2 + b_3 + b_5 = 1.$$

Then an error estimate ε_n for the scheme (4) can be calculated by the formula

$$\varepsilon_n = y_{n+1} - y_{n+1,1}.$$

When choosing the coefficients b_i, $1 \le i \le 4$, one can be guided by different considerations. For instance, if the function $g(y)$ is completely responsible for stiffness of the problem (3), which is the case for many problems (2) for $B = \partial f(y)/\partial y$, then it makes sense to take the set of coefficients

$$b_1 + b_3 + b_4 + b_5 = 0 \text{ and } b_2 = 1$$

or

$$b_1 + b_2 + b_4 + b_5 = 0 \text{ and } b_3 = 1.$$

This technique of the error estimation is used with advantage when implementing the (2,1)-method with analytical calculation of the Jacobi matrix. However, if, for instance, in the problem (2) a diagonal approximation of the Jacobi matrix is used, then for many problems (3) we may not consider the function $\varphi(y)$ as a non-stiff part. In this case, such an estimate may result in the loss of calculation accuracy due to arising instability of the explicit part of the numerical formula (4). From this reasoning, in (7) the coefficients $b_1 + b_5 = 1$ and $b_2 = b_3 = b_5 = 0$ are taken. In this case, (7) is rearranged to the form

$$y_{n+1,1} = y_n + h[\varphi(y_n) + g(y_n)].$$

Numerical results show that the application of this scheme in the estimate results is more reliable control of calculation accuracy.

We point out an important feature of the proposed error estimate. From L-stability of the scheme (4), it follows that for the stability function $Q(x,z)$ we have $Q(x,z) \to 0$ as $z \to -\infty$. For the exact solution

$$y(t_{n+1}) = \exp(x + z)y(t_n)$$

of the problem (6) a similar property holds, hence, it is natural to require that the error estimate ε_n approaches zero as $z \to -\infty$. However, for the proposed estimate we have $\varepsilon_n = O(z)$. Thus, to improve the asymptotic behaviour, instead of ε_n we consider the estimates $\varepsilon_n(j_n)$ of the form $\varepsilon_n(j_n) = D_n^{1-jn}\varepsilon_n$, $1 \le j_n \le 3$. Observe, that in the sense of the principal term, i. e. the first term of Taylor expansion of an error in powers of h, the estimates ε_n and $\varepsilon_n(j_n)$ coincide for any value of j_n, besides, $\varepsilon_n(3) \to 0$ as $z \to -\infty$. Now, for calculation accuracy control we can use the inequality $\|\varepsilon_n(j_n)\| \le \varepsilon$, $1 \le j_n \le 3$, where ε is the required accuracy of calculations. Notice, that the use of $\varepsilon_n(j_n)$ instead of ε_n does not result in considerable increase of a computational cost. For $z \to 0$, the estimate $\varepsilon_n(1) = \varepsilon_n$ is in

agreement with the behaviour of an error and there is no need to check it for other values of j_n. With the drastic increase of the step, the behaviour of ε_n may become inadequate which manifests itself in unreasonable decrease of the step and repeated calculations of a solution. Thus, when implementing an integration algorithm, the inequality for accuracy control is used as follows. For each n the smallest value of j_n which provides this inequality is taken. If it does not hold for any value of j_n, then the step decreases and the solution is recalculated.

IV. A Numerical Scheme for Non-Autonomous Problems

We consider the Cauchy problem for a non-autonomous system of the form

$$y' = \varphi(t, y) + g(t, y), \quad y(t_0) = y_0, \quad t_0 \le t \le t_k,$$

where y, φ, and g are real vector functions of dimension N and t is an independent variable.

Further, we again assume that the function $g(t, y)$ is completely responsible for the stiffness, and $\varphi(t, y)$ is the non-stiff part. For the numerical solution of a non-autonomous problem we consider a method of the form

$$y_{n+1} = y_n + p_1k_1 + \ldots + p_4k_4, \quad D = E - ahg'_n,$$

$$k_1 = h\varphi(t_n, y_n),$$

$$Dk_2 = h[\varphi(t_n, y_n) + g(t_n + ch, y_n)], \quad Dk_3 = k_2, \quad (8)$$

$$k_4 = hf(t_n + [\beta_{41} + \beta_{42} + \beta_{43}]h,$$
$$y_n + \beta_{41}k_1 + \beta_{42}k_2 + \beta_{43}k_3),$$

where E is the identity matrix; $g'_n = \partial g(t_n, y_n)/\partial y$; k_i are the stages of the method; c, a, p_i, β_{4j} are numerical coefficients.

To study the scheme (8), we use Taylor expansion of the stages k_i in powers of h up to the terms of order of h^2. Substituting these series in the first formula of (8), we get

$$y_{n+1} = y_n + (p_1 + p_2 + p_3 + p_4)h\varphi_n +$$
$$+ (p_2 + p_3)hg_n + (\beta_{41} + \beta_{42} + \beta_{43})p_4h^2\varphi'_{tn} +$$
$$+ c(p_2 + p_3)g'_{tn} + (\beta_{41} + \beta_{42} + \beta_{43})p_4h^2\varphi'_{yn}\varphi_n +$$
$$+ (\beta_{42} + \beta_{43})p_4h^2\varphi'_{yn}g_n + a(p_2 + 2p_3)h^2g'_{yn}\varphi_n +$$
$$+ a(p_2 + 2p_3)h^2g'_{yn}g_n + O(h^3),$$

where the elementary differentials are calculated at an approximate solution.

Taylor expansion of the exact solution $y(t_{n+1})$ in the neighbourhood of the point t_n has the form

$$y(t_{n+1}) = y(t_n) + h(\varphi + g) + \frac{1}{2}h^2(\varphi'_t + g'_t +$$
$$+ \varphi'_y\varphi + \varphi'_y g + g'_y\varphi + g'_y g) + O(h^3),$$

where the elementary differentials are calculated at the exact solution. Comparing the series for the condition $y_n = y(t_n)$, we arrive at the second-order accuracy conditions for the scheme (7), i. e.

$$p_1 + p_2 + p_3 + p_4 = 1, \quad p_2 + p_3 = 1,$$

$$(\beta_{41} + \beta_{42} + \beta_{43})p_4 = \frac{1}{2},$$

$$c(p_2 + p_3) = \frac{1}{2}, \quad (\beta_{42} + \beta_{43})p_4 = \frac{1}{2},$$

$$a(p_2 + 2p_3) = \frac{1}{2}.$$

This yields $c = 0.5$. With considerations similar to those for the scheme (4), we obtain the coefficients for the numerical formula (8) of the form

$$a = 1 - \frac{\sqrt{2}}{2}, \ \beta_{41} = \beta_{42} = 0, \ c = \frac{1}{2}, \ \beta_{43} = \frac{2}{3},$$

$$p_4 = -p_1 = \frac{3}{4}, \ p_2 = a, \ p_3 = 1 - a.$$

An inequality for calculation accuracy control is constructed similarly to that for the scheme (4), where in the estimate ε_n an approximation to a solution, obtained with the second-order accuracy method (8), and an approximate solution, calculated by a first-order method of the form

$$y_{n+1,1} = y_n + h[\varphi(t_n, y_n) + g(t_n + 0.5h, y_n)]$$

are used. The choice of the step with respect to the accuracy is performed in the same way as in the case of an autonomous system.

V. The Analysis of Numerical Results

In what follows, the proposed algorithm is called ASODE2. Freezing the Jacobi matrix, i.e. the use of the matrix

$$D_n = E - ahg'_{yn}$$

at several integration steps, is performed by the following rule. If the Jacobi matrix is not

recalculated, then the integration step remains the same to keep the stability of the numerical scheme. An attempt to use the former matrix is performed after each successful integration step. The following three reasons result in unfreezing:

1) violation of an inequality for calculation accuracy control;

2) the number of steps with a frozen matrix exceeds i_h;

3) the forecasted integration step exceeds the last successful step by the factor of q_h.

The parameters i_h and q_h can be used to adjust the method to a specific problem. If $i_h \to \infty$ and $q_h \to \infty$, then the number of integration steps with one and the same Jacobi matrix increases. If $i_h = 0$ and $q_h = 0$, then the matrix is not frozen. Hence, for a large-scale system of ordinary differential equations, it makes sense to take i_h and q_h sufficiently large. In the numerical results presented below, $i_h = 20$ and $q_h = 2$.

All the examples below are rearranged to the form (2). The required calculation accuracy is $\varepsilon = 10^{-2}$. The calculations were performed with PC Intel(R) Core i7-3770S CPU@3.10GHz with double precision. The scheme (4) is of second-order accuracy, hence, there is no sense in higher-order precision in this case. The norm $\|\zeta\|$ in inequalities for accuracy control is calculated by the formula

$$\| \zeta \| = \max_{1 \le i \le N} \left\{ \frac{| \zeta_i |}{| y_n^i | + r} \right\},$$

where i is the number of components, and r is a positive parameter.

If the inequality $|y_n^i| < r$ holds for the i-th component of a solution, then an absolute error εr is controlled, otherwise the relative error ε is controlled. In the calculations, the parameter r is taken so that an actual accuracy for all components of the solution is not lower than the required one. Below is, if, idec, isol denote the total number of integration steps, of right-hand sides of the system (1), of decompositions of the Jacobi matrix, and of calculations of backward Gauss, respectively.

A. Example 1 [4]

$$y_1' = -0.013y_1 - 1000y_1y_3, \quad y_2' = -2500y_2y_3,$$

$$y_3' = -0.013y_1 - 1000y_1y_3 - 2500y_2y_3, \qquad (9)$$

$$t \in [0, 50], \quad y_1(0) = 1, \quad y_2(0) = 1, \quad y_3(0) = 0,$$

$$h_0 = 2.9 \cdot 10^{-4}.$$

The problem (9) is solved by the method (4) with a diagonal approximation of the Jacobi matrix, i. e. in the numerical formula (4) the diagonal Jacobi matrix with the diagonal entries b_{ii} of the form

$$b_{11} = -0.013 - 1000y_3; \; b_{22} = -2500y_3;$$

$$b_{33} = -1000y_1 - 2500y_2$$

is used.

Since in this case the computational cost of the method (4) is close to that of explicit methods, this method is compared in terms of efficiency with the well-known Merson method [3] of the fourth-order accuracy. Calculating an approximate solution with accuracy $\varepsilon = 10^{-2}$ by the ASODE2 algorithm requires 687 steps, the remaining costs are calculated from the form of the scheme (4). The solution of the problem by Merson method requires 400,627 calculations of the right-hand side. In the case of full Jacobi matrix of system (9), the ASODE2 algorithm without freezing Jacobi matrix for the problem (9) requires 38 steps, 38 decompositions of the matrix, and 108 calculations of backward Gauss. The remaining costs are calculated from the form of the scheme (4). In calculations with freezing the Jacobi matrix, the computational cost is as follows:

$$\text{is} = \text{if} = 98, \; \text{idec} = 15, \; \text{isol} = 288.$$

B. Example 2 [4]

$$y_1' = -55y_1 + 65y_2 - y_1y_2,$$

$$y_2' = 0.0785(y_1 - y_2), \quad y_3' = 0.1y_1, \qquad (10)$$

$$t \in [0, 500], \quad y_1(0) = y_2(0) = 1, \quad y_3(0) = 0,$$

$$h_0 = 2 \cdot 10^{-2}.$$

The problem (10) is solved by the method (4) with the diagonal approximation of Jacobi matrix where

$$b_{11} = -55 - y_3; \; b_{22} = -0.0785y_3; \; b_{33} = 0.$$

An approximate solution with accuracy $\varepsilon = 10^{-2}$ by the ASODE2 algorithm is calculated

in 4,953 steps. The solution of the problem by Merson method requires 80,713 calculations of the right-hand side. In the case of the full Jacobi matrix of system (10), the ASODE2 algorithm without freezing Jacobi matrix requires 81 steps, 81 decompositions of Jacobi matrix, and 388 calculations of backward Gauss. In calculations with freezing the matrix, the computational cost is as follows:

is = if = 338, idec = 24, isol = 1,124.

C. Example 3 [8]

$$\begin{gathered} y_1' = 77.27[y_1(1 - 8.375 \cdot 10^{-6} y_1 - y_2) + y_2], \\ y_2' = (y_3 - (1 + y_1)y_2) / 77.27, \\ y_3' = 0.161(y_1 - y_3), \\ t \in [0, 360], \quad y_1(0) = 1, \quad y_2(0) = 2, \\ y_3(0) = 3, \quad h_0 = 10^{-6}. \end{gathered} \tag{11}$$

The problem (11) is solved by the method (4) with the diagonal approximation of Jacobi matrix where

$$b_{11} = 77.27(1 - 1.675 \cdot 10^{-7} y_1 - y_2);$$
$$b_{22} = -(1+y_1)/77.27; \; b_{33} = -0.161.$$

An approximate solution with accuracy $\varepsilon = 10^{-2}$ is calculated by the ASODE2 algorithm in 19,964 steps. Solving the problem by Merson method requires 23 700,664 calculations of the right-hand side. In the case of the full Jacobi matrix of the system (11), the ASODE2 algorithm without freezing Jacobi matrix requires 2,449 steps, 2,652 decompositions of Jacobi matrix, and 6,964 calculations of backward Gauss. The computational cost of the calculations with freezing the matrix is as follows:

is = if = 19,807, idec = 3,431, isol = 50,924.

VI. Conclusion

The proposed integration algorithm serves for the numerical solution of the problems of mechanics of continua after the space discretization by the finite element or finite difference method. In this case, in the problem (3) splitting into the functions $g(y)$ and $\varphi(y)$ is natural, $g(y)$ is a symmetric part related to the second-order differentiation operator and $\varphi(y)$ is a nonsymmetric part (convective terms) related to the first-order differentiation operator. The implementation of the numerical formula (4) requires solving a linear system of algebraic equations twice. In the problems of mechanics of continua, efficiency of an integration algorithm can be improved by means of special methods for linear systems with a symmetric matrix that is positive in many cases.

The scheme (4) can also be applied to locally unstable problems. In this case $\varphi(y)$ is responsible for the eigenvalues of Jacobi matrix with a positive real part. Contrary to A-stable or L-stable methods which usually have a small instability domain and are A-stable or L-stable not only in the left half-plane but in the right half-plane of the plane $\{h\lambda\}$ as well, explicit methods of Runge – Kutta type are unstable practically in the whole right half-plane, hence, they are preferable for determining an unstable solution. For locally unstable problems, splitting the right-hand side of a system of ordinary differential equations into functions $\varphi(y)$ and $g(y)$ from physical considerations usually does not involve difficulties.

The presented numerical results are not oriented to the solution of the problems of mechanics of continua or locally unstable problems, but are related to the study of possibilities of the integration algorithm for some conventional test examples.

The test examples are taken in order to demonstrate different features of the integration algorithm. In the case of similar behavior of several test problems, the simplest example is taken.

The purpose of the calculations is to verify working efficiency of the algorithm with variable step and freezing Jacobi matrix, reliability of the inequality for computation accuracy control and to study possibility of calculations with a diagonal approximation of Jacobi matrix. In the last case the computational cost per step for the proposed algorithm is close to that for explicit methods. In particular, from the analysis of numerical results for stiff problems, it follows that, in the case where methods with unbounded stability domain may not be applied, the algorithm (4) is considerably

more efficient than the Merson method being the most popular among explicit numerical schemes of Runge – Kutta type.

The work is supported by Russian Foundation of Fundamental Researches (projects 11-01-00106 and 11-01-00224).

REFERENCES

1. **Cooper G.J., Sayfy A.** Additive Runge – Kutta methods for stiff ordinary differential equations. *Mathematics of Computation*, 1983, Vol. 40, No. 161, pp. 207–218.

2. **Kaps P., Rentrop P.** Generalized Runge – Kutta methods of order four with step size control for stiff ordinary differential equations. *Numerical Math.*, 1979. No. 33, pp. 55–68.

3. **Merson R.H.** An operational methods for integration processes. *Proc. Symp. on Data Proc.* Weapons Research Establishment, Salisbury, Australia. 1957, pp. 329–330.

4. **Novikov E.A.** Explicit methods for stiff systems. Novosibirsk: Nauka, 1997. (rus)

5. **Novikov E.A., Shitov Yu.A., Shokin Yu.I.** One-step iteration-free methods for solving stiff systems. *Soviet Math. Dokl.*, 1989, Vol. 38, No. 1, pp. 212–216. (rus)

6. **Novikov E.A.** The additive third of order method for solving stiff of nonautonomous problems. *Journal of Applied and Industrial Mathematics*, 2010, Vol. 4, No. 4, pp. 1–12.

7. **Novikov E.A., Shornikov Yu.V.** Computer simulation of stiff hybrid systems. Novosibirsk: Publishing house NGTU, 2012, 450 p.

8. **Rosenbrock H.H.** General implicit processes for the numerical solution of differential equations. *Computer J.* 1963, No. 5, pp. 329–330.

9. **Hairer E., Wanner G.** Solving ordinary differential equations. Stiff and differential-algebraic problems. Berlin: Springer-Verlag, 1991. 528 p.

СПИСОК ЛИТЕРАТУРЫ

1. **Cooper G.J., Sayfy A.** Additive Runge – Kutta methods for stiff ordinary differential equations. *Mathematics of Computation*, 1983, Vol. 40, No. 161, pp. 207–218.

2. **Kaps P., Rentrop P.** Generalized Runge – Kutta methods of order four with step size control for stiff ordinary differential equations. *Numerical Math.*, 1979. No. 33, pp. 55–68.

3. **Merson R.H.** An operational methods for integration processes. *Proc. Symp. on Data Proc.* Weapons Research Establishment, Salisbury, Australia. 1957, pp. 329–330.

4. **Новиков Е.А.** Явные методы для жестких систем. Новосибирск: Наука, 1997. 192 с.

5. **Новиков Е.А., Шитов Ю.А., Шокин Ю.И.** Одношаговые безытерационные методы решения жестких систем // ДАН СССР. 1988. Т. 301. № 6. С. 1310–1314.

6. **Novikov E.A.** The additive third of order method for solving stiff of nonautonomous problems. *Journal of Applied and Industrial Mathematics*, 2010, Vol. 4, No. 4, pp. 1–12.

7. **Новиков Е.А., Шорников Ю.В.** Компьютерное моделирование жестких гибридных систем. Новосибирск: НГТУ, 2012. 450 с.

8. **Rosenbrock H.H.** General implicit processes for the numerical solution of differential equations. *Computer J.* 1963, No. 5, pp. 329–330.

9. **Hairer E., Wanner G.** Solving ordinary differential equations. Stiff and differential-algebraic problems. Berlin: Springer-Verlag, 1991. 528 p.

НОВИКОВ Евгений Александрович – *доктор физико-математических наук, профессор, главный научный сотрудник отдела вычислительной математики Института вычислительного моделирования Сибирского отделения РАН.*

660036, Россия, Красноярск, Академгородок, 50

novikov@icm.krasn.rr

Scientific journal

ST. PETERSBURG STATE POLYTECHNICAL UNIVERSITY JOURNAL.
PHYSICS AND MATHEMATICS
№ 4-2 (182) 2013

The founder of the journal is the Federal State Budgetary Educational Institution of Higher Professional Education – St. Petersburg State Polytechnical University.

The journal is registered with the Federal Service for Supervision in the Sphere of Telecom, Information Technologies and Mass Communications (ROSKOMNADZOR).
Certificate ПИ № ФС77-52146 issued December 11, 2012.

Digital typesetting by *A.N. Smirnov*

The Polytechnical University Publishing House is headed by *A.V. Ivanov*

Approved for print December 27, 2013. Paper size: 60×84 1/8 Print run: 1000
Offset printing; Convent. Print. Sheets – 21.71; Account. & Publ. lists – 21.7

St. Petersburg State Polytechnical University.
Polytechnical University Publishing House,
member of the Publishing-Polygraphic Association of Universities of Russia.
University and publishing house address:
29 Politekhnicheskaya St., St. Petersburg, 195251, Russia.

Научное издание

НАУЧНО-ТЕХНИЧЕСКИЕ ВЕДОМОСТИ
САНКТ-ПЕТЕРБУРГСКОГО ГОСУДАРСТВЕННОГО ПОЛИТЕХНИЧЕСКОГО УНИВЕРСИТЕТА.
ФИЗИКО-МАТЕМАТИЧЕСКИЕ НАУКИ
№ 4-2 (182) 2013

Учредитель – Федеральное государственное бюджетное образовательное учреждение высшего профессионального образования «Санкт-Петербургский государственный политехнический университет»

Журнал зарегистрирован Федеральной службой по надзору в сфере информационных технологий и массовых коммуникаций (Роскомнадзор).
Свидетельство о регистрации ПИ № ФС77-51457 от 19.10.2012 г.

Телефон редакции 294-22-85

E-mail: physics@spbstu.ru

Компьютерная верстка *А.Н. Смирнова*

Директор Издательства Политехнического университета *А.В. Иванов*

Лицензия ЛР № 020593 от 07.08.97

Подписано в печать 27.12.2013. Формат 60×84 1/8. Бум. тип. № 1.
Печать офсетная. Усл. печ. л. 21,71. Уч.-изд. л. 21,71. Тираж 1000. Заказ

Санкт-Петербургский государственный политехнический университет
Издательство Политехнического университета
член Издательско-полиграфической ассоциации университетов России
Адрес университета и издательства: 195251, Санкт-Петербург, ул. Политехническая, д. 29.

УСЛОВИЯ ПУБЛИКАЦИИ СТАТЕЙ

в журнале «Научно-технические ведомости Санкт-Петербургского государственного политехнического университета. Физико-математические науки»

ОБЩИЕ ПОЛОЖЕНИЯ

Журнал «Научно-технические ведомости Санкт-Петербургского государственного политехнического университета. Физико-математические науки» является периодическим печатным научным рецензируемым изданием. Зарегистрирован в Федеральной службе по надзору в сфере информационных технологий и массовых коммуникаций (Свидетельство ПИ №ФС77-52144 от 11 декабря 2012 г.) и распространяется по подписке агентства «Роспечать» (индекс издания 71823).

С 2008 г. выпускается в составе сериального периодического издания «Научно-технические ведомости СПбГПУ» (ISSN 1994-2354). Сохраняя преемственность и продолжая научные и публикационные традиции сериального издания «Научно-технические ведомости СПбГПУ», издается под сдвоенными международными стандартными сериальными номерами **ISSN 1994-2354, (сериальный) ISSN 2304-9782**. С 2012 г. начат выпуск журнала в двуязычном оформлении.

Издание входит в Перечень ведущих научных рецензируемых журналов и изданий (перечень ВАК) и принимает для печати материалы научных исследований, а также статьи для опубликования основных результатов диссертаций на соискание ученой степени доктора наук и кандидата наук по следующим основным научным направлениям: **Физика, Математика, Механика, Астрономия**. Научные направления журнала учитываются ВАК Минобрнауки РФ при защите докторских и кандидатских диссертаций в соответствии с Номенклатурой специальностей научных работников.

Журнал представлен в Реферативном журнале ВИНИТИ РАН и включен в фонд научно-технической литературы (НТЛ) ВИНИТИ РАН, а также в международной системе по периодическим изданиям “Ulrich’s Periodicals Directory”. Индексирован в базе данных «Российский индекс научного цитирования» (РИНЦ).

Периодичность выхода журнала – 4 номера в год.

Редакция журнала соблюдает права интеллектуальной собственности и со всеми авторами научных статей заключает издательский лицензионный договор.

2. ТРЕБОВАНИЯ К ПРЕДСТАВЛЯЕМЫМ МАТЕРИАЛАМ

2.1. Оформление материалов

1. Объем статей докторов наук, профессоров, докторантов, соискателей ученой степени доктора наук, как правило, – 12–20 страниц формата А-4. Количество рисунков не должно превышать четырех, таблиц – трех, литературных источников – пятнадцати.

2. Объем статей преподавателей, сотрудников, соискателей ученой степени кандидата наук, как правило, – 8–15 страниц формата А-4, объем статей аспирантов – 8 страниц формата А-4. Количество рисунков не должно превышать трех, таблиц – двух, литературных источников – десяти.

3. Авторы должны придерживаться следующей обобщенной структуры статьи: вводная часть (0,5–1 стр., актуальность, существующие проблемы); основная часть (постановка и описание задачи, изложение и суть основных результатов); заключительная часть (0,5–1 стр., предложения, выводы), список литературы (оформление по ГОСТ 7.07-2009).

4. Число авторов статьи не должно превышать трех человек.

5. Набор текста осуществляется в редакторе MS Word, формулы – в редакторе MS Equation. Таблицы набираются в том же формате, что и основной текст.

Шрифт – TNR, размер шрифта основного текста – 14, интервал – 1,5, таблицы большого размера могут быть набраны 12 кеглем. Параметры страницы: поля слева – 3 см, сверху, снизу – 2,5 см, справа – 2 см, текст размещается без переносов. Абзацный отступ – 1 см.

2.2. Представление материалов

Вместе с материалами статьи должны быть обязательно представлены:

- номер УДК в соответствии с классификатором (в заголовке статьи);
- аннотация (2–3 предложения) на русском и английском языках;
- ключевые слова (5–7) на русском и английском языках;
- сведения об авторах на русском и английском языках: ФИО, место работы, должность, ученое звание, ученая степень, контактные телефоны, e-mail;
- аспиранты предоставляют документ отдела аспирантуры, заверенный печатью;
- рецензия на имя зам. главного редактора, подписанная специалистом, имеющим ученую степень доктора наук и/или ученое звание профессора. Рецензия должна быть ОБЯЗАТЕЛЬНО заверена в отделе кадров. Рецензент несет ответственность за содержание статьи, достоверность представленных материалов.
- акт экспертизы о возможности опубликования материалов в открытой печати.

Предоставление всех материалов осуществляется по электронной почте на адрес редакции: physics@spbstu.ru .

2.3. Рассмотрение материалов

Предоставленные материалы (п. 2.2) первоначально рассматриваются редакционной коллегией и передаются для рецензирования. После одобрения материалов, согласования различных вопросов с автором (при необходимости) редакционная коллегия сообщает автору решение об опубликовании статьи. В случае отказа в публикации статьи редакция направляет автору мотивированный отказ.

При отклонении материалов из-за нарушения сроков подачи, требований по оформлению или как не отвечающих тематике журнала материалы не публикуются и не возвращаются.

Редакционная коллегия не вступает в дискуссию с авторами отклоненных материалов.

Публикация материалов аспирантов очной бюджетной формы обучения осуществляется бесплатно в соответствии с очередностью.

При поступлении в редакцию значительного количества статей их прием в очередной номер может закончиться ДОСРОЧНО.

Более подробную информацию можно получить по телефону редакции:
(812) 294-22-85 с 10.00 до 18.00 – Александра Сергеевна
или по e-mail: physics@spbstu.ru